

AN ABSTRACT OF THE DISSERTATION OF

Choah Shin for the degree of Doctor of Philosophy in Mathematics

presented on May 24, 2021.

Title: Multiphase Flow and Transport in Porous Media with Phase Transition at Multiple Scales: Modeling, Numerical Analysis, and Simulation

Abstract approved: \_\_\_\_\_

Malgorzata S. Peszyńska

In this dissertation we consider two application specific flow and transport models in porous media at multiple scales: 1) methane gas transport models for hydrate formation and dissociation in the subsurface under two-phase conditions, and 2) coupled flow and biomass-nutrient model for biofilm growth in complex geometries with biofilm, and its impact via upscaling from pore scale to Darcy scale on Darcy scale permeability. Both projects are motivated by the challenges from real-life applications in the subsurface.

First we consider the simplified methane gas transport models at Darcy scale under equilibrium and non-equilibrium conditions. The equilibrium model (EQ) is a conservation law with a nonsmooth space-dependent flux function, similar to those that are known in other applications including the two-phase flow in a heterogeneous porous medium, traffic flow on roads, and nonlinear elasticity in mixed materials. There are two unknowns in (EQ) models which are bound together by a relationship called nonlinear complementarity constraint and represented by a multivalued graph. Our main result is the weak stability of an upwind-implicit scheme for a regularized (EQ). To our best knowledge, this is the first such result for the transport model. We also consider kinetic models which approximate (EQ) and are useful when we simulate the hydrate phase change at shorter time scales, e.g., after a seismic event. After a rigorous analysis of three kinetic models, we focus on the analysis of a particular model robust across the unsaturated and saturated conditions. We also prove the weak stability of this model and confirm the rate of convergence  $O(\sqrt{h})$  for both equilibrium and kinetic models. We choose various equilibrium and non-equilibrium scenarios relevant to the applications, and we provide 1d simulation results which illustrate the theory.

Next we study the coupled biomass-nutrient-flow dynamics in a complicated pore scale geometry. Our goal is to describe a new monolithic coupled flow and biomass-nutrient

model and to show its robustness through various numerical experiments. The biomass-nutrient model is of variational inequality type blended with nonsingular diffusivity to ensure the volume constraint while enhancing the biofilm growth mechanism. For the flow, we consider the Brinkman flow with spatially varying permeability which accounts for the flow in (somewhat) permeable domains as well as around these. We apply the flow and biofilm growth model to the entire domain so that the model and the coupling are monolithic. Our overall scheme follows operator splitting and time lagging: we solve advection explicitly by upwind method and diffusion-reaction together using CCFD with time-lagged diffusion coefficients. For flow, we use our version of the Marker-And-Cell method adapted to the heterogeneous Brinkman model on a time-staggered grid. We also present simulation results to show the robustness of our model. To handle the sensitivity of the biomass-nutrient model to its initial data, we introduce a new modeling construction which “promotes” the adhesion of biofilm to the surface. Then we perform the Monte Carlo simulations and construct the probability distributions of upscaled permeability which represent the randomness of complex geometry with biofilm.

©Copyright by Choah Shin

May 24, 2021

All Rights Reserved

Multiphase Flow and Transport in Porous Media with Phase Transition at Multiple  
Scales: Modeling, Numerical Analysis, and Simulation

by  
Choah Shin

A DISSERTATION

submitted to

Oregon State University

in partial fulfillment of  
the requirements for the  
degree of

Doctor of Philosophy

Presented May 24, 2021  
Commencement June 2021

Doctor of Philosophy dissertation of Choah Shin presented on May 24, 2021

APPROVED:

---

Major Professor, representing Mathematics

---

Head of the Department of Mathematics

---

Dean of the Graduate School

I understand that my dissertation will become part of the permanent collection of Oregon State University libraries. My signature below authorizes release of my dissertation to any reader upon request.

---

Choah Shin, Author

## ACKNOWLEDGEMENTS

Throughout my graduate school I have received tremendous support and assistance.

First and foremost, I would like to express my sincere gratitude to my advisor Dr. Malgorzata Peszyńska for her patience, invaluable guidance, leadership, and encouragement and for making me feel continuously supported during my study at OSU. She has been instrumental in my academic and professional developments and achievements, and her insightful advice pushed me to sharpen my thoughts and advance to the next level. I am honored to have her as my advisor.

I would also like to thank Dr. Ralph Showalter, Dr. Robert Higdon, Dr. Mina Ossiander, and Dr. Todd Palmer for serving on my committee. The doors to Dr. Ralph Showalter, Dr. Robert Higdon, and Dr. Mina Ossiander were always open for me whenever I needed advice. I also would like to acknowledge that Dr. Todd Palmer's comments after my prelim exam gave me confidence in my research progress.

I would like to sincerely thank Dr. Mark White for giving me an opportunity to conduct research on methane hydrate at Pacific Northwest National Laboratory. Through this internship I expanded my horizon and pictured my future as a researcher.

Further, I would like to acknowledge the National Science Foundation (NSF) Mathematical Sciences Graduate Internship (MSGI) program for giving me an opportunity to gain internship experience at the National Renewable Energy Laboratory (NREL). While the research conducted at NREL was not directly related to my dissertation, there is no doubt that I advanced my computing skills to develop my simulator for my research. I would like to sincerely thank my mentor, Dr. Michael Martin, at NREL for providing me this research opportunity which built a solid stepping stone on my journey and confident about my goal.

I would like to thank Larry Martin and Joyce O'Neill for the generous support with the endowed fellowship 2019-20. This fellowship made it possible for me to focus on my research.

The research in this dissertation was partially funded by the National Science Foundation (NSF) project NSF DMS-1522734 "Phase transitions in porous media across multiple scales," and NSF DMS-1912938 "Modeling with Constraints and Phase Transitions in Porous Media" (Principal Investigator Malgorzata Peszyńska).

I would also like to thank our BIO2020 team members and Dr. Joseph Umhoefer for your great work. With everyone's contribution we made it possible to publish our

collaborative work successfully.

Special thanks to my friend Dr. Azhar Alhammali for the times we shared throughout the graduate school as well as those times afterward. Without her my journey in graduate school would have been so much harder.

Finally, I would like to thank my parents Oksoo and Keeja Shin for believing in me. None of this work would have been possible without their love and support. Last but not least, I would like to thank my brother Dr. Heewhan Shin for his encouragement while writing this dissertation.

## TABLE OF CONTENTS

	<u>Page</u>
1 Introduction .....	1
1.1 Numerical analysis and simulations of methane transport in hydrate zone under equilibrium and kinetic conditions .....	2
1.2 Coupled biomass-nutrient-flow model in porous media .....	4
2 Background .....	6
2.1 Notation .....	6
2.1.1 Functional spaces .....	7
2.1.2 Special graphs .....	7
2.2 Notation and preliminaries on ODEs with monotone graphs .....	8
2.2.1 Monotone operators .....	10
2.2.2 Evolution ODE with a graph .....	11
2.2.3 Evolution ODE system with graph .....	12
2.3 Notation and preliminaries on flow models .....	13
2.3.1 Darcy flow .....	14
2.3.2 Stokes flow .....	16
2.4 Notation and facts on upscaling via volume averaging .....	18
2.5 Numerical methods for flow and transport .....	20
2.5.1 Discretization of space and time .....	21
2.5.2 Notation for numerical approximations .....	22
2.5.3 Cell-centered finite difference method .....	22
2.5.4 Marker-And-Cell (MAC) method for Stokes flow .....	24
2.5.5 Conservative methods for scalar conservation law .....	26
2.5.6 Operator splitting method .....	28
2.6 Newton's method .....	29
3 Methane gas transport in hydrate stability zone .....	32
3.1 Background on methane hydrate .....	33
3.2 Notation and equilibrium model .....	34
3.2.1 Notation and assumptions for Darcy scale methane hydrate models	34
3.2.2 Mass conservation equations .....	36
3.2.3 Pressure equation .....	36
3.3 Phase equilibria for hydrate crystal formation .....	37
3.3.1 Equilibrium model with multivalued graphs .....	38

TABLE OF CONTENTS (Continued)

		<u>Page</u>
3.4	Summary of coupled thermo-transport model under equilibrium condition	39
3.5	Approximation schemes and resolving coupled components	40
	3.5.1 Time-stepping with macro time steps and concentration time steps.	41
	3.5.2 Spatial discretization.	42
	3.5.3 Notation for stability analysis	43
4	Algorithm, analysis, and simulation for methane hydrate model under equilibrium closure	44
4.1	Assumptions for analysis	44
4.2	First-order upwind scheme for equilibrium model	45
4.3	Literature notes on the rate of convergence	45
4.4	Stability analysis for equilibrium model	47
	4.4.1 Assumptions required for the stability of (4.2) in a hydrate reservoir	48
	4.4.2 Proof of Proposition 4.4.1 on the stability of upwind scheme (4.3) for $u_t + f(x, t; u)_x = 0$ when $f$ is smooth	49
4.5	Numerical results and convergence	52
4.6	Summary	58
5	Modeling, analysis, and simulation for methane hydrate model under non-equilibrium conditions	61
5.1	Kinetic models of hydrate formation: literature background	62
5.2	Kinetic batch reactor model for hydrate evolution in liquid-hydrate conditions	63
	5.2.1 Three batch kinetic models	63
	5.2.2 Properties for the kinetic model	66
	5.2.3 Discrete schemes for batch kinetic models and their properties	67
	5.2.4 Properties of schemes (KIN1), (KIN2), and (KIN3)	69
	5.2.5 Illustration of (KIN1), (KIN2), (KIN3) in batch setting.	74
5.3	Summary of kinetic transport model combining (3.12a) with (KIN3) model	76
5.4	Scheme for kinetic model and its stability	77
	5.4.1 TV-stability for the kinetic scheme (5.31)	78
	5.4.2 TV stability in time	80

TABLE OF CONTENTS (Continued)

	<u>Page</u>
5.5	Simulation results ..... 82
5.5.1	Equilibrium and kinetic schemes under varying environmental and thermodynamic conditions and sensitivity to macro steps ..... 82
5.6	Summary ..... 85
6	Biofilm growth model in complex geometry ..... 87
6.1	Background on biofilm and modeling challenges ..... 87
6.2	Notation for biomass-nutrient dynamics ..... 90
6.2.1	Notation for pore scale geometry with microbial species ..... 90
6.2.2	Notation for microbial species ..... 91
6.2.3	Notation for nutrient and reactions ..... 92
6.3	Constrained transport model ..... 93
6.4	Numerical approximation ..... 95
6.4.1	Spatial discretization ..... 96
6.4.2	Time discretization ..... 96
6.4.3	Convergence of the CCFD scheme for biomass-nutrient model ..... 97
6.4.4	Computational complexity of biomass-nutrient solver ..... 98
6.5	Biofilm growth in the nutrient-rich system ..... 99
7	Monolithic multiphysics model for coupling biomass-nutrient model with pore scale flow ..... 101
7.1	Heterogeneous Brinkman flow model at pore scale ..... 103
7.1.1	MAC method for heterogeneous Brinkman flow ..... 104
7.1.2	Computational complexity for the flow solver and upscaling ..... 104
7.2	Illustration of heterogeneous Brinkman flow and upscaling ..... 105
7.3	Coupled biomass-nutrient-flow dynamics ..... 110
7.3.1	Computational complexity of coupled biomass-nutrient-flow solver . 111
7.3.2	Simulation results for coupled flow and biomass-nutrient dynamics . 111
7.4	Conclusions ..... 114
8	Biomass-nutrient dynamics with surface attraction component ..... 116
8.1	“Promoting” biofilm adhesion to surfaces ..... 117

TABLE OF CONTENTS (Continued)

	<u>Page</u>
8.2 Uncertainty in biofilm growth depending on initial data and upscaled permeability.....	118
8.2.1 Monte Carlo simulations .....	121
8.2.2 Comparison of DNS to non-DNS approaches for biofilm domain generation .....	127
9 Summary, conclusions, and outlook .....	129
References .....	130

## LIST OF FIGURES

<u>Figure</u>	<u>Page</u>
2.1 Illustration of special graphs. Left: $\text{sgn}(x)$ . Right: $H(x)$ . . . . .	8
2.2 Numerical solution for Ex. 2.2.1 with initial condition $(u^0, v^0)$ . Left: Case (a) for $A(u) = \frac{10u}{1+10u}$ . Right: Case (b) for $A(u) = u^4$ . Blue circles represent the evolution from $(u_{(1)}^0, v_{(1)}^0)$ and red diamonds represent the evolution from $(u_{(2)}^0, v_{(2)}^0)$ . . . . .	9
2.3 Illustration of $G$ and $G^{-1}$ for Ex. 2.2.2. . . . .	10
2.4 Illustration of the resolvent $\mathcal{R}_\lambda^A$ where $\lambda = 1$ for Ex. 2.2.3. . . . .	11
2.5 Illustration of (left) resolvent $\mathcal{R}_\tau^A$ and (right) evolution towards equilibria for Ex. 2.2.4 when $\tau = 0.1$ . Different markers indicate $(U^n, U^n)$ that evolve towards an equilibrium on $A(u)$ . . . . .	13
2.6 An illustration of $\Omega$ for Darcy flow model. . . . .	15
2.7 Slices of $\mu$ -CT data of synthetic porous media (glass beads) processed in [114]. The resolution of (a) pore scale domain without biofilm and (b) pore scale domain with biofilm is $204 \times 204$ . $\Omega_r$ in white, $\Omega_v$ in black, and the biofilm phase $\Omega_b$ in gray. . . . .	16
2.8 Illustration of Hagen-Poiseuille flow between two parallel plates at rest. . . . .	17
2.9 Illustration of $D$ superimposed in $D^*$ for horizontal flow. . . . .	19
2.10 (a) Discretization of $D$ into 4 macrocells. (b) Subsets $D_L$ and $D_R$ of $D$ for horizontal flow, and (c) subsets $D_B$ and $D_T$ of $D$ for vertical flow . . . . .	19
2.11 2d staggered grid for CCFD and MAC methods. . . . .	22
2.12 The sparsity pattern of MAC discretization for Ex. 2.5.2. . . . .	26
3.1 Illustration of graph $E_*$ with data from Ulleung Basin case UBGH2-7 [110], where $\chi^*(x) \approx 0.0024e^{-0.012x}$ . Left: the portion of $E_* = E_*(x)$ for a fixed $x$ . Right: multivariate view of $(\chi, S) \in E_*(x)$ . . . . .	38
4.1 Illustration of $\chi^*(x)$ , and of the flux function $f(x; u)$ with data from Ulleung Basin case UBGH2-7 [110]. Left: typical $\chi^*(x)$ in homogeneous sediment, with values $\chi^*(x)$ highlighted at $x = 20$ , and $x = 40$ . Right: the flux function $f(x; u)$ for $x = 20$ , and $x = 40$ . Note that the flux function $f(x, t; u)$ is piecewise linear in $u$ and features a corner at $u = \chi^*(x)$ . . . . .	46
4.2 Comparison of the numerical solution $(U^\Delta, X^\Delta, S^\Delta)$ with the analytical solution $(u, \chi, S)$ at $T = 1$ with $M = 100$ and $\nu = 0.9$ for Ex. 4.5.1. Top: case with for $\chi^*(x) = 1 - 0.26x$ . Bottom: case with $\chi^*(x) = e^{-0.5x}$ . . . . .	53
4.3 Illustration of flux $f$ and its regularization $f^\epsilon$ at some fixed $x \in \Omega$ . . . . .	54
4.4 Numerical solution $(U^{\epsilon, \Delta}, X^{\epsilon, \Delta}, S^{\epsilon, \Delta})$ of Ex. 4.5.2 at $t = 10$ [ky] with $M = 100$ compared with the analytical solution $(u, \chi, S_h)$ . . . . .	54

LIST OF FIGURES (Continued)

<u>Figure</u>	<u>Page</u>	
4.5	Left: $L_1$ -error between the numerical solution $(U^{\epsilon,\Delta}, X^{\epsilon,\Delta}, S^{\epsilon,\Delta})$ and the analytical solution $(u, \chi, S)$ at $T = 10$ [ky]; from Ex. 4.5.2. Right: Convergence of the numerical solution $(U^\Delta, X^\Delta, S^\Delta)$ to the analytical solution $(u, \chi, S)$ at $T = 10$ [ky]. . . . .	56
4.6	Transport in heterogeneous domain from Ex. 4.5.3 at $T = 2.4$ . Top: layers of heterogeneous sediment with different maximum solubility curves $\chi^*$ at $x = 1$ and $x = 2$ . Bottom: numerical solution. Of interest is behavior at the interfaces caused by the jumps of $\chi^*(x)$ . . . . .	57
4.7	Evolution of methane gas transport by advection and diffusion for Ex. 4.5.4. (Top) $t = 40$ [kyr] and (bottom) $t = 80$ [kyr]. . . . .	59
4.8	Reproduction of anomalies in $u_h$ and $S_h$ on heterogeneous domain $\Omega = [0, 3]$ with $\chi^*(x) = e^{-0.5x}I_{[0,2]}(x) + I_{(2,3]}(x)$ . . . . .	59
5.1	Illustration of typical $\chi(x, t), S(x, t)$ at some $t$ in hydrate reservoir (top) $x \in \Omega$ . For this illustration we choose $R = 2\chi^*$ . Top: plot of $\chi, S$ in equilibrium, with $\chi(x, t) \leq \chi^*(x), S(x, t) \geq 0$ and $(\chi(x, t), S(x, t)) \in E_*(x)$ as in (3.6). Middle: illustration of the graph $(\chi, S) \in E_*$ at the point A (equilibrium), and at the points B and C out of equilibrium (not on $E_*$ ) but within the physically meaningful region $(\chi, S) \in D^0 = [0, R] \times [0, 1]$ . The contours $u(\chi, S) = u^0$ of (5.3) in $D^0$ for $\frac{u^0}{\chi^*}$ equal 0.4, 0.6, ..., 1.8, with the curve $u(\chi, S) = u^0 = \chi^*$ separating the “saturated” region $D_+^0$ shaded in gray from the “un-saturated” region $D_-^0$ which is in white. The parts $E_*^+$ and $E_*^-$ of $E_*$ are in green and magenta. Bottom: an example of $\chi^*(x), \chi(x), S(x)$ in a reservoir in out of equilibrium conditions when (B) $\chi_{new}^* < \chi^*$ , and (C) when $\chi_{new}^* > \chi^*$ . . . . .	64
5.2	Simulation results for Ex. 5.2.1 illustrating schemes (KIN1), (KIN2), and (KIN3). Left: $(X^0, S^0) = (0.2, 0.8)$ . Right: $(X^0, S^0) = (1.4, 0.4)$ . The solutions to all schemes lie on the curve $u(X^n, S^n) = U^0$ and converge towards the equilibrium point $(X^\infty, S^\infty)$ on the portion $E_*^+$ of the graph $E$ . Solutions to (KIN2) and (KIN3) are indistinguishable. . . . .	74
5.3	Simulation results of unsaturated case in Ex. 5.2.2 illustrating the behavior of kinetic models (KIN1), (KIN2), and (KIN3) with $(X^0, S^0) = (0.25, 0.2) \in E_*^-$ . We use $\tau = 1$ (left) and $\tau = 0.2$ (right). The solutions to (KIN1) and (KIN2) become unphysical after a few time steps when the curve $u(\chi, S)$ crosses the $E_*^-$ graph; the solutions to (KIN3) remain in $D_-^0$ . In addition, while in $D_-^0$ , the solutions to (KIN2) and (KIN3) are indistinguishable. . . . .	75
5.4	The numerical solutions generated by (KIN $_j$ ) for $j = 1, 2, 3$ are the same with (5.26) for $(X^0, S^0) \in D_+^0$ . For unsaturated cases, $(X_{\text{KIN1}}^n, S_{\text{KIN1}}^n) = (X_{\text{KIN2}}^n, S_{\text{KIN2}}^n)$ . . . . .	76

LIST OF FIGURES (Continued)

<u>Figure</u>	<u>Page</u>
5.5 Comparison of the kinetic and equilibrium model solutions at $T = 1$ with $M = 100$ , and $\nu = 0.9$ for Ex. 5.5.1. Top: rate $k_3 = 10$ . Bottom: rate $k_3 = 100$ . . . . .	83
5.6 Convergence of the numerical solutions of Ex. 5.5.1 for $M = \{100, 200, \dots, 1000\}$ to the fine grid solution $M = 50000$ with $k_3 = 100$ at $T = 1$ . . . . .	83
5.7 Top: initial condition $\chi(x, 0)$ and $S(x, 0)$ from Sec. 5.5.1. Bottom: results of Ex. 5.5.2 with $k_3 = 0.01$ . On both figures $\chi_0^*$ indicates the original $\chi^* _{t=0}$ . . . . .	84
6.1 Schematic picture of biofilm domain $x \in [0, 1]$ and the cell density $B(x)$ plotted with a solid blue curve. On the left we show the mechanism of cell growth schematically and “shoving” when the cell density exceeds the maximum $B^* = 1$ . On the right we show the notation from (6.1). In the region $\Omega_b$ some cells can be very small, and some quite large. Note that in a continuum model, it is likely that $B > 0$ everywhere and thus $\Omega_0 = \emptyset$ . When the maximum cell density is reached, the cells redistribute. This mechanism is modeled differently in various models; see [131] for discussion. . . . .	91
6.2 Processed micro-CT images from [114] at resolution $202 \times 202$ . $\Omega_b$ is in gray, $\Omega_0$ in white, and $\Omega_r$ in black. . . . .	91
6.3 Plots of singular diffusivity $d_B$ . Left: $d_B(\alpha; B)$ from [131] with $\alpha = 2$ . Right: $d_B(\alpha, \beta; B)$ from [33] with $\alpha = \beta = 2$ . . . . .	94
6.4 Illustration of realistic single-pore geometry $\Omega$ with $\Omega_r$ in black, $\Omega_b$ in gray, and $\Omega_0$ in white. . . . .	99
6.5 Pore-plugging with biofilm in a nutrient-rich environment for Ex. 6.5.1 using the nonsingular constrained model (6.6) at the selected time $t$ [h] as shown. Images on the rightmost column are at the final time shown when the pore is plugged up. (Top) micro-pore $L = 0.01$ , (middle) meso-pore $L = 0.1$ , and (bottom) macro-pore $L = 1$ , in [mm], as labelled on the leftmost panel. We see that in the micro-pore the biomass spreads first and then grows, while the opposite is seen in the macro-pore case, with the meso-pore being intermediate. . . . .	100
7.1 Illustration of pore scale geometries $\Omega$ considered in this chapter. Cartoons of (a) channel with a bio-gel, (b) channel with biofilm at the walls, (c) converging channels as in [22], and (d) many-pore geometry. In all figures, $\Omega_r$ is in black, $\Omega_b$ is in gray, and $\Omega_0$ is in white. . . . .	102
7.2 Illustration of velocity profiles for Ex. 7.2.1 for $L \in \{0.01, 0.1, 1\}$ and $k_b \in \{0, 10^{-5}, 10^{-4}, \infty\}$ : (Top) $L = 0.01$ . (Middle) $L = 0.1$ . (Bottom) $L = 1$ . See Tab. 7.2 for data. Figures (d), (h), and (l) show the velocity profiles at the center of biofilm obstacle $ u(L/2, y) $ . . . . .	106

LIST OF FIGURES (Continued)

<u>Figure</u>	<u>Page</u>
7.3 Permeability $K_\Omega = K_\Omega(k_b; w/H)$ from Ex. 7.2.2 depending on the width $w$ of biofilm layer relative to the channel width $H$ and on the biofilm phase permeability. For reference we present the match with Thullner’s model from [145], with Thullner parameter $b = 1.81$ . . . . .	107
7.4 Flow through channels filled with biofilm of different width for Ex. 7.2.3 for (a) $k_b = \infty$ , (b) $k_b = 10^{-3}$ [mm <sup>2</sup> ], and (c) $k_b = 0$ . The width of the middle channel is about half of that for other channels. . . . .	108
7.5 For Ex. 7.2.4, (a) a sketch of $\Omega$ with rock in the middle (black) and surrounding biofilm (gray), and slices of velocity profiles with the permeability of biofilm: (b) $k_b = 0$ , (c) $k_b = 10^{-4}$ [mm <sup>2</sup> ], and (d) $k_b = \infty$ . . . . .	109
7.6 Illustration for Ex. 7.3.1 in a study of a micro-channel. Top: geometry of the domain including the initial biomass domain and the information about the boundaries. Bottom: evolution of velocity, biofilm and nutrient profiles at selected time $t \in \{1.44, 2.88, 4.32\}$ [s]. . . . .	112
7.7 Ex. 7.3.2 biofilm–nutrient dynamic in complex geometry. Top: $B(x, t)$ , middle: $N(x, t)$ , and bottom: $ u(x, t) $ , as indicated in the leftmost panel. Two simulation cases are shown when $k_b = 0$ (biofilm is impermeable), and $k_b = 10^{-4}$ (biofilm is partially permeable). From left to right the columns show the initial condition at $t = 0$ , and the results at $t = 0.1$ (essentially identical for impermeable and permeable biofilm), and the results at $t = 1$ separately for impermeable and permeable biofilm. The regions indicated with ellipses at $t = 1$ show the differences in biofilm growth depending on $k_b$ . The units are as usual $L$ [mm], $t$ [h]. . . . .	113
8.1 Contours of the attraction coefficient $a(x)$ defined by (8.2) (left) $A = 0$ , (middle) $A = 1$ in single-pore geometry, and (right) $A = 1$ in vertical lice from $\mu$ -CT column of glass beads. pore scale geometries are illustrated in Fig. 8.2. . . . .	117
8.2 Illustration of (left) idealized single-pore geometry with $M = 50 \times 50$ voxels, and (right) vertical slice from $\mu$ -CT column of glass beads with $M = 152 \times 114$ voxels. $\Omega_r$ is in black, and $\Omega_n$ in white. . . . .	118
8.3 Generation of $\Omega_b(0)$ with the biomass-nutrient for single-pore geometry on $50 \times 50$ grid, with simulation parameters for cases (a–d) are given in Tab. 8.1. Top row: randomly chosen regions $\Omega_b^{(i)}$ used for initialization in $B(x, 0) = B_0 \mathbb{1}_{\Omega_b}(x)$ for each case (a–d), with small relative volume $V_b = 0.0045$ in (a–b) and larger volume $V_b = 0.03$ in (c–d). Middle and bottom rows: regions $\Omega_b^{(i)}$ obtained with the BN model at the time $t^{(i)}$ when the corresponding obstruction volume $V_o(t^{(i)}) = 0.3$ ; each region was obtained by simulation with initial conditions shown in the top row, respectively. Smaller $V_b$ and $A = 0$ corresponds to less pronounced coating behavior. . . . .	120

LIST OF FIGURES (Continued)

<u>Figure</u>	<u>Page</u>
8.4 Realization of $\Omega_b^{(i)}$ : (left) $V_b = 0.0045, B_0 = 0.6B^*$ , (middle) $V_b = 0.03, B_0 = 0.8B^*$ , (right) $V_b = 0.07, B_0 = 0.6B^*$ .....	121
8.5 Dependence of $K_\Omega(t)$ on $V_o(t)$ with the BN model (6.6) discussed in Sec. 6.3. Results for Ex. 8.2.1 are shown for 10 selected out of $I = 100$ realizations of geometries generated with $V_b$ and $A$ as shown. ....	122
8.6 Results of the BN model with $V_b(0) = 0.0045$ and $A$ as shown. Left: one of the realizations $\Omega_b^{*,(i)}$ for $V_o = 0.1$ . Middle: histogram of $(K_{(i)})_i$ for $V_o \in \{0.1, 0.2, 0.3\}$ . Right: mean and standard deviation of $(K_{(i)}/K_0)_i$ for $V_o \in \{0.1, 0.2, 0.3\}$ .....	123
8.7 Results of the BN model with $V_b(0) = 0.03$ and $A$ as shown. Left: one of the realizations $\Omega_b^{*,(i)}$ for $V_o = 0.1$ . Middle: histogram of $(K_{(i)})_i$ for $V_o \in \{0.1, 0.2, 0.3\}$ . Right: mean and standard deviation of $(K_{(i)}/K_0)_i$ for $V_o \in \{0.1, 0.2, 0.3\}$ .....	124
8.8 Results of the BN model with $V_b(0) = 0.07$ and $A$ as shown. Left: one of the realizations $\Omega_b^{*,(i)}$ for $V_o = 0.1$ . Middle: histogram of $(K_{(i)})_i$ for $V_o \in \{0.1, 0.2, 0.3\}$ . Right: mean and standard deviation of $(K_{(i)}/K_0)_i$ for $V_o \in \{0.1, 0.2, 0.3\}$ .....	125

## LIST OF TABLES

Table	Page
2.1 Numerical solutions to Ex. 2.2.1. ....	9
2.2 Equilibria $(U^n, V^n)$ at $t = 10$ for selected $(u^0, v^0)$ for Ex. 2.2.4. ....	13
3.1 Notations used in Sec. 3–5 .....	35
5.1 Simulation reference data and results generated by the equilibrium model (EQ) with $K = 1$ for Ex. 5.5.2. Pressure $P$ , temperature $T$ , and depth $D$ are in the units of [MPa], [K], and [mbsl] .....	85
5.2 Simulation results at $t = 150$ [y] with kinetic model for Ex.5.5.2 with $\Delta t = K\tau$ . (*) The results in the last macro-column differ are higher for the EQ model by one digit. ....	85
6.1 Symbols for the variables and parameters used commonly for biomass-nutrient dynamics, with typical values adapted from [33, 39, 114] or as indicated. ....	89
7.1 Notations for flow and upscaled permeability with typical values adapted from [114]. ....	102
7.2 Data and results for Ex. 7.2.1. (a – c) micro-pore, (e–g) meso-pore, (i–k) macro-pore. ....	106
7.3 Results for converging channels in Ex. 7.2.3: permeability $K_\Omega$ and maximum flow rate $\ u\ _\infty$ depending on $k_b$ . ....	108
7.4 Results of Ex. 7.2.4. ....	110
7.5 Results for Ex. 7.3.2 at $t = 1$ [h]. ....	114
8.1 Parameters for the DNS model and simulations of $(B, N)$ described in Sec. 6.3. Simulations cases (a,b,c,d) for Ex. 8.2.1 are presented.....	119
8.2 Sensitivity of the probability distribution of $K_{(i)}/K_0$ to the simulation parameters $V_b$ and $A$ for the geometries $\Omega_b^*$ obtained with DNS for pore coating scenarios. The values $K$ presented here correspond to three selected values of the relative volume $V_o = \frac{ \Omega_b^* }{ \Omega_n }$ from the set $\{0.1, 0.2, 0.3\}$ . ....	126

## LIST OF APPENDICES

	<u>Page</u>
1 Semismooth Newton method to solve $f(x) = 0$ .....	30
2 Time stepping (macro-time steps) $m = 1, 2, \dots, M$ .....	42



# Multiphase Flow and Transport in Porous Media with Phase Transition at Multiple Scales: Modeling, Numerical Analysis, and Simulation

## 1 Introduction

Scientific discovery and innovation have improved the quality of life as we seek to advance the frontiers of knowledge and solve problems such as of natural phenomena. The multiphase flow and transport through porous media are omnipresent in nature and in environmental, biological and medical science and engineering field [8, 11, 127]. The study of Darcy scale models generally reply on empirical data obtained for cores extracted from soil and rock, and the pore scale models rely primarily on imaging and micro-fluidic experiments. For many instances, the experiments are not feasible due to technical and economical challenges.

One can also study such phenomena using numerical simulations. Numerical simulation of fluid flow and transport aids in understanding the complex behavior of fluids, and can aid in the management of resources involving processes in porous media such as groundwater management, oil and gas productions, and many other applications including modeling human tissue. However, developing an accurate, stable, robust and consistent model for complex flow and transport phenomena is challenging as each model presents challenges unique to a certain application, and to a length and time scale at which they are applied. In this dissertation we use conservative and stable schemes and wherever possible we provide analyses and tests of these properties.

**Mathematical modeling and numerical analysis results in this dissertation.** In this dissertation we present our results for two applications involving two very specific models of multiphase flow. These are methane hydrate and biofilm-nutrient models coupled with the flow. These are important applications overviewed below in Sec. 1.1 and 1.2.

The research described in this dissertation comprises results published in three papers:

[106] M. Peszynska, C. Shin, “Stability of a numerical scheme for methane transport in hydrate zone under equilibrium and non-equilibrium conditions.” Computational Geoscience, March 2021, accepted, in print.

- [131] C. Shin, A. Alhammali, L. Bigler, N. Vohra, M. Peszynska, “Coupled flow and biomass-nutrient growth at pore scale with permeable biofilm, adaptive singularity and multiple species.” *Mathematical Biosciences and Engineering*, 2021, 18(3): 2097 – 2149.
- [115] M. Peszynska, J. Umhoefer, C. Shin, “Reduced model for properties of multiscale porous media with changing geometry.” *Computation*, 2021, 9(3), 28.

These papers were written with collaborators, therefore we extract the specific contributions to which we contributed most substantially. Throughout we make clear the specific contributions of the author of this dissertation. In particular, for the methane hydrate model we present a rigorous analysis of the stability of a numerical scheme as well as ample simulation results which illustrate the model and the findings from the analysis. For the biofilm-nutrient-flow dynamics, we present the first monolithic coupled model of flow and biofilm growth. While the analysis for this system is out of reach, we perform testing of modeling variants as well as of upscaling including the considerations of uncertainty.

**Outline of the dissertation.** The dissertation starts in Ch. 2 by providing background and notation. Next we continue to describe the results in these papers [106, 115, 131]. The results in [106] are partitioned into Ch. 3, 4, and 5. Then we discuss the parts of [115, 131] which the author of this dissertation contributed in Ch. 6–8. In the end, we summarize our work and provide current and future work in Ch. 9.

First we motivate and overview the results and provide a statement on our contributions.

### 1.1 Numerical analysis and simulations of methane transport in hydrate zone under equilibrium and kinetic conditions

In Ch. 3–5, we describe the work presented in [106], a rigorous stability analysis of the first-order upwind method for methane gas transport in the subsurface with phase transition along with simulation results which illustrate the theory and show the flexibility of the model for use in the studies, e.g., of methane transport due to the climate change. The author’s contribution is described in detail at the end of the section.

**Overview.** Methane hydrate, also known as “Ice That Burns” is an ice-like crystal made of methane molecules enclosed in a cage made by water. Methane hydrate is abundant in deep sub-sea sediments whenever favorable conditions of high pressure, low temperature,

and a large supply of methane holds. Methane hydrate is also found in the Arctic below the permafrost.

To explain the presence and shape of hydrate deposits found in nature, as well as to understand the methane flux as a response to climate change, various simulations were carried out; see, e.g., [25, 26, 40, 53, 79, 80, 81, 87, 94, 110, 111, 147, 153, 165, 166]. These simulations are typically carried out at the basin time scales of several kilo-years or at least years or months. The presence of hydrate is explained with a postulate of supply of gas from deep Earth sources or by the existence of biogenic sources of methane such as microbial species; see [80, 110, 147]. Recent studies focus also on the dissociation of hydrate deposits in response to environmental conditions such as an increase in average 9 temperatures and address the impact of hydrate on the balance of greenhouse gases [10, 25, 29, 55, 137] at the time scales of years or decades.

Hydrate has also been evaluated as a potential energy source [92, 124, 143]. In particular, in pilot projects in Japan and Alaska [92, 141, 142], the recovery of methane is enabled by lowering the pressure in the wells which triggers hydrate dissociation and release of a large amount of gas. A similar mechanism contributes to environmental hazards while drilling [17, 52, 136], with the characteristic time scale of days.

Although there has been a lot of active research and simulations of hydrate evolution, to our knowledge, no analysis of numerical schemes was reported. Our objective has been to provide the first numerical analysis for a family of simplified methane gas transport models with hydrate formation and dissociation in methane hydrate zone under equilibrium and non-equilibrium states which we frame as a conservation law with a nonsmooth space- and time-dependent flux function. In this dissertation we describe first the model for methane gas transport in the gas hydrate stability zone in Ch. 3. Next we provide rigorous stability proofs for the equilibrium model in Ch. 4 and for the kinetic model in Ch. 5 along with simulation results for selected scenarios.

**Author's contribution.** The author of this dissertation contributed in equal parts to (i) the rigorous proof of the stability of the upwind finite volume discretization of the reduced equilibrium model, (ii) study of regularization of flux functionals, (iii) analysis of the kinetic batch reactor model, (iv) kinetic equation development and analysis, and (v) designed and performed simulations as well as (vi) demonstration of the convergence of the numerical methods at the rate  $O(\sqrt{h})$ .

## 1.2 Coupled biomass-nutrient-flow model in porous media

In Ch. 6–7 and Ch. 8 we present part of the work reported in [115, 131] on a coupled model of biomass-nutrient and flow and upscaling involving uncertainty and reduced models. In Ch. 6–7 we present the biomass-nutrient model with constraint and discuss the biofilm growth pattern in a realistic pore scale geometry. We also introduce a pore scale flow model that allows fluid flows through permeable biofilm phase, and explains the coupling of flow model with the biomass-nutrient model. These materials correspond to Sec. 4–5 of [131]. In Ch. 8, we describe the work presented in Sec. 3 and part of Sec. 6 of [115]. The author’s contributions are described in detail at the end of the section.

**Overview.** Biofilms are composed of microbial cells and the extracellular polymeric substance (EPS) that microbes produce for their own protection. As authors of [22, 31] stated, “the overwhelming majority of bacteria live in porous environments” such as “soil-like materials, industrial filters” and medical devices, we see that there is significant interest in studying biofilm. Scientists and engineers use microbes to alter the flow paths in porous media in various applications. The understanding and quantitative modeling of microbial growth in porous media are important, e.g., in selective plugging for the needs of enhanced oil and gas recovery, as well as in carbon sequestration [22, 35, 84, 144].

The study of biofilm at pore scale often faces challenges in experiments and imaging [35, 96, 114, 139, 144]. Observations of microbial growth in synthetic or real porous media are difficult since imaging is intrusive and harmful to living organism and can alter its reproduction behavior [14, 108, 114]. Thus, sometimes the best one can do is to study the upscaled properties such as  $K_{\Omega}$  as in [114] with the flow confined to the pore region without biofilm. Moreover, the typical length scale for the processes at pore scale is in micrometers [ $\mu\text{m}$ ] rather than [mm]; the latter are considered, e.g., in the detailed studies in bulk fluid [19, 63, 170]. Another challenge is in detecting a clear interface between the biofilm phase and the bulk fluid when we also need to identify the boundary between the rock and the fluid region. In fact, the character itself of the biomass-nutrient dynamics coupled to the flow may be distinct from that in an unconfined setting. In particular, [31] points out the importance and influence of “streamers” (long filamentous structure) on the clogging of pore scale in contrast to the surface attached biofilm.

The challenge of the coupled nature of flow motivated us to improve the model presented in [114] by applying a variant of the Brinkman flow model to the entire domain rather

than a staggered-in-time treatment. Thus these extensions shall allow (a) more complex spreading and growth mechanisms than those we proposed in [114], (b) permeable biofilm phase, and an easy generalization to (c) multiple microbial species. For a new adaptive model we developed, we refer readers to [131] since this dissertation only focuses on the monolithic coupled biomass-nutrient-flow model. Our model in [131] is also available for a multiscale study with which we upscale the flow properties affected by biofilm growth to Darcy scale.

At Darcy scale, only the Darcy properties, such as porosity  $\phi$  (average volume fraction of the voids) and permeability  $K_\Omega$  (average proportionality coefficient in Darcy's law for momentum equation) can be found by experiment. One can also derive these quantities from the detailed geometry of porous media at the pore scale. There are also relationships between  $\phi$  and  $K_\Omega$  formulated from experiments and theoretical considerations. In particular, there is a well-known porosity-permeability correlation such as Carman-Kozeny [9] which is derived from the pore scale the geometry of an isotropic Darcy scale porous medium. In a more general context, the wide variety of porous media and the uncertainty of the actual values of  $\phi$  and  $K_\Omega$  in heterogeneous reservoirs led to research on the stochastic modeling of  $\phi(x, \omega)$  and  $K_\Omega(x, \omega)$  such as in [21, 99, 100], where  $\omega$  is the random parameter which stands for uncertainty due to experimental and modeling errors. Since  $K_\Omega$  depends on the multitude of parameters, it is very difficult to quantify  $\omega$ . This randomness of  $K_\Omega$  clearly increases when the evolving geometry starts from random initial conditions. These facts motivate us to study the sensitivity of the biomass-nutrient model to initial data and to introduce a modeling parameter for the biofilm surface attraction feature.

**Author's contribution.** For the work reported in Ch. 6–7, the author of this dissertation contributed to (vii) developing the MATLAB BN\_Flow simulation code [132] for coupled biomass-nutrient-flow dynamics. We also (viii) constructed examples that demonstrate the robustness of the monolithic biomass-nutrient-flow model.

For the work presented in Ch. 8, the author developed (ix) the biomass-nutrient model modification which enables the rock surface detection through an additional attraction parameter on the reaction term. The author also (x) performed the Monte Carlo simulations to generate realistic geometries with biofilm per case using the direct numerical simulation (DNS) and (xi) reported the upscaled permeability probabilities which were compared with the results produced by reduced models presented in [115].

## 2 Background

In this chapter we provide background for our work on mathematical modeling, analysis, and simulation of flow and transport models at multiple scales. The topic is vast, therefore we focus on the overview and the essential details only. We start by defining the notations commonly used throughout this dissertation. Then we give mathematical preliminaries on (i) ordinary differential equations (ODEs) with nonlinear relations, (ii) scalar conservation laws, (iii) phase-field model, (iv) flow models, (v) volume averaging upscaling method, and (vi) numerical methods for models to be described.

### 2.1 Notation

In this section we define the notations and special graphs that are repeatedly used in this dissertation.

Let  $\Omega$  be an open, connected, bounded region in  $\mathbb{R}^d$  for  $d \in \{1, 2, 3\}$  with boundary of  $\Omega$  denoted by  $\partial\Omega$  or  $\Gamma$ . The position variable is  $x = (x_k)_{k=1}^d$  in  $\Omega$  with its Euclidean norm  $|x|$ . Partial derivatives are denoted by  $\partial_t, \partial_k, \nabla = (\partial_1, \dots, \partial_d)$  for time  $t$  and  $x$ .

We use  $\mathbf{n} = (n_1, n_2, \dots, n_d)^T$  to denote the outward normal vector to  $\Gamma$ . The normal derivative on  $\Gamma$  is defined as

$$\nabla u \cdot \mathbf{n} = \frac{\partial u}{\partial \mathbf{n}} = \sum_{k=1}^d \frac{\partial u}{\partial x_k} n_k.$$

**Definition 2.1.1.** *Definition for subdifferential in [134](p. 81) Let  $\varphi : \Omega \rightarrow \mathbb{R}$  be convex and proper. The subdifferential of  $\varphi$  at  $u \in \text{domain}(\varphi)$  is the set of all functionals  $u^* : \in \Omega'$  such that*

$$u^*(v - u) \leq \varphi(v) - \varphi(u), \quad v \in \Omega,$$

*and is denoted by  $\partial\varphi(u)$ . Each such  $u^* \in \partial\varphi(u)$  is also called a subdifferential of  $\varphi$  at  $u$ .*

We use  $\mathbb{1}_S(x)$  and  $I_S(x)$  to denote the characteristic function and the indicator function of some set  $S$ , respectively, and they are defined as

$$\mathbb{1}_S(x) = \begin{cases} 1, & x \in S, \\ 0, & x \notin S, \end{cases} \quad \text{and} \quad I_S(x) = \begin{cases} 0, & x \in S, \\ \infty, & x \notin S. \end{cases}$$

### 2.1.1 Functional spaces

For functional spaces, we closely follow the notations used in [74, 135].

Let  $C^m(\Omega)$  denote the space of continuous functions whose derivatives up to order  $m \geq 0$  are also continuous. We use the subscript 0 to indicate the space with compact support, e.g.,

$$C_0^\infty(\Omega) = \{u \in \cap_{m \geq 1} C^m(\Omega) \mid \text{supp}(u) \text{ is compact}\}$$

which is also called as the space of test functions.

The Lebesgue space is denoted by  $L^p(\Omega)$  with the usual  $L^p$ -norm  $\|\cdot\|_p$ . In this dissertation, we consider spaces for  $p \in \{1, 2, \infty\}$ . We use  $H^k(\Omega)$  to denote the Sobolev space

$$H^k(\Omega) = \{u \in L^2(\Omega) \mid \partial^\alpha u \in L^2, |\alpha| \leq k\}$$

where  $\partial^\alpha u$  represents the weak derivative of  $u$  of order  $|\alpha|$ , equipped with the norm

$$\|u\|_{H^k(\Omega)} = \sqrt{\sum_{|\alpha| \leq k} \|\partial^\alpha u\|_2^2}.$$

$H^k(\Omega)$  together with the inner product is Hilbert space.

We use  $L^\infty(0, T; L^p(\Omega))$  to denote the function space of both time and space as introduced in [73, 74]

$$L^\infty(0, T; L^p(\Omega)) = \{u : \|u\|_{p,T} < \infty\},$$

where the  $L^p$ -norm over  $[0, T]$  is defined as

$$\|u\|_{p,T} = \int_0^T \|u(\cdot, t)\|_p dt.$$

From now on, we use  $L^\infty(L^p)$  to denote the space  $L^\infty(0, T; L^p(\Omega))$ .

### 2.1.2 Special graphs

In this section we provide special graphs used in this dissertation.

We consider the graph

$$\text{sgn}(x) = \begin{cases} -1, & x < 0, \\ 0, & x \in [-1, 1], \\ 1, & x > 0. \end{cases}$$

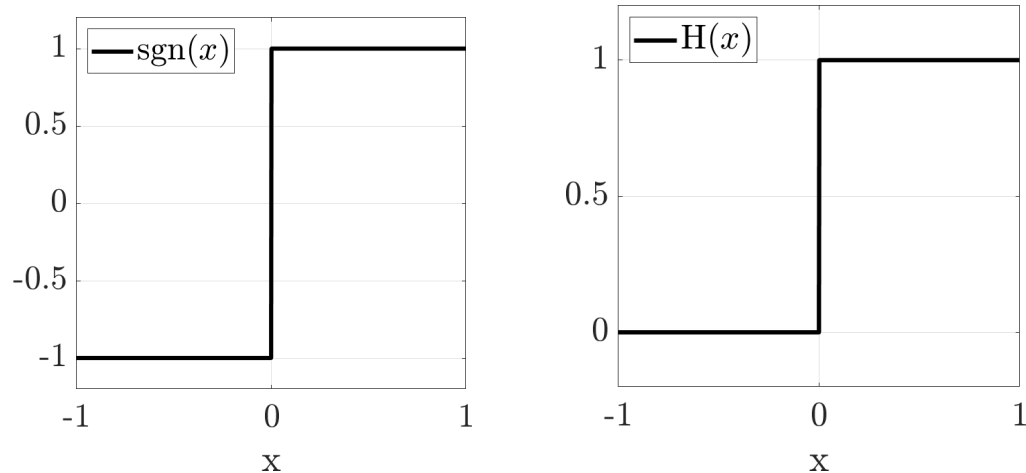


Figure 2.1: Illustration of special graphs. Left:  $\text{sgn}(x)$ . Right:  $H(x)$ .

This graph  $\text{sgn}(x)$  is distinct from the single valued discontinuous function  $\text{sgn}_0(x)$  which agrees with  $\text{sgn}(x)$  for  $x \neq 0$  but assigns 0 to  $x = 0$ . The Heaviside graph  $H(x) = \frac{1}{2}(1 + \text{sgn}(x))$  assigns 0 to  $x < 0$ , 1 to  $x > 0$ , and the set  $[0, 1]$  to  $x = 0$ . We also use  $x_+ = \max(0, x)$ . Fig. 2.1 illustrates these special graphs.

## 2.2 Notation and preliminaries on ODEs with monotone graphs

In this section we recall the evolution equations with monotone multi-valued graphs on  $\mathbb{R}$ . These concepts extend what is known for the initial value problem

$$\frac{du}{dt} + A(u) = f, \quad u(0) = u^0, \quad (2.1)$$

where  $A : \mathbb{R} \rightarrow \mathbb{R}$  is a monotone increasing function. The extensions we discuss are useful for modeling phase equilibria and kinetic schemes; we shall need the notation and basic properties in our estimates and analysis in Sec. 3–5.

The comprehensive details on the general abstract Hilbert space setting and the monotone multi-valued operators are provided, e.g., in [12, 134].

We start with an example of a system of two coupled differential equations similar to (2.1). Consider a monotone increasing relationship  $v = A(u)$  with  $A : \mathbb{R} \rightarrow \mathbb{R}$ . When  $u = u(t)$  and  $v = -v(t)$ , and these are in equilibrium, then  $v(t) = A(u(t))$  at every time instance  $t$ . It is possible however that the system starts away from an equilibrium, i.e.,  $v(0) \neq A(u(0))$ . If  $A$  is monotone increasing, then the system  $(u(t), v(t))$  evolves towards the equilibrium  $(u^\infty, v^\infty)$  as  $t \rightarrow \infty$ , i.e.,  $v(t) - A(u(t)) \rightarrow 0$  as  $t \rightarrow \infty$ . We denote this quantity  $Q = v - A(u)$  and show a concrete example.

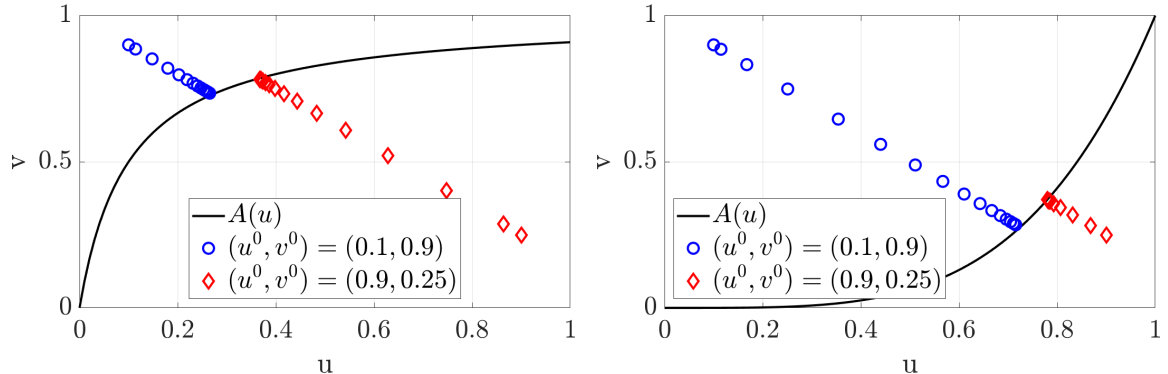


Figure 2.2: Numerical solution for Ex. 2.2.1 with initial condition  $(u^0, v^0)$ . Left: Case (a) for  $A(u) = \frac{10u}{1+10u}$ . Right: Case (b) for  $A(u) = u^4$ . Blue circles represent the evolution from  $(u_{(1)}^0, v_{(1)}^0)$  and red diamonds represent the evolution from  $(u_{(2)}^0, v_{(2)}^0)$ .

Case	$(u_{(1)}^0, v_{(1)}^0)$	$(U_{(1)}^{50}, V_{(1)}^{50})$	$(u_{(2)}^0, v_{(2)}^0)$	$(U_{(2)}^{50}, V_{(2)}^{50})$
(a)	(0.1, 0.9)	(0.2701, 0.7299)	(0.9, 0.25)	(0.3651, 0.7849)
(b)	(0.1, 0.9)	(0.7245, 0.2755)	(0.9, 0.25)	(0.7800, 0.3700)

Table 2.1: Numerical solutions to Ex. 2.2.1.

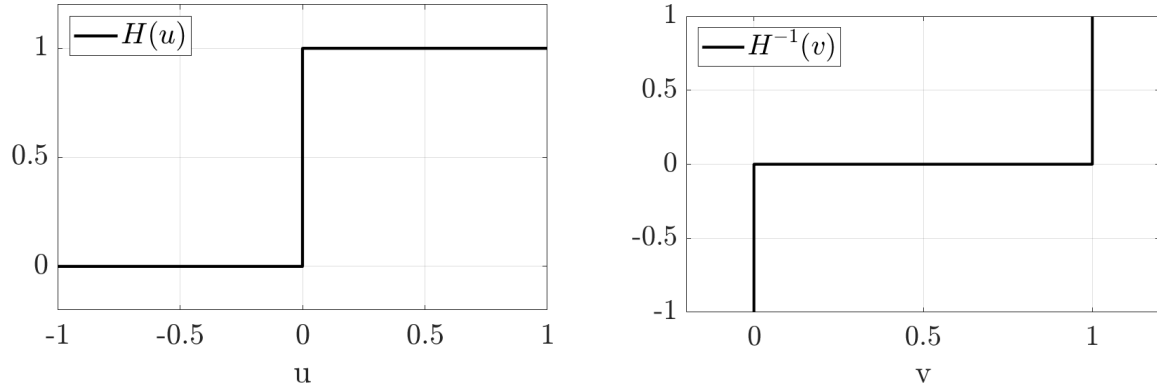
**Example 2.2.1** (Evolution towards equilibrium  $Q = 0$ ). *In this example we show the solution to  $Q = 0$  as an evolution of a kinetic system:*

$$\frac{du}{dt} = Q; \quad \frac{dv}{dt} = -Q; \quad Q = v - A(u). \quad (2.2)$$

We consider two cases: (a) concave monotone function  $A(u) = \frac{10u}{1+10u}$  and (b) function  $A(u) = u^4$  which is convex for  $u \geq 0$ . Let the subscripts  $(i)$  and  $(i)$  indicate different initial conditions. Starting at two different initial conditions:  $(u_{(1)}^0, v_{(1)}^0) = (0.1, 0.9)$  and  $(u_{(2)}^0, v_{(2)}^0) = (0.9, 0.25)$ , we calculate the numerical solutions  $(U_{(i)}^n, V_{(i)}^n)$  for  $i \in \{1, 2\}$  using a builtin ODE solver `ode45` in MATLAB.

In Fig. 2.2, we illustrate the evolution of numerical solutions  $(U_{(1)}^n, V_{(1)}^n)$  in blue circles and  $(U_{(2)}^n, V_{(2)}^n)$  in red diamonds. They evolve towards an equilibrium on  $A(u)$ , and the approximate values of equilibrium for each case are shown in Tab. 2.1, i.e.,  $(u_{(i)}^\infty, v_{(i)}^\infty) \approx (U_{(i)}^{50}, V_{(i)}^{50})$  for  $i \in \{1, 2\}$ . Our results shows the conservation of total quantity, i.e.,  $u_{(i)}^0 + v_{(i)}^0 = U_{(i)}^n + V_{(i)}^n$  as expected since we have  $(u + v)_t = 0$  from the sum of two ODEs in (2.2).

In what follows we extend this system to the case when  $A$  is a multivalued graph.

Figure 2.3: Illustration of  $G$  and  $G^{-1}$  for Ex. 2.2.2.

### 2.2.1 Monotone operators

Let  $A \subset \mathbb{R} \times \mathbb{R}$  be a multivalued operator. Its domain and range are defined as

$$\text{dom}(A) = \{u : \exists b : (a, b) \in A\} \subset \mathbb{R}, \quad \text{range}(A) = \cup_{u \in \text{dom}(A)} Au \subset \mathbb{R}.$$

We will write  $v \in A(u)$  to denote some selection  $v$  out of the set  $\text{range}(A)$ . Since this selection is not unique, we use the symbol “ $\in$ .” The inverse of  $A$  is defined as

$$A^{-1} = \{(b, a) : (a, b) \in A\}.$$

**Example 2.2.2.** Consider  $G = H(x)$ , the heaviside graph. Then the inverse of  $G$  is  $G^{-1} = \{0\} \cup (0, 1) \cup \{1\} \times (-\infty, 0) \cup \{0\} \cup (0, \infty)$ . Illustration of  $G$  and  $G^{-1}$  are shown in Fig. 2.3.  $G^{-1}$  is also a subdifferential of  $\partial I_{[0,1]}(v)$ .

**Definition 2.2.1.** Let  $A$  be a multivalued operator.  $A$  is monotone if

$$\forall (u_1, v_1), (u_2, v_2) \in A, (u_1 - u_2, v_1 - v_2) \geq 0.$$

$A$  is maximal monotone if  $I + A$  is onto  $\mathbb{R}$ .

**Definition 2.2.2** (Resolvent). Let  $A$  be a monotone operator. For  $\lambda > 0$ ,  $\lambda A$  is also a monotone operator, and the resolvent

$$\mathcal{R}_\lambda^A = (I + \lambda A)^{-1} \tag{2.3}$$

is a contractive function.

The solution to  $u + \lambda A(u) \ni f$  is unique and given by  $u = \mathcal{R}_\lambda^A(f)$ .

**Example 2.2.3.** We consider the Heaviside graph  $H(u)$  as before in Ex. 2.2.2. The resolvent  $\mathcal{R}_\lambda^A(u) = (I + \lambda A)^{-1}(u) = (u - \lambda)_+$  is as shown on Fig. 2.4.

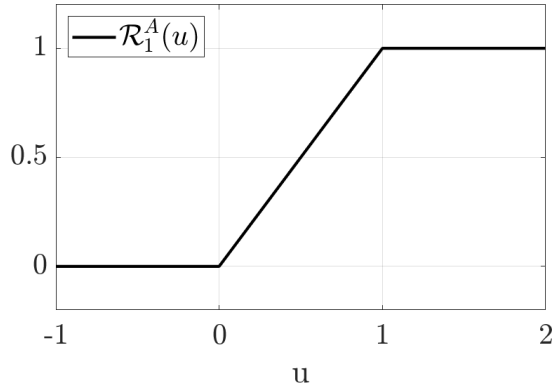


Figure 2.4: Illustration of the resolvent  $\mathcal{R}_\lambda^A$  where  $\lambda = 1$  for Ex. 2.2.3.

## 2.2.2 Evolution ODE with a graph

Now we extend the simple ODE (2.1) to allow  $A$  to be multivalued as in the section above.

The resolvent  $\mathcal{R}_\lambda^A$  helps to define the solution to an evolution problem

$$\frac{du}{dt} + A(u) \ni f; \quad u(0) = u^0, \quad (2.4)$$

where  $f \in L^1(0, T)$  is some given input and  $u^0 \in \text{dom}(A) \subset \mathbb{R}$  is some initial data. The solution  $u(t) \in C^0(\mathbb{R})$  to (2.4) is defined as the limit as  $\tau \rightarrow 0$  of the fully implicit finite difference step function solutions  $U^n \approx u(t^n)$ , with  $t^n = n\tau$ , to the inclusion

$$\frac{U^n - U^{n-1}}{\tau} + A(U^n) \ni f^n, \quad n \geq 1. \quad (2.5)$$

In spite of the symbol  $\ni$ , the step solution  $U^n \in \text{dom}(A)$  to (2.5) is uniquely defined by  $U^n = \mathcal{R}_\tau^A(U^{n-1} + \tau f^n)$ . Once we know  $U^n$ , the actual selection  $A(U^n) = f^n - \frac{U^n - U^{n-1}}{\tau}$  is given uniquely from (2.5).

In this dissertation we use various single-valued approximation  $A_\lambda \approx A$  which are maximal monotone when  $A$  is. One is the Yosida approximation  $A_\lambda = \frac{1}{\lambda}(I - \mathcal{R}_\lambda^A)$  which provides another way to define the solution  $u(t)$  to (2.4) as the limit as  $\lambda \rightarrow 0$  of  $u_\lambda(t)$ , the family of solutions to the ODE

$$\frac{du_\lambda}{dt} + A_\lambda(u_\lambda) = f.$$

We also note that (2.4) is the gradient flow of some convex functional  $\mathcal{A}$  of which  $A$  is the subgradient. This feature helps to understand the solvability of the problem.

### 2.2.3 Evolution ODE system with graph

Now we extend our discussion of (2.4) and consider the following system on  $\mathbb{R} \times \mathbb{R}$

$$\frac{d}{dt}u = Q, \frac{d}{dt}v = -Q; \quad u(0) = u^0, v(0) = v^0. \quad (2.6)$$

We are now interested in the case when  $Q(u, v) \in v - A(u)$  is multi-valued with a monotone operator  $A$ . Here the first and the second equations have similar properties to (2.4) but are coupled. Adding the two equations leads to  $u(t) + v(t) = \text{const} = u^0 + v^0$ . With the abstract theory from [134], it is easy to show that the system (2.6) is well-posed in  $\mathbb{R} \times \mathbb{R}$ . We also see that the solutions  $(u(t), v(t))$  evolve towards some  $(u^\infty, v^\infty)$  which is at the intersection of the graph  $G$  with the manifold  $u + v = u^0 + v^0 = c^0$ . Moreover, since the graph  $Q(v) = v - A(u) = v - A(c^0 - v)$  is monotone in  $v$ , the evolution of  $v$  governed by  $\frac{d}{dt}v + Q(v) \ni 0$  is the gradient flow of the convex functional  $\mathcal{Q}$ , the primitive of  $Q$ .

#### Numerical solution to kinetic problem with monotone graph.

We can approximate the solution  $(u(t), v(t))$  to (2.6) by the Backward Euler method. In this section we give an explicit formula for  $(U^n, V^n)$  using resolvent, and illustrate with an example.

First we use the Backward Euler method to write the kinetic system (2.6) in discrete form:

$$\frac{U^n - U^{n-1}}{\tau} = V^n - A^n, \quad (2.7a)$$

$$\frac{V^n - V^{n-1}}{\tau} = A^n - V^n, \quad (2.7b)$$

$$A^n \in A(U^n). \quad (2.7c)$$

To write  $U^n$  explicitly, we solve (2.7b) for  $V^n$  in terms of  $A^n$ :

$$V^n = \frac{\tau}{1 + \tau} V^n - \frac{\tau}{1 + \tau} A^n, \quad (2.8)$$

and substitute (2.8) in (2.7a). Then solve for  $U^n$  so that  $U^n$  only depends on the data from previous time step:

$$U^n = \mathcal{R}_{\frac{\tau}{1+\tau}}^A \left( U^{n-1} + \frac{\tau}{1+\tau} V^{n-1} \right). \quad (2.9)$$

The from the sum of (2.7a) and (2.7b), we get

$$V^n = U^{n-1} + V^{n-1} - U^n. \quad (2.10)$$

We will revisit this in Sec. 5.2.

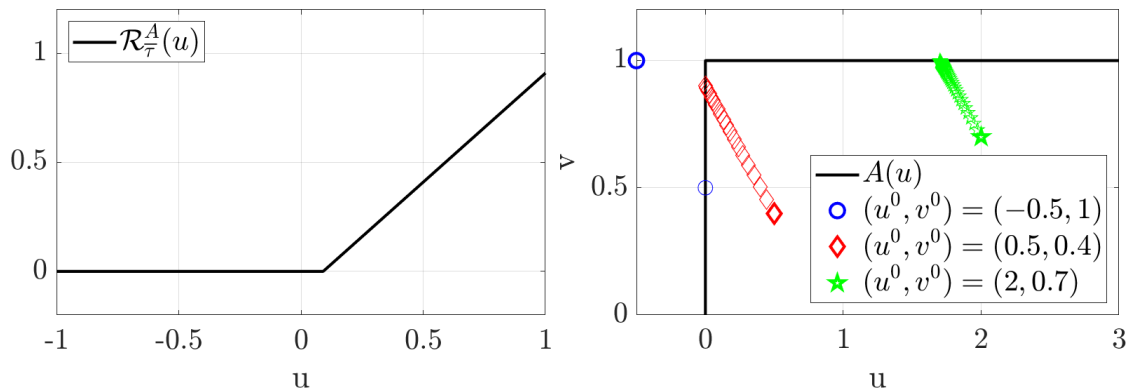


Figure 2.5: Illustration of (left) resolvent  $\mathcal{R}_{\bar{\tau}}^A$  and (right) evolution towards equilibria for Ex. 2.2.4 when  $\tau = 0.1$ . Different markers indicate  $(U^n, V^n)$  that evolve towards an equilibrium on  $A(u)$ .

$(u^0, v^0)$	$(-0.5, 1)$	$(0.5, 0.4)$	$(2, 0.7)$
$(U^n, V^n)$	$(0, 0.5)$	$(0, 0.9)$	$(1.7, 1)$

Table 2.2: Equilibria  $(U^n, V^n)$  at  $t = 10$  for selected  $(u^0, v^0)$  for Ex. 2.2.4.

**Example 2.2.4** (Evolution of a kinetic system with monotone graph). *Consider a kinetic system (2.6) with*

$$A(u) = \begin{cases} (-\infty, 1], & u = 0, \\ 1, & u > 0. \end{cases}$$

The solution  $(u^n, v^n)$  can be obtained exactly using (2.9) and (2.10).

In (2.9) the resolvent  $\mathcal{R}_{\bar{\tau}}^A$  is defined as

$$\mathcal{R}_{\bar{\tau}}^A(\xi) = (\xi - \bar{\tau})_+$$

where  $\bar{\tau} = \frac{\tau}{1+\tau}$ . The illustration of  $\mathcal{R}_{\bar{\tau}}^A$  for  $\tau = 0.1$  is shown in Fig. 2.5 on the left. The right figure shows the evolution of  $(U^n, V^n)$  toward an equilibria on  $A$  from an initial state  $(u^0, v^0)$  with values listed in Tab. 2.2.

### 2.3 Notation and preliminaries on flow models

We review here flow models for an incompressible fluid in the laminar flow regime: Darcy, Stokes, and heterogeneous Brinkman flows. These models are length scale dependent and related using the multi-scale homogenization strategy such as volume averaging methods by [108].

The Darcy scale is the scale of  $O(1 \text{ [cm]})$  or above, at which the study of flow and other properties does not recognize the space available to fluid flow and transport and the space with solid impermeable particles, but rather relies on average properties found experimentally in a laboratory using core samples. In particular, of interest is the porosity  $\phi$ , the ratio of the volume available for fluid flow and transport to the volume of entire porous medium, and permeability  $K_\Omega$ , the coefficient of proportionality in Darcy flow between volumetric flow and pressure gradient. The coefficients  $\phi$  and  $K_\Omega$  represent the geometrical information about rock and non-rock regions together through, e.g., the averaged representation of pore scale processes over a representative elementary volume (REV).

Next we discuss the scale significantly below the Darcy scale. We refer to the scales of  $O(1 \text{ [nm]})$  to  $O(1 \text{ [\mu m]})$  as pore scale. At this scale we recognize the fluid-rock interface  $\Gamma$ . To resolve the flow and transport pattern at pore scale we must know the detail of pore geometry. Digital imaging tools such as X-ray,  $\mu$ -CT, and Scanning Electron Microscopy provide the information of porous media [45, 47]; however, the tomographic analysis for the high-resolution image of porous media is computationally demanding [123, 161]. Even if we have the full geometry, resolving the flow in a complex domain is not always feasible as we may encounter computational barriers [47, 126]. The pore scale processes in REVs are qualitatively connected to computationally efficient macroscopic models through upscaling techniques; we discuss the volume averaging upscaling method in Sec. 2.4.

In this section we start by stating the Darcy flow model. We define the additional notation for pore scale geometry which we need for pore scale flow models. Then we describe the Stokes flow in Sec. 2.3.2.

### 2.3.1 Darcy flow

In 1856, Henry Darcy, the French hydraulic engineer, discovered the empirical law of the linear relation between the flow rate and the pressure gradient based on the experiments. This empirical law is called Darcy's law and is widely used to describe the laminar flow pattern of an incompressible fluid in a porous medium  $\Omega$  [45, 67]. The Darcy flow model [9] in  $\Omega$  is given as

$$\begin{cases} \langle \mathbf{u} \rangle = -\frac{K_\Omega}{\mu} (\nabla \langle p \rangle - \rho g \nabla d), & \text{in } \Omega, \\ \nabla \cdot \langle \mathbf{u} \rangle = 0, & \text{in } \Omega, \end{cases} \quad (2.11a)$$

where  $K_\Omega \in \mathbb{R}^{d \times d}$  is the known permeability tensor of  $\Omega$ ,  $\mu \in \mathbb{R}$  is the dynamic viscosity of fluid,  $\rho \in \mathbb{R}$  is the density of an incompressible fluid,  $g$  is the magnitude, and  $d : \Omega \rightarrow \mathbb{R}$  is

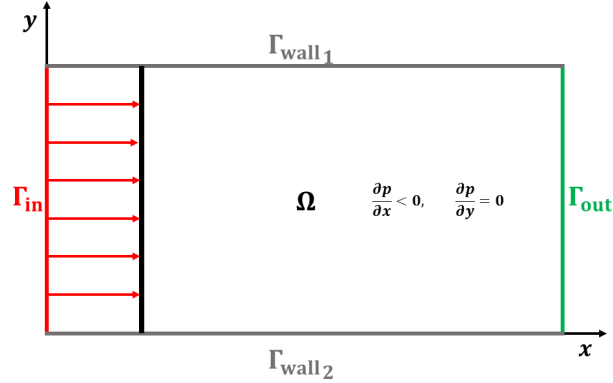


Figure 2.6: An illustration of  $\Omega$  for Darcy flow model.

the depth function satisfying  $\nabla d = 0$  for the horizontal flow and  $\nabla d = -1$  for the vertical flow. Here  $\langle \mathbf{u} \rangle : \Omega \rightarrow \mathbb{R}^d$  and  $\langle p \rangle : \Omega \rightarrow \mathbb{R}$  are the averaged representation of pore scale velocity  $u$  and pressure  $p$ , respectively, where the volume average  $\langle \cdot \rangle$  of a quantity over a volume  $V \subset \Omega$  is defined by

$$\langle \mathbf{u} \rangle(x) = \frac{1}{|V|} \int_{\xi \in V} u(\xi) d\xi.$$

Now we illustrate the Darcy flow.

**Example 2.3.1** (Darcy flow in an isotropic porous medium). *Consider a fluid flows horizontally through an isotropic porous medium  $\Omega \subset \mathbb{R}^2$  of permeability  $K_\Omega \in \mathbb{R}$ ; see Fig. 2.6 for a schematic diagram of this example with  $\Omega = [x_o, x_f] \times [y_o, y_f]$ . The boundary  $\Gamma$  of  $\Omega$  is composed of inlet  $\Gamma_{in}$ , outlet  $\Gamma_{out}$ , and the walls  $\Gamma_{wall}$  parallel to the flow direction. In this illustrative example we impose the no-flow boundary conditions on  $\Gamma_{wall}$ , the Neumann pressure boundary condition on inlet  $\Gamma_{in}$  and the Dirichlet pressure boundary condition on outlet  $\Gamma_{out}$*

$$\begin{cases} \langle \mathbf{u} \rangle \cdot \mathbf{n} = 0, & \text{on } \Gamma_{wall} \\ \langle \mathbf{u} \rangle \cdot \mathbf{n} = u_{in} & \text{on } \Gamma_{in}, \\ \langle p \rangle = p_{out}, & \text{on } \Gamma_{out} \end{cases} \quad (2.11b)$$

where  $\mathbf{n}$  is the normal vector. Let the pressure gradient  $\partial_x p = -c < 0$ .

The direction of flow is determined by the pressure boundary conditions as  $\langle \mathbf{u} \rangle \propto \langle p \rangle$ . To ensure the flow direction from inlet to outlet for the case of Fig. 2.6, we need to have  $\langle p \rangle|_{\Gamma_{in}} > \langle p \rangle|_{\Gamma_{out}}$ . It is easy to obtain the analytical solution  $(\langle u \rangle, \langle v \rangle, \langle p \rangle)$  to Ex. 2.3.1

$$\langle u \rangle = \frac{cK_\Omega}{\mu}, \quad \langle v \rangle = 0, \quad \langle p \rangle = -c(x - x_f) + p_{out}. \quad (2.12)$$

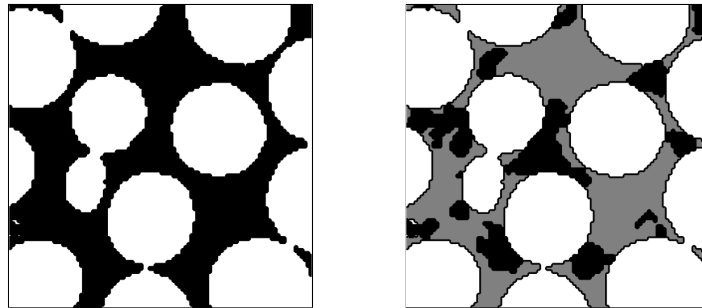
(a)  $\phi \approx 0.44$ (b)  $\phi \approx 0.157$ 

Figure 2.7: Slices of  $\mu$ -CT data of synthetic porous media (glass beads) processed in [114]. The resolution of (a) pore scale domain without biofilm and (b) pore scale domain with biofilm is  $204 \times 204$ .  $\Omega_r$  in white,  $\Omega_v$  in black, and the biofilm phase  $\Omega_b$  in gray.

If the Dirichlet pressure boundary condition  $\langle p \rangle = p_{in}$  is imposed at  $\Gamma_{in}$  instead of the Neumann pressure boundary condition, the constant  $c$  in (2.12) is

$$c = \frac{p_{out} - p_{in}}{x_f - x_o}.$$

For Darcy flow, we must know the permeability tensor  $K_\Omega$ . One can obtain  $K_\Omega$  from experiment or from pore scale simulations using the volume averaging upscaling method based on pore scale data. We explain this in Sec. 2.4.

### 2.3.2 Stokes flow

At the pore scale, we distinguish the rock region  $\Omega_r$  and the non-rock region  $\Omega_n$  in  $\Omega$ , so that  $\Omega = \Omega_r \cup \Omega_n \cup \Gamma_{rn}$  where  $\Gamma_{rn}$  represents the interface between  $\Omega_r$  and  $\Omega_n$ . Fig. 2.7 shows processed  $\mu$ -CT slices from [114] such pore scale domains that the Stokes flow is applicable.

In this section we describe the incompressible Newtonian fluid flow with Reynolds number less than 1 in some rigid porous domain  $\Omega$ .

Generally, the flow velocity  $\mathbf{u} : \Omega_n \rightarrow \mathbb{R}^d$  and pressure  $p : \Omega_n \rightarrow \mathbb{R}$  of an incompressible fluid are described by the Navier-Stokes equations together with a mass conservation equation and appropriate boundary conditions:

$$\rho \left( \frac{\partial \mathbf{u}}{\partial t} + \mathbf{u} \cdot \nabla \mathbf{u} \right) - \mu \Delta \mathbf{u} + \nabla p = f, \quad \text{in } \Omega_n, \quad (2.13a)$$

$$\nabla \cdot \mathbf{u} = 0, \quad \text{in } \Omega_n, \quad (2.13b)$$

where  $f$  is the forcing term. The second equation (2.13b) is the continuity equation that is derived from the mass conservation of the incompressible fluid.

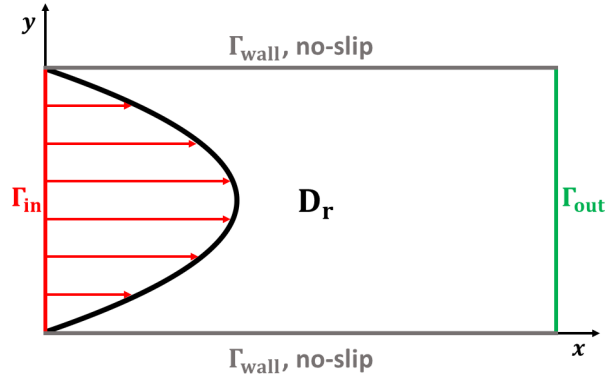


Figure 2.8: Illustration of Hagen-Poiseuille flow between two parallel plates at rest.

Under the laminar regime, the viscous effect dominates the inertial force. In turn, the Navier-Stokes equation (2.13a) reduces to the steady-state Stokes equations. The Stokes flow in  $\Omega_n$  for an incompressible fluid [37] is expressed as

$$-\mu\Delta\mathbf{u} + \nabla p = f, \quad \text{in } \Omega_n, \quad (2.14a)$$

$$\nabla \cdot \mathbf{u} = 0, \quad \text{in } \Omega_n. \quad (2.14b)$$

We now illustrate the Stokes flow in a channel, also known as Hagen-Poiseuille flow.

**Example 2.3.2** (Hagen-Poiseuille flow). *We consider the 2-dimensional pressure driven laminar flow between two parallel plates at rest; see Fig. 2.8. We impose the no-slip no-flow boundary conditions on  $\Gamma_{wall} \cup \Gamma_{rn}$ , the Dirichlet boundary condition on  $\Gamma_{in}$ , and the natural outflow boundary condition on  $\Gamma_{out}$  as described in [37]:*

$$\begin{cases} \mathbf{u} = 0, & \text{on } \Gamma_{wall} \cup \Gamma_{rn}, \\ \mathbf{u} = u_D, & \text{on } \Gamma_{in}, \\ \mu\nabla\mathbf{u} \cdot \mathbf{n} - p\mathbf{n} = 0, & \text{on } \Gamma_{out}. \end{cases} \quad (2.14c)$$

*The incompressible fluid flows through the fluid flow region  $\Omega_f \subset \Omega = [x_o, x_f] \times [y_o, y_f]$  in the horizontal direction, neglecting gravitational forces, between the parallel walls at rest. This flow is called the Hagen-Poiseuille flow and is the solution to the boundary value problem (2.14).*

We provide the well known analytical solution now. Recall the notations for velocity  $\mathbf{u} = (u, v)$  and some point  $\mathbf{x} = (x, y) \in \Omega$ . Since  $\frac{dp}{dy} = 0$ , the only non-zero velocity component is  $u$ . The analytical solution to this Hagen-Poiseuille flow is

$$u(x, y) = \frac{1}{2\mu}(y - y_o)(y - y_f)\frac{dp}{dx}, \quad (2.15a)$$

$$v(x, y) = 0, \quad (2.15b)$$

$$p(x, y) = (x - x_f) \frac{dp}{dx}, \quad (2.15c)$$

with  $\frac{dp}{dx} < 0$  to ensure the flow direction from left to right in this case. Note that  $u(x, y)$  is the fully developed parabolic velocity profile in  $\Omega_n$ .

## 2.4 Notation and facts on upscaling via volume averaging

The heterogeneous nature of porous media makes it difficult to resolve the global flow pattern using a pore scale flow model. An alternate way to obtain the experimentally derived Darcy's law is by using homogenization which effectively extracts the homogeneous properties of complex medium with pore scale data.

The ideas of homogenization has long history. Many authors contributed to mathematical theory of homogenization, and much work was devoted to numerical homogenization; we provide first a few main representative references. The interest in the homogenization for flow in porous media arose in 1980s. Tartar [140] presented the rigorous mathematical derivation of Darcy's law as an asymptotic limit of Stokes equations. His work applied to the periodic perforated domain. In [32], Durlflosky presented the numerical homogenization method to generate the full permeability tensor  $K_\Omega$  of a domain  $\Omega$  that satisfies the Darcy's law with volume averaged velocities and pressure gradients over the entire  $\Omega$ . More information on volume averaging is in [158].

The Durlflosky method was adapted to Stokes flow in [109] which we now follow and describe the systematic volume averaging upscaling method.

Let  $L_\Omega$  be the characteristic length of a Darcy scale porous medium  $\Omega$ . We consider a REV of  $\Omega$  and denote by  $D$ . The characteristic length  $L$  of  $D$  must satisfy  $\frac{L}{L_\Omega} \ll 1$  to ensure the separation of scales. We also suppose that the full geometry of  $D$  is known. To calculate the upscaled permeability  $K_\Omega$ , we need the velocity and pressure data in  $D$ . The flow and pressure profiles in  $D$  can be found numerically using the MAC method described in Sec. 2.5.4 for the Stokes model (2.14) subject to the boundary conditions (2.14c). When  $D$  has complex geometry, it is difficult to hard-code the boundary conditions. Alternately, one can superimpose  $D$  in a large enough bulk fluid domain  $D^*$  to avoid complications at the boundaries while we allow fluids enter  $D$  naturally. For example in [109], the hourglass example was handled in this way by embedding  $D = (-1, 1)^2$  in  $D^* = (-10, 10) \times (1, 1)$  to simulate the horizontal flow. Authors in [46] showed the length of  $D^*$  should be at least  $5L$

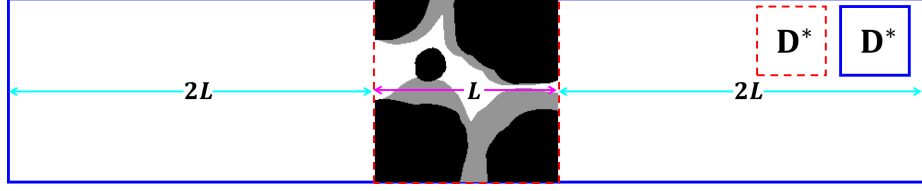


Figure 2.9: Illustration of  $D$  superimposed in  $D^*$  for horizontal flow.

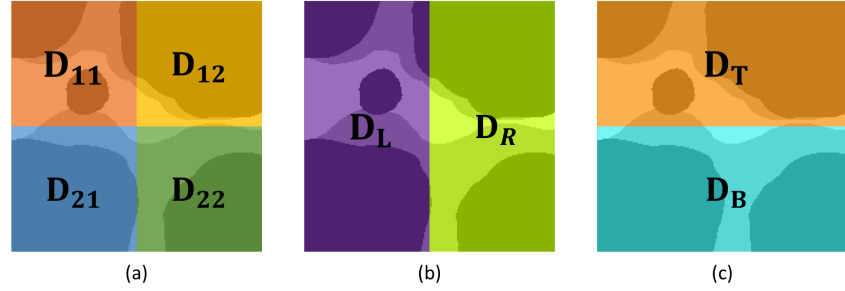


Figure 2.10: (a) Discretization of  $D$  into 4 macrocells. (b) Subsets  $D_L$  and  $D_R$  of  $D$  for horizontal flow, and (c) subsets  $D_B$  and  $D_T$  of  $D$  for vertical flow

with  $D$  in the middle of  $D^*$  to avoid boundary effects; a sketch of  $D$  in  $D^*$  for horizontal flow is shown in Fig. 2.9.

Now we are ready to describe how to get the permeability tensor corresponding to  $D$ . Let  $m \in \mathbb{N}$  be the number of simulations of flows in  $D^*$  and  $\mathbf{u}_h^m = (u_h^m, v_h^m)$ ,  $p_h^m$  denote the numerical approximation of pore scale velocity and pressure values in  $D$  with zeros assigned to  $\mathbf{u}_h^m, p_h^m$  in  $D_r$  and  $D_o$  for impermeable obstructions. Consider the coarse-grid discretization of  $D$ : 4 macrocells as illustrated in Fig. 2.10(a). We define 4 subsets of  $D$  as in Fig. 2.10(b-c):  $D_L = D_{11} \cup D_{21}$ ,  $D_R = D_{12} \cup D_{22}$ ,  $D_B = D_{21} \cup D_{22}$ , and  $D_T = D_{11} \cup D_{12}$ . Let  $x_c$  denote the centroid of a subset  $D_c$  of  $D$  defined as

$$x_c = \frac{1}{|D_c|} \int_{D_c} x \, dx, \quad c \in \{L, R, T, B\}.$$

Each component of averaged velocity  $\mathbf{U}_h^m = (U_h^m, V_h^m)$  in  $D$  is calculated using

$$\begin{cases} U_h^m &= \frac{1}{|D|} \int_D u_h^m = \frac{\phi}{|D_n|} \int_{D_n} u_h^m, \\ V_h^m &= \frac{1}{|D|} \int_D v_h^m = \frac{\phi}{|D_n|} \int_{D_n} v_h^m, \end{cases}$$

with  $(u_h^m, v_h^m) = 0$  on  $D_r$ . Similarly, we calculate the average pressure  $P_{c,h}^m$  in  $D_c \subset D$  for  $c \in \{L, R, T, B\}$ :

$$P_{c,h}^m = \frac{1}{|D_c|} \int_{D_c} p_h^m = \frac{\phi_c}{|D_c \cap D_f|} \int_{D_c \cap D_f} p_h^m,$$

where  $\phi_c = \frac{|D_c \cap D_f|}{|D_c|}$ . Using the averaged pressure  $P_{c,h}^m$ , we approximate the pressure gradient:

$$(G_{LR}^m, G_{TB}^m) = -\nabla P^m \approx \left( \frac{P_{L,h}^m - P_{R,h}^m}{x_R - x_L}, \frac{P_{B,h}^m - P_{T,h}^m}{x_T - x_B} \right).$$

These averaged values satisfy the Darcy's law (2.11):

$$\mathbf{U}_h^m = -\frac{K_\Omega}{\mu} \nabla P^m. \quad (2.16)$$

If  $D$  is isotropic, we only need one simulation data to calculate  $K_\Omega \in \mathbb{R}$ . For the horizontal flow we have  $V_h^1 = 0$  and  $G_{BT}^1 = 0$ , so we can solve for  $K_\Omega$  from

$$U_h^1 = -\frac{K_\Omega}{\mu} G_{LR}^1.$$

For an anisotropic medium  $D \subset \mathbb{R}^2$ , we need at least 2 experiments to get the unique  $K_\Omega = [K_{xx}, K_{xy}; K_{yx}, K_{yy}] \in \mathbb{R}^{2 \times 2}$ . Each experiments satisfy (2.16) and yields to following system:

$$\begin{bmatrix} U_h^1 \\ V_h^1 \\ U_h^2 \\ V_h^2 \end{bmatrix} = \frac{1}{\mu} \begin{bmatrix} G_{LR}^1 & G_{BT}^1 & & \\ & & G_{LR}^1 & G_{BT}^1 \\ G_{LR}^2 & G_{BT}^2 & & \\ & & G_{LR}^2 & G_{BT}^2 \end{bmatrix} \begin{bmatrix} K_{xx} \\ K_{xy} \\ K_{yx} \\ K_{yy} \end{bmatrix},$$

which allows us to reconstruct the full permeability tensor  $K_\Omega$ .

## 2.5 Numerical methods for flow and transport

We briefly review now the numerical methods used for flow and transport models which we need to conduct research presented in this dissertation pore scale geometry.

We start with numerical methods for flow models: Darcy and Stokes flows. To solve Darcy flow (2.11), we substitute  $\langle \mathbf{u} \rangle$  into the continuity equation  $\nabla \cdot \langle \mathbf{u} \rangle = 0$  to get the pressure equation:

$$-\nabla \cdot (K \nabla p) = f. \quad (2.17)$$

For simplicity, we use  $p$  for  $\langle p \rangle$  and  $K$  for  $K_\Omega/\mu$ . The right hand side of (2.17) contains the gravity term. We use the cell-centered finite difference (CCFD) method [125] to solve for  $p$ .

To solve the Stokes equations (2.14), we use the Marker-And-Cell (MAC) method [51,102] and write a saddle point problem:

$$\begin{bmatrix} A & B \\ B^T & \end{bmatrix} \begin{bmatrix} \mathbf{u} \\ p \end{bmatrix} = F,$$

where the block matrix is symmetric positive semi-definite.

Then in Sec. 2.5.5 we describe the conservative methods for the advection equation

$$u_t + f_x = 0.$$

We close this section by reviewing the operator splitting method for the transport model:

$$u_t + Au + Du + Ru = 0,$$

where A, D, and R refer to advection, diffusion, and reaction operators, respectively.

### 2.5.1 Discretization of space and time

We consider a mesh  $V$  on  $\Omega \subset \mathbb{R}^d$ ,  $d \in \{1, 2, 3\}$ . Let  $M$  be the number of cells or volumes  $V_i$  in  $V$  so that  $\cup_{i=1}^M V_i = V$ .

For  $d = 1$ , consider  $\Omega = [x_o, x_f] \subset \mathbb{R}$ . Let  $(x_{i-1/2})_{i=1}^{M+1}$  be an increasing sequence of real numbers in  $\Omega$ :

$$x_o = x_{1/2} < x_{3/2} < \cdots < x_{M-1/2} < x_{M+1/2} = x_f$$

where  $x_{i\pm 1/2}$  represent the cell edges of a cell  $V_i = (x_{i-1/2}, x_{i+1/2})$ . We also use  $\partial V_i$  to denote the edges of a cell  $V_i$ . The mesh size is  $h_i = x_{i+1/2} - x_{i-1/2}$ , and the measure of  $\Omega$  is denoted by  $|\Omega| = \sum_{i=1}^M h_i$ . For simplicity, we present numerical methods on the uniform mesh, i.e.,  $h = h_i$  for all  $i \in \{1, 2, \dots, M\}$ .

If  $\Omega = [x_o, x_f] \times [y_o, y_f] \subset \mathbb{R}^2$ , we discretize  $\Omega$  into  $M = M_x \times M_y$  rectangles  $V_{i,j} = (x_{i-1/2}, x_{i+1/2}) \times (y_{j-1/2}, y_{j+1/2})$  for  $i \in \{1, 2, \dots, M_x\}$  and  $j \in \{1, 2, \dots, M_y\}$ . The values on cell edges are defined at  $(x_{i\pm 1/2}, y_j)$  and  $(x_i, y_{j\pm 1/2})$ . A sketch of 2-dimensional staggered grid is shown in Fig. 2.11. Similarly, we can discretize  $\Omega \subset \mathbb{R}^3$ .

Let  $\tau$  denote the time step size and  $n$  be the number of time steps, so that the time after  $n$  iterations is  $t = n\tau$ . We also use  $T$  to denote the final time after  $N$  iterations:  $T = N\tau$ .

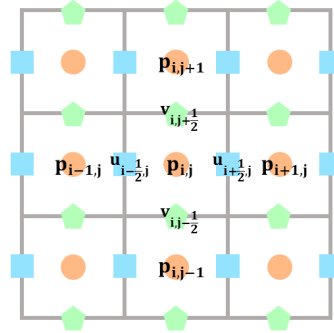


Figure 2.11: 2d staggered grid for CCFD and MAC methods.

## 2.5.2 Notation for numerical approximations

In this section we define the notation for 2-dimensional Cartesian grid  $V$ .

Every rectangular cell  $V_{i,j}$  is also denoted by  $V_k$  for  $k = i + (j - 1)M_x$ . We use subscripts  $\{n,w,s,e\}$  to indicate the neighboring cells of  $V_k$ , i.e.,

$$V_n = V_{i,j+1}, V_w = V_{i-1,j}, V_s = V_{i,j-1}, V_e = V_{i+1,j}.$$

The edges of a cell  $V_k$  is denoted by  $E_{k,\alpha} = \{E_n, E_w, E_s, E_e\}$  where subscripts  $\{n, w, s, e\}$  indicate the edges above, left, below, and right.

The grid function at  $t = t^n$  is denoted by  $U^n$  and the discrete approximation of the cell average of  $u(x, t^n)$  over  $V_k$  is defined as

$$U_k^n = \frac{1}{|V_k|} \int_{V_k} u(x, t^n) dx, \quad (2.18)$$

for all  $k \in \{1, 2, \dots, M\}$ . In this dissertation, we use the constant approximation at the cell centers; thus, we can write

$$U_k^n = u(x_k, t^n).$$

Let  $\Gamma_D$  and  $\Gamma_N$  denote the Dirichlet and Neumann boundaries of  $\Omega$ , respectively.

## 2.5.3 Cell-centered finite difference method

We consider the elliptic problem in  $\Omega \subset \mathbb{R}^d$  for  $d \in \{1, 2, 3\}$

$$-\nabla \cdot (K \nabla p) = f, \quad x \in \Omega, \quad (2.19a)$$

$$p = p_D, \quad x \in \Gamma_D, \quad (2.19b)$$

$$K \nabla p \cdot n = p_N, \quad x \in \Gamma_N, \quad (2.19c)$$

where  $K \in \mathbb{R}^{d \times d}$  is a symmetric positive definite matrix,  $f \in L^2(\Omega)$ , and  $\mathbf{n}$  is the unit outward normal to  $\Gamma_N$ . As mentioned earlier, we can derive (2.19a) from Darcy flow (2.11) with  $K = K_\Omega/\mu$  containing the physical property of  $\Omega$ . For simplicity we assume  $K = K(x) \in \mathbb{R}$  and uniform grid, i.e.,  $h = h_x = h_y$ .

Now we implement the cell-centered finite difference (CCFD) method for (2.19a) for  $d = 2$ . Recall that  $P_k$  denotes the pressure at the cell center  $\mathbf{x}_k = (x_i, y_j)$ . By applying the 5-point stencil, we get

$$-\nabla \cdot (K \nabla p) \approx \sum_{\alpha \in \{n, w, s, e\}} \frac{1}{h} K|_{E_{k, \alpha}} \frac{P_k - P_\alpha}{h}.$$

Here  $K|_{E_{k, \alpha}}$  at cell edges are calculated using harmonic average:

$$K|_{E_\alpha} = \left( \frac{2K_k K_\alpha}{K_k + K_\alpha} \right)^{-1}. \quad (2.20)$$

The Neumann boundary condition is straight forward. On  $\Gamma_N$ , we have

$$K \nabla p \cdot \mathbf{n} \approx K|_{\Gamma_N} p_N.$$

On  $\Gamma_D$  we use the one-sided derivative so that

$$K \nabla p \cdot \mathbf{n} \approx 2K|_{\Gamma_D} \frac{P_k - p_D}{h}.$$

If  $\Gamma = \Gamma_N$ , the solution  $p$  is unique up to a constant. We can choose a solution  $p$  such that  $\int_\Omega p \, dx = 0$ .

**Example 2.5.1** (CCFD in 1d). *Let  $d = 1$ ,  $K = 1$ , and  $\Omega = [a, b]$ . We can write the discrete linear system for (2.19a) with Dirichlet boundary conditions,  $P(a, t) = P_a$  and  $P(b, t) = P_b, \forall t$ , in the matrix form  $AP = F$  where*

$$A = \frac{1}{h^2} \begin{bmatrix} 2 & -1 & & & \\ -1 & \ddots & \ddots & & \\ & \ddots & \ddots & -1 & \\ & & -1 & 2 & \end{bmatrix}, \quad F = \frac{1}{h^2} \begin{bmatrix} P_a \\ 0 \\ \vdots \\ 0 \\ P_b \end{bmatrix}.$$

We can solve the linear system  $AP = F$  directly or iteratively for  $P = [P_1, P_2, \dots, P_M]^T$ .

According to the authors of [125], CCFD is equivalent to the Raviart-Thomas mixed finite element method (MFEM) of the lowest order (RT<sub>0</sub>) on the rectangular grid using a

special quadrature rule and eliminating fluxes. Using this relation, they showed the first order convergence for pressure and velocity. In [155], the superconvergence for both pressure and velocity were obtained for CCFD on rectangular grids. Arbogast et al. extended this result to full tensor coefficients on triangular and logically rectangular grids [5, 6].

One of the advantages of using CCFD is that it eliminates the calculation of the fluxes at the cell edges when we consider coupling of flow and transport models. In next section we describe the MAC method which solves for the pressure at the cell centers and velocities at the cell edges.

#### 2.5.4 Marker-And-Cell (MAC) method for Stokes flow

The Marker and Cell (MAC) method is the finite difference method on a staggered grids which was introduced as the first technique that successfully resolved the incompressible fluid flow [51]. This method is also known as the most popular and simplest method to approximate the pore scale flows such as the steady state Stokes equations and Navier-Stokes equations [42, 50]. Authors of [42, 50] showed that the MAC method converges with  $O(h)$  for both velocity in  $H^1$ -norm and pressure in  $L^2$ -norm on uniform rectangular grids. Later in 2014, Li and Sun [76] proved the superconvergence for velocity on non-uniform rectangular grids, i.e., the second order convergence for velocity in  $L^2$ -norm. They also showed that if the pressure error is  $O(h^2)$ , then we have the superconvergence for pressure as well.

We recall the steady-state Stokes equations (2.14)

$$-\mu\Delta\mathbf{u} + \nabla p = f, \quad x \in D_n, \quad (2.21a)$$

$$\nabla \cdot \mathbf{u} = 0, \quad x \in D_n, \quad (2.21b)$$

with boundary conditions (2.14c).

We assume the notations as introduced in Sec. 2.5.3. With  $\mathbf{u} = [u, v]^T$  and  $f = [f_1, f_2]^T$ , we can rewrite (2.21) as

$$-\mu\Delta u + p_x = f_1, \quad (2.22a)$$

$$-\mu\Delta v + p_y = f_2, \quad (2.22b)$$

$$u_x + v_y = 0. \quad (2.22c)$$

Here we have 3 unknowns  $(u, v, p)$ , and they are defined at different locations on the staggered grid. Recall the illustration of staggered grid in Fig. 2.11. As before, the pressure  $p_k$

is defined at the center of the cell  $V_k$ . The  $x$ -directional velocity component  $u_k$  is defined at the center of cell edges  $E_{k,\alpha}$ ,  $\alpha \in \{w, e\}$  and the  $y$ -directional velocity component  $v_k$  is defined at the center of cell edges  $E_{k,\alpha}$ ,  $\alpha \in \{n, s\}$ . We use the 5-point stencil for  $\Delta u$  and  $\Delta v$ , and the cell-centered difference for  $p_x$  and  $p_y$ . For simplicity, let  $h = h_x = h_y$ . Then we can write (2.22a) at  $(x_{i+1/2}, y_j)$  as

$$\mu \frac{4U_{i+1/2,j} - U_{i-1/2,j} - U_{i+3/2,j} - U_{i+1/2,j-1} - U_{i+1/2,j+1}}{h^2} + \frac{P_{i+1,j} - P_{i,j}}{h} = f_{1,i+1/2,j}.$$

Similarly, we can write one for (2.22b).

In the case of the horizontal flow discussed in Ex. 2.3.2, we discretize the boundary values as follows

$$U_{1/2,j} = u_D(y_j), \quad V_{0,j\pm 1/2} = 0, \quad (2.23a)$$

$$\mu \frac{U_{M_x+3/2,j} - U_{M_x+1/2,j}}{x} - P_{M_x+1,j} = 0, \quad V_{M_x+1,j\pm 1/2} = V_{M_x,j\pm 1/2}. \quad (2.23b)$$

Then the linear system for MAC method is

$$\begin{bmatrix} \mu A_u & & B_u^T \\ & \mu A_v & B_v^T \\ B_u & B_v & \end{bmatrix} \begin{bmatrix} U \\ V \\ P \end{bmatrix} = F, \quad (2.24)$$

where  $A_u U$ ,  $A_v V$ ,  $B_u^T P$ ,  $B_v^T P$  are approximations of  $-\mu \Delta u$ ,  $-\mu \Delta v$ ,  $p_x$ ,  $p_y$ , respectively. Here  $F$  contains the boundary information.

**Example 2.5.2** (Illustration of MAC method). *Recall Ex. 2.3.2. We apply the MAC method on the staggered grids of  $5 \times 5$  voxels. Fig. 2.12 shows the sparsity pattern for the stiffness matrix of (2.24). We verify the superconvergence of the MAC method by comparing the numerical solution of this Poiseuille flow to the analytical solution (2.15) for  $L = 1$ .*

We test the MAC method on the staggered grids of  $M \times M$  voxels for

$$M \in \{20, 40, 80, 160, 320, 640\}$$

and solve (2.24) for  $(\mathbf{u}_h, p_h)$  directly. We obtain the superconvergence for velocity  $\mathbf{u}_h$  and the usual first order convergence for pressure  $p_h$  in  $L^2$ -norm:

$$\|\mathbf{u} - \mathbf{u}_h\|_{L^2} = O(h^{2.2579}) \quad \text{and} \quad \|p - p_h\|_{L^2} = O(h^{0.9752}).$$

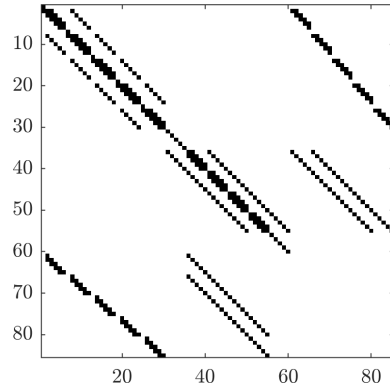


Figure 2.12: The sparsity pattern of MAC discretization for Ex. 2.5.2.

### 2.5.5 Conservative methods for scalar conservation law

Many continuum physics problems arise in science and engineering such as fluid dynamics, traffic flows, semiconductor device simulations, electromagnetics, and meteorology involve the study of conservation laws. In this section we closely follow the description of conservation laws and of numerical schemes as in [44, 73].

We consider the initial value problem (IVP):

$$u_t + f(u)_x = 0, \quad (x, t) \in \mathbb{R} \times \mathbb{R}_+, \quad (2.25a)$$

$$u(x, 0) = u_0(x), \quad x \in \mathbb{R}, \quad (2.25b)$$

where  $u = u(x, t)$  is the conserved quantity such as mass, momentum and energy, and  $f \in C^1(\mathbb{R} \times \mathbb{R}_+)$  is associated flux.

We can approximate the solution  $u$  of (2.25) numerically. The conservative finite volume method approximate the solution  $u$  by the sum of discrete solutions  $U_k$  over control volumes  $V_k$  where  $U_k$  is the averaged quantity (2.18). We consider the integral form of (2.25) over  $V_k = [x_{k-1/2}, x_{k+1/2}]$  with cell size  $h = x_{k+1/2} - x_{k-1/2}$  for one time step  $[t^n, t^{n+1}]$ :

$$\begin{aligned} \frac{1}{h} \int_{x_{k-1/2}}^{x_{k+1/2}} u(x, t^{n+1}) dx &= \frac{1}{h} \int_{x_{k-1/2}}^{x_{k+1/2}} u(x, t^n) dx \\ &\quad - \frac{1}{h} \left[ \int_{t^n}^{t^{n+1}} f(u(x_{k+1/2}, t)) dt - \int_{t^n}^{t^{n+1}} f(u(x_{k-1/2}, t)) dt \right]. \end{aligned} \quad (2.26)$$

Using (2.25) and some approximation to the fluxes

$$F_{k\pm 1/2}^n \approx \frac{1}{\tau} \int_{t^n}^{t^{n+1}} f(u(x_{k\pm 1/2}, t)) dt,$$

we can derive a conservative finite volume method.

**Definition 2.5.1** (Conservative finite volume method). *We say a numerical method for (2.25a) is conservative if it is written in the form*

$$U_j^{n+1} = U_j^n - \frac{\tau}{h} \left[ F_{j+1/2}^n - F_{j-1/2}^n \right], \quad (2.27)$$

where the numerical fluxes may depend on the neighboring quantities

$$F_{j+1/2}^n = F(U_{j-p}^n, U_{j-p+1}^n, \dots, U_{j+q}^n); \quad F_{j-1/2}^n = F(U_{j-p-1}^n, U_{j-p}^n, \dots, U_{j+q-1}^n).$$

In this dissertation, we consider the simplest case with  $p = 0$  and  $q = 1$ :

$$U_j^{n+1} = U_j^n - \frac{\tau}{h} \left[ F(U_j^n, U_{j+1}^n) - F(U_{j-1}^n, U_j^n) \right], \quad (2.28)$$

where the numerical flux  $F(U_j, U_{j+1}) \approx \frac{1}{\tau} \int_{t^n}^{t^{n+1}} f(u(x_{j+1/2}, t)) dt$  for all  $j \in \{1, 2, \dots, M\}$ .

**Definition 2.5.2** (consistency). *The conservative method (2.27) is consistent with (2.25a) if  $F$  is Lipschitz continuous, i.e.,*

$$|F(v_1, \dots, v_r) - F(w_1, \dots, w_r)| \leq L \max\{|v_1 - w_1|, \dots, |v_r - w_r|\}$$

where  $r = p + q$  and  $L$  is a Lipschitz constant.

**Definition 2.5.3** (CFL condition). *The Courant-Friedrichs-Lewy (CFL) condition is a necessary stability condition for any numerical method, so that the physical domain of dependence of the PDE completely lie inside the numerical domain of dependence. The CFL number or Courant number is defined as*

$$\nu = \frac{\tau}{h} \max |f'(u)| \leq 1.$$

**Definition 2.5.4** (Upwind method). *The upwind scheme is (2.28) with the numerical flux*

$$F(U_j, U_{j+1}) = \begin{cases} f(U_j), & (f(U_j) - f(U_{j+1})) / (U_j - U_{j+1}) \geq 0, \\ f(U_{j+1}), & (f(U_j) - f(U_{j+1})) / (U_j - U_{j+1}) < 0. \end{cases} \quad (2.29)$$

**Remark 2.5.1.** *The upwind finite volume method can also be interpreted as the finite difference method with cell centered discretization. In this case, we can also prove the consistency of this upwind finite volume method using the analogue of finite difference method.*

**Definition 2.5.5** (Monotone method [73](Sec. 15.7)). *Consider (2.25a) with two sets of initial data  $u_0$  and  $v_0$ . Suppose that  $u_0(x) \leq v_0(x)$  for all  $x$ . If the numerical solution  $U, V$  evolved from  $u_0$  and  $v_0$ , respectively, holds*

$$U_j^n \leq V_j^n \text{ for all } j \implies U_j^{n+1} \leq V_j^{n+1} \text{ for all } j,$$

then the conservative method that generate  $U, V$  is called a monotone method.

**Definition 2.5.6** (Godunov's method). *An example of monotone method is the Godunov's method. The numerical flux for Godunov's method is*

$$F(U_j, U_{j+1}) = \begin{cases} \min_{U_j \leq U^* \leq U_{j+1}} f(u^*), & U_j \leq U_{j+1}, \\ \max_{U_j \leq U^* \leq U_{j+1}} f(u^*), & U_j > U_{j+1}. \end{cases}$$

**Remark 2.5.2.** *If the flux  $f$  is a nondecreasing function, the Godunov flux  $F(U_j, U_{j+1})$  reduces to  $F(U_j, U_{j+1}) = f(U_j)$  which is the upwind method. Again, for a nonincreasing function  $f$ , the Godunov flux  $F(U_j, U_{j+1}) = f(U_{j+1})$  agrees with upwind method.*

For  $d \geq 2$ , we may compute  $U^n$  by sweeping in each direction as explained in [74]. This may introduce an error unless  $\partial_x f$  and  $\partial_y f$  commute, but this error is generally smaller than the errors from numerical methods. We refer readers to [74] for details.

### 2.5.6 Operator splitting method

To solve the transport model with reaction, we use the operator splitting method [75] to handle advection term explicitly first by the conservative method, then the diffusion-reaction terms implicitly by the cell centered finite difference method.

We consider an advection-diffusion-reaction equation

$$u_t + \nabla \cdot (f(u; q)) - \nabla \cdot (D \nabla u) = g \quad (2.30)$$

with the given flow velocity  $q$ , diffusivity  $D$ , and source  $g$ . Here  $f(u; q)$  can be nonlinear, i.e.,  $f(u; q) = q \max\{1, u\}$ .

First we solve the advection step explicitly with some transport method

$$U_h^{n*} - U_h^{n-1} + \tau \nabla_h \cdot (f(U_h^{n-1}; q_h)) = 0,$$

where  $U_h^{n*}$  denotes the intermediate solution after the advection. We can approximate the Darcy flow  $q_h$  by cell-centered finite difference (CCFD) method [157] and pore scale flows (Stokes and heterogeneous Brinkman flows) by the Marker and Cell (MAC) method [51]. Here  $\nabla_h \cdot (f(U_h^{n-1}; q_h))$  denotes the explicit upwind fluxes.

Then we solve the reaction and diffusion steps together,

$$(I + \tau A_h^D) U_h^n = U_h^{n*} + \tau g_h^n. \quad (2.31)$$

Another possibility is to solve the reaction steps separately

$$U_h^{n**} - U_h^{n*} = \tau g_h^{n*},$$

followed by the diffusion step

$$(I + \tau A_h^D)U_h^n = U_h^{n**},$$

where  $A_h^D$  is the discrete counterpart of  $-\nabla \cdot (D\nabla)$ .

The operator splitting approach is computationally efficient compare to unsplitting approach, especially for complicated problems. This operator splitting method is first-order accurate due to a "splitting error" of  $O(\tau)$ . For some special cases we may maintain order of accuracy of method used, e.g., Lax-Wendroff method for advection step and the two-stage Runge-Kutta method for diffusion and reaction; see for example [74](Ch. 17).

## 2.6 Newton's method

In this section we describe the Semismooth Newton's method that we use to find a solution of the nonsmooth operator equation, e.g., the reaction-diffusion step (2.31).

We start by briefly recalling the Newton's method for a nonlinear system with a smooth nonlinearity. Then we provide some preliminary materials before we state the semismooth Newton's method. We closely follow the notation and method presented in [61, 119, 149].

Newton's method is one the of most powerful tool to solve systems of nonlinear equations [101]

$$\text{Given } f : \mathbb{R}^n \rightarrow \mathbb{R}^m, \text{ find } x^* \in \mathbb{R}^n \text{ such that } f(x^*) = 0. \quad (2.32)$$

The classical Newton's method assumes that the function involved must be continuously differentiable at least in the neighborhood of the solution. We can obtain the Newton's method for smooth systems by replacing the complicated nonlinear  $f$  by its linearization:

$$x_{k+1} := x_k + s_k; \quad \nabla f(x_k)s_k = -f(x_k). \quad (2.33)$$

If  $\nabla f(x_k)$  is Lipschitz continuous and nonsingular for each  $k$ , (2.33) is well-defined and  $x_k \rightarrow x^*$  q-quadratically [61].

Suppose now that  $f$  is only locally Lipschitz. We need to introduce the notion of Newton's method for semismooth systems as defined in [119, 149]. We first define the Clark's generalized gradient.

**Definition 2.6.1** (Clark's generalized Jacobian). Let  $U$  be a open subset of  $\mathbb{R}^n$  and  $f : U \rightarrow \mathbb{R}$  be locally Lipschitz. Clark's subdifferential of  $f$  at  $x \in U$  is defined as

$$\partial f(x) := \text{co}\left\{ \lim_{k \rightarrow \infty} f'(x_k) : x_k \rightarrow x, x_k \in D_f \right\}$$

where  $D_f$  is the set of all points where  $f$  is differentiable and  $f'(x_k)$  is the Jacobian of  $f$  at  $x_k$ . An element of  $\partial f(x)$  is called as the subgradient.

Next we define the notion of semismoothness of  $f$ .

**Definition 2.6.2** (semismooth function).  $f$  is semismooth at  $x \in \mathbb{R}^n$  if it is locally Lipschitz and for all  $h \in \mathbb{R}^n$ , the limit

$$\lim_{\substack{M \in \partial f(x+th') \\ h' \rightarrow h, t \rightarrow 0^+}} Mh'$$

exists and is finite.

**Definition 2.6.3** ( $\alpha$ -order semismooth).  $f$  is  $\alpha$ -order semismooth,  $0 < \alpha \leq 1$ , at  $x \in \mathbb{R}^n$  if it is locally Lipschitz, directionally differentiable at  $x$ , and if

$$\max_{M \in \partial f(x+h)} \|f(x+h) - f(x) - Mh\|_2 = O(\|h\|_2^{1+\alpha}) \quad \text{as } h \rightarrow 0.$$

Now we are ready to describe the nonsmooth version of Newton's method:

$$x_{k+1} := x_k + s_k; \quad M_k s_k = f(x_k), \quad (2.34)$$

where  $M_k \in \partial f(x_k)$ .

**Algorithm 1:** Semismooth Newton method to solve  $f(x) = 0$

- 1 Guess  $x_0$ .
- 2 **while**  $f(x_k) \neq 0$  or stopping criteria not met **do**
- 3     Choose  $M_k \in \partial f(x_k)$ .
- 4     Solve  $M_k s_k = -f(x_k)$  for  $s_k$ .
- 5     Update  $x_{k+1} \leftarrow x_k + s_k$ .
- 6     Advance  $k$  by 1.
- 7 **end**

**Theorem 2.6.1** (local convergence of (2.34) [119](Theorem 3.2)). Suppose that  $x^*$  is a solution of

$$f(x) = 0,$$

where  $f$  is locally Lipschitz and semismooth at  $x^*$ , and all  $M \in \partial f(x^*)$  are nonsingular. Then the iterative method (2.34) is well-defined and convergent to  $x^*$  in a neighborhood of  $x^*$ . If in addition  $f$  is  $\alpha$ -order semismooth at  $x^*$ , the convergence of (2.34) is of order  $1 + \alpha$ .

**Theorem 2.6.2** (global convergence of (2.34) [119](Theorem 3.3)). *Suppose that  $f$  is locally Lipschitzian and semismooth on  $S = \{x \in \mathbb{R}^n : \|x - x^0\| \leq r\}$ . Also suppose that any  $M \in \partial F(x)$ ,  $x, y \in S$ ,  $V$  is nonsingular,*

$$\begin{aligned} \|M^{-1}\| &\leq \beta, \\ \|M(y - x) - f'(x; y - x)\| &\leq \gamma \|y - x\|, \\ \|f(y) - f(x) - f'(x; y - x)\| &\leq \delta \|y - x\|, \end{aligned}$$

where  $\alpha = \beta(\gamma + \delta)$  and  $\beta\|F(x^0)\| \leq r(1 - \alpha)$ . Then the iterates (2.34) remain in  $S$  and converge  $q$ -superlinearly to the unique solution  $x^*$  in  $S$ . Moreover, the error estimate

$$\|x^k - x^*\| \leq [\alpha/(1 - \alpha)] \|x^k - x^{k-1}\|$$

holds for  $k \in \mathbb{N}$ .

We provide few examples of subgradients.

**Example 2.6.1** (Piecewise smooth nonlinear function). *If  $f(x) = |x|$ , then the sign graph  $\text{sgn}(x)$ , defined in Sec. 2.1, is a subgradient of  $f$ , i.e.,  $\text{sgn}(x) \in \partial f$ .*

**Example 2.6.2.** *If  $f(x) = \max\{0, x\}$ , then the Heaviside graph  $H(\cdot)$  defined in Sec. 2.1 is a subgradient of  $f$ .*

### 3 Methane gas transport in hydrate stability zone

The following three chapters are from the work presented in [106] on the methane hydrate formation and dissociation in hydrate stability zone. In this chapter we closely follow the results published in [106](Sec. 3 and 5). We explain the model and provide preliminary materials for our numerical analysis and simulation results which we discuss in Ch. 4 and Ch. 5. We first explain the physical behavior of methane hydrate in nature in Sec. 3.1, follow by the review of the methane gas transport model in the hydrate stability zone which was introduced in [107,110,111] in Sec. 3.2. Then in Sec. 3.3, we describe the phase equilibria graph which we will also discuss further in Ch. 5. This chapter is closed by providing the temporal and spatial discretization and notations used for our analyses and simulations in Sec.3.5.

Our objective is to analyze discrete models for hydrate formation and dissociation which describes methane transport coupled to phase behavior under equilibrium and non-equilibrium conditions. The equilibrium model is a simplified version of the comprehensive model [80] presented earlier in [110,111]. Kinetic models from the literature [38,48,49,62,153] are formulated for the general context of three-phase equilibria; our model resembles these but covers both unsaturated as well as saturated conditions in liquid-hydrate conditions. The scheme combines finite volume spatial discretization with implicit-explicit time discretization, and uses the formal mathematical framework of multivalued graphs. This framework for the equilibrium model is equivalent to variable switching as we demonstrated in [41]. Our analysis of the kinetic model with this framework supports the understanding of the equilibrium as the limit of kinetic model under fast reaction rates.

To our knowledge, our analysis is the first of this kind for advective transport in either the equilibrium or kinetic setting for hydrate models. Our analysis applies only to the simplified model with which we simulate hydrate phase change. The analysis we present does not directly apply to the possibly strongly coupled effects like evolving hydraulic properties which are critical for simulation of hydrate evolution and recycling. Our results are therefore the first step towards future work on the analysis of schemes for more comprehensive models.

### 3.1 Background on methane hydrate

Methane is present in sub-ocean sediments and Arctic regions due to biogenic sources and from upward fluxes from the deeper Earth layers [80]. It is transported by diffusion and advective fluxes, and can be present in liquid, gas or solid phases. The partition of methane component between phases depends on the pressure, temperature, and the amount of methane component. With small amounts of methane and at large depths (i.e., large pressures), methane is dissolved in the aqueous (liquid) brine phase denoted by  $l$ . With larger amounts of methane and at low temperatures, the solid phase made of methane and water in fixed proportions precipitates; this solid phase denoted by  $h$  is called methane hydrate (clathrate or methane ice). At higher temperatures, the hydrate phase is not stable and free gas phase forms. A typical distribution of phases in sub-ocean sediments is that the solid hydrate phase is stable and present at low temperatures; specifically, this occurs above the so-called Bottom of Hydrate Stability Zone (BHSZ). In turn, below BHSZ, only the gas phase is stable. Phase equilibria represent the tendency of a system to maintain low energy, and correspond to the most stable distribution of components between phases.

The phase distributions may not always follow equilibria; this is common at short time scales, e.g., after seismic events which alter the distribution of gases and sediments, or during production of gas from subsurface. The time scales of hydrate formation or dissociation is on the order of hours or days [136,168]. In production scenarios [56,77,92,93,167] this time scale is comparable to that of the transport processes. Comprehensive subsurface transport simulators including STOMP, TOUGH, PFLOTTRAN, GEOS, Geo-COUS implement the complex kinetic exchange model in the applications using depressurization or thermal stimulation to aid methane recovery from hydrate; see e.g., the recent international code comparison studies [160,162] led by DOE/NETL.

Some other computational models use kinetics rather than equilibria to implement or to approximate phase behavior regardless of the time scale considered [25,122,147]. For modeling methane in the environment at large spatial scales, e.g., methane flux response to environmental temperature variations or abrupt geological events, some authors use kinetic models [15,48,49,147,153].

Our work addresses equilibrium models as well as certain selected scenario of non-equilibria. We do not account for the presence of free gas such as ex-solved gas or from buoyant gas travelling upwards above BHSZ. The analysis of a model involving gas is the

subject of current work.

## 3.2 Notation and equilibrium model

In this section we describe a model accounting for methane transport above BHSZ in a porous reservoir  $\Omega \subset \mathbb{R}^d$ , over time  $t$ , under the assumption of phase equilibria. For phase equilibria we closely follow the comprehensive model in [80] in hydrate zone which is simplified in [110, 111] for the purposes of efficient simulations. This reduced model is motivated by analyzing the real reservoir data and experimental observations. We refer readers to [41, 107] for the well-posedness analysis of this reduced model.

Below we recall the equilibrium model from [107]; it is the same as that in [110, 111] under the assumption of constant salinity. We discuss the motivation and details of kinetic models in Ch. 5.

### 3.2.1 Notation and assumptions for Darcy scale methane hydrate models

We use the notation introduced in Sec. 2.1 and closely follow the notation from [107]. The different symbols for equilibrium and kinetic models with typical parameter values are listed in Tab. 3.1.

**Assumptions.** We make the following assumptions in the model development.

(A1) The reservoir  $\Omega$  is in the hydrate stability zone, i.e., only the liquid and hydrate phases are stable.

(A2) Free gas is not present in  $\Omega$ , i.e., there is abundant water present for hydrate formation; see [80].

In addition, the following assumptions are made for the sake of presentation and analysis, but are not needed for the computational model or for simulations.

(A3) Liquid and hydrate phases are incompressible.

(A4) The sediment is rigid, and the porosity  $\phi(x, t) \approx \phi(x)$  is fixed.

(A5) Salinity  $\chi_{lS}(x, t) = \chi_{lS}^{sw} = \text{const.}$  equals seawater salinity  $\chi_{lS}^{sw}$ .

Symbol	Description	Value/Units
$\rho_l$	Liquid density	1030 [kg/m <sup>3</sup> ]
$\rho_h$	Hydrate density	925 [kg/m <sup>3</sup> ]
$\chi, \chi_{Mh}$	Mass fraction of methane in liquid and hydrate phase	[kg/kg]
$S$	Hydrate saturation	[-]
$R$	$\rho_h \chi_{Mh} / \rho_l$	0.1203 [kg/kg]
$\chi^*$	Maximum solubility of methane, $\chi^* \approx \chi^*(P, T, \chi_{lS}^{sw})$ $\max_x \chi^* \approx 2.4 \times 10^{-3}$ [kg/kg] for UBGH2-7 in [110]	[kg/kg]
$\phi$	Porosity	[-]
$K_\Omega$	Permeability	[m <sup>2</sup> ]
$\mu_l$	Liquid phase viscosity	$8.9 \times 10^{-4}$ [Pa · s]
$q$	Darcy velocity given by (3.4b)	[m/s]
$d_m$	Diffusivity	[m <sup>2</sup> /s]
$F_M$	Source of methane	[kg/kg]
$P$	Pressure	[MPa]
$T$	Temperature	[K]
$\chi_{lS}$	salinity	0.035 [kg/kg]
$E_*$	Phase equilibria which relates $(\chi, S)$	
$W_*$	Inverse graph of $E_*$	
$E_*^0$	Physically meaningful portion of $E_*$	

Table 3.1: Notations used in Sec. 3–5

### 3.2.2 Mass conservation equations

Consider  $(x, t)$  at a point  $x \in \Omega$  and time  $t > 0$ . We denote the mass fraction of methane in the liquid phase by  $\chi(x, t)$  and the volume fraction of hydrate by  $S(x, t)$ . With (A1) and (A2), the total mass density of methane at  $(x, t)$  is

$$\rho_l u = (1 - S)\rho_l \chi + S\rho_h \chi_{Mh}$$

with  $\rho_l, \rho_h$  denoting mass density of brine and of hydrate, respectively, and  $\chi_{Mh}$  denoting the mass fraction of methane in the hydrate phase, which is a known fixed constant. The mass conservation equation for methane component in porous sediment of porosity  $\phi$  is thus

$$\partial_t (\phi \rho_l u) + \nabla \cdot (q \rho_l \chi) - \nabla \cdot (\rho_l d_m \nabla \chi) = F_M. \quad (3.1a)$$

Here  $d_m$  is the diffusivity of methane gas, and  $q$  is the Darcy flux defined below. Also,  $F_M$  accounts for methane sources, e.g., biogenic production of methane by microbes, or sink terms relevant for the production scenarios. We also rewrite

$$u = (1 - S)\chi + RS = \chi + S(R - \chi), \quad (3.1b)$$

with  $R = \frac{\rho_h \chi_{Mh}}{\rho_l}$ . In practice, with the values reported in [110];  $R = 0.1203$  [kg/kg], we have  $\rho_l = 1030$  [kg/m<sup>3</sup>],  $\rho_h = 925$  [kg/m<sup>3</sup>], while  $\max_x \chi^*(x) \approx 2.4 \times 10^{-3}$  [kg/kg] for the case of UBGH2-7 as given in [110]. From now on we will assume

$$0 < \chi^* < R. \quad (3.2)$$

With the single equation (3.1) involving two variables  $u$  and  $S$  or  $\chi$  and  $S$ , we close the system by either assuming equilibrium conditions binding  $\chi$  and  $S$ , or setting up a non-equilibrium model which evolves towards the equilibrium.

The model (3.1) is complemented with the mass conservation equation for water component whose concentration is  $1 - \chi$  in liquid phase and  $1 - \chi_{Mh}$  in the hydrate phase. The model for water mass conservation is

$$\partial_t (\phi [(1 - S)\rho_l(1 - \chi) + S\rho_h(1 - \chi_{Mh})]) + \nabla \cdot (q \rho_l(1 - \chi)) = 0. \quad (3.3)$$

### 3.2.3 Pressure equation

The pressure equation follows by adding (3.1a) with (3.1b) and (3.3); with Darcy's law we obtain

$$\partial_t (\phi [(1 - S)\rho_l + S\rho_h]) + \nabla \cdot (q \rho_l) - \nabla \cdot (\rho_l d_m \nabla \chi) = F_M, \quad (3.4a)$$

$$q = -\frac{K_\Omega}{\mu_l}(\nabla P - \rho_l G \nabla d), \quad (3.4b)$$

with Darcy flux  $q$ , pressure  $P(x, t)$ , permeability  $K_\Omega$  of  $\Omega$ , liquid phase viscosity  $\mu_l$ , and depth  $d = d(x)$ . Here  $K_\Omega = K_\Omega(x; S)$  depends on the presence of hydrate in the pore-space, with empirical data, e.g., in [80]. Typically  $K_\Omega(\cdot; S)$  decreases with  $S$ , and the porous matrix is plugged up with hydrate when hydrate saturation is close to 1.

At large time scales such as in basin modeling, the pressure follows distribution close to hydrostatic with  $q = 0$ . Otherwise, there can be gas fluxes with  $q \neq 0$ , e.g., from deep in the Earth's crust upwards, and we must solve (3.4) under given boundary conditions. One practical scenario is when  $q$  is given at the bottom of the reservoir, and a fixed pressure is known at the top, e.g., from the known height of water column. Rewriting (3.4) as

$$\nabla \cdot q = \frac{F_M}{\rho_l} + \nabla \cdot (d_m \nabla \chi) + \partial_t \left( \phi S \frac{\Delta \rho}{\rho_l} \right), \quad \text{for } \Delta \rho = \rho_l - \rho_h, \quad (3.5)$$

allows to study contributions to local variations of  $q$ . We see that the magnitude of the first and second terms on the right hand side is modest in realistic settings [110]. However, the third term may contribute to the local increase of velocity due to the density difference  $\Delta \rho$  whenever  $S \uparrow$  increases rapidly.

### 3.3 Phase equilibria for hydrate crystal formation

The formation of a hydrate crystal out of liquid phase usually involves the processes of nucleation, diffusion of molecules towards the existing cages, and the adsorption of new crystals; see e.g., molecular dynamics simulations in [136, 154] at time scales of  $10^{-6}$  [s]. At the reservoir time scales of transport, the hydrate formation or dissociation is modeled by an aggregate of the microscopic processes; one assumes either an equilibrium presented here or a kinetic model which is discussed in Ch. 5.

At equilibrium, the hydrate forms only if the methane concentration  $\chi$  in water has reached its maximum solubility denoted by  $\chi^*$ . When the hydrate crystals form, we have that  $S > 0$  and  $\chi = \chi^*$ , the saturated case. When  $\chi < \chi^*$ , no hydrate exists, and  $S = 0$ . This is expressed by the constraint

$$\begin{cases} \chi \leq \chi^*, & S = 0, \\ \chi = \chi^*, & S \geq 0. \end{cases} \quad (3.6)$$

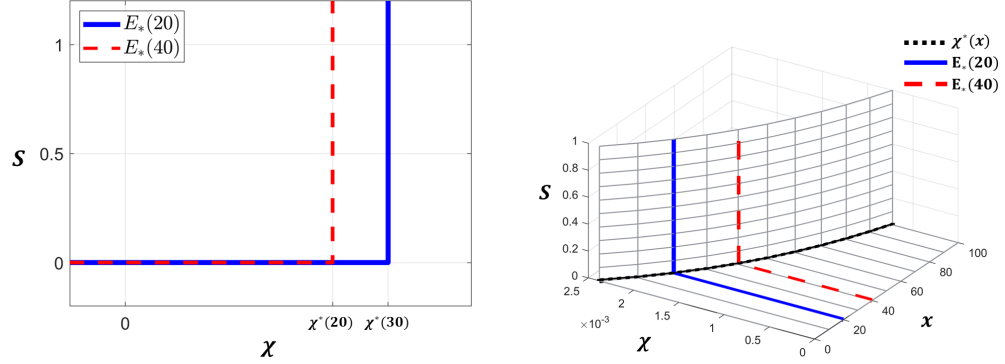


Figure 3.1: Illustration of graph  $E_*$  with data from Ulleung Basin case UBGH2-7 [110], where  $\chi^*(x) \approx 0.0024e^{-0.012x}$ . Left: the portion of  $E_* = E_*(x)$  for a fixed  $x$ . Right: multivariate view of  $(\chi, S) \in E_*(x)$ .

Next we write an explicit formula for the dependence of the total amount of methane  $u$  on  $(\chi, S)$ . At a given  $(x, t)$  with  $\chi^*(x, t)$  known, we have

$$u = \begin{cases} \chi, & u \leq \chi^*, S = 0, \\ (1 - S)\chi^* + SR, & u \geq \chi^*, S \geq 0. \end{cases} \quad (3.7)$$

Conversely, given  $u$ , the equilibrium values  $\chi$  and  $S$  satisfying (3.6) are given uniquely

$$\chi = \min\{\chi^*, u\} \quad \text{and} \quad S = \frac{(u - \chi^*)_+}{R - \chi^*}. \quad (3.8)$$

The relationship (3.8) can be used at any  $(x, t)$  to get the unique values  $\chi(x, t)$  and  $S(x, t)$  from  $u(x, t)$ . The quantity  $\chi^* = \chi^*(P, T, \chi_{lS})$  depends on the pressure  $P$  and temperature  $T$ , and salinity  $\chi_{lS}$ . This dependence is resolved sequentially in our computational model: over some macro time step  $P, T$  are kept constant and  $\chi^*$  depends on  $x$  only. This is discussed in detail later in Sec. 3.5.1. We refer readers to [110] for details in calculating  $\chi^*$  when  $(P, T, \chi_{lS})$  change.

### 3.3.1 Equilibrium model with multivalued graphs

The formulas (3.6)–(3.8) are simple and explicit. For the needs of the kinetic model to be defined in Ch. 5, we write that the variables  $(\chi, S)$  “live” on the graph  $E_* = E_*^- \cup E_*^+$  defined as

$$(\chi, S) \in E_* = (-\infty, \chi^*] \times \{0\} \cup \{\chi^*\} \times [0, \infty), \quad (3.9)$$

with  $E_*^- = (-\infty, \chi^*] \times \{0\}$ ,  $E_*^+ = \{\chi^*\} \times [0, \infty)$ , as illustrated in Fig. 3.1.

The inverse graph  $W_* = E_*^{-1}$  is

$$W_*(S) \ni \chi \equiv (S, \chi) \in W_* = \{0\} \times (-\infty, \chi^*] \cup [0, \infty) \times \{\chi^*\}.$$

It is easy to see that both  $E_*$  and  $W_*$  are maximal monotone. We then write  $S \in E_*(\chi)$  or  $\chi \in W_*(S)$ . These graphs are set-valued, but in evolution models, the particular selection out of these graphs is actually unique, as discussed in Sec. 2.2.

**Remark 3.3.1.** *Not all the points on the graph  $E_*$  (3.9) are physically meaningful. In particular, any reasonable calculated values of concentrations and saturations should satisfy  $\chi \geq 0$  and  $0 \leq S < 1$ . We use  $E_*^0 = \{(\chi, S) \in E_* : \chi \geq 0; S < 1\}$  to denote the physically meaningful portion of  $E_*$ . In addition, from (3.2) and (3.7) we see that if  $(\chi, S) \in E_*^0$ , then  $u$  satisfies*

$$0 \leq u(\chi, S) < R. \quad (3.10)$$

*Conversely, for any  $u$  which satisfies (3.10), we have from (3.2) that  $(\chi, S)$  given by (3.8) satisfies  $0 \leq \chi \leq \chi^*$  and  $0 \leq S < 1$ .*

### 3.4 Summary of coupled thermo-transport model under equilibrium condition

We summarize now the methane transport model in a form amenable to discretization and analyses. First we outline how the thermodynamic conditions on  $(P, T)$  and  $\chi^*$  are handled.

$$\text{Assume known } T(x, t), \text{ or solve an appropriate energy equation} \quad (3.11a)$$

under some initial and boundary conditions.

$$\text{Assume known } P(x, t), q(x, t), \text{ or find these from (3.4)} \quad (3.11b)$$

under some boundary conditions.

$$\text{Calculate } \chi^*(x, t) = \chi^*(P(x, t), T(x, t), \chi_{lS}(x, t)). \quad (3.11c)$$

For (3.11c) we use the approach described in [110] based on estimates of  $\chi^*$  generated by CSMGem, semi-empirical model from [146], and the parametric model from [27] using algebraic curve fitting model for equilibrium pressure,  $P_{eq}$ , given in [86]. In examples in this dissertation, we assume  $\chi_{lS} = \chi_{lS}^{sw}$  as declared in (A5).

Next, use mass conservation (3.1) which we divide by  $\rho_l$  upon (A3). The equilibrium model, with  $u(x, t)$  given by (3.7) is

$$\partial_t(\phi u) + \nabla \cdot (q\chi) - \nabla \cdot (d_m \nabla \chi) = \frac{F_M}{\rho_l}, \quad x \in \Omega, t > 0, \quad (3.12a)$$

$$\chi(x, t) = \min\{\chi^*(x, t), u(x, t)\}, \quad x \in \Omega, t > 0, \quad (3.12b)$$

$$u(x, 0) = u_{init}(x), \quad x \in \Omega, \quad (3.12c)$$

$$\text{Assume boundary conditions for } \chi(x, t), \quad x \in \partial\Omega, t > 0. \quad (3.12d)$$

We comment now on the couplings. The equilibrium model (3.12) and non-equilibrium model (5.29) which will be discussed in Ch. 5 are strongly coupled to the thermodynamic conditions given in (3.11c) and to the flux  $q$  found by (3.11b). For the time scales of interest in this context, most significant are the parametrizations of (3.12b) and (5.29b) by the quantity  $\chi^* = \chi^*(x, t)$  found in (3.11b). On the other hand,  $\chi^*(x, t)$  depends primarily on the temperature and much less on  $P(x, t)$ . At the same time, the conductivities in the energy equation are less sensitive to  $S$  than the quantities in the pressure equation; see, e.g., data in [80].

In turn, the solution to (3.11) depends on the solution to the methane transport (3.12) or (5.29). In particular, as (3.5) indicates, the local variations in  $q(x, t)$  are due to  $\nabla \cdot q \approx \partial_t(\phi[S \frac{\Delta \rho}{\rho_t}])$ , which require re-computing  $q$ . In addition, the permeability  $K_\Omega$  in (3.11b) depends on  $S$ , and the resulting local pressure variation may affect  $\chi^*$  by the appearance of micro-cracks; see, e.g., [24, 94].

These inter-dependencies can be resolved by iteration, time-lagging, or variable freezing; we discuss these next.

### 3.5 Approximation schemes and resolving coupled components

The choice of time-stepping and spatial discretization depends on the objectives of simulation and on the competing demands of modeling accuracy, and efficiency and robustness of the solver. In this dissertation we are interested in modeling hydrate evolution in natural environment. The simulation scenarios we consider may involve response to changing boundary conditions for temperature or pressure such as due to the warming sea waters or sudden change in the sediment depth. We consider that these inputs vary in time on the scale of years or kiloyears but not as strongly as in production scenarios on the scale of days or hours. This assumption on the time scale motivates the choice of time stepping. The simplest way to resolve the couplings is to consider the variables  $P(x)$  and  $T(x)$  as time-independent over the simulation time scale, i.e., “freeze them” over  $[0, T]$ , and to solve the equilibrium model (3.12). This strategy is adopted in many hydrate models at basin

scale where the pressure and temperature are assumed known between any large geologic events and where  $P(x)$ ,  $T(x)$  follow closely the hydraulic gradient and geothermal gradient, respectively; see, e.g., [110, 111, 147]. For simulation over shorter time scales, this approach may require recomputing  $P(x)$  and  $T(x)$  over shorter time frames whenever the external controls change. With the equilibrium model (3.12), the system is immediately brought to equilibrium in the first transport step. To simulate a gradual return to equilibrium, we must use the kinetic model (5.29).

The most complex and comprehensive way to resolve the couplings is to use fully implicit coupling for the equilibrium model [80] and for the kinetic model [48, 49]; see also general subsurface simulators described in [160]. However, a fully implicit solution for several independent variables including phase behavior requires delicate time-stepping with advanced strategies to ensure global convergence and robustness of the Newton solver.

As an intermediate strategy between the most complex and most simple, the coupling including the evaluation of thermodynamic conditions can be handled in a sequential manner or by time-lagging. Our analysis applies in this setting. Here (3.11) is solved at (almost) every time step. Once  $(P, T, \chi^*)$  are known, (3.12) or (5.29) follow. This is similar to a strategy common in reservoir simulation and compositional models called IMPES or IMPEC in which the pressure equation and thermodynamics conditions in (3.11) and the concentration equations (3.12) are solved at separate time schedules with large pressure time steps  $\Delta T$ , and small transport steps  $\tau = \Delta T/K$ . See, e.g., [90, 105, 156] where  $K > 1$  was used. The sequential and time-lagging strategies carry some modeling error compared to the fully implicit model; the error decreases when small time steps are used. Additional iterations to decrease this error can be carried out over the macro time step; see recent analysis on multi-rate schemes for coupled flow and geomechanics in [3, 49]; additionally, stabilization terms may improve convergence in [65, 120]. If needed, we can also set  $K = 1$  and  $\tau = \Delta T$ .

In our computational models we follow the time lagging strategy with macro-time steps but without iteration. Authors of [111] used this strategy for hydrate basin modeling. For simplicity, we assume uniform time stepping below.

### 3.5.1 Time-stepping with macro time steps and concentration time steps.

The concentration time step  $\tau = \frac{T}{N}$  for (3.12) or (5.29) is chosen to satisfy some stability constraints. The macro time step  $\Delta T = K\tau$  for (3.11) is chosen to be small

enough so that  $\chi^*(x, t), q(x, t)$  respond to the model inputs for pressure and temperature. Here  $K \geq 1$ . Now,  $MK = N$  and  $T = M\Delta T = MK\tau = N\tau$ .

$$0 = t^0 < t^1 < \dots < t^n = n\tau < \dots < t^N = T = N\tau, \quad \text{with } t^n = n\tau, \quad n = 0, 1, \dots, N.$$

$$0 = T^0 < T^1 < \dots < T^m = m\Delta T < \dots < T^M = T = M\Delta t, \quad \text{with } m = 0, 1, \dots, M.$$

Note that  $T^m = m\Delta T = mK\tau = t^{mK}$ . We outline our algorithm.

<b>Algorithm 2:</b> Time stepping (macro-time steps) $m = 1, 2, \dots, M$	
<b>1</b>	<b>while</b> $t \in [T^{m-1}, T^m]$ <b>do</b>
<b>2</b>	Assume $S _{T^{m-1}}$ is known.
<b>3</b>	Solve (3.11) for $(T, P, q, \chi^*) _{T^m}$ .
<b>4</b>	Set the values $(q, \chi^*), t \in [T^{m-1}, T^m]$ from $(q, \chi^*) _{T^{m-1}}$ or by interpolating between these and $(q, \chi^*) _{T^{m-1}}$ .
<b>5</b>	<b>for</b> $n = (m-1)K + 1 : mK$ <b>do</b>
<b>6</b>	Assume $(q, \chi^*), t \in [T^{m-1}, T^m] = [t^{(m-1)K}, t^{mK}]$ known.
<b>7</b>	Solve the concentration problem (3.12) or (5.29) for $(S, \chi) _{t^n}$
<b>8</b>	<b>end</b>
<b>9</b>	With $n = mK$ , set $S _{T^m} = S _{t^n}$ . Advance to the next macro-time step with $m := m + 1$ .
<b>10</b>	<b>end</b>

We devote Ex. 5.5.2 in Sec. 5.5.1 to the study of sensitivity of simulations to  $\Delta T$ .

### 3.5.2 Spatial discretization.

We set up hexahedral grid over  $\Omega$  and use finite volume type approximations. Our schemes are first-order in time, with explicit in time upwind treatment of advection, and implicit treatment of phase behavior and diffusion at every time step. For simplicity we define the schemes for 1d case with  $x \in \Omega = (0, D^{max})$  where  $x = 0$  is set at BHSZ pointing upwards towards the seafloor and the upward flux  $q(x, t) > 0$ . We cover  $\Omega$  with uniform size grid cells  $[x_{j-1/2}, x_{j+1/2}]$ , each with center at  $x_j = (j + 1/2)h$  where  $h = x_{j+1/2} - x_{j-1/2}$ . The cell grid values are denoted by  $V_j \approx v(x_j)$ , and  $V_j^n \approx v(x_j, t^n)$ . The Darcy flux  $q$  are defined at the cell edges  $q_{j\pm 1/2}^n$ , and the fluxes  $q\chi$  are approximated as is done for the space-dependent flux in the ‘‘color equation’’ [74][Chapter 9].

We skip the presentation of schemes for (3.11) which are standard; see, e.g., [80, 104]. However, our treatment of phase equilibria and of kinetics requires care. In Ch. 4 we define

numerical schemes for the concentration steps (3.12) and in Ch. 5 for (5.29). They share the mass conservation equation discretized as follows.

We approximate  $U_j^n \approx u(x_j, t^n)$  and  $X_j^n \approx \chi(x_j, t^n)$  discretizing the mass conservation (3.12a) and (5.29a) parts of (3.12) and (5.29) by

$$\begin{aligned} \Phi_j(U_j^n - U_j^{n-1}) + \frac{\tau}{h}(q_{j-1/2}^{n-1}X_j^{n-1} - q_{j-3/2}^{n-1}X_{j-1}^{n-1}) + \frac{d_m\tau}{h^2} [2X_j^n - X_{j-1}^n - X_{j+1}^n] \\ = \frac{\tau F_M(x_j, t^n)}{\rho_l}. \end{aligned} \quad (3.13)$$

We approximate the initial data

$$U_j^0 = \frac{1}{h} \int_{x_{j-1/2}}^{x_{j+1/2}} u_{init}(x) dx.$$

The initial data in the approximation to (5.29) is defined analogously.

The equation (3.13) is complemented with the discrete version of (3.12b) for the equilibrium model or with discrete version of (5.29b) for the kinetic model, and with appropriate statement on the boundary conditions. These are stated in Ch. 4 and 5 along with the analysis of their stabilities.

### 3.5.3 Notation for stability analysis

Recall the notation defined in Sec. 2.5.1–2.5.2. For some grid function  $U^n = (U_j^n)_j$  with  $U_j^n \approx u(x_j, t^n)$  for  $(x_j, t^n) \in [x_{j-1/2}, x_{j+1/2}] \times [t^n, t^{n+1})$ , we let  $U^\Delta$  represent the collection of all  $(U^n)^n$ . We recall  $\|U^n\|_1 = h \sum_j |U_j^n|$ , and the total variation  $TV(U^n)$  and total variation in time  $TV_T(U^\Delta)$ :

$$\begin{aligned} TV(U^n) &= \sum_{j \in \mathbb{Z}} |U_j^n - U_{j-1}^n|, \\ TV_T(U^\Delta) &= \sum_{n=0}^{T/\tau} [\tau TV(U^n) + \|U^n - U^{n-1}\|_1]. \end{aligned}$$

For the kinetic problem which will be discussed in Ch. 5, we work with

$$\|(X^n, \Psi^n)\|_{\Delta,1} = \|X^n\|_1 + \|\Psi^n\|_1,$$

and  $TV(X^n, \Psi^n)$  and  $TV_T(X^\Delta, \Psi^\Delta)$  extended similarly to product space.

## 4 Algorithm, analysis, and simulation for methane hydrate model under equilibrium closure

In this chapter we analyze the first-order upwind discretization for (3.12) and present the Darcy scale simulations in homogeneous and heterogeneous subsea sediments. This chapter corresponds to the materials presented in [106](Sec. 6 and 8.1).

The outline of this chapter is as follows. We first state the assumptions for analysis in Sec. 4.1 and describe our numerical scheme in Sec. 4.2. The literature on the rate of convergence of numerical schemes including the Upwind method and Godunov's method is discussed in Sec. 2.28 for a scalar conservation law

$$\partial_t u + \partial_x f = 0 \tag{4.1}$$

is explained in Sec. 4.3. We provide the first rigorous stability proof of the first-order upwind scheme for the methane gas transport model (4.1) with  $f = f(x, t; u)$  in Sec. 4.4. In Sec. 4.5 we present simulation results in homogeneous and heterogeneous subsea sediments and verify the well-known rate of convergence  $O(\sqrt{h})$ . We also include a simulation result that demonstrate the undercooling effect caused by diffusion in Remark 4.5.1.

Our study of  $TV_T(U^\Delta)$  for (3.12) helps us to predict the variability and the challenges to the numerical solution depending on the data. We show that  $TV_T(U^\Delta)$  increases in time depending on the variability and smoothness of data  $\chi^*(x, t)$  and  $q(x, t)$ . Stability along with consistency of the discrete schemes leads to the convergence of numerical schemes. Our analysis is also useful to understand the sensitivity of the model (3.12) on its data.

### 4.1 Assumptions for analysis

We analyze only the scheme (3.13) for transport model complemented by an equilibrium or kinetic closure to be stated, under assumptions (A1-A5) from Sec. 3.2. We assume that the data  $\chi^*(x, t)$  and  $q(x, t)$  found by (3.11) are known over each macro-time step  $[T^{m-1}, T^m]$  and varies in some predictable fashion. As usual, to study the accumulation of the discretization error in time, we set  $F_M = 0$ . We also set  $d_m = 0$  to focus on the advection dominated case. We consider the transport problem on  $x \in \mathbb{R}$  (that is,  $j \in \mathbb{Z}$ ) rather than  $x \in \Omega$ , which avoids dealing with a mixture of boundary and initial conditions in the analysis. For this we assume that initial data and the solution to the transport prob-

lem have compact support in some  $\Omega_S \subset \mathbb{R}$  with measure  $|\Omega_S| = \omega_S$ , hence this reduces summing over  $j \in \mathbb{Z}$  to  $j \in \mathbb{Z}^0$ . Clearly, realistic simulations consider a bounded domain and boundary conditions.

Finally, we assume the sediment is homogeneous with  $\phi(x) = \phi_0 = \text{const.}$ , and we drop  $\phi_0$  while keeping the notation unchanged, but the analysis could be amended easily as long as  $\phi(x)$  is smooth and bounded away from 0. In particular, in (3.12) we could change variables and set  $\bar{u} = u(x, t)\phi(x)$  with  $\chi(x, t) = \min\{\chi^*(x, t), \frac{\bar{u}(x, t)}{\phi(x)}\}$ .

## 4.2 First-order upwind scheme for equilibrium model

The scheme we consider is the first-order upwind and explicit in time. We now restate (3.13) under the assumptions from Sec. 4.1 amended by the discrete version of (3.12b):

$$\frac{1}{\tau}(U_j^n - U_j^{n-1}) + \frac{\tau}{h}(q_{j-1/2}^{n-1}X_j^{n-1} - q_{j-3/2}^{n-1}X_{j-1}^{n-1}) = 0, \quad j \in \mathbb{Z}^0, \quad n = 1, 2, \dots, N, \quad (4.2a)$$

$$X_j^n = \min\{\chi^*(x_j, t^n), U_j^n\}, \quad j \in \mathbb{Z}^0, \quad n = 1, 2, \dots, N. \quad (4.2b)$$

We analyze this scheme recognizing its familiar upwind character

$$U_j^n = U_j^{n-1} - \frac{\tau}{h} [F_j^{n-1} - F_{j-1}^{n-1}] \quad (4.3a)$$

with

$$F_j^{n-1} = q_{j-1/2}^{n-1}X_j^{n-1} = f(x_j, t^{n-1}; U_j^{n-1}), \quad (4.3b)$$

for a conservation law with the flux function  $f(x, t; u)$  which we set from (3.1) under the assumptions from Sec. 4.1

$$\partial_t u + \partial_x f = 0; \quad \text{for } x \in \mathbb{R}, t \in [0, T], \quad (4.4a)$$

$$f(x, t; u) = q(x, t)\chi(x, t) = q(x, t) \min\{\chi^*(x, t), u(x, t)\}, \quad (4.4b)$$

$$u(x, 0) = u_{init}(x). \quad (4.4c)$$

The function  $f$  is illustrated in Fig. 4.1 for a typical homogeneous unconsolidated sand reservoir with data from Ulleung Basin [110], with  $x$  pointing upwards and  $q(x, t) \approx \text{const} > 0$ .

## 4.3 Literature notes on the rate of convergence

For a scalar conservation law (4.1), when  $f = f(u)$ , proving  $TV_T(U^\Delta)$  is bounded is usually the first step in analysis of convergence [73, 74]. In particular, it is well known [73]

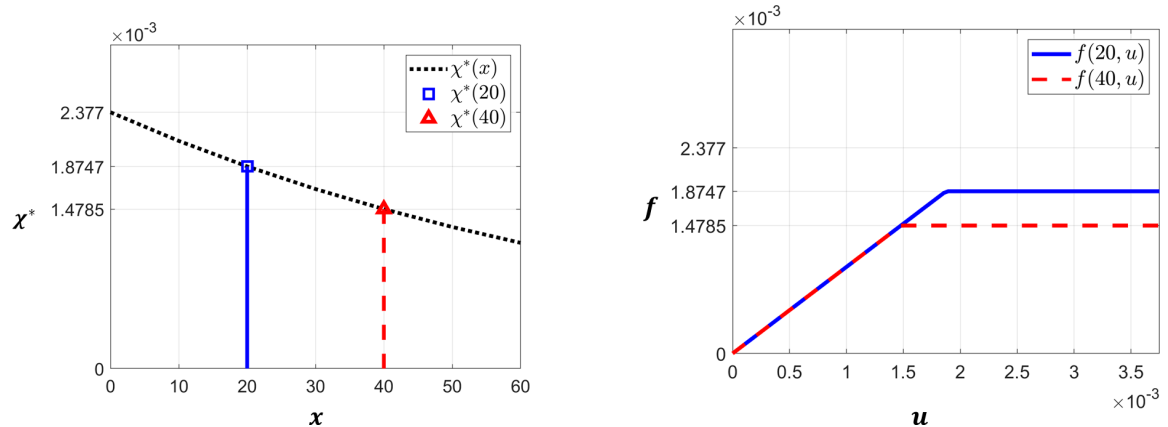


Figure 4.1: Illustration of  $\chi^*(x)$ , and of the flux function  $f(x; u)$  with data from Ulleung Basin case UBGH2-7 [110]. Left: typical  $\chi^*(x)$  in homogeneous sediment, with values  $\chi^*(x)$  highlighted at  $x = 20$ , and  $x = 40$ . Right: the flux function  $f(x; u)$  for  $x = 20$ , and  $x = 40$ . Note that the flux function  $f(x, t; u)$  is piecewise linear in  $u$  and features a corner at  $u = \chi^*(x^*)$ .

that under the Courant–Friedrichs–Lewy (CFL) condition, the first-order upwind scheme (4.3) is stable and converges at the rate of  $O(\sqrt{h})$  in  $L^1$  [18, 68, 69, 83, 128, 138], and the solutions obey a maximum principle. The proof in [128] states, in fact, that  $O(\sqrt{h})$  is the best convergence rate for a first-order monotone scheme when there is a shock in the solution.

However, when  $f = f(x; u)$ , the solutions to (4.1) may not, in general, obey the maximum principle. This can be explained quickly. Writing

$$u_t + f(x; u)_x = 0$$

in quasilinear form

$$u_t + f_u(x; u)u_x = -f_x(x, u),$$

we see that the solutions along the characteristics travelling with velocity  $f_u$  may grow or decay due to the source term  $-f_x$ . If  $f_x < 0$  with  $|f_x| \leq L_f$ , the solution may grow pointwise as  $O(L_f t)$ , and its total variation of the solution need not be bounded either.

The analysis of schemes for the case  $f = f(x; u)$  depends on the properties of  $f$ . For the linear case  $f \propto q(x)u$  with smooth  $q(\cdot)$ , the narrative in [74][Chapter 9] shows that the upwind scheme similar to (4.3) uses the correct solution of the Riemann problem in the Godunov scheme. For Lax-Friedrichs scheme, the analysis in [59, 60] shows the convergence rate to be  $O(h)$  in  $L^P_{\text{loc}}$  as long as  $f$  is smooth in  $u$ . Moreover, if  $f$  is separable, i.e.  $f(x, u) = a(x)b(u)$  for some  $a(\cdot)$  and  $b(\cdot)$ , and  $f$  is smooth in  $u$ , the first-order Godunov with Engquist-Osher fluxes give convergence rate of  $O(h)$  in  $L^1$  [148].

The problem we consider in (4.4) is the closest to that analyzed in [82]. The analysis in [82] rewrites (4.1) as a resonant  $2 \times 2$  system of conservation laws

$$\begin{cases} \partial_t u + \partial_x f(a; u) &= 0, \\ \partial_t a &= 0. \end{cases}$$

When  $a, a'$  and the initial data are of bounded variation, then  $TV(U^n)$  for  $U^n$  found with Godunov scheme grows linearly with respect to time, with the rate depending on  $TV(a')$  [82][Eqn (75)]. Translating our problem (4.4) to this framework, we have  $f(a; u)$  which is, at best, piecewise smooth, in homogeneous sediments.

Our interest is in the idealized methane transport model at equilibrium (4.4) which features piecewise smooth  $f(x, t; u)$  given by (4.4b); this flux function  $f$  is neither separable nor smooth in  $u$ . We formulate, therefore, our own auxiliary stability result for (4.3) similar to those known, e.g., from [74]. Surprisingly, we did not find it stated in literature, thus we provide detailed proof which also only applies to smooth  $f(x, t; u)$ . We prove that  $TV(U^n)$  can grow mildly in time; we also consider bounds for  $TV_T(U^\Delta)$  which are not discussed in [82].

#### 4.4 Stability analysis for equilibrium model

**Proposition 4.4.1.** *Consider (4.4) and suppose that  $f \in C_b^2(\bar{\Omega} \times \mathbb{R}_+ \times \mathbb{R})$  and is nondecreasing in  $u$ . Let the time step size  $\tau$  be small enough so that*

$$\max_{(x,t,u)} \left| \frac{\tau}{h} f_u(x, t; u) \right| \leq 1. \quad (4.5)$$

*Let also some initial data  $U^0$  be given, with bounded variation,  $U^\Delta$  be the solution to (4.3) with compact support of measure bounded by  $\omega_S$ , and*

$$L_1 = \max_{(x,t,u)} \{ |f_{xu}(x, t; u)|, |f_{xx}(x, t; u)| \}, \text{ and} \quad (4.6a)$$

$$L_2 = \max_{(x,t,u)} \{ |f_u(x, t; u)|, |f_x(x, t; u)| \}. \quad (4.6b)$$

*Then for all  $n > 0$ , we have*

$$TV(U^n) \leq C_1(T) = TV(U^0)e^{TL_1} + 2\omega_S(e^{TL_1} - 1), \quad (4.7a)$$

$$\|U^{n+1} - U^n\|_1 \leq \tau C_2(T) \text{ with } C_2(T) = L_2(C_1(T) + \omega_S), \quad (4.7b)$$

$$TV_T(U^\Delta) \leq C_3(T) = T(C_1(T) + C_2(T)). \quad (4.7c)$$

To apply Proposition 4.4.1 to (4.2), we consider  $f(x, t; u)$  defined in (4.4b) depending on the physical data  $q, \chi^*$ . We see that  $f$  is continuous nondecreasing and piecewise linear in  $u$  and differentiable except where  $u(x, t) = \chi^*(x, t)$ . Since  $f$  is at best piecewise smooth in  $u$ , Proposition 4.4.1 applies only to some regularization of (4.4)

$$\begin{cases} \partial_t u^\epsilon + \partial_x f^\epsilon(x, t; u^\epsilon) = 0, \\ u^\epsilon(x, 0) = u_{init}(x), \end{cases} \quad (4.8)$$

in which  $f$  is approximated with some  $C^2$  smooth, positive nondecreasing function  $f^\epsilon$ . Since we can make  $f^\epsilon \approx f$  arbitrarily close, we trust that (4.8) closely resembles (4.4); we illustrate this regularization in Ex. 4.5.2 in Sec. 4.5.

Next question is whether the assumptions on  $f^\epsilon$  itself are reasonable for a real hydrate reservoir simulation. First, the problem (4.4) is only a simplification of the strongly coupled dynamical problem (3.11)–(3.12), and our stability analysis does not explain or refer to the strength of the couplings. Instead, we make a-priori assumptions on the data which allow to conclude stability and predict the variability of solutions. In particular, we predict variability of  $u$  quantified by  $TV_T(U^\Delta)$  depending on the constants  $L_1, L_2$  given in (4.6); these are small only when  $q, q_x$ , the lithology and  $\chi^*$  vary smoothly. We discuss these in detail below.

#### 4.4.1 Assumptions required for the stability of (4.2) in a hydrate reservoir

From the form of (4.4) and properties of  $f$ , we expect its solution  $u(x, t)$  to feature a family of right and left states travelling at different speeds due to the ‘‘corner’’ of  $f$  at  $u = \chi^*$ . In particular, the speed of the state for any  $u > \chi^*$  is zero; this leads to  $S > 0$ , i.e., the growth of immobile amount of methane trapped as solid hydrate with the appearance of sharp bands of hydrate. We rewrite (4.8) in the quasi-linear form

$$u_t^\epsilon + f_u^\epsilon(x, t; u^\epsilon) u_x^\epsilon = -f_x^\epsilon(x, t; u^\epsilon), \quad (4.9)$$

which illustrates that the solution  $u \approx u^\epsilon$  and the corresponding  $S \approx S^\epsilon$  grow along its characteristics with a rate bounded by the source  $-f_x^\epsilon$ . To quantify, we define

$$L_q = \max_{(x,t)} |q(x, t)|, \quad (4.10a)$$

$$L_{q_x} = \max_{(x,t)} |q_x(x, t)|, \quad (4.10b)$$

$$L_{\chi^*} = \max_{(x,t)} |\chi_x^*(x, t)|, \quad (4.10c)$$

$$L_3 = \max_{(x,t)} |\chi_t^*(x, t)|. \quad (4.10d)$$

**Remark 4.4.1.** Assume that  $\chi^*$  and  $q$  vary mildly so that  $L_1, L_2, L_{\chi^*}$  are finite and that

$$\frac{\tau}{h}L_q \leq 1, \quad (4.11)$$

so that (4.5) holds. Then the scheme (4.2) for the equilibrium model is weakly stable.

We comment now on the constants  $L_1, L_2, L_{\chi^*}$  in realistic reservoirs. Assume first the quasi-static case in a homogeneous reservoir with  $P(x)$  and  $T(x)$  fixed in time  $t$ , and with  $0 < q = L_q$ . In this case,  $\|f_x\|_\infty = L_q L_{\chi^*}$ . Consider for example  $\chi^*(x) = a \exp(-bx)$  from [110] given with some  $a > 0$  and small  $b > 0$ . Now  $L_{\chi^*} = ab$ ,  $f_x < 0$ ,  $\|f_x\|_\infty = L_q ab$  and  $L_1 = \|f_{xx}\|_\infty = L_q ab^2$  is small. In turn, we can check that  $L_2 = L_q \max(1, ab)$ . These stability constants correlate well with the predictions of hydrate band growth in nature which are large when  $q$  is large.

Consider next heterogeneous reservoirs. Here the maximum solubility  $\chi^*(x)$  depends on the type of sediment, e.g., in grain size [24]. Consequently, close to some interfaces between different sediment layers, hydrate can accumulate much faster than elsewhere [24, 121, 151]. The locally high hydrate accumulation can be predicted from (4.9), since at a discontinuity of  $\chi^*$ , its weak derivative  $\partial_x \chi^*$  is a Dirac term which may cause a dramatic local increase of  $U_j^n$  and of the saturation  $S_j^n$ . We illustrate this later in Ex. 4.5.3 in Sec. 4.5.

Finally, we consider the time dependent case closest to the strongly coupled hydrate systems when  $q = q(x, t)$  and  $\chi^* = \chi^*(x, t)$  and when  $T = T(x, t)$  and  $P = P(x, t)$ . Now the magnitude of  $f_x$  comes from both  $q_x \chi^*$  and  $q \chi_x^*$  which may have opposite signs and disparate magnitudes depending, e.g., on the solutions of (3.5). It is hard to predict these a-priori, and we can only make assumptions that the constants in Remark 4.4.1 are bounded. Simulation with  $\chi^* = \chi^*(x, t)$  which varies in time is considered in Ex. 5.5.2 in Sec. 5.5.

#### 4.4.2 Proof of Proposition 4.4.1 on the stability of upwind scheme (4.3) for $u_t + f(x, t; u)_x = 0$ when $f$ is smooth

We adapt the proof in [74][Chapter 12] to the case when  $f = f(x, t; u)$ ; we require the boundedness of  $f_{xx}$  and  $f_{xu}$  uniformly in time. The proof is broken to three parts. First we bound the difference  $|\Delta U_j^n|$  between two adjacent values depending on  $|\Delta U_j^{n-1}|$  and  $|\Delta U_{j-1}^{n-1}|$ . From this we conclude about  $TV(U^n)$ . Last we address  $TV_T(U^\Delta)$ .

**Local bounds on  $|\Delta U_j^n|$ .** We first subtract (4.3) at  $j - 1$  from that at  $j$  to get

$$\Delta U_j^n = \Delta U_j^{n-1} - \frac{\tau}{h} \underbrace{[F_j^{n-1} - F_{j-1}^{n-1}]}_{(a)} + \frac{\tau}{h} \underbrace{[F_{j-1}^{n-1} - F_{j-2}^{n-1}]}_{(b)},$$

where  $\Delta U_j^{n*}$  denotes  $U_j^{n*} - U_j^{n*-1}$  for  $n* = n$  and  $n - 1$ . Since  $f$  is smooth, we can rewrite

$$\begin{aligned} (a) &= f(x_j, t^{n-1}; U_j^{n-1}) - f(x_j, t^{n-1}; U_{j-1}^{n-1}) + f(x_j, t^{n-1}; U_{j-1}^{n-1}) - f(x_{j-1}, t^{n-1}; U_{j-1}^{n-1}) \\ &= f_u(x_j, t^{n-1}; \tilde{U}_j^{n-1}) \Delta U_j^{n-1} + f_x(\tilde{x}_j, t^{n-1}; U_{j-1}^{n-1}) h, \end{aligned}$$

where  $\tilde{U}_j^{n-1} \in (U_{j-1}^{n-1}, U_j^{n-1})$  and  $\tilde{x}_j \in (x_{j-1}, x_j)$ , and similarly

$$(b) = f_u(x_{j-1}, t^{n-1}; \tilde{U}_{j-1}^{n-1}) \Delta U_{j-1}^{n-1} + f_x(\tilde{x}_{j-1}, t^{n-1}; U_{j-2}^{n-1}) h$$

where  $\tilde{U}_{j-1}^{n-1} \in (U_{j-2}^{n-1}, U_{j-1}^{n-1})$  and  $\tilde{x}_{j-1} \in (x_{j-2}, x_{j-1})$ . After the substitution, we get

$$\begin{aligned} \Delta U_j^n &= \left(1 - \frac{\tau}{h} f_u(x_j, t^{n-1}; \tilde{U}_j^{n-1})\right) \Delta U_j^{n-1} + \frac{\tau}{h} f_u(x_{j-1}, t^{n-1}; \tilde{U}_{j-1}^{n-1}) \Delta U_{j-1}^{n-1} \\ &\quad - \tau \underbrace{\left[ f_x(\tilde{x}_j, t^{n-1}; U_{j-1}^{n-1}) - f_x(\tilde{x}_{j-1}, t^{n-1}; U_{j-2}^{n-1}) \right]}_{(c)}. \end{aligned}$$

Applying mean value theorem to  $f_x$  terms, we rewrite (c) as

$$\begin{aligned} (c) &= f_x(\tilde{x}_j, t^{n-1}; U_{j-1}^{n-1}) - f_x(\tilde{x}_j, t^{n-1}; U_{j-2}^{n-1}) + f_x(\tilde{x}_j, t^{n-1}; U_{j-2}^{n-1}) - f_x(\tilde{x}_{j-1}, t^{n-1}; U_{j-2}^{n-1}), \\ &= f_{xu}(\tilde{x}_j, t^{n-1}; \bar{U}_{j-1}^{n-1}) \Delta U_{j-1}^{n-1} + f_{xx}(\bar{x}_j, t^{n-1}; U_{j-2}^{n-1}) (\tilde{x}_j - \tilde{x}_{j-1}), \end{aligned}$$

where  $\bar{U}_{j-1}^{n-1} \in (U_{j-2}^{n-1}, U_{j-1}^{n-1})$  and  $\bar{x}_j \in (\tilde{x}_{j-1}, \tilde{x}_j) \subseteq (x_{j-2}, x_j)$ . Next we substitute (c) to get

$$\begin{aligned} \Delta U_j^n &= \left(1 - \frac{\tau}{h} f_u(x_j, t^{n-1}; \tilde{U}_j^{n-1})\right) \Delta U_j^{n-1} + \frac{\tau}{h} f_u(x_{j-1}, t^{n-1}; \tilde{U}_{j-1}^{n-1}) \Delta U_{j-1}^{n-1} \\ &\quad - \tau \left[ f_{xu}(\tilde{x}_j, t^{n-1}; \bar{U}_{j-1}^{n-1}) \Delta U_{j-1}^{n-1} + f_{xx}(\bar{x}_j, t^{n-1}; U_{j-2}^{n-1}) (\tilde{x}_j - \tilde{x}_{j-1}) \right]. \end{aligned}$$

Then we take the absolute value of both sides and apply the triangle inequality. Since the CFL condition (4.5) holds, we get

$$\begin{aligned} |\Delta U_j^n| &\leq \left(1 - \frac{\tau}{h} f_u(x_j, t^{n-1}; \tilde{U}_j^{n-1})\right) \left| \Delta U_j^{n-1} \right| + \frac{\tau}{h} f_u(x_{j-1}, t^{n-1}; \tilde{U}_{j-1}^{n-1}) \left| \Delta U_{j-1}^{n-1} \right| \\ &\quad + \tau \left| f_{xu}(\tilde{x}_j, t^{n-1}; \bar{U}_{j-1}^{n-1}) \Delta U_{j-1}^{n-1} \right| + 2\tau h \left| f_{xx}(\bar{x}_j, t^{n-1}; U_{j-2}^{n-1}) \right| \end{aligned}$$

**Estimates on  $TV(U^n)$ .** Now we take the sum over  $j \in \mathbb{Z}$ , keeping in mind the compact support of  $U^\Delta$ , which reduces any sums over  $\mathbb{Z}$  to those over some finite set  $\mathbb{Z}^0$ . We obtain

$$\begin{aligned} TV(U^n) &\leq TV(U^{n-1}) - \frac{\tau}{h} \sum_{j \in \mathbb{Z}^0} f_u(x_j, t^{n-1}; \tilde{U}_j^{n-1}) \left| \Delta U_{j-1}^{n-1} \right| + \frac{\tau}{h} \sum_{j \in \mathbb{Z}^0} f_u(x_{j-1}, t^{n-1}; \tilde{U}_{j-1}^{n-1}) \left| \Delta U_{j-1}^{n-1} \right| \\ &\quad + \tau \sum_{j \in \mathbb{Z}^0} \left| f_{xu}(\tilde{x}_j, t^{n-1}; \bar{U}_{j-1}^{n-1}) \Delta U_{j-1}^{n-1} \right| + 2\tau \sum_{j \in \mathbb{Z}^0} \left| f_{xx}(\bar{x}_j, t^{n-1}; U_{j-2}^{n-1}) \right| h. \quad (4.12) \end{aligned}$$

Re-indexing the third term on the right-hand-side of (4.12), the second and the third terms cancel each other. Using the definition of  $L_1$ , we have

$$TV(U^n) \leq TV(U^{n-1}) + \tau L_1 \sum_{j \in \mathbb{Z}^0} \left| \Delta U_{j-1}^{n-1} \right| + 2\tau L_1 \sum_{j \in \mathbb{Z}^0} h.$$

Since  $|supp(f)| \leq \omega_S$ , we have  $\sum_{j \in \mathbb{Z}^0} h \leq \omega_S$ . By re-indexing the second term, we get the following:

$$TV(U^n) \leq TV(U^{n-1})(1 + \tau L_1) + 2\tau L_1 \omega_S.$$

We repeat this inequality recursively to obtain

$$TV(U^n) \leq TV(U^0)(1 + \tau L_1)^n + 2\tau L_1 \omega_S \sum_{k=0}^{n-1} (1 + \tau L_1)^k.$$

From Bernoulli inequality,  $1 + \tau L_1 \leq e^{\tau L_1}$ , we get  $(1 + \tau L_1)^n \leq e^{n\tau L_1} \leq e^{TL_1}$  and we sum up the finite series to see that (4.7a) holds with

$$C_1(T) = TV(U^0)e^{TL_1} + 2\omega_S(e^{TL_1} - 1).$$

**Variation in time.** We rewrite (4.3) as

$$U_j^n - U_j^{n-1} = -\frac{\tau}{h} \left[ f_u(x_j, t^{n-1}; \tilde{U}_j^{n-1}) \Delta U_j^{n-1} + f_x(\tilde{x}_j, t^{n-1}; U_{j-1}^{n-1}) h \right],$$

where  $\tilde{U}_j^{n-1} \in (U_{j-1}^{n-1}, U_j^{n-1})$  and  $\tilde{x}_j \in (x_{j-1}, x_j)$ . Take the absolute values of both sides and apply the triangle inequality to get

$$\left| U_j^n - U_j^{n-1} \right| \leq \frac{\tau}{h} L_2 \left( \left| \Delta U_j^{n-1} \right| + h \right).$$

Next, we multiply both sides by  $h$  and sum over  $j \in \mathbb{Z}^0$  to get

$$\|U^n - U^{n-1}\|_1 \leq \tau L_2 [TV(U^{n-1}) + \omega_S].$$

Since  $TV(U^n) \leq C_1(T)$  from (4.7a), now (4.7b) holds with

$$C_2(T) = L_2(C_1(T) + \omega_S).$$

Finally, to get (4.7c), we combine (4.7a) and (4.7b), and obtain

$$TV_T(U^\Delta) \leq C_3(T) = \sum_{n=0}^{T/\tau} \tau (C_1(T) + C_2(T)) = T(C_1(T) + C_2(T)).$$

This stability proof and the discussion in Sec. 4.4.1 complete our analysis of the equilibrium case. Based on Proposition 4.4.1, we expect the rate of convergence  $O(\sqrt{h})$  for the solutions to (4.2); this is confirmed by numerical experiments in Sec. 4.5.

## 4.5 Numerical results and convergence

In this section we provide examples for equilibrium model. Our goal is to confirm the theory and in particular demonstrate convergence of the schemes for reasonably realistic cases as well as to demonstrate the practical limitations. We set the CFL number

$$\nu = L_q \frac{\tau}{h} < 1,$$

and consider only 1d simulations.

For the equilibrium model we compare the numerical solution obtained by our scheme (4.2) with an analytical solution, and we study effects of regularization; we also confirm the rate of convergence of  $O(\sqrt{h})$ .

**Example 4.5.1** (Model case for equilibrium model with analytical solution). *Let  $\Omega = (-1, 3)$ ,  $R = 2$ ,  $\chi_L = 1$ ,  $q = 1$ , and the initial condition  $u_{init}(x) = \chi_L H(x+1)H(-x)$  for (4.4) features a “box”-like profile. We consider  $\chi^*(x) = e^{-0.5x}$  independent of time. For additional interest, we also consider  $\chi^*(x) = 1 - 0.26x$ .*

The analytical solution to (4.4) with  $u_{init}(x) = \chi_L H(-x)$  can be found in [107]. We modify it for the present case of “box” shaped  $u_{init}(x)$ , so we get

$$\begin{aligned} \chi(x, t) &= \min\left(1, \frac{\chi^*(x)}{\chi_L}\right) u_{init}(x - qt), \\ S(x, t) &= -\frac{\max(0, t - \frac{x}{q}) q \chi_x^*(x) \mathbb{1}_{G_0(t)}(x)}{R - \chi^*(x)}, \\ u(x, t) &= \chi(x, t) + (R - \chi^*(x)) S(x, t), \end{aligned}$$

where  $G_0(t) = \{x : x_L < x \leq qt\}$  with  $x_L$  satisfying  $\chi^*(x_L) = \chi_L$ , the position where first hydrate formation is observed.

We apply scheme (4.2) to obtain  $(U^\Delta, X^\Delta, S^\Delta)$  at  $T = 1$  with  $M = 100$  and  $\nu = 0.9$ . Illustrations are provided in Fig. 4.2. We see that  $(U^\Delta, X^\Delta, S^\Delta)$  are close to the analytical solution  $(u, \chi, S)$ . As  $U^\Delta$  propagates to the right,  $X^\Delta$  satisfies the constraint  $X_j^n \leq \chi^*(x_j)$ , and the undissolved methane produces  $S_j^n > 0$ , i.e., we see the “blow-up” behavior of  $U^\Delta$  with  $S_j^n$  as expected.

Comparing the two cases of  $\chi^*(x) = 1 - 0.26x$  and  $\chi^*(x) = e^{-0.5x}$ , we see that the magnitude of  $\chi_x^*$  is more pronounced for the latter case. In  $U^\Delta$  and  $S^\Delta$  we see small rarefactions at the back of the traveling wave, typical for an increasing concave flux function such as  $f$  given by (4.4b).

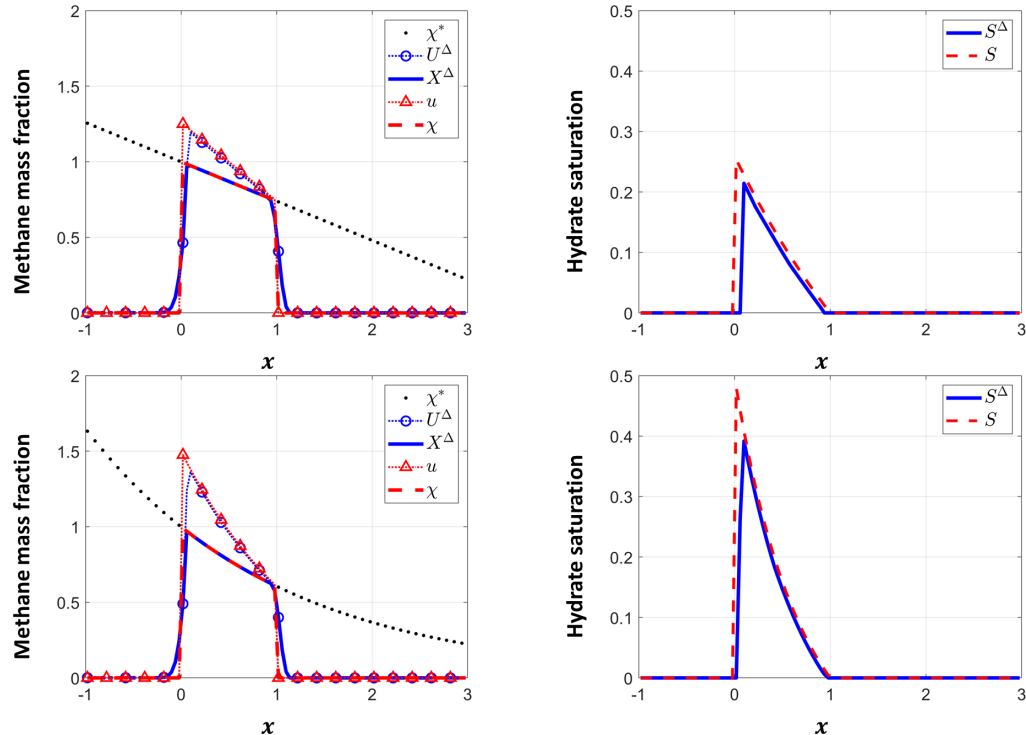


Figure 4.2: Comparison of the numerical solution  $(U^\Delta, X^\Delta, S^\Delta)$  with the analytical solution  $(u, \chi, S)$  at  $T = 1$  with  $M = 100$  and  $\nu = 0.9$  for Ex. 4.5.1. Top: case with for  $\chi^*(x) = 1 - 0.26x$ . Bottom: case with  $\chi^*(x) = e^{-0.5x}$ .

In our next example we evaluate effects of regularization in order to understand the closeness of  $u$  and  $u^\epsilon$ , the solutions to (4.4) and (4.8), respectively. With  $f^\epsilon$  chosen to be really close to  $f$ , we can make the difference between  $U^\Delta$  and the solution to the regularized model  $U^{\epsilon,\Delta}$  arbitrarily small. For comparison we use the case with the analytical solution from [107], which we adapt to the use of realistic data from Ullung Basin.

**Example 4.5.2** (Convergence rate and regularization; homogeneous domain, basin time scale). We consider (4.4) with  $u_{init}(x) = \chi_L H(-x)$  on  $\Omega = (0, D^{max})$  where  $D^{max}$  and  $\chi^*$  are computed using the reference data measured from the Ullung basin site UBGH2-7 of [110] with constant salinity of  $\chi_{IG}^{sw} = 3.5\%$ . Let  $q = 5 \times 10^{-3}$  [m/y],  $\chi_L = 2 \times 10^{-3}$ , and  $R = 0.1203$ . We examine the result at  $T = 10$  [ky].

The flux function  $f(x; u)$  given by (4.4b) has a corner at  $u = \chi^*(x)$  at every  $x$ . We regularize with  $f^\epsilon$  which replaces  $f$  on  $(x, u) \in \Omega \times [\chi^*(x) - \epsilon, \chi^*(x) + \epsilon]$  by a smooth polynomial. Here  $\epsilon$  is a regularization parameter; we choose  $\epsilon = \alpha h$  with  $\alpha = 10^{-4}$ . See the illustration of  $f$  and  $f^\epsilon$  in Fig. 4.3. In Fig. 4.4 we illustrate the analytical solution as well as the numerical solution  $U^{\epsilon,\Delta}$  to the regularized problem at  $t = 10$  kyrs with  $M = 100$  and  $\nu = 0.9$ . We do not show  $U^\Delta$  separately because it is virtually indistinguishable from  $U^{\epsilon,\Delta}$ .

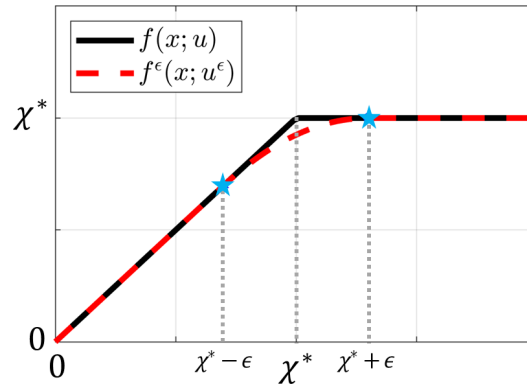


Figure 4.3: Illustration of flux  $f$  and its regularization  $f^\epsilon$  at some fixed  $x \in \Omega$ .

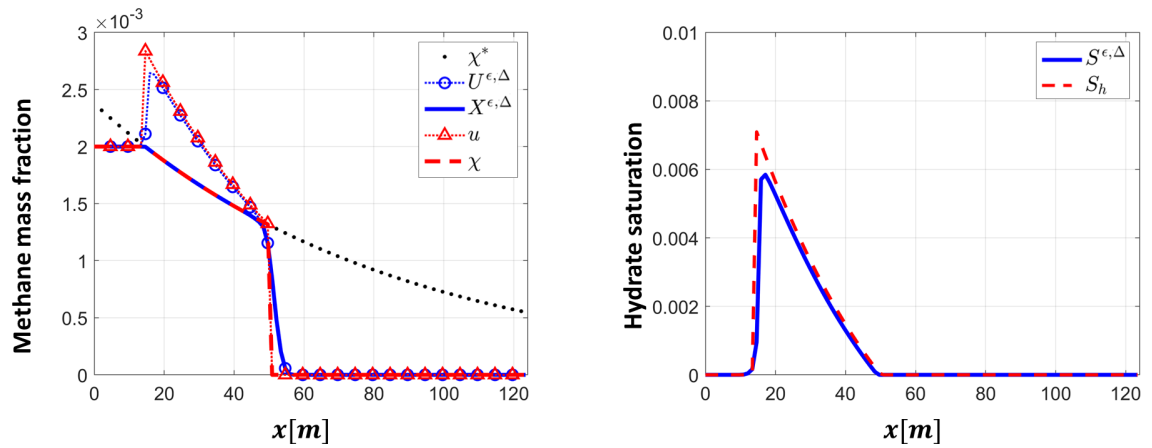


Figure 4.4: Numerical solution  $(U^{\epsilon,\Delta}, X^{\epsilon,\Delta}, S^{\epsilon,\Delta})$  of Ex. 4.5.2 at  $t = 10$  [ky] with  $M = 100$  compared with the analytical solution  $(u, \chi, S_h)$ .

We first examine the qualitative behavior. As predicted by the analytical solution, we observe the rapid growth of total methane content  $U^{\epsilon,\Delta}$  and the hydrate accumulation  $S^{\epsilon,\Delta}$  because  $R < 1$  while  $S^{\epsilon,\Delta}$  is inversely related to  $R$ . At  $t = 10$  [ky], the hydrate saturation reaches about 10%.

Next we compare  $U^\Delta$  and  $U^{\epsilon,\Delta}$ . With  $\epsilon = O(h)$ , their difference is small. In particular, when  $M = 100$ , we have

$$\begin{aligned}\|U^\Delta - U^{\epsilon,\Delta}\|_1 &= 3.52 \times 10^{-4}, \\ \|X^\Delta - X^{\epsilon,\Delta}\|_1 &= 1.32 \times 10^{-4}, \\ \|S^\Delta - S^{\epsilon,\Delta}\|_1 &= 2.20 \times 10^{-3}.\end{aligned}$$

When we increase  $M$  by a factor of 10,  $M \rightarrow 1000$ , errors decrease by a factor of  $10^{-2}$ :

$$\begin{aligned}\|U^\Delta - U^{\epsilon,\Delta}\|_1 &= 9.41 \times 10^{-6}, \\ \|X^\Delta - X^{\epsilon,\Delta}\|_1 &= 2.99 \times 10^{-6}, \\ \|S^\Delta - S^{\epsilon,\Delta}\|_1 &= 5.46 \times 10^{-5}.\end{aligned}$$

We also check the rate of convergence using a fine grid solution with  $100 \leq M \leq 6400$ , plotted in Fig. 4.5.

$$\begin{aligned}\|u - U^\Delta\|_1 &= O(h^{0.52}), \\ \|\chi - X^\Delta\|_1 &= O(h^{0.5}), \\ \|S - S^\Delta\|_1 &= O(h^{0.55}).\end{aligned}$$

The order is similar for the solutions to the regularized model, with the error slightly bigger due to the modeling error. We have

$$\begin{aligned}\|u - U^{\epsilon,\Delta}\|_1 &= O(h^{0.51}), \\ \|\chi - X^{\epsilon,\Delta}\|_1 &= O(h^{0.50}), \\ \|S - S^{\epsilon,\Delta}\|_1 &= O(h^{0.51}).\end{aligned}$$

Our next example challenges the theory since it is set for heterogeneous sediment. This example is inspired by [24]; see our 2d simulation in [103] which accounts also for the flow and fracturing.

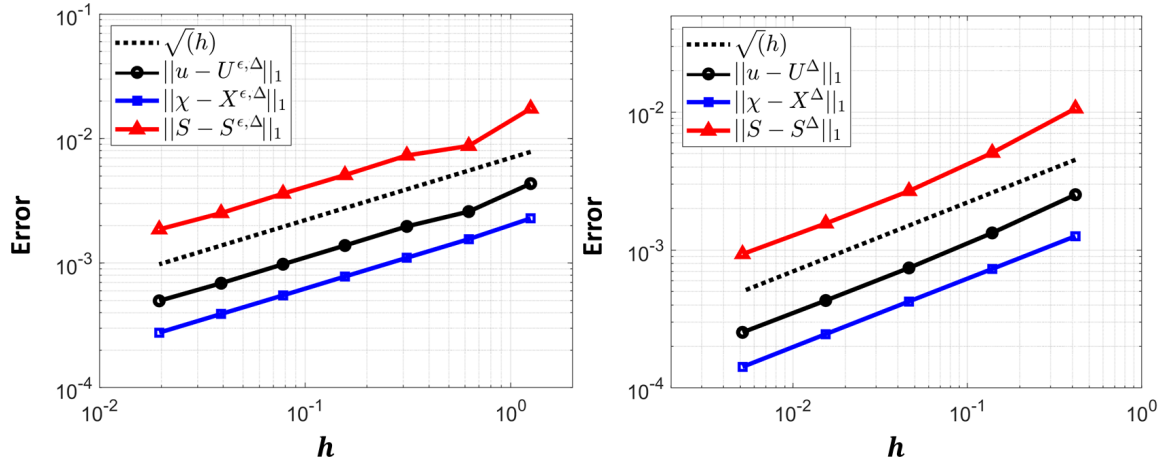


Figure 4.5: Left:  $L_1$ -error between the numerical solution  $(U^{\epsilon,\Delta}, X^{\epsilon,\Delta}, S^{\epsilon,\Delta})$  and the analytical solution  $(u, \chi, S)$  at  $T = 10$  [ky]; from Ex. 4.5.2. Right: Convergence of the numerical solution  $(U^\Delta, X^\Delta, S^\Delta)$  to the analytical solution  $(u, \chi, S)$  at  $T = 10$  [ky].

**Example 4.5.3** (Model problem in heterogeneous domain motivated by [24]). *Consider advection of methane gas through 3 layers of sediments. Let  $\Omega = \cup_{i=1}^3 \Omega_i$  where  $i$  indicates each layer, each with different methane solubility curves:*

$$\begin{aligned}\chi_1^*(x) &= -0.3x + 1, \\ \chi_2^*(x) &= e^{-0.2(x-1)} - 0.2, \\ \chi_3^*(x) &= -0.1x + 0.75\end{aligned}$$

shown in Fig. 4.6. We use  $R = 2$ ,  $q = 1$ ,  $d_m = 0$  and  $u_{init}(x) = 0.8H(-x)$ .

The domain and the solutions are illustrated in Fig. 4.6 where the shaded blocks correspond to different layers. We focus on the behavior near the interfaces at  $x = 1$  and  $x = 2$ . As the front of methane enters Layer 2 at  $x = 1$ , we expect to see methane hydrate dissociation since  $\chi^*(1^+) > \chi^*(1^-)$  allows more methane gas to dissolve in the water. In contrast, at  $x = 2$ , there is a reduction in maximum solubility;  $\chi^*(2^+) < \chi^*(2^-)$ : this cause a sudden formation of hydrate at the interface as in [24, 121, 151]. The simulation captures the hydrate dissociation at  $x = 1$  and the formation at  $x = 2$ . The sharp spike at  $x = 2$  makes sense since the weak derivative  $\partial_x f(x, u)$  at the discontinuity at  $x = 2$  is a Dirac source  $\delta(x - 2)$ .

In reality, the methane gas transport is diffusion dominated. Now we consider the case with  $d_m > 0$ .

**Example 4.5.4** (Methane transport by advection and diffusion in homogeneous domain, UBGH2-7 in [110]). *We consider methane gas transport by advection and diffusion through*

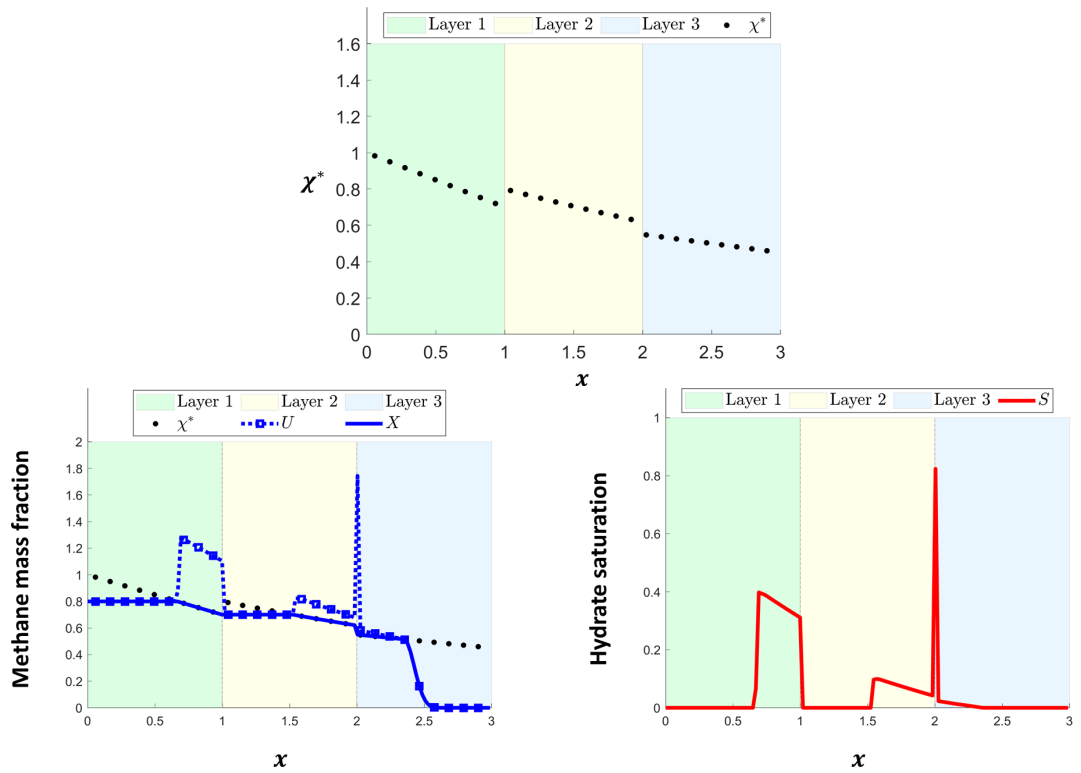


Figure 4.6: Transport in heterogeneous domain from Ex. 4.5.3 at  $T = 2.4$ . Top: layers of heterogeneous sediment with different maximum solubility curves  $\chi^*$  at  $x = 1$  and  $x = 2$ . Bottom: numerical solution. Of interest is behavior at the interfaces caused by the jumps of  $\chi^*(x)$ .

$\Omega = (0, 124)$  [m] which we reference the UBGH2-7 site [110]. As in previous examples, this region  $\Omega$  is free of methane initially. The only source of methane is the upward flux from the center of Earth. In this example we use the realistic values:  $q = 1$  [mm/y],  $d_m = 3 \times 10^{-2}$  [m<sup>2</sup>/y], and  $u_{init}(x) = 2 \times 10^{-3}H(-x)$ . To adapt the behavior of methane gas at the exit of  $\Omega$  that they tend to fade away rapidly, we impose the homogeneous Dirichlet boundary condition at the outlet.

When we solve the advection-diffusion model (3.12) with nonzero  $q$  and  $d_m$ , we can use the operator splitting described in Sec. 2.5.6. The advection step is treated by the upwind scheme (4.3). After the advection step with  $U_h^{n*}$ , we take the diffusion step. In this case we need extra care since the diffusion term  $\nabla \cdot (d_m \nabla \chi)$  depends on  $\chi$  instead of  $u$ . The numerical scheme for the diffusion step is

$$\begin{cases} U_h^n - U_h^{n*} + \tau A_h^{d_m} X_h^n = 0, \\ X_h^n - \min(\chi_h^*, U_h^n) = 0, \end{cases}$$

where  $A_h^{d_m} X_h^n \approx \nabla \cdot (d_m \nabla \chi)$ . We can solve this nonlinear system by using the Semismooth Newton method described in Sec. 2.6. Fig. 4.7 shows the evolution of methane gas transport by advection and diffusion. We see that methane gas travelled with  $d_m > 0$  and well distributed before we see first hydrate formation. The spikes in  $u_h$  and  $S_h$  are not as sharp as in previous examples due to diffusion.

**Remark 4.5.1.** *On the heterogeneous domain, we observed anomalies in  $u_h$  and  $S_h$  near the interface between two different regions where  $\chi^*$  is not differentiable. See Fig. 4.8 for the reproduction of those anomalies. This behavior of hydrate spike has not been observed in Ex. 4.5.3, so they are due to diffusion. According to [121, 151], those anomalies (hydrate spikes) near the interfaces are expected and understood as a consequence of undercooling, i.e., the depression of hydrate melting point.*

## 4.6 Summary

In this chapter we considered equilibrium phase behavior for hydrate in two-phase conditions typical in sediments above the BHSZ. Our objective was to rigorously study the stability of numerical method for transport. We provided justification why the commonly used numerical scheme is stable and robust, and showed convergence with rate  $O(\sqrt{h})$  consistent with that for monotone scheme and scalar conservation law in the presence of

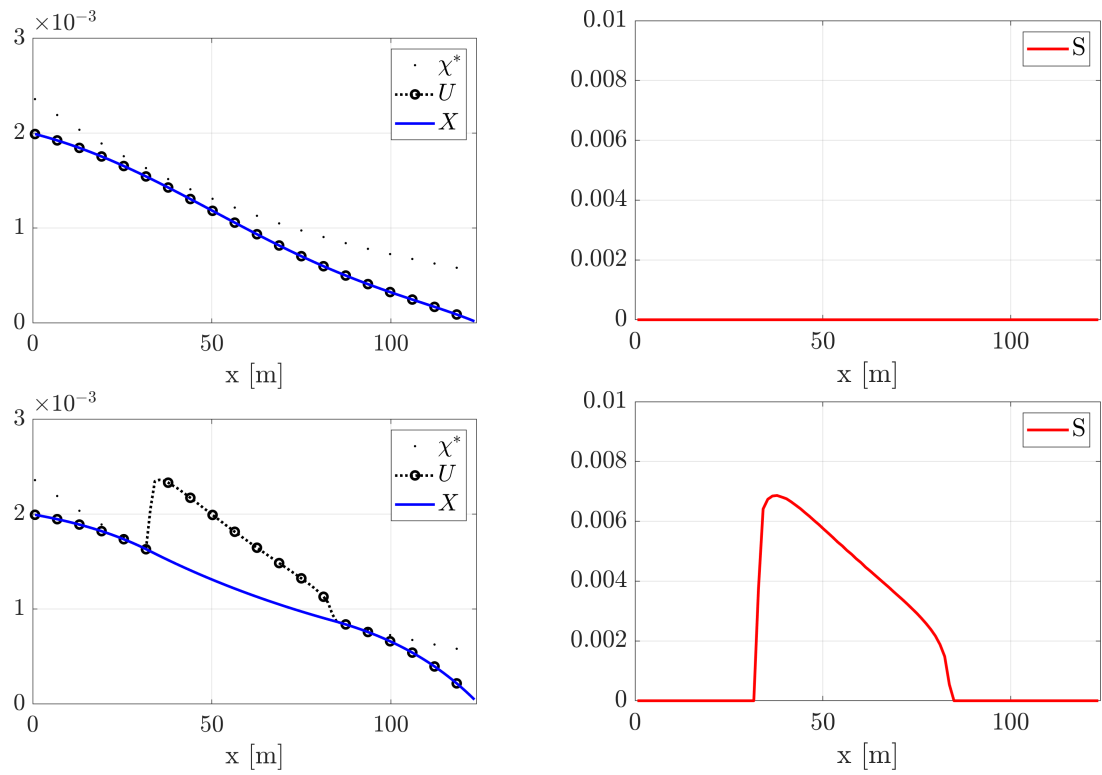


Figure 4.7: Evolution of methane gas transport by advection and diffusion for Ex. 4.5.4. (Top)  $t = 40$  [kyr] and (bottom)  $t = 80$  [kyr].

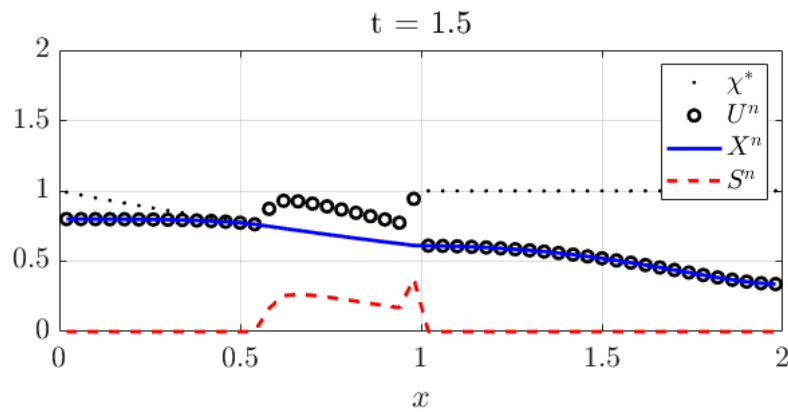


Figure 4.8: Reproduction of anomalies in  $u_h$  and  $S_h$  on heterogeneous domain  $\Omega = [0, 3]$  with  $\chi^*(x) = e^{-0.5x} I_{[0,2]}(x) + I_{(2,3]}(x)$ .

discontinuities. We also explained the presence of “spikes” of hydrate saturation similar to those observed in nature. The rigorous numerical analysis results we demonstrate for hydrate model is new. Our current work is to extend the analysis for three-phase conditions.

## 5 Modeling, analysis, and simulation for methane hydrate model under non-equilibrium conditions

In this chapter we discuss the kinetic model for hydrate formation and dissociation presented in [106](Sec. 4, 7, 8.2, 8.3, 10). Below we discuss kinetic models for hydrate starting with literature review in Sec. 5.1. In Sec. 5.2 we introduce and analyze three different versions of homogeneous "batch reactor" models, which explain our choice for coupling with the methane transport model summarized in Sec. 5.3. Then we present our stability result for kinetic model and show the weak stability in time in Sec. 5.4 followed by numerical examples in Sec. 5.5 and the conclusion in Sec. 5.6.

**Overview.** Kinetic models are common in geochemistry and chemical engineering [72, 172] and describe the evolution of a system towards thermodynamic equilibrium from some initial conditions out of equilibrium, e.g., in the processes of adsorption, phase transitions, and crystal precipitation and dissolution.

A general kinetic model must predict the evolution of all relevant variables towards an equilibrium from some out-of-equilibrium state. For hydrate evolution, a kinetic model is complemented by other equations which describe the evolution of all of  $(T, P, \chi, S)$  towards some equilibrium  $(T^\infty, P^\infty, \chi^\infty, S^\infty)$  starting from some initial  $(T^0, P^0, \chi^0, S^0)$ . The kinetics is coupled to the transport and constitutive equations, and would account for the presence of gas phase and capillary effects.

In the framework of our reduced model for liquid-hydrate zone discussed in Ch. 3–4, we assume  $(P, T)$  are fixed over some time interval  $(t^{old}, t^{new})$  with  $t^{new} = t^{old} + \Delta t$ . In equilibrium the variables  $(\chi(x, t), S(x, t)) \in E_*(x)$  at every  $t$ . If the  $(P, T)$  conditions change at  $t^{new}$ , and a new  $\chi_{new}^* = \chi^*(x, t^{new})$  is given, the variables  $(\chi, S)$  are out of the equilibrium with respect to the new graph  $E_*^{new}$ . If  $\Delta t$  is really large, we can assume they immediately adjust to the new equilibrium. Otherwise, we need a kinetic model to describe the evolution of  $(\chi, S)$  towards  $E_*^{new}$ .

## 5.1 Kinetic models of hydrate formation: literature background

Following [16, 38, 48, 49, 62, 169], the kinetics of gas-liquid-hydrate phase system involves an exchange term  $Q$  proportional to the driving force in the three phase conditions,

$$\frac{d}{dt}S = Q = k(f_g - f_{eq}), \quad (5.1)$$

where  $k > 0$  is the hydrate formation or the dissociation rate, and where  $f_g, f_{eq}$  are the local gas fugacity, and the equilibrium fugacity at the given pressure and temperature, respectively. This expression (5.1) predicts that the hydrate forms when  $f_g > f_{eq}$ , and dissociates when  $f_g < f_{eq}$ . In [48, 49], the authors propose  $Q \propto (P - P_{eq})$  with  $P_{eq}$  equal the equilibrium pressure for a given fixed  $T$ , and this approach models a response to the increase or decrease in pressure. A physically grounded expression for  $k$  is complex [146]. The rate  $k \propto A_s$ , the surface area available for the reaction to occur which is proportional to the effective porosity  $\phi(1 - S)$ . In a three phase system the hydrate formation rate  $k$  also depends on the availability of water and methane (thus on the gas and aqueous phase saturations  $S_g$  and  $S_w$ ); but for hydrate dissociation the rate  $k$  depends on availability of hydrate (thus on  $S = 1 - S_g - S_w$ ). Therefore, (5.1) is in general hysteretic; see also [168]. From mathematical point of view, the presence of  $S$  or  $(1 - S)$  in  $k$  keeps the variable  $S$  in physically meaningful domain  $S \in [0, 1]$ . Model (5.1) is designed to work in the saturated case when  $S^\infty > 0$ , and  $\chi^\infty = \chi^*$ .

Our focus is on liquid-hydrate systems. For these, according to [15, 25], the driving force  $f_g - f_{eq}$  in (5.1) can be expressed by the difference of methane concentration at the liquid-gas equilibrium and maximum methane solubility  $\chi^*$  at three-phase equilibrium state for the given  $P$  and  $T$ . With no free gas,  $Q$  becomes

$$Q = k(\chi - \chi^*), \quad (5.2)$$

similar to that for crystal formation from saturated or oversaturated mixtures in geochemistry [72, 172]. We extend (5.2) so it can work well across the two-phase saturated as well as in single phase unsaturated conditions when  $S^\infty = 0$ , and  $\chi^\infty < \chi^*$ . We explain this extension in Sec. 5.2 with further details given in Sec. 5.2.2. Our model is robust even when coupled to the transport model. In the future we hope to extend it to the three phase equilibria extending (5.1).

## 5.2 Kinetic batch reactor model for hydrate evolution in liquid-hydrate conditions

Consider an isolated system with  $P, T$  fixed and a fixed amount  $u(\chi, S) = u^0$  of methane, and ignore any transport contributions or sources to focus on the distribution of methane between liquid and hydrate phases. The values  $(\chi(t), S(t))$  live on a fixed curve

$$u(\chi, S) = \chi(1 - S) + RS = u^0 = u(\chi^0, S^0), \quad (5.3)$$

in the  $(\chi, S)$  plane. With some given  $\chi^*$ , and a corresponding fixed multi-valued graph  $E_*$ , for a given  $u^0$ , the equilibrium point lies at the intersection of the curve (5.3) with the graph  $E_*$  which can be found from (3.8). The graph  $E_*$  and the curves (5.3) are illustrated in Fig. 5.1 with point (A) corresponding to an equilibrium case.

The case out of equilibrium (points (B) and (C) in Fig. 5.1) is when the pair  $(\chi, S)$  on (5.3) is away from  $E_*$ . For example we can have  $\chi(t) > \chi^*$  (B), or  $S(t) > 0$  with  $\chi(t) < \chi^*$  (C). As  $t \uparrow \infty$ , the points  $(\chi(t), S(t))$  evolve from some  $(\chi^0, S^0)$  towards some  $(\chi^\infty, S^\infty)$  on  $E_*$  along the curve (5.3) according to some kinetic model with exchange rate  $Q$ .

We postulate now some conditions on  $(\chi^0, S^0)$  and  $u^0$  to guarantee that the kinetics leads to physically meaningful  $(\chi^\infty, S^\infty)$  on  $E_*$ . In particular, from Remark 3.3.1 we see that  $u^\infty = u(\chi^\infty, S^\infty)$  should satisfy  $0 \leq u^\infty < R$ ; thus, we must have  $0 \leq u^0 = u(\chi^0, S^0) < R$ . Also, non-negativity must be imposed on  $(\chi, S)$ . In summary, we consider the physically meaningful region  $(\chi, S) \in D^0 = [0, R] \times [0, 1]$ .

Next, we aim to predict whether a given  $u^0 = u(\chi^0, S^0)$  leads to  $(\chi^\infty, S^\infty) \in E_*^-$  or to  $(\chi^\infty, S^\infty) \in E_*^+$ . In the latter saturated case we have  $\chi^\infty = \chi^*$  and  $S^\infty \in [0, 1]$ , and  $u^0 = u^\infty = \chi^\infty + (R - \chi^\infty)S^\infty \geq \chi^*$  by (3.2). In the former case we have  $u^0 \leq \chi^*$ . It is thus convenient to decompose  $D^0 = D_-^0 \cup D_+^0$  as follows:

$$\begin{aligned} D_+^0 &= \{(\chi, S) \in D^0 : u(\chi, S) \geq \chi^*\}; \\ D_-^0 &= \{(\chi, S) \in D^0 : u(\chi, S) \leq \chi^*\}. \end{aligned}$$

Fig. 5.1 provides illustration of these definitions, and motivates our subsequent analyses.

### 5.2.1 Three batch kinetic models

Our objective is to construct a model which works well in all of  $D^0$ . We start with (5.2) dubbed (KIN1) which works in  $D_+^0$ . We include  $S$  in  $k_2$  in a simpler model (KIN2) which works well also in  $D_+^0$  only. Finally to allow the evolution towards a possible equilibrium on

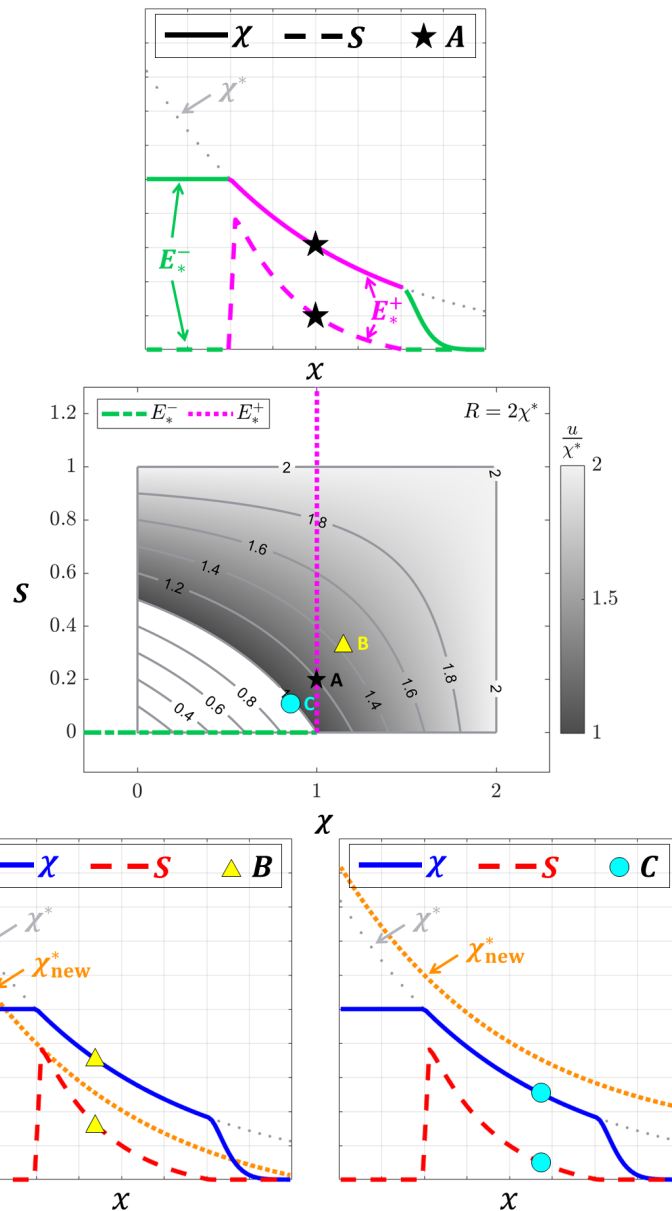


Figure 5.1: Illustration of typical  $\chi(x, t), S(x, t)$  at some  $t$  in hydrate reservoir (top)  $x \in \Omega$ . For this illustration we choose  $R = 2\chi^*$ . Top: plot of  $\chi, S$  in equilibrium, with  $\chi(x, t) \leq \chi^*(x), S(x, t) \geq 0$  and  $(\chi(x, t), S(x, t)) \in E_*(x)$  as in (3.6). Middle: illustration of the graph  $(\chi, S) \in E_*$  at the point A (equilibrium), and at the points B and C out of equilibrium (not on  $E_*$ ) but within the physically meaningful region  $(\chi, S) \in D^0 = [0, R] \times [0, 1]$ . The contours  $u(\chi, S) = u^0$  of (5.3) in  $D^0$  for  $\frac{u^0}{\chi^*}$  equal 0.4, 0.6, ..., 1.8, with the curve  $u(\chi, S) = u^0 = \chi^*$  separating the “saturated” region  $D^0_+$  shaded in gray from the “un-saturated” region  $D^0_-$  which is in white. The parts  $E_*^+$  and  $E_*^-$  of  $E_*$  are in green and magenta. Bottom: an example of  $\chi^*(x), \chi(x), S(x)$  in a reservoir in out of equilibrium conditions when (B)  $\chi^*_{new} < \chi^*$ , and (C) when  $\chi^*_{new} > \chi^*$ .

$E_*^-$  or on  $E_*^+$ , we combine these two possible equilibria in (KIN3) using an abstract setting with the graph  $E_*$ . Each (KINj) has some rate  $k_j$ . In  $D_+^0$  and under some assumptions all three models are equivalent to one another. Only (KIN3) is coupled later with the transport model.

**(KIN1).** The model (5.2) from [72, 172] splits  $u(t)$  as a sum of the methane amount in the  $h$  phase and of the amount in the  $l$  phase, and prescribes the evolution

$$(\text{KIN1}) \quad \begin{cases} \frac{d}{dt}((1-S)\chi) &= -Q, \\ R\frac{d}{dt}(S) &= Q, \\ Q &= k_1(\chi - \chi^*), \\ (\chi(0), S(0)) &= (\chi^0, S^0). \end{cases} \quad (5.4)$$

This model is very intuitive: in particular, we see that  $S \uparrow$  when  $\chi > \chi^*$ . However, (KIN1) works well only in  $D_+^0$  when  $u^0 \geq \chi^*$ , i.e., when the equilibrium point  $S^\infty \geq 0$ . When  $u^0 < \chi^*$  since  $k_1$  does not involve  $S$ , the model leads to an equilibrium outside  $D^0$  with  $S^\infty < 0$ . Moreover, the corresponding numerical scheme requires solution of a nonlinear algebraic equation which must be done with some care; see Sec. 5.2.2.

**(KIN2).** Next we aim to improve (KIN1). We split

$$u = \chi + S(R - \chi) = \chi + \psi,$$

with  $S = \frac{\psi}{R - \chi}$ . The variable  $\psi$  interpreted as the ‘‘amount of methane stored in the hydrate phase over the saturated amount in liquid’’. Given initial data  $(\chi^0, S^0)$ , we calculate  $\psi^0 = S^0(R - \chi^0)$ , and postulate the evolution

$$(\text{KIN2}) \quad \begin{cases} \frac{d}{dt}(\chi) &= -Q, \\ \frac{d}{dt}(\psi) &= Q, \\ Q &= k_2(\chi - \chi^*), \\ (\chi(0), \psi(0)) &= (\chi^0, \psi^0). \end{cases} \quad (5.5)$$

Now (KIN2) model is linear in  $\chi$  and  $\psi$ , and  $Q$  is monotone in  $\chi$ : the curves  $\chi + \psi = u^0$  are simply the lines in the  $(\chi, \psi)$  plane. These properties simplify the implementation and analysis. However, similarly as in (KIN1),  $Q$  involves properly only the equilibria on  $E_*^+$ , and thus (KIN2) works well only in  $D_+^0$ .

**(KIN3).** We modify (KIN2) so that when  $u^0 < \chi^*$ ,  $Q$  leads to some equilibrium on  $E_*^-$ , but when  $u^0 \geq \chi^*$ , the model works identically to (KIN2) and leads correctly to some equilibrium on  $E_*^+$ . An elegant way to do it is to replace  $\chi^*$  in the definition of  $Q$  in (KIN2)

by a selection  $w \in w_*(\psi)$  which defaults to  $\chi^*$  on  $E_*^+$ . Here  $w_* = e_*^{-1}$ , and  $e_* = r_* E_*$  is a rescaled version of  $E_*$ , with a fixed  $r_* = R - \chi^*$ . When  $\psi > 0$ , we have  $w = \chi^*$ , but when  $\psi = 0$ ,  $w \in [0, \chi^*]$ . Also,  $S \in E_*(\chi)$  is equivalent to  $\psi \in e_*(\chi)$  and  $\chi \in w_*(\psi)$ . The (KIN3) model we implement and analyze reads

$$(KIN3) \quad \left\{ \begin{array}{l} \frac{d}{dt}(\chi) = -Q, \\ \frac{d}{dt}(\psi) = Q, \\ Q = k_3(\chi - w), \\ w \in w_*(\psi), \\ (\chi(0), \psi(0)) = (\chi^0, \psi^0). \end{array} \right. \quad (5.6)$$

The solution  $(\chi, \psi)$  and the selection  $w$  are unique. The exchange term  $Q$  is monotone in  $\chi$  while  $-Q$  is monotone in  $\psi$ , which make the analysis and implementation easy. As in (KIN2), at any point of time one can calculate  $S$  from  $\psi$  and  $\chi$ .

We provide details on (KIN1), (KIN2) and (KIN3) in Sec. 5.2.2. These inform our analysis of methane transport coupled to (KIN3).

### 5.2.2 Properties for the kinetic model

In this Section we provide details of fully implicit schemes for models batch reactor models (KINj),  $j = 1, 2, 3$ , respectively (5.4), (5.5), and (5.6). Our analysis motivates and supports the construction of the model (KIN3) which works across unsaturated and saturated conditions. Furthermore, our analysis helps to identify physically meaningful variables  $(\chi, S)$  when working in non-isolated system, and to guide time stepping control. We define the discrete schemes in Sec. 5.2.3, and analyze their solvability and properties of solutions in Sec. 5.2.4. We illustrate the schemes and their properties in Sec. 5.2.5.

Let each model (KINj) have its own rate  $k_j > 0$ . We define  $\bar{k}_j = \tau k_j$ , and  $\tilde{k}_j = \frac{\bar{k}_j}{1 + \bar{k}_j}$ . We denote by  $(X^\infty, S^\infty)$  the equilibrium values on graph  $E$ .

We consider a uniform time step  $\tau > 0$ , and  $t^n = n\tau$ , and we seek the approximations  $X^n \approx \chi(t^n)$ ,  $S^n \approx S(t^n)$  in one step  $[t^{n-1}, t^n)$  using the initial conditions  $X^{n-1}, S^{n-1}$ . Other variables including  $\Psi^n \approx \psi(t^n)$  and quantities such as  $Q^n$ , are denoted analogously. The total methane content  $U^n = X^n + (R - X^n)S^n$ . The solutions corresponding to model (KINj) are denoted with subscripts (KINj) e.g., we use notation  $X_{KINj}^n$ . When more compact notation is desired, and there is no need to indicate the time step, we use simpler notation, e.g.,  $X_j$ . When no distinction between models is needed, we drop subscript  $j$ , and denote the new time step value sought  $X = X_{KINj}^n$  while we set the previous time step values equal

$\bar{X} = X_{\text{KINj}}^{n-1}$ . With this notation, each scheme advances  $(\bar{X}, \bar{S})$  to the new time step value  $(X, S)$ .

### 5.2.3 Discrete schemes for batch kinetic models and their properties

The schemes are fully implicit: for (KIN2) and (KIN3) the solutions can be calculated with a closed formula, but (KIN1) requires an additional solvers. We prove various properties, and compare the models.

**Discrete scheme for (KIN1).** Given  $(\bar{X}, \bar{S}) = (X_{\text{KIN1}}^{n-1}, S_{\text{KIN1}}^{n-1})$ , find  $(X, S)$  for which

$$(1 - S)X - (1 - \bar{S})\bar{X} = \bar{k}_1(\chi^* - X), \quad (5.7a)$$

$$RS - R\bar{S} = \bar{k}_1(X - \chi^*). \quad (5.7b)$$

**Solver for (5.7):** the calculation of  $(X, S)$  from (5.7) is coupled and not explicit. To get a useful formula, we first calculate formally from (5.7b)

$$S = \frac{\bar{k}_1(X - \chi^*)}{R} + \bar{S}. \quad (5.8)$$

Then we substitute (5.8) in (5.7a), and rearrange to get a quadratic equation for  $X$

$$X = \frac{\bar{k}_1}{R}(R - X)(\chi^* - X) + \bar{S}X + (1 - \bar{S})\bar{X}. \quad (5.9)$$

The solvability of (5.9) is addressed in Property (B) proven below; we also suggest a practical solver.

**(KIN1) summary: Given  $(\bar{X}, \bar{S}) = (X_{\text{KIN1}}^{n-1}, S_{\text{KIN1}}^{n-1})$ :**

Solve (5.9) for  $X$ .

Calculate  $S$  from (5.8).

Set  $(X_{\text{KIN1}}^n, S_{\text{KIN1}}^n) = (X, S)$ .

**Discrete scheme for (KIN2).** Given  $(\bar{X}, \bar{S}) = (X_{\text{KIN2}}^{n-1}, S_{\text{KIN2}}^{n-1})$ , calculate  $\bar{\Psi} = \bar{S}(R - \bar{X})$ , and find  $(X, \Psi)$  for which

$$X - \bar{X} = \bar{k}_2(\chi^* - X), \quad (5.10a)$$

$$\Psi - \bar{\Psi} = \bar{k}_2(X - \chi^*). \quad (5.10b)$$

**Solver for (5.10):** since (5.10a) is linear, we rearrange to get

$$X = \tilde{k}_2\chi^* + (1 - \tilde{k}_2)\bar{X}. \quad (5.11)$$

Substituting to (5.10b) we get

$$\Psi = \bar{\Psi} + \tilde{k}_2(\bar{X} - \chi^*). \quad (5.12)$$

After some algebra, we obtain also an explicit formula

$$S = \frac{\bar{k}_2(\bar{X} - \chi^*) + (1 + \bar{k}_2)(R - \bar{X})\bar{S}}{(R - \bar{X}) + \bar{k}_2(R - \chi^*)}. \quad (5.13)$$

**(KIN2) summary: Given**  $(\bar{X}, \bar{S}) = (X_{\text{KIN2}}^{n-1}, S_{\text{KIN2}}^{n-1})$ :

Calculate  $\bar{\Psi} = \bar{S}(R - \bar{X})$ .

Calculate  $X$  from (5.11),  $\Psi$  from (5.12), and  $S$  from (5.13).

Set  $(X_{\text{KIN2}}^n, S_{\text{KIN2}}^n) = (X, S)$ .

**Discrete scheme for (KIN3).** Given  $(\bar{X}, \bar{S}) = (X_{\text{KIN3}}^{n-1}, S_{\text{KIN3}}^{n-1})$ , calculate  $\bar{\Psi} = \bar{S}(R - \bar{X})$ , and find  $(X, \Psi, W)$  for which

$$X - \bar{X} = \bar{k}_3(W - X), \quad (5.14a)$$

$$\Psi - \bar{\Psi} = \bar{k}_3(X - W), \quad (5.14b)$$

$$W \in w_*(\Psi). \quad (5.14c)$$

**Solver for (5.14):** At a first glance, the scheme is more complicated than (5.10). However, we can exploit various properties of monotone graphs to simplify. First we calculate formally

$$X = \tilde{k}_3 W + (1 - \tilde{k}_3)\bar{X}, \quad (5.15)$$

which we substitute in (5.14b) and rearrange as

$$\Psi + \bar{k}_3 W = \bar{\Psi} + \bar{k}_3(\tilde{k}_3 W + (1 - \tilde{k}_3)\bar{X}), \quad W \in w_*(\Psi). \quad (5.16)$$

After a few steps of algebra we get

$$\Psi + \tilde{k}_3 W = \bar{\Psi} + \tilde{k}_3 \bar{X}, \quad W \in w_*(\Psi). \quad (5.17)$$

Now we use the resolvent  $\mathcal{R}_{\tilde{k}_3}^{w^*}(\cdot)$  of  $w^*$  as defined in (2.3) to solve (5.17) for  $\Psi \in \text{domain}(w_*)$ ,

$$\Psi = \mathcal{R}_{\tilde{k}_3}^{w^*}(\bar{\Psi} + \tilde{k}_3 \bar{X}).$$

Since this resolvent function has a simple form  $\mathcal{R}_{\tilde{k}_3}^{w^*}(w) = (w - \tilde{k}_3 \chi^*)_+$ , with a few more substitutions we get

$$\Psi = (\bar{\Psi} + \tilde{k}_3(\bar{X} - \chi^*))_+, \quad (5.18)$$

an explicit formula giving  $\Psi$  in terms of  $\bar{X}, \bar{\Psi}$ . Once  $\Psi$  is known, we calculate the auxiliary variable  $W$  from (5.17) by back-substituting (5.18), and we have  $W = \frac{\bar{\Psi} - \Psi}{k_3} + \bar{X}$ ; thus  $W = \chi^*$  if  $\Psi \geq 0$ , and  $W = \bar{X} + \frac{\bar{\Psi}}{k_3}$ , otherwise. These calculations allow to calculate  $X$  explicitly

$$X = \tilde{k}_3 \chi^* + (1 - \tilde{k}_3) \bar{X}, \quad \text{if } \Psi \geq 0, \quad \text{and } X = \bar{X} + \bar{\Psi}, \quad \text{otherwise.} \quad (5.19)$$

**(KIN3) summary: Given  $(\bar{X}, \bar{S}) = (X_{\text{KIN3}}^{n-1}, S_{\text{KIN3}}^{n-1})$ :**

Calculate  $\bar{\Psi} = \bar{S}(R - \bar{X})$ .

Calculate  $\Psi$  from (5.18).

Given  $\Psi$ , calculate  $X$  from (5.19).

Calculate auxiliary variables  $W = \frac{\bar{\Psi} - \Psi}{k_3}$ , and  $S = \frac{\Psi}{R - X}$ .

Set  $(X_{\text{KIN3}}^n, S_{\text{KIN3}}^n) = (X, S)$ .

#### 5.2.4 Properties of schemes (KIN1), (KIN2), and (KIN3)

Suppose that

$$(\bar{X}, \bar{S}) \in D^0. \quad (5.20)$$

Also, denote  $\bar{\Psi} = (R - \bar{X})\bar{S}$ . Below we prove solvability of (5.7), (5.10), and (5.14) as well as analyze qualitative properties of their solutions which we arrange in a list (A-B-C-D-E). Since each of the schemes is a one-step scheme, it is sufficient to only consider the properties of one step solutions  $(X, S)$  depending on  $(\bar{X}, \bar{S})$ .

##### **Property (A): mass conservation.**

If the solutions to any scheme  $j = 1, 2, 3$  exist, they satisfy  $U^n = u(X^n, S^n) = U^0$  where  $u(X, S)$  is given by (3.1b). In other words, for each scheme, the solutions  $(X^n, S^n)$  stay on the curve  $u(X^n, S^n) = U^0$ , and we have

$$S_j = \frac{U^0 - X_j}{R - X_j} = \frac{\bar{X} + (R - \bar{X})\bar{S} - X_j}{R - X_j}. \quad (5.21)$$

The map  $S_j = S_j(X_j)$  is smooth and invertible when  $0 \leq X_j < R$ .

*Proof.* The first part follows immediately by adding the two equations defining each scheme for one step, and following for  $n > 0$  inductively. Analysis of (5.21) is straightforward.  $\square$

##### **Property (B): solvability of schemes.**

Schemes (KIN2), (KIN3) are uniquely solvable, and (KIN1) is solvable depending on data and if  $\tau$  is small enough.

*Proof.* The solutions to schemes (KIN2) and (KIN3) can be calculated from explicit algebraic expressions depending on the data  $(\bar{X}, \bar{S})$ ; thus the conclusion is immediate.

However, scheme (KIN1) (5.7) requires a solution to the quadratic equation (5.9) which we frame as  $p(X) = 0$  with

$$p(X) = \frac{\bar{k}_1}{R}(R - X)(\chi^* - X) + \bar{S}X + (1 - \bar{S})\bar{X} - X. \quad (5.22)$$

We see that  $p(\cdot)$  in (5.22) is a quadratic polynomial with  $p(0) = \bar{k}_1\chi^* + (1 - \bar{S})\bar{X}$ , and  $p(R) = \bar{S}R - R + (1 - \bar{S})\bar{X}$ . Also,  $p'(X) = \frac{2\bar{k}_1}{R}(X - X_R) + \bar{S} - 1$ , where  $X_R = \frac{R + \chi^*}{2}$ . Now consider the root of  $p(X) = 0$ . From (5.20) we have that  $p(0) > 0$ , and  $p(R) = (1 - \bar{S})(\bar{X} - R) < 0$ . Since  $p(\cdot)$  is continuous, we see that the root to  $p(X) = 0$  exists in  $[0, R]$  and in fact is in  $[0, R)$ . Since, in addition,  $p(\cdot)$  is convex with  $p''(X) = \frac{2\bar{k}_1}{R} > 0$ , we find that this root is unique in  $[0, R)$ , and is given from the quadratic formula

$$X = \frac{R(1 - \bar{S}) + \bar{k}_1(R + \chi^*) - \sqrt{(R(1 - \bar{S}) + \bar{k}_1(R + \chi^*))^2 - 4\bar{k}_1R(\bar{k}_1\chi^* + \bar{X}(1 - \bar{S}))}}{2\bar{k}_1} \quad (5.23)$$

On the other hand, the second root given by a modification of (5.23) always exists in  $(R, \infty)$  but is unphysical.  $\square$

**Lemma 5.2.1.** *Consider (KIN1) scheme. Suppose (5.20) holds and consider the smaller root  $X = X_1 \in [0, R)$  of (5.22). Then (i)  $S_1 < 1$ .*

*(ii) If  $\bar{X} < \chi^*$ , then  $\bar{X} < X < \chi^*$ . If  $\chi^* < \bar{X}$ , then  $\chi^* < X < \bar{X}$ . If  $\bar{X} = \chi^*$ , then  $X = \bar{X}$ , and  $S = \bar{S}$ .*

*(iii) If  $(\bar{X}, \bar{S}) \in D_+^0$ , then  $S_1 \geq 0$  for any  $\bar{k}_1$ .*

*(iv) On the other hand, suppose  $(\bar{X}, \bar{S}) \in D_-^0$ . If  $\bar{S} = 0$ , then  $S_1 < 0$ . If  $\bar{S} > 0$ , then for large  $\bar{k}_1$  it is possible that  $S_1 \leq 0$ .*

*Proof.* To prove (i), we recall Property (A) and (5.21). Since  $u < R$ , we have  $S_1 = \frac{U^0 - X_1}{R - X_1} < 1$ .

To prove (ii), assume  $\bar{X} < \chi^*$ . First we collect the terms of (5.22) with  $X$  on the left hand side of the equation. Then subtract  $(1 - \bar{S})\chi^*$  on the both sides of the equation to get

$$(\chi^* - X) \left[ (1 - \bar{S}) + \frac{\bar{k}_1}{R}(R - X) \right] = (1 - \bar{S})(\chi^* - \bar{X}).$$

Since  $\bar{S} < 1$ , and  $X < R$ , the second term on the left hand side and the first term on the right hand side are positive. Thus (i) the sign of  $\chi^* - X$  is the same as that of  $\chi^* - \bar{X}$ .

Further, rearrange  $p(X) = 0$  as in the proof of Property B to read

$$\frac{\bar{k}_1}{R}(R - X)(\chi^* - X) = (1 - \bar{S})(X - \bar{X}).$$

Similarly, as above, we conclude that the sign of  $X - \bar{X}$  is the same as that of  $\chi^* - X$ , which completes the proof of (ii).

To prove (iii), take some  $(\bar{X}, \bar{S}) \in D_+^0$  so that  $u(\bar{X}, \bar{S}) \geq \chi^*$ . By property (ii), we can have  $\bar{X} > X > \chi^*$ , or  $\bar{X} < X < \chi^*$ . (We omit the trivial case  $X = \bar{X}$ ). In the first case by (5.8), we have  $S_1 = \frac{\bar{k}_1(X - \chi^*)}{R} + \bar{S} \geq \bar{S} \geq 0$ . In the second case by property A,  $(X, S_1)$  is on the curve  $u(X, S_1) = u(\bar{X}, \bar{S}) \geq \chi^*$  which is above the curve  $u(X, S) = \chi^*$ . Thus,  $S_1 \geq 0$ .

To prove (iv), take  $(\bar{X}, \bar{S}) \in D_-^0$ , so we must have  $\chi < \chi^*$ . With  $\bar{S} = 0$  we get from (5.8) that  $S_1 = \frac{\bar{k}_1(X - \chi^*)}{R} < 0$ . Even if  $\bar{S} > 0$ , it is possible to find  $\bar{k}_1$  large enough so that  $\bar{S} \leq \frac{\bar{k}_1(\chi^* - \chi)}{R}$ . For illustration, the curve  $u(X, S_1) = u(\bar{X}, \bar{S}) \leq \chi^*$  is in this case below the curve  $u(X, S) = \chi^*$ , thus  $S_1 \leq 0$ .  $\square$

**Property C: the solutions to (KINj) stay physically meaningful:**  $(X_j, S_j) \in D^0$ , under some conditions for  $j = 1, 2$  and unconditionally for  $j = 3$ .

(i) The solutions  $(X_j, S_j)$  satisfy  $0 \leq X_j < R$  and  $S_j < 1$  for all  $j$ .

(ii) In addition,  $S_3 \geq 0$  unconditionally.

(iii) Let  $j = 1, 2$ . If  $(\bar{X}, \bar{S}) \in D_+^0$ , then  $S_j \geq 0$ . If  $(\bar{X}, \bar{S}) \in D_-^0$  and either  $\bar{S} > 0$  with  $\bar{k}_j$  small enough, then  $S_j > 0$ . However, if  $(\bar{X}, \bar{S}) \in D_-^0$  and either  $\bar{S} = 0$  or if  $\bar{k}_j$  is large, then it is possible that  $S_j < 0$ .

*Proof of Property C.* (i) For (KIN1) Property B shows (i) for the correct root selected by the solver. For (KIN2), (5.11) shows that  $X_2$  is a convex combination of  $\bar{X}$  and  $\chi^*$ ; thus,  $0 \leq X_2 < R$ . For (KIN3), when  $\bar{S} + \tilde{k}_3(\bar{X} - \chi^*) \geq 0$ ,  $X_3$  is a convex combination of  $\bar{X}$  and  $\chi^*$ , and the same argument applies. Otherwise,  $X_3 = \bar{X} + \bar{S}(R - \bar{X}) < R$ , and  $0 \leq X_3 < R$ . To prove  $S_j < 1$ , we see that  $X_j < R$  and by Property A  $u(X_j, S_j) = u(\bar{X}, \bar{S}) < R$ ; thus from (5.21) it follows that  $S_j < 1$ .

To show (ii) consider (KIN3) first. we have  $\Psi_3 \geq 0$  from (5.18); thus  $S_3 \geq 0$ . For scheme (KIN1), we use Lemma 5.2.1. For scheme (KIN2), we recall (5.12). To check if  $0 \leq \Psi_2 = \bar{\Psi} + \tilde{k}_2(\bar{X} - \chi^*)$ , we first consider  $\bar{X} \geq \chi^*$  (which implies  $(\bar{X}, \bar{S}) \in D_+^0$ ). This yields  $\Psi_2 \geq \bar{\Psi} \geq 0$ , thus  $S_2 \geq 0$ . With  $\bar{X} < \chi^*$ , however, we find that to guarantee  $\psi \geq 0$ , we must have  $\tilde{k}_2 < \frac{\bar{\Psi}}{(\chi^* - \bar{X})}$ . For these, we recall  $\frac{\bar{\Psi}}{(\chi^* - \bar{X})} = \frac{u - \bar{X}}{(\chi^* - \bar{X})}$ , and this quantity  $\frac{u - \bar{X}}{(\chi^* - \bar{X})} \geq 1$  in  $D_+^0$  while we have that for any  $\tau$ ,  $0 < \tilde{k}_2 < 1$ . We conclude that (KIN2) can

produce unphysical  $S_2 \leq 0$  only for  $(\bar{X}, \bar{S}) \in D_-^0$ . If  $\bar{\Psi} = 0$ , we always have  $\Psi_2 < 0$  and  $S_2 < 0$ .  $\square$

**Property D: stability of each scheme in  $Q$ .**

We have  $|Q_j| < |\bar{Q}|$  for each scheme.

*Proof of property D.* We recall that  $Q_j = k_j(X_j - \chi^*)$  for  $j = 1, 2$ , and  $Q_3 = k_3(X_3 - W)$  for (KIN3). We consider the bounds for  $j = 1$  and (KIN1) first. We want to show  $|\chi^* - X_j| \leq |\chi^* - \bar{X}|$ . To this aim, we subtract  $\chi^*$  from both sides of (5.9), rearrange, and add  $-\bar{S}\chi^*$  to both sides, and rearrange again to get

$$\left(1 - \bar{S} + \frac{\bar{k}_1}{R}(R - X)\right)(\chi^* - X_1) = (1 - \bar{S})(\chi^* - \bar{X}).$$

Next we take absolute value of both sides while we multiply them by  $k_1$ . Since  $1 - \bar{S} > 0$  and  $\frac{\bar{k}_1}{R}(R - X) > 0$  from property C, we get, as desired

$$|Q_1| < \frac{1 - \bar{S}}{1 - \bar{S} + \frac{\bar{k}_1}{R}(R - X)} |\bar{Q}_1| < |\bar{Q}_1|.$$

For (KIN2), we add  $\chi^* - X_2$  to both sides of (5.10a) to get

$$\bar{Q} = (1 + \bar{k}_2)Q_2.$$

By  $1 + \bar{k}_2 > 1$ , it is easy to see  $|Q_2| < |\bar{Q}|$ .

For (KIN3), the proof  $|\bar{Q}_3| < |Q_3|$  is a special homogeneous case of a more general proof. We first consider Yosida approximation  $w_\lambda \approx w_*$ , or some other regularization which maintains the monotonicity properties of the graph  $w_*$ . Given  $(\bar{X}, \bar{\Psi})$ , we seek the solution  $(X_\lambda, \Psi_\lambda)$  to the regularization of (5.14) with  $Q_\lambda = X_\lambda - w_\lambda(\Psi_\lambda)$ , and  $\bar{Q} = \bar{X} - w_\lambda(\bar{\Psi})$

$$X_\lambda - \bar{X} + \bar{k}_3 Q_\lambda = 0, \quad (5.24a)$$

$$\Psi_\lambda - \bar{\Psi} - \bar{k}_3 Q_\lambda = 0. \quad (5.24b)$$

Next we multiply (5.24b) by  $w'_\lambda(\Psi')$  with some  $\Psi' \in (\bar{\Psi}, \Psi_\lambda)$  to get

$$w_\lambda(\Psi_\lambda) - w_\lambda(\bar{\Psi}) - \bar{k}_3 w_\lambda(\Psi') Q_\lambda = 0. \quad (5.25)$$

Subtract (5.25) from (5.24a) and take absolute value to get

$$(1 + \bar{k}_3(1 + w_\lambda(\Psi'))) |Q_\lambda| = |\bar{Q}|.$$

Since  $1 + \bar{k}_3(1 + w_\lambda(\bar{\Psi})) > 1$ , we get the inequality  $|Q_\lambda| < \frac{1}{1 + \bar{k}_3} |\bar{Q}|$  as desired. Taking the limit as  $\lambda \rightarrow 0$  gives the desired result.  $\square$

**Property (E): (conditional) equivalence of schemes.**

(i) Let  $k_2 = k_3$ . The schemes (KIN2) and (KIN3) give the same numerical solutions  $X_2 = X_3$  if and only if  $(\bar{X}, \bar{S}) \in D_+^0$ . (ii) Moreover, if

$$k_1 = \frac{R\bar{k}_2(1 - \bar{S})}{(R - \bar{X}) + \tilde{k}_2(R - \chi^*)}, \quad (5.26)$$

then the one-step solution to (KIN2) coincides with that for (KIN1).

*Proof.* To prove (i), we want to check if  $X_2 = X_3$  by setting the right hand sides of (5.11) and (5.15) equal to each other. This identity holds if  $\chi^* = \min\left(\bar{X} + (1 - \tilde{k})\bar{\Psi}, \chi^*\right)$ , which is equivalent to

$$\bar{S} \geq \frac{\tilde{k}(\chi^* - \bar{X})}{R - \bar{X}}. \quad (5.27)$$

Now, if  $(\bar{X}, \bar{S}) \in D_+^0$ , we have  $U = \bar{U} \geq \chi^*$ , which means  $\bar{S} \geq \frac{\chi^* - \bar{X}}{R - \bar{X}} \geq \frac{\tilde{k}(\chi^* - \bar{X})}{R - \bar{X}}$  for any  $k$  and  $\tau$ . Conversely, for (5.27) to hold, we must have  $U \geq \chi^*$  since  $\tilde{k}$  can be made arbitrarily close to 1.

To prove (ii), we want to calculate  $k_2$  in terms of  $k_1$  and previous time step data  $(\bar{X}, \bar{S})$ . Of course this is, in principle, always possible; the difficulty is to actually find this expression explicitly. We are able to do this and to obtain (5.26). We explain the process below.

Recall from (5.21) that  $S_j$  is a well defined invertible function of  $X_j \in [0, R]$ . In addition, for each scheme  $j$ , clearly each  $(X_j, S_j)$  is a function of  $(\bar{X}, \bar{S})$  and of  $k_j$ . If these were given explicitly, one could write, e.g.,  $S_1 = S_2$  and attempt to solve for the dependence of  $k_1$  on  $k_2$  explicitly. Alternatively, one could do the same starting with  $X_1 = X_2$  to get  $k_1$  in terms of  $k_2$ . However, the solver for (KIN1) does not give either  $X_1$  nor  $S_1$  explicitly depending on  $k_1, \bar{X}, \bar{S}$ , and these direct strategies fail.

Instead, another possibility arises: we calculate  $k_1 = k_1(\bar{X}, \bar{S}; X_1)$  with  $\frac{\partial k_1}{\partial X_1} \neq 0$  after some analysis. Next we assume  $X_1 = X_2$  and substitute  $X_2 = X_2(k_2, \bar{X}, \bar{S})$  from (5.11). With this, we get an expression with  $k_1$  in terms of  $(k_2, \bar{X}, \bar{S})$ , which is luckily explicit.

To get  $k_1 = k_1(\bar{X}, \bar{S}; X_1)$ , we recall (5.8) which binds together the constants  $k_1, \bar{S}$  and the variables  $X_1, S_1$ . With (5.21) we eliminate  $S_1$  and get a relationship between  $k_1, \bar{S}, \bar{X}$  and  $X_1$ , and we solve for  $\bar{k}_1$

$$\bar{k}_1 = \frac{R(\bar{X} - X_1)(1 - \bar{S})}{(R - X_1)(X_1 - \chi^*)}. \quad (5.28)$$

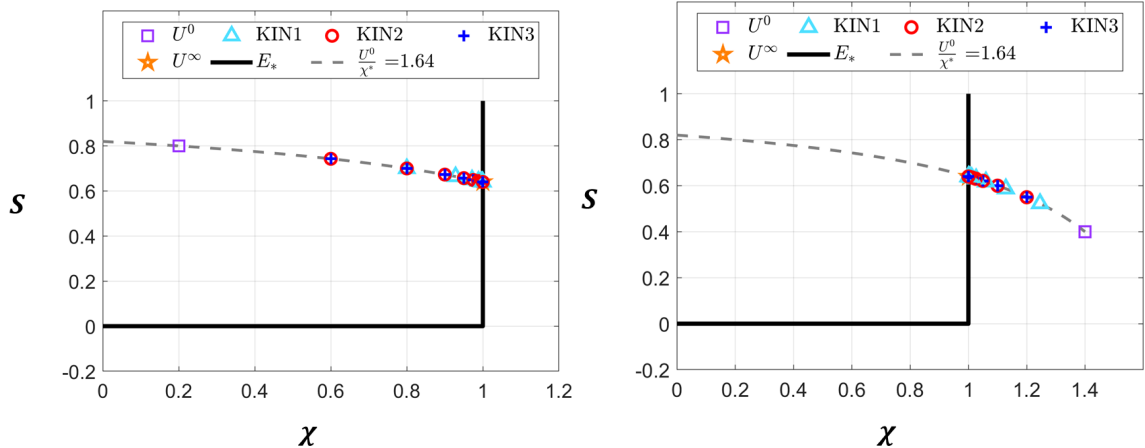


Figure 5.2: Simulation results for Ex. 5.2.1 illustrating schemes (KIN1), (KIN2), and (KIN3). Left:  $(X^0, S^0) = (0.2, 0.8)$ . Right:  $(X^0, S^0) = (1.4, 0.4)$ . The solutions to all schemes lie on the curve  $u(X^n, S^n) = U^0$  and converge towards the equilibrium point  $(X^\infty, S^\infty)$  on the portion  $E_*^+$  of the graph  $E$ . Solutions to (KIN2) and (KIN3) are indistinguishable.

Now we assume  $X_1 = X_2$ , recall (5.11) in which  $X_2$  is given  $X_2 = X_2(\bar{X}, \bar{S}, k_2)$  explicitly and substitute this expression into (5.28) to get

$$\bar{k}_1 = \frac{R(\bar{X} - \tilde{k}_2\chi^* - (1 - \tilde{k}_2)\bar{X})(1 - \bar{S})}{(R - \tilde{k}_2\chi^* - (1 - \tilde{k}_2)\bar{X})(\tilde{k}_2\chi^* + (1 - \tilde{k}_2)\bar{X} - \chi^*)} = \frac{R\bar{k}_2(1 - \bar{S})}{(R - \bar{X}) + \tilde{k}_2(\bar{X} - \chi^*)},$$

which, upon some algebra, is equivalent to (5.26).  $\square$

### 5.2.5 Illustration of (KIN1), (KIN2), (KIN3) in batch setting.

We illustrate now the three kinetic models with some numerical experiments. Our goal is to emphasize the similarities as well as the differences between these models. We employ the fully implicit schemes presented in Sec. 5.2.3. In the examples we use data  $R = 2$ ,  $\chi^* = 1$ , and  $k_j = 1$  for all  $j = 1, 2, 3$ .

**Example 5.2.1** (Saturated case). *Suppose that  $u^0 = 1.64 > \chi^*$ ; so the equilibrium state is  $(\chi^\infty, S^\infty) = (1, 0.64)$  on the  $E_*^+$  portion of the  $E$  graph, and this example falls in the saturated regime. We consider two cases (I)  $(X^0, S^0) = (0.2, 0.8)$  and (II)  $(X^0, S^0) = (1.4, 0.4)$ . Both are in saturated regime  $(X^0, S^0) \in D_+^0$ . We use  $\tau = 1$ .*

Fig. 5.2 illustrates the properties of the schemes from Sec. 5.2.3. We notice first that the property (A) holds: the numerical solutions  $(X_j^n, S_j^n)$  given by (5.7), (5.10), and (5.14) live on the curve  $U^n = u(X^n, S^n) = U^0 = u^0 = 1.64$ , and as predicted by property (C), they stay in  $D^0$  and are physical.

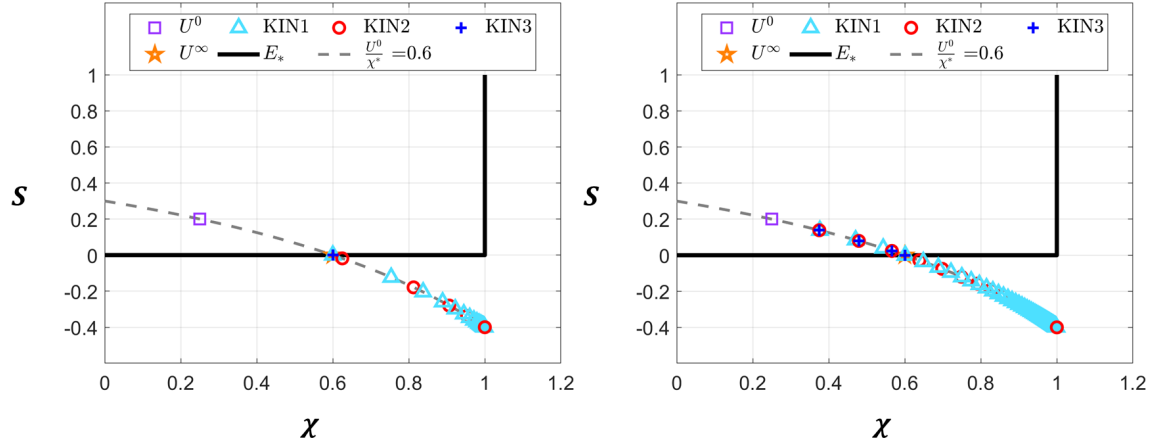


Figure 5.3: Simulation results of unsaturated case in Ex. 5.2.2 illustrating the behavior of kinetic models (KIN1), (KIN2), and (KIN3) with  $(X^0, S^0) = (0.25, 0.2) \in E_*^-$ . We use  $\tau = 1$  (left) and  $\tau = 0.2$  (right). The solutions to (KIN1) and (KIN2) become unphysical after a few time steps when the curve  $u(\chi, S)$  crosses the  $E_*$  graph; the solutions to (KIN3) remain in  $D_+^0$ . In addition, while in  $D_+^0$ , the solutions to (KIN2) and (KIN3) are indistinguishable.

Second, according to property (D) the solutions to every scheme converge towards the equilibrium point  $(X^\infty, S^\infty)$  on the portion  $E_*^+$  of the graph  $E_*$ , i.e., their distance  $Q$  from the equilibrium decreases. Third, as predicted by property (E), the solutions to (KIN2) and (KIN3) are indistinguishable while the solutions to (KIN1) proceed at a rate different than that for (KIN2).

**Example 5.2.2** (Unsaturated case). *Suppose that  $u^0 = 0.6$ . Thus, the equilibrium state  $(\chi^\infty, S^\infty) = (0.6, 0) \in E_*^-$ . Now we choose  $(X^0, S^0) = (0.25, 0.2) \in D_+^0$ . We use large  $\tau = 1$  or small  $\tau = 0.5$ .*

Fig. 5.3 demonstrates the results of the three models depending on the time step. First, we see that all solutions live on curve  $U^n = u(X^n, S^n) = u^0 = 0.6$ . Second, for smaller  $\tau$  we see that (KIN2) and (KIN3) coincide while in  $D_+^0$ .

However, only the solutions  $(X_{\text{KIN3}}^n, S_{\text{KIN3}}^n)$  to model (KIN3) converge to the equilibrium state on  $E_*^-$  and stay physical for all time steps. In contrast, the solutions to (KIN1) and (KIN2),  $(X_{\text{KIN1,2}}^n, S_{\text{KIN1,2}}^n)$  give unphysical solutions with negative saturations  $S_j^n < 0$ , and appear to converge to  $X_j^\infty = \chi^*$  with  $S_j^\infty = -0.4$  for which  $Q_j = 0$ . In fact,  $(X_{\text{KIN1,2}}^n, S_{\text{KIN1,2}}^n)$  cross the graph  $E_*^-$ , as predicted above. In particular, for  $\tau = 1$ , we have  $(X_{\text{KIN1}}^n, S_{\text{KIN1}}^n) \approx (0.7536, -0.1232)$  for  $n = 2$  and  $(X_{\text{KIN2}}^n, S_{\text{KIN2}}^n) \approx (0.625, -0.0182)$  for  $n = 1$ . For  $\tau = 0.5$  this happens for larger  $n$ .

**Example 5.2.3** (Equivalence of (KIN1) and (KIN2)). *In this example we illustrate property E.ii. In each case we show that the solutions to (KIN1) are the same as those of (KIN2)*

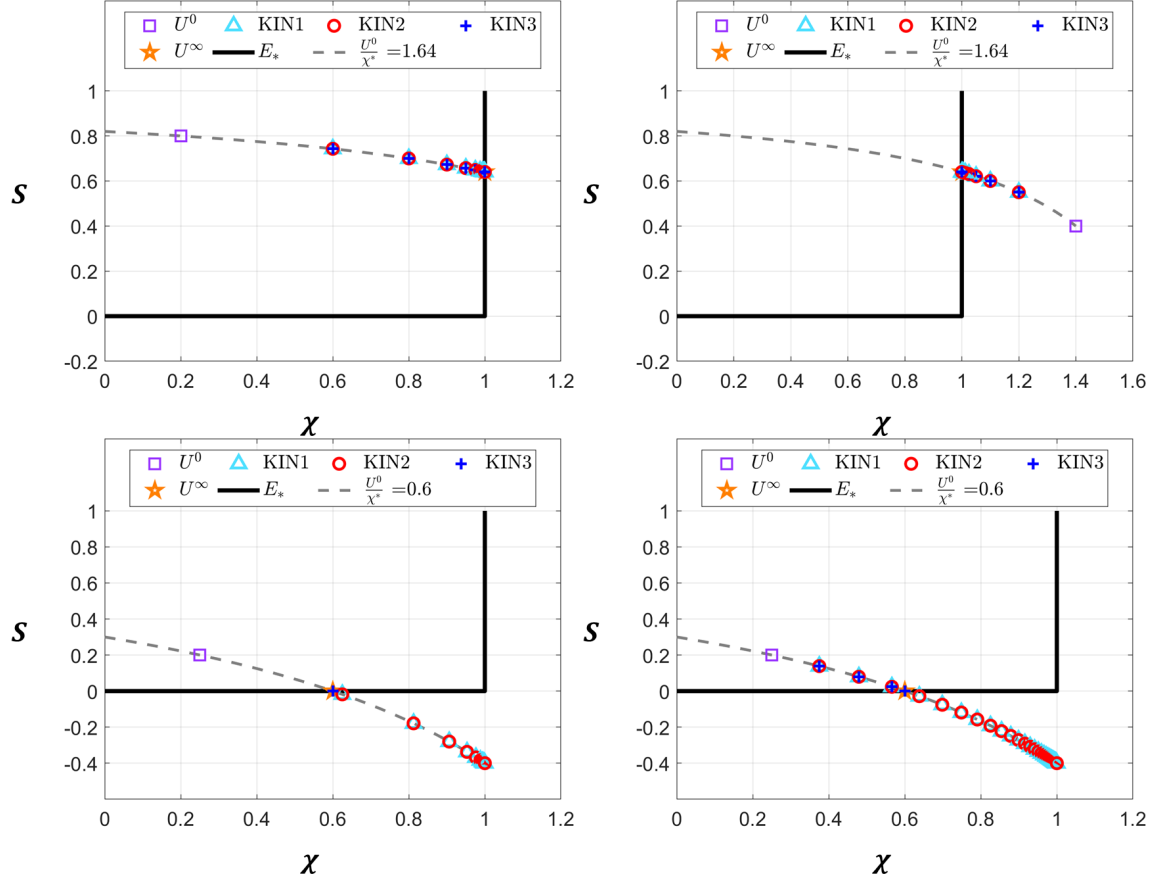


Figure 5.4: The numerical solutions generated by (KINj) for  $j = 1, 2, 3$  are the same with (5.26) for  $(X^0, S^0) \in D_+^0$ . For unsaturated cases,  $(X_{\text{KIN1}}^n, S_{\text{KIN1}}^n) = (X_{\text{KIN2}}^n, S_{\text{KIN2}}^n)$ .

when  $k_1$  is appropriately chosen depending on  $k_2$  and previous time step values. In turn, (KIN3) solutions are identical to (KIN2) in  $D_+^0$ . See Fig. 5.4.

### 5.3 Summary of kinetic transport model combining (3.12a) with (KIN3) model

The kinetic model rewrites (3.12a) in terms of  $\chi$  and  $\psi$ . To achieve a convenient symmetric form, we replace  $\partial_t(\phi u) = \phi \partial_t(\chi + \psi) = \phi \partial_t(\chi) + \phi Q$  with  $Q = -k_3(w - \chi)$  given as in (5.6). The model completed with appropriate initial data for  $\chi$  and  $\psi$  and boundary data for  $\chi$  reads

$$\partial_t(\phi \chi) - \phi k_3(w - \chi) + \nabla \cdot (q \chi) - d_m \nabla^2 \chi = \frac{F_M}{\rho l}, \quad x \in \Omega, t > 0, \quad (5.29a)$$

$$\partial_t(\psi(x, t)) + k_3(w - \chi(x, t)) = 0, \quad w \in w_*(x, t; \psi), \quad (5.29b)$$

$$\chi(x, 0) = \chi_{init}(x), \quad \psi(x, 0) = \psi_{init}(x), \quad x \in \Omega. \quad (5.29c)$$

$$\text{Assume boundary conditions for } \chi(x, t), \quad x \in \partial\Omega, t > 0. \quad (5.29d)$$

## 5.4 Scheme for kinetic model and its stability

Now we consider a numerical scheme for the kinetic model (5.29). We implement the general case with source terms and diffusion and approximate  $\chi(x_j, t^n) \approx X_j^n$  and  $\psi(x_j, t^n) \approx \Psi_j^n$  with  $U_j^n = X_j^n + \Psi_j^n$ . Given  $(X_j^{n-1}, \Psi_j^{n-1})$ , we find  $(X_j^n, \Psi_j^n, W_j^n)$  as solutions to the local nonlinear system at every  $j$ ; in this local problem the kinetic terms  $Q_j^n$  are handled implicitly. We set  $k = \tau k_3$ . The scheme (3.13) under assumptions from Sec. 4.1 in the form directly amenable to analysis reads

$$(X_j^n - X_j^{n-1}) - k(W_j^n - X_j^n) + \frac{\tau}{h}(q_{j-1/2}^{n-1}X_j^{n-1} - q_{j-3/2}^{n-1}X_{j-1}^{n-1}) = 0, \quad (5.30a)$$

$$(\Psi_j^n - \Psi_j^{n-1}) + k(W_j^n - X_j^n) = 0, \quad (5.30b)$$

$$W_j^n \in w_*(x_j; \Psi_j^n) \quad (5.30c)$$

In practice we solve (5.30) as follows, denoting  $\tilde{k} = \frac{k}{1+k}$ . Given previous time step values  $(X_j^{n-1}, \Psi_j^{n-1})_j$ , at every  $j$  we solve for  $(X_j^n, \Psi_j^n)$  the local nonlinear system

$$X_j^n - k(W_j^n - X_j^n) = F_j^n, \quad F_j^n = X_j^{n-1}(1 - \frac{\tau}{h}q_{j-1/2}^{n-1}) + \frac{\tau}{h}q_{j-3/2}^{n-1}X_{j-1}^{n-1}, \quad (5.31a)$$

$$\Psi_j^n + k(W_j^n - X_j^n) = G_j^n, \quad G_j^n = \Psi_j^{n-1}, \quad W_j^n = w_*(x_j; \Psi_j^n). \quad (5.31b)$$

This is a  $2 \times 2$  nonlinear stationary system of equations with a maximal monotone graph  $w_*$ . It is uniquely solvable with the following explicit formulas which follow from Sec. 2.2. Since (5.31a) is linear in  $X_j^n$ , we can formally calculate  $X_j^n = \frac{1}{1+k}(F_j^n + kW_j^n)$ . After we plug this to (5.31b), we get  $\Psi_j^n + \tilde{k}w_*(\Psi_j^n) = G_j^n + \tilde{k}F_j^n$ . Applying the resolvent  $\mathcal{R} = \mathcal{R}_k^{w_*} = (I + \tilde{k}w_*)^{-1}$  of  $w_*$ , we obtain  $\Psi_j^n = \mathcal{R}(G_j^n + \tilde{k}F_j^n)$ . We substitute to get  $W_j^n$  and  $X_j^n$ . Finally we can calculate the saturations  $S_j^n = \frac{\psi_j^n}{R - X_j^n}$ .

For stability of the scheme, we need an auxiliary result formulated for (5.31) with indices dropped and with inputs  $F, G$  and outputs  $X, \Psi$ .

**Lemma 5.4.1.** *Consider (5.31) with the right hand side  $(F, G)$  and solutions  $(X, \Psi, W)$ . Consider also the right hand side  $(\bar{F}, \bar{G})$  with the corresponding solutions  $(\bar{X}, \bar{\Psi}, \bar{W})$  to (5.31). The following comparison principle and stability hold*

$$|X - \bar{X}| + |\Psi - \bar{\Psi}| \leq |F - \bar{F}| + |G - \bar{G}|, \quad (5.32a)$$

$$|X| + |\Psi| \leq |F| + |G|. \quad (5.32b)$$

We also have  $W - \bar{W} = \frac{1}{\tilde{k}}(G - \bar{G}) + (\Psi - \bar{\Psi})(1 - \frac{1}{\tilde{k}})$ .

*Proof.* The result (5.32a) is a special case in  $\mathbb{R} \times \mathbb{R}$  of the result in [54] for  $a(u) + c(u - v) = f; b(v) - c(u - v) = g$ , where  $a(\cdot)$  is maximal monotone,  $b(\cdot)$  is strongly monotone and continuous, and  $c(\cdot)$  is maximal monotone single valued. The stability result (5.32b) follows from the comparison principle (5.32a). In turn, the algebraic formula for  $W - \bar{W}$  follows directly from algebra.  $\square$

#### 5.4.1 TV-stability for the kinetic scheme (5.31)

Now we prove properties of (5.31). Throughout we assume that the CFL condition (4.11) holds, and that the constants  $L_3, L_{\chi^*}$  are finite.

First we apply the stability part of Lemma 5.4.1 directly to (5.31) to obtain

$$|X_j^n| + |\Psi_j^n| \leq |X_j^{n-1}| \left(1 - \frac{\tau}{h} q_{j-1/2}^{n-1}\right) + \frac{\tau}{h} q_{j-3/2}^{n-1} |X_{j-1}^{n-1}| + |\Psi_j^{n-1}|. \quad (5.33)$$

Multiplying by  $h$  and summing both sides over  $j \in \mathbb{Z}^0$ , and collapsing the first two terms on the right hand side, we obtain the stability result. We obtain that scheme (5.31) is stable in the product space

$$\|(X^n, \Psi^n)\|_{\Delta,1} \leq \|(X^{n-1}, \Psi^{n-1})\|_{\Delta,1}. \quad (5.34)$$

Next we prove weak TV-stability which reveals the dependence of  $w_* = w_*(x_j; \cdot)$  on  $x_j$ .

**Proposition 5.4.1.** *Assume  $\chi^*(x)$  is smooth so that  $L_3$  and  $L_{\chi^*}$  given by (4.6) are finite. Assume also  $(X^\Delta, \Psi^\Delta)$  have compact support with measure bounded by  $\omega_S$ . If CFL condition (4.11) holds, then*

$$TV(X^n, \Psi^n) \leq TV(X^0, \Psi^0) + C_4 T, ; C_4 = 2k_3 \omega_S L_{\chi^*}. \quad (5.35)$$

*Proof.* We write the system (5.31) at  $(x_j, t^n)$  and at  $(x_{j-1}, t^n)$ . We set  $\Psi = \Psi_j^n$  and  $\bar{\Psi} = \Psi_{j-1}^n$  with analogous notation for other variables, and consider

$$X - kW + kX = F, \quad (5.36a)$$

$$\Psi + kW - kX = G; W \in w_*(\Psi), \quad (5.36b)$$

$$\bar{X} - k\bar{W} + k\bar{X} = \bar{F}, \quad (5.36c)$$

$$\bar{\Psi} + k\bar{W} - k\bar{X} = \bar{G}; \bar{W} \in v_*(\bar{\Psi}). \quad (5.36d)$$

Here for shorthand we denoted the graph  $w_*(x_j, t^n)$  by  $w_*$  and a different graph  $w_*(x_{j-1}, t^n)$  at  $x_{j-1}$  by  $v_*(\cdot)$ . Since the graphs  $w_*$  and  $v_*$  are not the same, we cannot directly apply

Lemma 5.4.1. Instead, we rewrite the third and fourth equations with  $w_*$  instead of  $v_*$ , move the difference between  $w_*$  and  $v_*$  to the right hand side, and examine the difference  $w_* - v_*$  due to their “height”, respectively,  $\chi^*(x_j, t^n)$  and  $\chi^*(x_{j-1}, t^n)$ .

For  $\psi > 0$  we can write

$$v_*(\psi) = w_*(\psi) - A_j h, \quad \psi > 0, \quad A_j = \frac{d}{dx} \chi^*(\bar{x}_j, t^n), \quad \bar{x}_j \in (x_{j-1}, x_j).$$

When  $\psi = 0$  both  $w_*$  and  $v_*$  are set-valued, and we must work with their Yosida approximations  $w_\lambda$  and  $v_\lambda$ . In fact for small  $\psi$  we have  $w_\lambda(\psi) = v_\lambda(\psi)$  while for any  $\psi$  and  $\lambda$  we have  $v_\lambda(\psi) = w_\lambda(\psi) - A_j(\lambda; \psi)h$ , with  $|A_j(\lambda; \psi)| \leq L_{\chi^*}$  from (4.10).

Reconsidering (5.36) with  $v_\lambda$  and  $w_\lambda$  instead of  $v_*$  and  $w_*$  but keeping the notation unchanged otherwise, we calculate  $k\bar{W} = kv_\lambda(\bar{\Psi}) = kw_\lambda(\bar{\Psi}) - khA_j$ , and the third and fourth equations read now

$$\begin{aligned} \bar{X} - kw_\lambda(\bar{\Psi}) + k\bar{X} &= \tilde{F} = \bar{F} - khA_j(\lambda; \bar{\Psi}), \\ \bar{\Psi} + kw_\lambda(\bar{\Psi}) - k\bar{X} &= \tilde{G} = \bar{G} + khA_j(\lambda, \bar{\Psi}). \end{aligned}$$

We can now apply the comparison principle from Lemma 5.4.1 for the maximal monotone  $w_\lambda$  and inputs  $F, G, \tilde{F}, \tilde{G}$ . We apply the uniform bound on  $A_j$  in (5.32a), notice  $|\tilde{F} - F| \leq |\bar{F} - F| + khL_{\chi^*}$  and  $|\tilde{G} - G| \leq |\bar{G} - G| + khL_{\chi^*}$ . Taking the limit as  $\lambda \rightarrow 0$ , we revert back to the original notation of (5.31) that

$$\begin{aligned} |X_j^n - X_{j-1}^n| + |\Psi_j^n - \Psi_{j-1}^n| &\leq |X_j^{n-1} - X_{j-1}^{n-1}| \left(1 - \frac{\tau}{h} q_{j-1/2}^{n-1}\right) + \left|\frac{\tau}{h} q_{j-3/2}^{n-1}\right| |X_{j-1}^{n-1} - X_{j-2}^{n-1}| \\ &\quad + |\Psi_j^{n-1} - \Psi_{j-1}^{n-1}| + 2khL_{\chi^*}. \end{aligned} \quad (5.37)$$

The term  $2khL_{\chi^*}$  will accumulate giving weak rather than strong stability. Summing (5.37) over those  $j \in \mathbb{Z}^0$  with  $\sum_j h \leq \omega_S$ , we collapse the first two terms on the right hand side, and with  $k = \tau k_3$ , we get

$$TV(X^n, \Psi^n) \leq TV(X^{n-1}, \Psi^{n-1}) + 2\tau k_3 \omega_S L_{\chi^*}. \quad (5.38)$$

Applying recursively, we obtain (5.35) with  $C_4 = 2k_3 \omega_S L_{\chi^*}$ .  $\square$

**Remark 5.4.1.** *The weak TV-stability result (5.35) in the product space for the kinetic problem (5.29) is similar to the weak stability (4.7a) we obtained for  $U^\Delta$  in the equilibrium model (4.4), with the difference in the constants depending on  $\chi^*(x)$ , and the absence of the factor  $(1 + \tau L_1)$  in (5.38) in the product space.*

### 5.4.2 TV stability in time

Given the known  $(X_j^{n-1}, \Psi_j^{n-1})_j$ , the next goal is to bound the terms  $X_j^n - X_j^{n-1}$  and  $\Psi_j^n - \Psi_j^{n-1}$ . For this, we need a handle on  $Q_j^n \propto W_j^n - X_j^n$  which quantifies the discrepancy from the equilibrium. We estimate  $Q_j^n$  in terms of  $Q_j^{n-1}$ .

**Lemma 5.4.2.** *Under the assumption of Proposition 5.4.1 we have that*

$$\|Q^n\|_1 \leq C_5(T).$$

To prove the lemma, we estimate the terms in a regularized version of (5.31). Additional challenge is to allow for possible variability of  $w_*$  in time. We consider some smooth single valued approximations  $w_\lambda$  of  $w_*|_{x_j, t^n}$  and  $v_\lambda$  of  $w_*|_{x_j, t^{n-1}}$ . The difference between these  $w_\lambda(\psi) - v_\lambda(\psi) = B_j^n(\psi)\tau$  can be estimated uniformly in  $\psi$  with  $|B_j^n| \leq L_3$ , where  $L_3$  is given in (4.10).

*Proof.* We rearrange (5.31), drop  $j$ , and seek the solution  $(X_\lambda^n, \Psi_\lambda^n)$  to the regularized problem

$$X_\lambda^n - X^{n-1} - kQ_\lambda^n = F^{n-1}, \quad (5.39a)$$

$$\Psi_\lambda^n - \Psi^{n-1} + kQ_\lambda^n = 0, \quad (5.39b)$$

where  $Q_\lambda^n = w_\lambda(\Psi_\lambda^n) - X_\lambda^n$  and  $F^{n-1} = -\frac{\tau}{h}q_{j-1/2}^{n-1}X_j^{n-1} + \frac{\tau}{h}q_{j-3/2}^{n-1}X_{j-1}^{n-1}$ . To get the estimates for  $Q_\lambda^n$  in terms of  $Q_\lambda^{n-1} = v_\lambda(\Psi^{n-1}) - X^{n-1}$ , we break the expression

$$w_\lambda(\Psi_\lambda^n) - v_\lambda(\Psi^{n-1}) = w_\lambda(\Psi_\lambda^n) - w_\lambda(\Psi^{n-1}) + w_\lambda(\Psi^{n-1}) - v_\lambda(\Psi^{n-1}) = b(\Psi_\lambda^n - \Psi^{n-1}) + B\tau.$$

Here  $b = w'_\lambda(\widetilde{\Psi}_\lambda) \geq 0$  with some  $\widetilde{\Psi}_\lambda$ , and  $B = B_j^n$  discussed above, with  $|B| \leq L_3$ . Now we multiply (5.39b) by  $b$  and subtract (5.39a) from (5.39b). Rearranging, we obtain

$$Q_\lambda^n(1 + k(1 + b)) = Q^{n-1} - F^{n-1} + B\tau.$$

We take absolute value, note  $b \geq 0$ , and pass to the limit with  $\lambda$ , to obtain the following with index  $j$ :

$$(1 + k) |Q_j^n| \leq |Q_j^{n-1}| + |F_j^{n-1}| + \tau |B_j^n|.$$

Here, with  $L_q$  and  $L_{q_x}$  defined in (4.10),  $|F_j^{n-1}|$  is bounded above:

$$\left| F_j^{n-1} \right| = \frac{\tau}{h} \left| q_{j-1/2}^{n-1} X_j^{n-1} - q_{j-1/2}^{n-1} X_{j-1}^{n-1} + q_{j-1/2}^{n-1} X_{j-1}^{n-1} - q_{j-3/2}^{n-1} X_{j-1}^{n-1} \right|$$

$$\begin{aligned}
&\leq \frac{\tau}{h} L_q \left| X_j^{n-1} - X_{j-1}^{n-1} \right| + \tau L_{q_x} \left| X_{j-1}^{n-1} \right| \\
&\leq \frac{\tau}{h} L_q \left( \left| X_j^{n-1} - X_{j-1}^{n-1} \right| + \left| \Psi_j^{n-1} - \Psi_{j-1}^{n-1} \right| \right) + \tau L_{q_x} \left( \left| X_{j-1}^{n-1} \right| + \left| \Psi_{j-1}^{n-1} \right| \right).
\end{aligned}$$

Multiply both sides by  $h$  and sum over  $j \in \mathbb{Z}^0$  with  $\sum_{j \in \mathbb{Z}^0} h \leq \omega_S$ . Then apply (5.34) and (5.35) to get

$$\begin{aligned}
(1+k)\|Q^n\|_1 &\leq \|Q^{n-1}\|_1 + \tau [L_q TV(X^{n-1}, \Psi^{n-1}) + L_{q_x} \|(X^{n-1}, \Psi^{n-1})\|_{\Delta,1} + L_3 \omega_S] \\
&\leq \dots \leq \|Q^0\|_1 + T [C_6(T) + L_3 \omega_S],
\end{aligned}$$

where  $C_6(T) = L_q(TV(X^0, \Psi^0) + C_4 T) + L_{q_x} \|(X^0, \Psi^0)\|_{\Delta,1}$ . With  $k > 0$ , we have completed the proof.  $\square$

**Lemma 5.4.3.** *Suppose (5.35) holds for  $(X, \Psi)$ . Then we have*

$$\|(X^n - X^{n-1}, \Psi^n - \Psi^{n-1})\|_{\Delta,1} \leq \tau C_7(T).$$

*Proof.* Rewrite (5.31) estimating in the form

$$\begin{aligned}
\left| X_j^n - X_j^{n-1} \right| &\leq k \left| Q_j^n \right| + \frac{\tau}{h} L_q \left| X_j^{n-1} - X_{j-1}^{n-1} \right| + \tau L_{q_x} \left| X_{j-1}^{n-1} \right|, \\
\left| \Psi_j^n - \Psi_j^{n-1} \right| &\leq k \left| Q_j^n \right|.
\end{aligned}$$

Next we multiply by  $h$ , take the sum over  $j \in \mathbb{Z}^0$  and add these to get

$$\begin{aligned}
\|(X^n - X^{n-1}, \Psi^n - \Psi^{n-1})\|_{\Delta,1} &\leq \tau [2k_3 \|Q^n\|_1 + L_q TV(X^{n-1}, \Psi^{n-1}) + L_{q_x} \|(X^{n-1}, \Psi^{n-1})\|_{\Delta,1}] \\
&\leq \tau [2k_3 \|Q^n\|_1 + C_6(T)].
\end{aligned}$$

With (5.34), (5.35) and the estimates for  $Q$  from Lemma 5.4.2, we get

$$\|(X^n - X^{n-1}, \Psi^n - \Psi^{n-1})\|_{\Delta,1} \leq \tau C_7(T) = \tau [2k_3 \|Q^0\|_1 + (1 + 2k_3 T) C_6(T) + 2k_3 T L_3 \omega_S].$$

$\square$

Combining Lemma 5.4.3 and (5.35), we conclude this main result.

**Proposition 5.4.2.** *Under hypotheses of Proposition 5.4.1 we have*

$$TV_T(X^n, \Psi^n) \leq C_8(T) = T [C_4 T + C_7(T)]. \quad (5.40)$$

Here  $C_4 = 2k_3 \omega_S L_{\chi^*}$ ,  $C_7(T) = [2k_3 \|Q^0\|_1 + (1 + 2k_3 T) C_6(T) + 2k_3 T L_3 \omega_S]$ , and  $C_6(T) = L_q(TV(X^0, \Psi^0) + C_4 T) + L_{q_x} \|(X^0, \Psi^0)\|_{\Delta,1}$ .

As in equilibrium case discussed in Sec. 4.4.1, this stability result depends on the variability of  $q$  and  $\chi^*$  and on the initial discrepancy from the equilibrium through the constants in (5.40).

## 5.5 Simulation results

In this section we illustrate the evolution of hydrate formation and dissociation using the kinetic model. We first compare the results of kinetic model with that of equilibrium model, which obviously shows that the kinetic solutions get closer to and eventually indistinguishable from those for the equilibrium model as the kinetic exchange rate increases. In Sec. 5.5.1 we illustrate the sensitivity of the kinetic model to the choice of macro time steps  $\Delta T$  from Sec. 3.5.1.

**Example 5.5.1** (Model case: equilibrium and kinetic models). *Let  $\Omega = (0, 2)$ ,  $q = 1$ ,  $R = 2$ . We use  $x_L = 0.35$ ,  $\chi^*(x) = e^{-0.5x}$ , and the initial condition  $u_{init}(x) = \chi_L H(-x)$  with  $\chi_L = 0.8395$ . We simulate the problem using both the equilibrium model and scheme (4.3), and with the kinetic model and scheme (5.31) when  $k_3 = 10$  and  $k_3 = 100$ . Here  $M = 100$  and  $\nu = q\tau/h = 0.9$ . We compare with the equilibrium solution at  $T = 1$ .*

Fig. 5.5 illustrates the results. We confirm that, as expected, the kinetic solution “lives” in the vicinity of the equilibrium solution. This closeness is more pronounced with larger  $k_3$ . In turn, Fig. 5.6 shows that the numerical solutions  $(U_{\text{KIN}}^\Delta, X_{\text{KIN}}^\Delta, S_{\text{KIN}}^\Delta)$  converges to the fine grid solutions  $(U_{\text{KIN},\text{fine}}^\Delta, X_{\text{KIN},\text{fine}}^\Delta, S_{\text{KIN},\text{fine}}^\Delta)$  at the order roughly of  $O(h^{0.5})$ :

$$\begin{aligned} \|U_{\text{KIN},\text{fine}}^\Delta - U_{\text{KIN}}^\Delta\|_1 &= O(h^{0.57}), \\ \|X_{\text{KIN},\text{fine}}^\Delta - X_{\text{KIN}}^\Delta\|_1 &= O(h^{0.56}), \\ \|S_{\text{KIN},\text{fine}}^\Delta - S_{\text{KIN}}^\Delta\|_1 &= O(h^{0.62}). \end{aligned}$$

### 5.5.1 Equilibrium and kinetic schemes under varying environmental and thermodynamic conditions and sensitivity to macro steps

We illustrate the dependence of the solutions to the equilibrium model and kinetic models depending on the choice of macro steps  $T^m = m\Delta T$  at which  $\chi^*$  is recomputed. We allow  $P = P(x, t)$  and  $T = T(x, t)$  to vary due to the changing environmental conditions and specifically due to the warming of ocean temperature and the sea level rise as predicted in [88] with the rate of sea level rise is 0.003 [m/y] and the rate of temperature rise at the seafloor of 0.01 [K/y]. Then we assume that the pressure (P), and temperature (T) at the seafloor vary linearly with respect to time  $t$  [y], with subscript *ref* and *eq* to denote the values at the seafloor and at the BHSZ, respectively.

$$P_{ref}(t) = \rho_l g D_{ref}(t), \quad D_{ref}(t) = D_{ref}(0) + 0.003t,$$

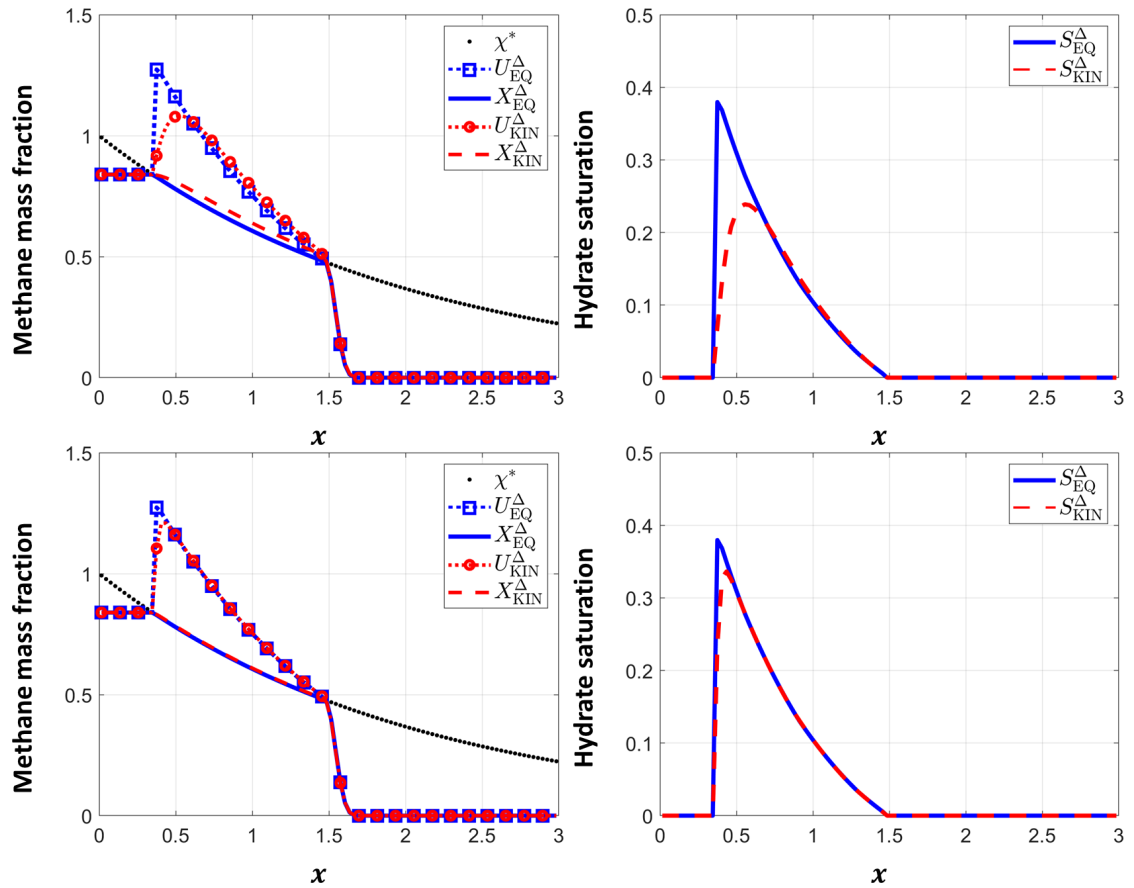


Figure 5.5: Comparison of the kinetic and equilibrium model solutions at  $T = 1$  with  $M = 100$ , and  $\nu = 0.9$  for Ex. 5.5.1. Top: rate  $k_3 = 10$ . Bottom: rate  $k_3 = 100$ .

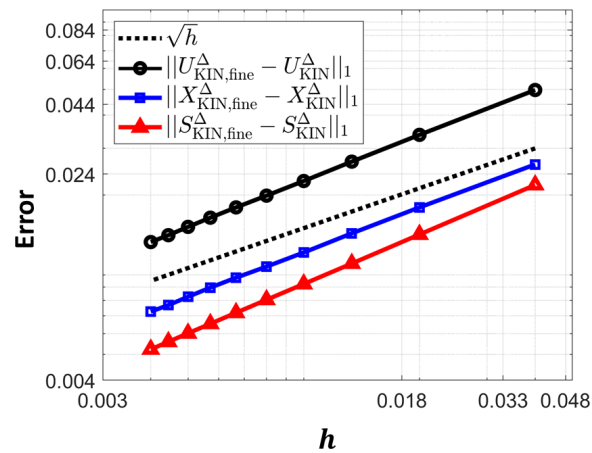


Figure 5.6: Convergence of the numerical solutions of Ex. 5.5.1 for  $M = \{100, 200, \dots, 1000\}$  to the fine grid solution  $M = 50000$  with  $k_3 = 100$  at  $T = 1$ .

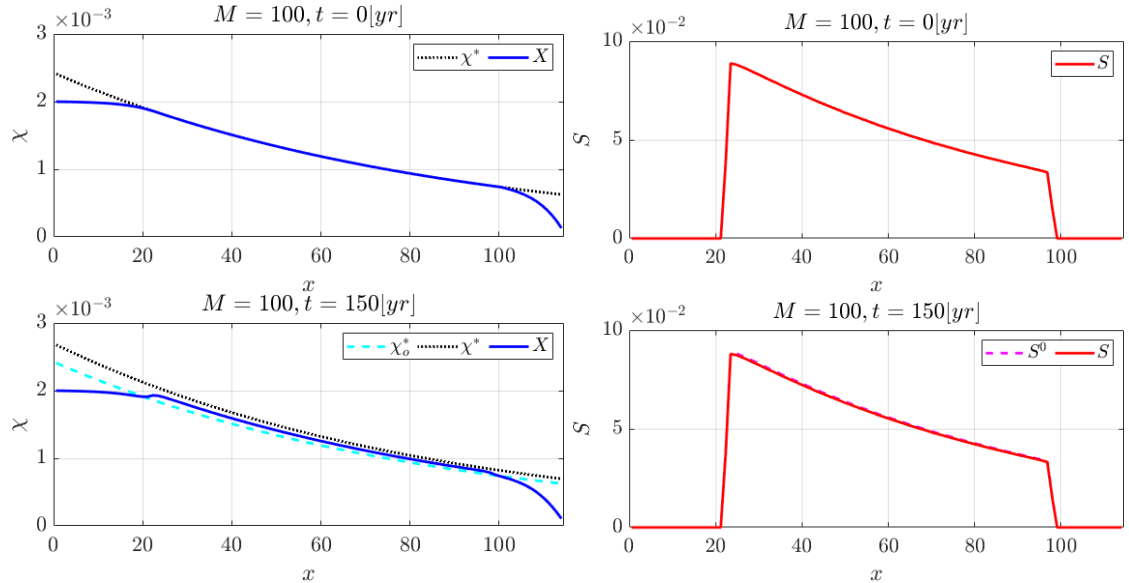


Figure 5.7: Top: initial condition  $\chi(x, 0)$  and  $S(x, 0)$  from Sec. 5.5.1. Bottom: results of Ex. 5.5.2 with  $k_3 = 0.01$ . On both figures  $\chi_0^*$  indicates the original  $\chi^*|_{t=0}$ .

$$T_{ref}(t) = T_{ref}(0) + 0.01t,$$

where  $\rho_l \approx 1030$  [kg/m<sup>3</sup>] is the density of seawater, and  $g = 9.8$  [m/s<sup>2</sup>]. Over 150 [y] we see the sea level rise by 0.45 [m] and  $T_{ref}$  increase by 1.5 [K]. Assume further that  $(P(x, t), T(x, t))$  vary linearly in  $\Omega$

$$P(x, t) = P_{ref}(t) + G_H(d_{sf}(x) - D_{ref}(t)),$$

$$T(x, t) = T_{ref}(t) + G_T(d_{sf}(x) - D_{ref}(t)),$$

where  $d_{sf}(x)$  is the depth below the sea level. We then recompute the equilibrium conditions at BHSZ using the parametric model from [110] responding to the increase in  $T_{ref}, P_{ref}$ .

We apply these varying conditions to simulate the dissociation in a hydrate reservoir from the state obtained with simulation in Ex. 4.5.2 run until 100 [ky]. We consider this state to be the initial state for this simulation at  $t = 0$ ; see Fig. 5.7 with  $\chi_0^*$  as shown. The changes in  $P$  and  $T$  in time require we recompute  $\chi^* = \chi^*(x, t)$  at the macro-time steps  $T^m = m\Delta T$  as discussed in Sec. 3.5.1. We adopt other parameters as in Ex. 4.5.2 but use a fixed  $\tau = 1$  [y] much smaller than that needed by CFL condition. We consider impact of  $\Delta T = K\tau$  with  $K = 1, 10, 50, 150$ .

**Example 5.5.2** (Hydrate dissociation due to warming waters). *We start from the equilibrium state shown in Fig. 5.7. At every macro-time step  $T^m = m\Delta T$ , we recompute  $\chi^*(x, T^m)$ . Using the parameters as in Ex. 4.5.2 with  $d_m = 3 \times 10^{-2}$  [m<sup>2</sup>/y], we simulate*

$t$ [y]	K	$P_{ref}$	$T_{ref}$	$D_{ref}$	$P_{eq}$	$T_{eq}$	$D_{eq}$	$10^2\ S\ _\infty$	$10^2S_2$	$\ S\ _1$
0	–	21.6500	273.55	2145.00	22.8849	294.6665	2268.49	8.8732	3.3524	4.3681
150	1	21.6545	275.05	2145.45	22.7999	294.6364	2259.99	8.7212	3.2854	4.2848

Table 5.1: Simulation reference data and results generated by the equilibrium model (EQ) with  $K = 1$  for Ex. 5.5.2. Pressure  $P$ , temperature  $T$ , and depth  $D$  are in the units of [MPa], [K], and [mbsl]

		$k_3 = 0.01$			$k_3 = 1$			$k_3 = 100$ and EQ		
$t$ [y]	$K$	$100\ S\ _\infty$	$100S_2$	$\ S\ _1$	$100\ S\ _\infty$	$100S_2$	$\ S\ _1$	$100\ S\ _\infty$	$100S_2$	$\ S\ _1$
150	1	8.7946	3.3185	4.3295	8.7181	3.2844	4.2855	8.7212	3.2854	4.2848
150	10	8.7905	3.3168	4.3276	8.7168	3.2839	4.2848	8.7212	3.2854	4.2847
150	50	8.7736	3.3096	4.3196	8.7160	3.2836	4.2842	8.7212*	3.2854	4.2841
150	150	8.7381	3.2948	4.3044	8.7144	3.2831	4.2831	8.7213*	3.2855	4.2830

Table 5.2: Simulation results at  $t = 150$  [y] with kinetic model for Ex.5.5.2 with  $\Delta t = K\tau$ . (\*) The results in the last macro-column differ are higher for the EQ model by one digit.

*hydrate dissociation using the (EQ) model at  $t \in [0, 150]$  [y], and plot the solutions at the final  $t^N = 150$  [y]. We compare the results to the numerical solutions generated by the equilibrium model (3.13) and the kinetic model (5.29), both are amended to include diffusion, depending on different rates  $k_3$  and the choice of  $\Delta T$ .*

At this time scale, dissociation proceeds slowly as shown by the decrease in the overall amount  $\|S\|_1$  as well as the peak amount  $\|S\|_\infty$ ; it is also interesting to test the magnitude  $S_2$  of the last peak before the decrease to seafloor. For all simulations the peak  $\|S\|_\infty$  is attained at  $x = 23.5$  [m], and the last saturation peak  $S_2$  corresponds to  $x = 96.8$  [m].

We find the difference between taking macro-time steps with  $K = 1$  up to  $K = 150$  is very small for both equilibrium and kinetic models, and the difference between kinetic model and equilibrium model is indistinguishable when  $k_3 = 100$ . This rate is still about 100 times less than the rate used in [121, 151].

## 5.6 Summary

In this chapter we investigated the robustness of a variety of kinetic models in the two-phase liquid-hydrate conditions. Such models are needed, e.g., during sudden rearrange-

ment of external controls on thermodynamic equilibria. Since the kinetic model popular in literature dubbed (KIN1) and its linear variant called (KIN2) work only in saturated conditions, we developed a model (KIN3) which is robust across the unsaturated and saturated conditions while it is equivalent to (KIN2) in saturated conditions. Next we combined this model (KIN3) with the transport model and were able to show its numerical stability. Our stability result is the first one to our knowledge. The extension of (KIN3) model for three phase conditions is subject to our current work.

## 6 Biofilm growth model in complex geometry

In this chapter we turn our attention to the study of biofilm growth in pore scale complex geometries which is important for a range of applications including biofouling and bioremediation in engineering applications, and in medicine including tissue engineering, e.g., in artificial regeneration of articular chondrocytes [129]. Mathematical models can aid in testing hypotheses for the experimental study of biofilm properties [19]. In [131] we presented a new model that describes biofilm-nutrient-flow dynamics in porous media at pore scale. The new model was developed by blending the idea of cell shoving mechanism introduced in discrete biomass models such as individual based models and cellular automata [4, 57, 66, 116, 117, 164], singular diffusivity model [33, 39], and variational inequality type [2, 114]. It is of continuum type and is a coupled system of partial differential equations with which we treat the processes monolithically.

In this dissertation we focus on the robust and relatively cost effective constrained nonsingular biomass-nutrient model coupled with a flow model that accounts for somewhat permeable biofilm domains. This corresponds to the material presented in our recent work [131](Sec. 4-5).

In this chapter we discuss the improved constrained nonsingular biomass-nutrient model which corresponds to Sec. 4 of [131]. The coupled flow and biomass-nutrient dynamics presented in [131](Sec. 5) is discussed in Ch. 7.

The outline of this chapter is as follows. We first provide the preliminary materials about biofilm and discuss the modeling challenges in Sec. 6.1. In Sec. 6.2, we introduce notations for the biomass-nutrient dynamics which we will also use later in Ch. 7–8. In Sec. 6.3, we describe the improved constrained biomass-nutrient model using the idea of singular diffusivity model. Then we discuss the numerical approximation scheme and its convergence in Sec. 6.4. We close this chapter by giving an example of biofilm growth in a realistic single pore in Sec. 6.5.

### 6.1 Background on biofilm and modeling challenges

Biofilms are complex structures made of a gel-like polymeric substance called EPS and of microbial cells which produce EPS. Given access to sufficient nutrient resources, the microbes multiply until their maximum density is achieved, after which the biofilm

domain expands through the interface with the surrounding liquid. In other words, the region occupied by the biofilm phase grows when the cells divide and are “shoved” by their neighbors; see a cartoon in Fig. 6.1 for a basic idea. The liquid and biofilm are separated by a sharp or diffuse interface, and together they form a fluid with very complex properties. The hypothesized purpose of biofilms in their various aggregative, architectural and protective types is to promote the growth and protect the cells, e.g., from environmental conditions such as desiccation, high temperature and competing microbes [19, 20, 78].

The modeling of biomass-nutrient dynamics depends on the length scale. A typical pore scale domain  $\Omega$  we consider has diameter  $L = O(10^a \text{ [mm]})$  with  $a \in [-2, 0]$ , while the microbial cells have size ranging in  $h_c \in [0.5, 20] \text{ [\mu m]}$  [66, 164]. However, typical pore sizes in meso-scale or unconsolidated porous media range in  $O(10^s) \text{ [\mu m]}$  with  $s \in [0, 1]$  [95] while the grain size in glass-bead packs used for observation can range from  $O(10^s) \text{ [\mu m]}$  with  $s \in [1, 2]$  [14, 23, 114, 130]. Depending on the length scales, the modelling challenges are treated differently. We focus on the continuum model and address the challenges below.

**Challenges addressed.** The primary challenge in modeling biomass-nutrient dynamics is to address the volume constraint of maximum cell density while we allow some microbial presence outside of the contiguous biofilm phase. Authors of [39] describe the biomass redistribution mechanism, the analogy of “shoving” from the discrete model [66, 164], using the singular diffusion model which allows fast biomass distribution as the concentration of biomass increase. One can implement a modified version of the singular diffusion model [131] with an upper bound to ensure no mechanism when biomass concentration reaches its maximum. However, its solutions may violate the biomass maximum constraint when the spreading speed is not fast enough. To overcome this issue, we can use the adaptive singular diffusion model, but this is computationally expensive because we seek for the right diffusion parameters in every time step. Alternatively, one can enforce the volume constraint through the parabolic variation inequality (PVI) approach as in [114]. This approach guarantees the volume constraint, but it might exclude some reactions that could take place at the free boundary between the biofilm and bulk fluid. We refer to review articles [19, 64, 78] for an overview of modeling challenges, more references, and applications in human engineering systems, e.g., in selective plugging [22, 35, 84, 144].

The second challenge is in treating the free boundary arising at the interface between the biofilm and the surrounding bulk fluid. The pore scale flow models range from Navier-

Symbol	Description	Value/Units
$\rho_B$	Dry mass density of biomass	$\sim 1.1$ [g/cm <sup>3</sup> ]
$\rho_B^*$	Maximum mass density of biomass	$24 \times 10^3$ [g/cm <sup>3</sup> ]
$\theta_w, \theta_b$	Volume fraction of water ( $w$ ) and biomass ( $b$ )	[–]
$B$	Concentration of biomass, defined by (6.2)	[–]
$B^*$	Maximum total concentration of biomass	1 [–]
$B_*$	Threshold for mature biofilm	$0.9B^*$ [–]
$N$	Concentration of the nutrient relative to $\rho_B^*$	[–] $\sim O(10^{-4})$ [kg/m <sup>3</sup> ]/ $\rho_B^*$
$k_N$	Monod half-life [can vary by factor $10^s$ , $s \approx 6$ ; see [163]]	same as $N$
$\kappa$	Specific substrate uptake rate	$\sim O(10^s)$ [1/h], $s \in [-2, 0]$
$\kappa_B$	Growth constant incorporating yield coefficient	$\sim O(1)$ [–]
$d_m$	Molecular diffusivity	6.84 [mm <sup>2</sup> /h]
$d_B$	Diffusivity of $B$	$\sim O(1)$ [mm <sup>2</sup> /h]
$d_N$	Diffusivity of $N$ ; see (6.6d)	$\sim O(1)$ [mm <sup>2</sup> /h]
$h, \tau$	Spatial and time discretization parameters	$\sim O(1)$ [ $\mu$ m], $O(1)$ [h]

Table 6.1: Symbols for the variables and parameters used commonly for biomass-nutrient dynamics, with typical values adapted from [33, 39, 114] or as indicated.

Stokes models extended by the inclusion of additional stress tensor in [19, 171] through Navier-Stokes models for large velocity in [114] and Stokes and Brinkman flow models in [70, 71]. As discussed in [131], the nutrient penetration in the biofilm phase influence the biofilm growth significantly. We account for somewhat permeable biofilm and employ the Brinkman flow with a spatially variable permeability depending on the quantity of biomass. Thus, the fluid flow allows some advection of nutrients within the biofilm phase as well as for the flow even when the pores are close to being plugged up.

Additional challenges arise when we couple the biofilm growth model with the ambient flow in porous domains. We apply this heterogeneous Brinkman flow model to the entire domain rather than a staggered-in-time treatment so that the coupling of flow and biomass-nutrient dynamic is monolithic.

## 6.2 Notation for biomass-nutrient dynamics

In this section we set up notations for the biofilm growth at pore scale which we will discuss for the rest of this dissertation. Most of the material is fairly standard. We also closely follow the notations from [39].

Let  $B$  be biomass concentration with its maximum possible biomass density  $B^*$ . The region

$$x : B_* \leq B(x, t) \leq B^*$$

with a threshold  $B_* \in (0, B^*]$  indicates what we call a “mature” biofilm which contains microbes as well as the biomass-produced extracellular polymer substance (EPS). Here we choose  $B_* = 0.9B^*$ . The precise definition and units of  $B, B_*, B^*$  will be given later in Sec. 6.2.2.

We also consider nutrient  $N$  which can be oxygen, carbon, glucose, ammonia, or more generically some substrate. The diffusivity of  $N$  depends on the nutrient type.

### 6.2.1 Notation for pore scale geometry with microbial species

We consider an open bounded pore scale domain  $\Omega = \Omega_r \cup \Omega_n \cup \Gamma_{\text{rn}}$  (rock, no-rock, wall interface) as discussed in Sec. 2.3.2. We allow  $\Omega_r = \emptyset$  and assume that the volume  $|\Omega_n| > 0$ . We recognize a fixed rock wall boundary  $\Gamma_{\text{rn}} = \partial\Omega_r \cap \partial\Omega_n$ , and consider the void region  $\Omega_n$  for flow of water and biofilm growth.

Next, we will identify the different regions in  $\Omega_n$  which the flow and the reaction processes have different properties; see Fig. 6.1 for illustration.

$$\Omega_0(t) = \{x : B(x, t) = 0\}, \text{ no microbes present; bulk fluid} \quad (6.1a)$$

$$\Omega_b(t) = \{x : B(x, t) > 0\}, \text{ microbes present} \quad (6.1b)$$

$$\Omega_*(t) = \{x : B_* \leq B(x, t) \leq B^*\}, \text{ mature biofilm} \quad (6.1c)$$

$$\Omega^*(t) = \{x : B(x, t) \geq B^*\}, B \text{ exceeds the maximum} \quad (6.1d)$$

$$\Omega_b^*(t) = \Omega_* \cup \Omega^*, \text{ biofilm domain.} \quad (6.1e)$$

The definition of regions such as  $\Omega_b$  varies in the literature, where it is used for convenience of notation, or in reference to the properties observed in experiments. In particular, in [114] we used x-ray micro-CT tomography imaging to identify the region  $\Omega_*$  as the opaque region

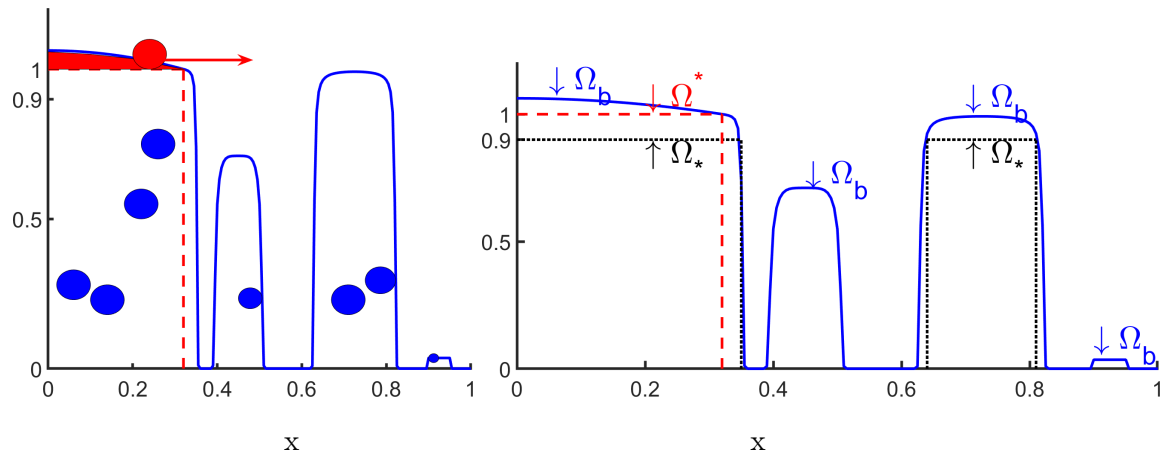


Figure 6.1: Schematic picture of biofilm domain  $x \in [0, 1]$  and the cell density  $B(x)$  plotted with a solid blue curve. On the left we show the mechanism of cell growth schematically and “shoving” when the cell density exceeds the maximum  $B^* = 1$ . On the right we show the notation from (6.1). In the region  $\Omega_b$  some cells can be very small, and some quite large. Note that in a continuum model, it is likely that  $B > 0$  everywhere and thus  $\Omega_0 = \emptyset$ . When the maximum cell density is reached, the cells redistribute. This mechanism is modeled differently in various models; see [131] for discussion.

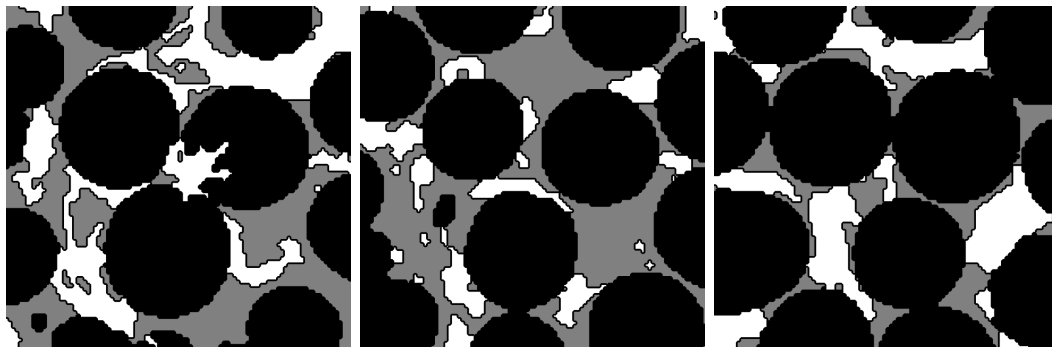


Figure 6.2: Processed micro-CT images from [114] at resolution  $202 \times 202$ .  $\Omega_b$  is in gray,  $\Omega_0$  in white, and  $\Omega_r$  in black.

from which the contrast agent barium is excluded; see Fig. 6.2 for the process micro-CT images from [114]. With some models,  $\Omega_b$  is assumed contiguous, i.e., simply connected, and only its boundary is tracked, but with other models including our model not so. In some literature the region  $\Omega_*$  is called the boundary layer in which much growth occurs and propagates the fastest.

## 6.2.2 Notation for microbial species

The many different models we cited in [131] come each with a different system of variables and units, and use different data, e.g., for rate constants in their examples. For example, the units for the biomass concentration  $B$  range from  $[\text{kg}/\text{m}^3]$ ,  $[\text{g}/\text{cm}^3]$ ,  $[\text{ppm}]$ , or  $[\text{g}/\text{L}]$ , or are non-dimensional, as in [36, 39]. We follow closely the non-dimensional

notation from [39]. The different symbols we define and typical parameter values are listed in Tab. 6.1.

Let  $\rho_w$  denote the water density. The water occupying  $\Omega$  or, more precisely,  $\Omega_n$ , has microbes and the dissolved nutrients. The mass and volume contribution of microbes compared to that of water is significant; their presence also changes the properties of the phase, and we address this later. The nutrients are not accounted for in mass balances.

We denote the (dry mass) density of biomass by  $\rho_B$ . The EPS has a different density  $\rho_{EPS} \approx 0.5\rho_B$ , but for simplicity we ignore this distinction here. At the microscopic level at any point  $x$  of the small volume  $\omega(x)$  surrounding  $x$  we have either water or microbial species present, thus it makes sense to define the volume occupied by the water  $\omega_w$  and by the microbes  $\omega_b$ , with  $\omega = \omega_w \cup \omega_b$ . Now we set the volume fractions of water and microbes as

$$\theta_w = \frac{|\omega_w|}{|\omega|}, \theta_b = \frac{|\omega_b|}{|\omega|}, \text{ with } \theta_w + \theta_b = 1.$$

The microbial mass density  $\rho_B\theta_b(x,t)$  vary in time and space. In some literature  $\theta_w$  is fixed; e.g., see  $\theta_w \approx 0.9$  [71], and thus expresses the ‘‘porosity’’ of biofilm. Since the cell have finite volume, there is a maximum density of cells allowed, e.g., it is given in [39] as  $\rho_B^* = 24 \times 10^3$  [g/cm<sup>3</sup>]. As in [39], we set

$$B = \theta_b \frac{\rho_B}{\rho_B^*}, \tag{6.2}$$

which are non-dimensional and is bounded above by the maximum  $B^*$ , that is

$$B \leq B^* = 1. \tag{6.3}$$

### 6.2.3 Notation for nutrient and reactions

We consider nutrient concentration  $N$ . We follow [39] where  $N$  is nondimensional with its unit involving the mass density of nutrient per  $\rho_B^*$ . We recall the well known Monod functions with the nutrient consumption  $m(N)$  given by the Monod expression

$$m(N) = \kappa \frac{N}{N + k_N}. \tag{6.4}$$

The constant  $k_N$  is called Monod half-life (in the same units as  $N$ ), and  $\kappa$  is the specific substrate uptake rate with a typical value =  $O([1/h])$ . The reaction rates used in mass balance equations for biomass and nutrient involve the growth and utilization rates

$$r_B^{growth}(B, N) = \kappa_B B m(N) = \kappa_B B \kappa \frac{N}{N + k_N}, \tag{6.5a}$$

$$r_N^{use}(B, N) = -Bm(N) = -B\kappa \frac{N}{N + k_N}, \quad (6.5b)$$

with typical values  $\kappa_B \approx 0.5$ , typically incorporating some yield coefficient and maximum uptake rate.

### 6.3 Constrained transport model

We now describe the constrained biomass-nutrient (BN) model presented in [131] which is an improved PVI model from [114] with singular diffusivity for biomass:

$$\partial_t B + \nabla \cdot (uB) - \nabla \cdot (d_B \nabla B) + \partial I_{(-\infty, B^*]}(B) = r_B^{growth}(B, N); \quad x \in \Omega_n, t > 0, \quad (6.6a)$$

$$\partial_t N + \nabla \cdot (uN) - \nabla \cdot (d_N \nabla N) = r_N^{use}(B, N); \quad x \in \Omega_n, t > 0, \quad (6.6b)$$

where  $u$  is advection flow velocity which we define later in Ch. 7,  $d_B$  and  $d_N$  and diffusion coefficients for biomass and nutrient, and  $\partial I_{(-\infty, B^*]}$  is the constraint operator. We explain these terms below.

For the biomass diffusivity  $d_B$ , we use the modified version of the singular diffusion model used in [33, 34, 39]. The singular character of the diffusivity model keeps the biofilm phase together as an aggregate but also allows it to spread as  $B \rightarrow B^*$ . The singular diffusion model in [33, 34, 39] is defined as

$$d_B(\alpha, \beta; B) = d_{B,0} \frac{B^\alpha}{(B^* - B)^\beta}$$

with the mobility coefficient  $d_{B,0}$ .  $d_B$  is singular as  $B \uparrow B^*$  and degenerate  $d_b \downarrow 0$  as  $B \downarrow 0$ .

**Diffusivity.** While the singular diffusivity achieves its modeling goals, it is also hard to deal with numerically as indicated in [33, 34] and confirmed by our own experiments not shown here. We modify this model in [131] by replacing  $B^*$  with  $\overline{B}^* > B^*$  to avoid the singularity at  $B^*$ . We also a single parameter  $\alpha = \beta$  since this is the choice in [33, 34, 39].

The modified  $d_B$  that we use here is

$$d_B(\alpha; B) = d_{B,0} \left( \frac{B}{\overline{B}^* - B} \right)^\alpha. \quad (6.6c)$$

Here the motility coefficient  $d_{B,0} \approx 7 \times 10^{-9}$  [m<sup>2</sup>/day], which is very small; about  $10^{-5}$  smaller than the molecular diffusivity  $d_m \approx 2 \times 10^{-4}$  [m<sup>2</sup>/day]. See Fig. 6.3 for comparison between two singular diffusion models.

Next we discuss  $d_N$  for which the experimental literature indicates a much decreased value in the very viscous  $\Omega_b$ . Following [39, 118, 163], we define  $d_{N,w}$  as the diffusivity of

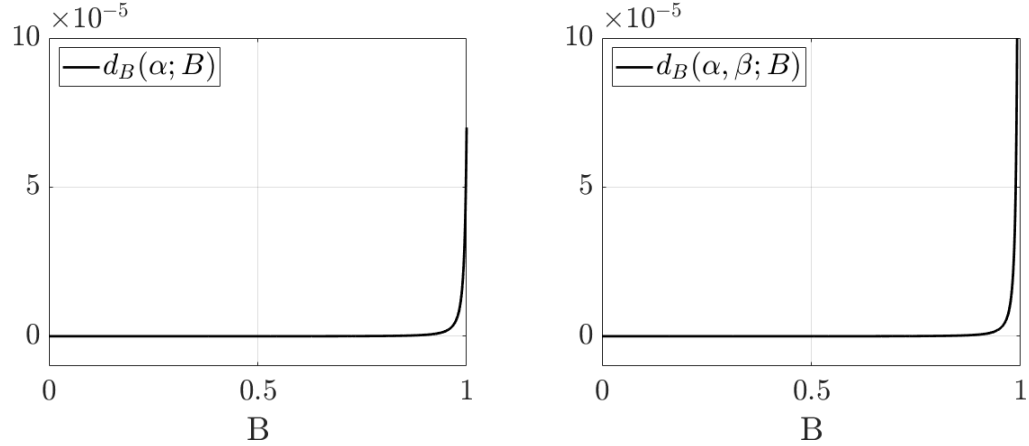


Figure 6.3: Plots of singular diffusivity  $d_B$ . Left:  $d_B(\alpha; B)$  from [131] with  $\alpha = 2$ . Right:  $d_B(\alpha, \beta; B)$  from [33] with  $\alpha = \beta = 2$ .

$N$  in  $\Omega_n \setminus \Omega_b^*$ ,  $d_{N,b}$  to be its decreased value in  $\Omega_b^*$ , and  $R_{N,bw} = d_{N,b}/d_{N,w}$ , with values  $R_{N,bw} \approx 0.4$  in [118], or even  $R_{N,bw} = 0.01$  for some nutrients [118, 163], with  $d_N$  given

$$\text{from [118]: } d_N(x, t) = \mathbb{1}_{\Omega_w}(x)d_{N,w} + \mathbb{1}_{\Omega_b^*}(x)d_{N,b}, \quad (6.6\text{da})$$

$$\text{from [39]: } d_N(x, t) = (B^* - B(x, t))d_{N,w} + B(x, t)d_{N,b}. \quad (6.6\text{db})$$

**Constraint operator.** We also recall that the constraint operator  $\partial I_{(-\infty, B^*]}$  is the subgradient of the indicator function  $I_{(-\infty, B^*]}$ , i.e.,

$$\partial I_{(-\infty, B^*]}(B) = \begin{cases} 0, & B \leq B^*, \\ [0, \infty), & B = B^*, \end{cases}$$

which enforces (6.3). It is a multivalued operator such as those discussed in Ch. 2. In practice, in the computational model,  $\partial I_{(-\infty, B^*]}(B)$  is replaced by a Lagrange multiplier  $\Lambda$  so that the constraint is enforced pointwise with

$$\max\{B^* - B, \Lambda\} = 0.$$

This is a well-known and well-studied construction known as parabolic variational inequality [7, 43, 134], and we refer, e.g., to [58] for its numerical analysis and to [1, 2] for its use in the context of biofilm models.

**Initial and boundary conditions.** We complete the model with initial and boundary conditions as follows. We set Neumann no-flux conditions on  $\Gamma$  for  $B$  and  $N$ . For some cases we also allow a Dirichlet boundary  $\Gamma_D \subset \Gamma$  through which nutrient can be supplied.

$$d_B \nabla B_k \cdot \mathbf{n}|_{\Gamma} = 0, \quad (6.6\text{e})$$

$$B(x, 0) = B_{init}(x), \quad x \in \Omega, \quad (6.6f)$$

$$N|_{\Gamma_D} = N_D, \quad (6.6g)$$

$$d_N \nabla N \cdot \mathbf{n}|_{\Gamma \setminus \Gamma_D} = 0, \quad (6.6h)$$

$$N(x, 0) = N_{init}(x), \quad x \in \Omega. \quad (6.6i)$$

The initial data is denoted by subscript *init* and the Dirichlet boundary data with subscript *D*. In general, we may allow non-smooth data, thus (6.6) is posed in the sense of distributions rather than in the classical sense.

Finally, we make this observation regarding the use of the constraint operator.

**Remark 6.3.1.** *The interpretation of the action of  $\partial I_{(-\infty, B^*]}(B)$  in (6.6a) is similar but not identical to the a-priori truncation of the source term such as in the model*

$$\partial_t B - \nabla \cdot (d_B(B) \nabla B) = r_B^{growth}(B, N) \mathbb{1}_{\{B \leq B^*\}}(B), \quad x \in \Omega_n. \quad (6.5)$$

*In this equation the source  $r_B^{growth} \mathbb{1}_{\{B \leq B^*\}}(B)$  prevents the growth above  $B^*$ , and is discontinuous in  $B$ . In contrast, in (6.6a) the operator  $\partial I_{(-\infty, B^*]}(B)$  acts to ensure  $B \leq B^*$  for all  $x$ . This is a subtle but important difference. In particular, an implicit solver for (6.5) generally struggles with the discontinuous character of the forcing, thereby requiring additional care. In contrast, our approach (6.6a) is quite robust.*

We also note the following.

**Remark 6.3.2.** *It is well known that biofilm formation is initiated by the adhesion of microbes to some wet surfaces. However, our model is not equipped with the surface adhesion mechanism, thus we must situate the initial biomass near the rock surfaces.*

This modeling problem is discussed in Ch. 8.

## 6.4 Numerical approximation

In this section we present the approximation of the coupled BN model (6.6) for  $d = 2$  that we applied in [131]. We generally follow the established notation, e.g., from [75], which we also briefly described in Sec. 2.5. We recall the notation and the convergence tests reported in [131].

### 6.4.1 Spatial discretization

We recall the uniform grid  $V = \cup_{i=1}^M V_i$  with size  $h$  covering  $\Omega \subset \mathbb{R}^2$ . Let  $(B_i, N_i)$  be biomass and nutrient densities defined at the center of  $V_i$  for  $i = 1, 2, \dots, M$ . The collections of  $(B_i)_i$  and  $(N_i)_i$  are denoted by  $B_h$  and  $N_h$ , respectively. Similarly, we define the Lagrange multiplier  $\lambda_h = (\lambda_i)_i$ .

### 6.4.2 Time discretization

We use time steps

$$0 = t^0 < t^1 < t^2 < \dots < t^N = T,$$

with uniform time step size  $\tau$  so that  $t^n = n\tau$ . For nonlinear terms we use time- or step- or iteration lagging. In other words, our methods can be called semi-implicit, with variants as indicated below.

We approximate the solution  $(B_h^n, N_h^n, \lambda_h^n)$  to (6.6) by operator splitting which we described in Sec. 2.5.6. We first solve the advection step explicitly with known previous time step data  $(B_h^{n-1}, N_h^{n-1}, \lambda_h^{n-1})$

$$\tilde{B}_h^n = B_h^{n-1} - \tau \nabla_h \cdot (u_h B_h^{n-1}), \quad (6.6a)$$

$$\tilde{N}_h^n = N_h^{n-1} - \tau \nabla_h \cdot (u_h N_h^{n-1}). \quad (6.6b)$$

Here  $\nabla_h \cdot (u_h B_h^{n-1})$  and  $\nabla_h \cdot (u_h N_h^{n-1})$  denote the explicit upwind fluxes which we discussed in Sec. 2.5.5.

Next we solve the reaction and diffusion steps together:

$$(I + \tau A_h^B(B_h^{n-1}))B_h^n + \tau \lambda_h^n = B_h^{n-1} + \tau r_B^{growth}(B_h^n, N_h^n), \quad (6.6c)$$

$$(I + \tau A_h^N(B_h^{n-1}))N_h^n = N_h^{n-1} + \tau r_N^{use}(B_h^n, N_h^n). \quad (6.6d)$$

The additional equation binding  $B_h^n$  and  $\lambda_h^n$  is

$$\min(B^* - B_j^n, \lambda_j^n) = 0, \quad \forall j. \quad (6.6e)$$

Another possibility is to solve the reaction step first separately with initial conditions  $(\tilde{B}_h^n, \tilde{N}_h^n)$  known after the advection step

$$\hat{B}_h^n = \tilde{B}_h^n + \tau r_B^{growth}(\tilde{B}_h^n, \tilde{N}_h^n),$$

$$\hat{N}_h^n = \tilde{N}_h^n + \tau r_N^{use}(\tilde{B}_h^n, \tilde{N}_h^n),$$

followed by the diffusion step with step-lagging of  $A_h^B, A_h^N$

$$\begin{aligned}(I + \tau A_h^B(\hat{B}_h^n))B_h^n &= \hat{B}_h^n, \\ (I + \tau A_h^N(\hat{B}_h^n))N_h^n &= \hat{N}_h^n.\end{aligned}$$

Other schemes and refinements are possible; see, e.g., [75, 113].

The diffusion-reaction step of (6.6) with CCFD can be written in the residual form and is solved using the semismooth Newton method which we described in Sec. 2.6. Due to the only piecewise-smooth character of (6.6e), the solver is expected to converge with a less than quadratic rate. However, with the typical time steps we use in our model, the solver can take usually under 3 iterations. Recall that CCFD is equivalent to the mixed finite element method in  $RT_0$  space, and we refer readers to [1, 2] for more on the finite element analysis with simulations testing different variants of mildly and fast growth  $d_B(B)$  other than (6.6c).

We do not use explicit non-dimensionalization of PDE models. Even though such a step provides useful insights and reduces dependence from the multitude of parameters to fewer, it is case dependent. Rather, our simulations for the rest of this dissertation are carried out with BN\_Flow codes [132] which use an internal self-consistent unit system.

As in every numerical model, it is important to check if it converges to the true solution. We recall the theory developed in [1, 2] for the Galerkin finite element discretization of the coupled biofilm-nutrient model similar to (6.6). We also recall some progress towards the mixed finite element or CCFD version of that model in [1]. While we do not have theoretical results for the full CCFD model presented above, we summarize the convergence test presented in [131].

### 6.4.3 Convergence of the CCFD scheme for biomass-nutrient model

Now we discuss convergence of the numerical scheme.

**Remark 6.4.1.** *In [1], the author discussed both theoretical and numerical convergence of the Galerkin finite element method of the BN model and showed that the order of convergence in  $\|\cdot\|_2$  is close to 1. Author also reported the numerical convergence of  $O(h^{3/2} + \tau^{3/2})$  in  $\|\cdot\|_{H^1(\Omega)}$ .*

Generally the CCFD schemes for linear parabolic problems with smooth solutions can

be shown to be second order accurate in  $h$  [155]. Our problem features nonlinearities, free boundaries, and advection terms treated by a first order upwind scheme.

**Remark 6.4.2.** *For the coupled flow and BN model, we use the first-order operator splitting method and the first-order upwind method for advection term. Thus the best rate of convergence that we can expect would be  $O(h + \tau)$ .*

Our BN model is nonlinear, and the physically meaningful analytical solutions are not available. It is well known that one can test the accuracy of a scheme using a predefined exact solution, and calculating the boundary conditions and the sources to fit the problem. This approach is also called the “method of manufactured solutions”. However, this approach is not easy to set-up for free boundary problems.

However, as discussed in [1], one can test the convergence of a scheme for parabolic variational inequality with a manufactured solution, but it is likely to be physically unrealistic because it would a-priori predict the moving boundary as biofilms grow through the interface.

Thus, in [131] we used the fine grid solutions with  $L = 1, h_{fine} = 2 \times 10^{-4}$  and  $\tau_{fine} = 2 \times 10^{-5}$  as a “proxy” for the true solution when testing convergence of the numerical results while varying  $\tau = O(h)$  for  $h \geq 2 \times 10^{-3}$  and  $\tau \geq 2 \times 10^{-4}$ . In [131](Sec. 8.3.1), we showed the convergence of the numerical models for the BN model (6.6) with  $u \equiv 0$ . We showed first-order convergence for both  $B$  and  $N$  in  $\|\cdot\|_1$  norm. In  $\|\cdot\|_2$  norm, the convergence is approximately order of 0.6 for  $B$  and 1 for  $N$ . This can be explained by smoothness of  $N$  and sharp gradients of  $B$ .

#### 6.4.4 Computational complexity of biomass-nutrient solver

In this section we provide estimates of overall computational cost to solve (6.6) for  $(B, N, \lambda)$ . The process involves a pre-processing step where we initialize the algorithm with some initial conditions and the main BN solver. We assume that there are  $M$  grid cells that include  $\Omega_r$ . However, since we consider the cells in  $\Omega_n$  only, we may have a lower computational cost.

The pre-processing step involves the initialization of algorithms with some initial and boundary conditions. This step costs  $O(M)$ .

The BN solver requires the solution of two coupled nonlinear PDEs for  $(B, N)$ , each of size  $M$ . Additionally, we keep track of and update the Lagrange multiplier  $\lambda$ , also of size

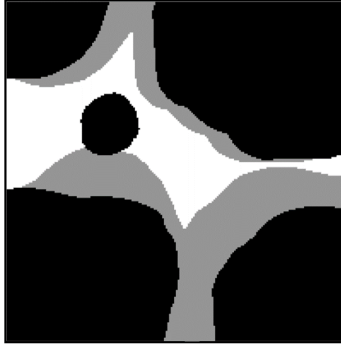


Figure 6.4: Illustration of realistic single-pore geometry  $\Omega$  with  $\Omega_r$  in black,  $\Omega_b$  in gray, and  $\Omega_0$  in white.

$M$ . In other words, we have  $3M$  unknowns:  $(B, N, \lambda)$ . The evolution takes over 100 to 1000 time-steps, depending on the case, and each requires on average about two iterations of the semi-implicit method. For each iteration, we require about  $100M$  operations to compute diffusion coefficients, Jacobian, residuals, and other operations. The cost of linear system solver for  $3M$  unknowns is  $O((3M)^3)$  at worst if we use some direct methods such as LU or QR in MATLAB. In our 2d case we work with a non-symmetric banded linear system which costs  $O(3pM)$  where  $p = 4M + 1$  is the band size. Then the total cost to solve for  $(B, N, \lambda)$  per time-step is  $O(12M^2 + 104M)$ . When we simulate until clogging, the total cost per simulation can go up to  $O(10^4 M^2)$ .

Generally, we expect  $M = O(10^4)$  for 2d simulations and  $M = O(10^6)$  in 3d. We find that generation of 2d biofilm domain using BN solver is feasible while 3d results may be unfeasible.

## 6.5 Biofilm growth in the nutrient-rich system

Now we are ready to illustrate the BN model with simulation. The example shown below corresponds to [131](Example. 3.5).

We aim to demonstrate the growth of biofilm using our constrained BN model (6.6) with  $u \equiv 0$  to study the dependence of biofilm growth to length scales. These simulations show that it is crucial to use realistic coefficients, geometry, and time and length scales.

**Example 6.5.1** (Biofilm growth pattern in a nutrient-rich porous medium). *Let  $\Omega$  be a realistic single-pore geometry that is shown in Fig. 6.4. We simulate the biofilm growth in nutrient-rich pore of  $\Omega = (0, L)^2$  [mm<sup>2</sup>] for  $L = \{0.01, 0.1, 1\}$  with other parameters as below with  $d_m = O(1$  [mm<sup>2</sup>/h]) until  $\Omega_n$  is filled up.*

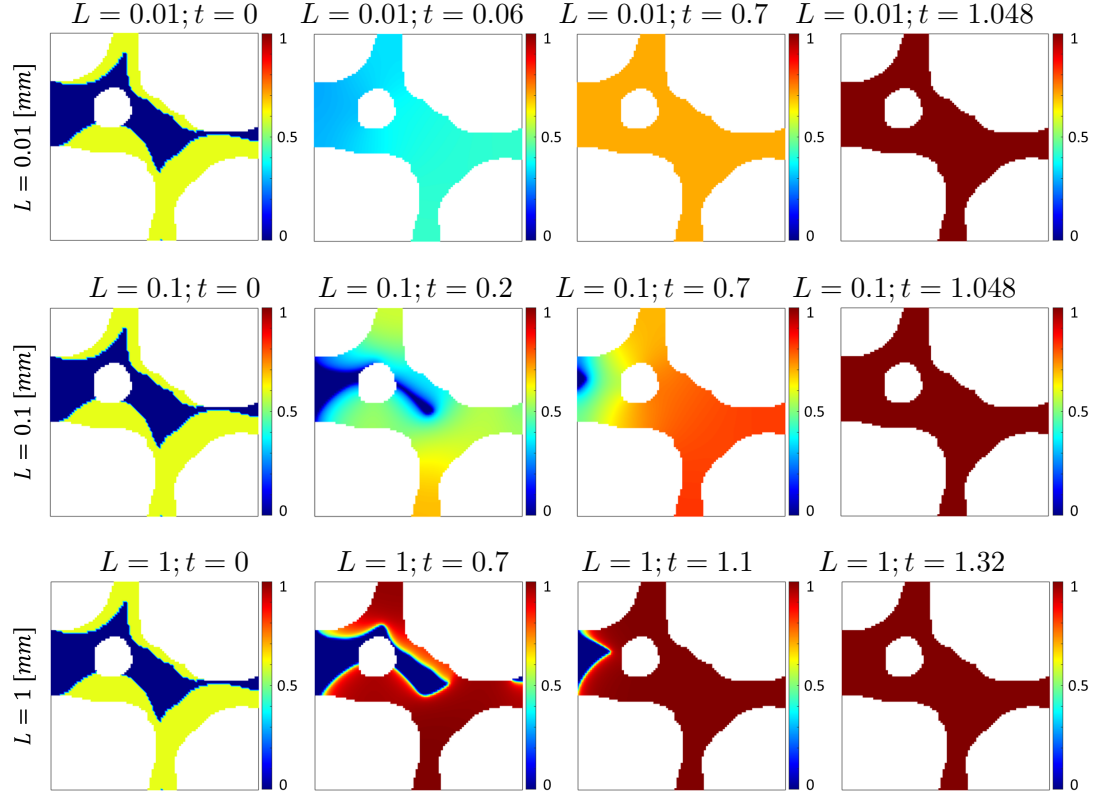


Figure 6.5: Pore–plugging with biofilm in a nutrient–rich environment for Ex. 6.5.1 using the nonsingular constrained model (6.6) at the selected time  $t$  [h] as shown. Images on the rightmost column are at the final time shown when the pore is plugged up. (Top) micro-pore  $L = 0.01$ , (middle) meso-pore  $L = 0.1$ , and (bottom) macro-pore  $L = 1$ , in [mm], as labelled on the leftmost panel. We see that in the micro-pore the biomass spreads first and then grows, while the opposite is seen in the macro-pore case, with the meso-pore being intermediate.

$B^*$	$B_*$	$B_{init}$	$N_{init} = N_D$	$d_{B,0}$	$d_{N,w}$	$R_{N,bw}$	$\kappa$	$\alpha$
1	$0.9B^*$	$0.6B^* \mathbb{1}_{\Omega_b(0)}$	100	$10^{-4}d_m$	$d_m$	0.1	2	2

The evolution of biofilm growth in  $\Omega$  of three different sizes  $L = \{0.01, 0.1, 1\}$  [mm] are shown in Fig. 6.5. As we can see in the left-most columns, we start with initial biomass  $B_0 = 0.6B^*$  occupying the qualitatively same  $\Omega_b(0)$ . As expected, the relatively large diffusivity in micro-pores ( $L = 0.01$  [mm]) compare to in meso- or macro-pores ( $L = 0.1$  [mm] or  $L = 1$  [mm], respectively) results micro-pores to be filled up faster than the other pores. Qualitatively, the pattern of formation is independent of the length  $L$  and the time  $t$ .

## 7 Monolithic multiphysics model for coupling biomass-nutrient model with pore scale flow

We now discuss the pore scale flow model in complex geometry with (partially) permeable biofilm phase and monolithic coupling of flow model to the constrained non-singular biomass-nutrient (BN) model (6.6). These correspond to the material presented in [131](Sec. 5).

**Challenges addressed.** It has been postulated that biofilm domain  $\Omega_b$  might be partially permeable to the fluid flow; thus also allowing advective transport of nutrient, and contributing to more substantial growth of biomass. We refer, e.g., to [71, 114] who used approaches other than the one we propose. In particular, the flow models in [71] are posed separately in  $\Omega_b$  and  $\Omega_n \setminus \Omega_b$  which creates difficulties of re-meshing or requires additional simplifications and assumptions to succeed. Our interest is in employing a flow model which would work well across different flow conditions in pores filled partially with biofilm and having variable permeability. In particular, the flow model should work for an essentially stationary flow at low Reynolds numbers as well as in complicated pore scale geometries with biofilm such as that in Fig. 7.1 across the different length scales. This interest is motivated by a plethora of work on partially permeable biofilm including in [22, 70, 144]. When biofilm in  $\Omega_b$  is close to impermeable, the flow goes primarily around the domain  $\Omega_b$ . When it is moderately permeable, some of the flow goes through  $\Omega_b$ . When its permeability is very high, the flow through  $\Omega_b$  is similar to the Stokes flow outside  $\Omega_b$ .

**Our approach.** Our main idea is to consider the particular version called heterogeneous Brinkman flow with a spatially variable permeability depending on the biomass amount, which allows (some) flow through the pores filled with somewhat permeable biofilm. This version was originally tested in [21] for the needs of a flow model with randomly dispersed obstacles.

We start by describing the heterogeneous Brinkman flow and its numerical method in Sec. 7.1. Then we study the dependence of the heterogeneous flow model to the length scale and the permeability of biofilm from examples in Sec. 7.2. Finally we discuss the coupling of the flow model and the BN model and study the coupled effects with examples in Sec. 7.3.

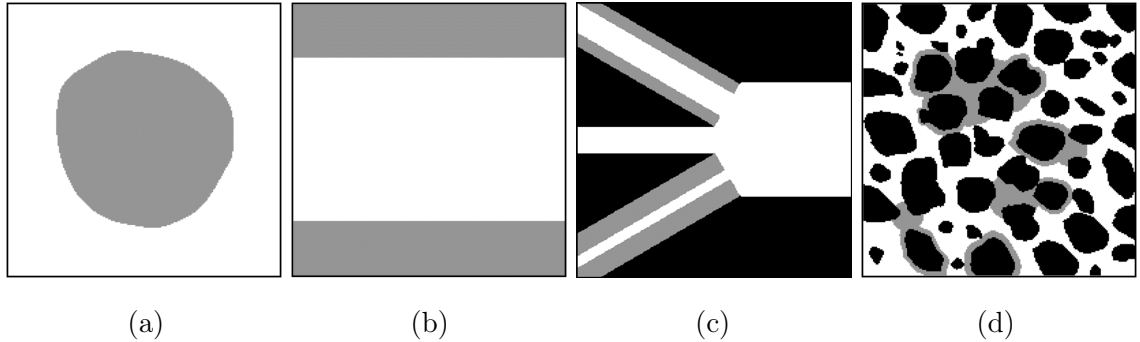


Figure 7.1: Illustration of pore scale geometries  $\Omega$  considered in this chapter. Cartoons of (a) channel with a bio-gel, (b) channel with biofilm at the walls, (c) converging channels as in [22], and (d) many-pore geometry. In all figures,  $\Omega_r$  is in black,  $\Omega_b$  is in gray, and  $\Omega_0$  is in white.

Symbol	Description	Value/Units
$\mu$	Viscosity	$8.9 \times 10^{-4}$ [Pa s]
$u$	Velocity in the Brinkman flow model	$\sim O(10^{-1})$ [mm/h]
$p$	Pressure in the Brinkman flow model	[Pa]
$k_b$	Resistance term in Brinkman flow model	[mm <sup>2</sup> ]
$K_\Omega$	Darcy permeability	$\sim O(10^{-7})$ [mm <sup>2</sup> ]

Table 7.1: Notations for flow and upscaled permeability with typical values adapted from [114].

## 7.1 Heterogeneous Brinkman flow model at pore scale

Brinkman model augments the well known Stokes model with the Darcy resistance term [13, 46]. We present its heterogeneous version

$$-\mu\Delta u + \mu k_{bx}^{-1}(x)u + \nabla p = f, x \in \Omega_n, \quad (7.1a)$$

$$\nabla \cdot u = 0, x \in \Omega_n, \quad (7.1b)$$

where  $u$  is the velocity,  $p$  is the pressure, and the resistance term  $\sim k_{bx}^{-1}$  related to the inverse of permeability is locally defined and  $k_{bx}(x) = k_b \mathbb{1}_{\Omega_b^*}(x)$ . We also include notation with values and unit in Tab. 7.1 for convenience. Of interest are the extreme cases when  $k_b \downarrow 0$ , i.e., the obstacle region  $\Omega_b$  is impermeable, and when  $k_b \uparrow \infty$  and the flow in the entire  $\Omega_n$  is essentially of Stokes type. We note that this means that  $k_{bx}$  implicitly depends on  $B(x, t)$ . The model (7.1) is stationary but with time-dependent data. One can expand this dependence to make it vary with  $B$  or with the amount of EPS, which would make  $k_{bx}$  vary smoothly with  $x$ , but we have not done this. This heterogeneous Brinkman flow is the stochastic immersed boundary Stokes model that was presented in [21] if we choose the penalization parameter  $\eta = \frac{k_{bx}(x)}{\mu}$ . Authors of [21] showed that the flow profiles between two parallel plates becomes similar to the Hagen-Poiseuille flow as  $\eta \rightarrow \infty$  and the flow rate decreases at  $O(\eta^{0.5})$ . We refer readers to [21] for the stability analysis.

We complete (7.1) with appropriate boundary conditions. Here we impose the no-slip condition on  $\Gamma_{rn}$  as well as the Dirichlet condition on the inflow  $\Gamma_{in}$ , and natural outflow conditions on  $\Gamma_{out}$ , both portions of  $\partial\Omega_n$ , respectively

$$u|_{\Gamma_{rn}} = 0, \quad u|_{\Gamma_{in}} = u_D(x), \quad \text{and} \quad \mu\nabla u \cdot \mathbf{n} - p\mathbf{n} = 0 \text{ on } \Gamma_{out}. \quad (7.1c)$$

In the examples we also use  $\bar{u}_D$  to denote the average of  $u_D(x)$  over  $\Gamma_{in}$ , and we usually set up a parabolic inflow profile on  $\Gamma_{in}$ .

We acknowledge here the important analyses of the influence of shear stress between the Stokes and Darcy domain discussed, e.g., in [30, 91, 97, 98]; these relate to the Beavers-Joseph-Saffman interface condition imposed at fixed interfaces such as soil-surface water interface. Instead, in our heterogeneous Brinkman flow (7.1) we allow the permeability  $k_{bx}$  to vary, and in which  $k_{bx}^{-1} \downarrow 0$  when  $B \downarrow 0$ , such as close to the interface  $\partial\Omega_b$ . This is important because the “interface” between  $\Omega_b$  and the “bulk fluid” may not be very well defined, and at the length scales involved we believe it is not critical to resolve the fine details of the fluid flow normal to that interface, see, e.g., the comments in [71]. In the end,

the heterogeneous Brinkman model we use in this paper improves on the use of Stokes flow outside  $\Omega_b^*$  with the no-slip condition as in [114], and we defer a more detailed study to future work.

### 7.1.1 MAC method for heterogeneous Brinkman flow

In this section we describe the numerical method for the heterogeneous Brinkman flow model (7.1). We first recall the MAC method for Stokes model (2.14) from Sec. 2.24. We can derive the MAC method for (7.1) by adding the diagonal entries of Darcy resistance term  $\sim k_{bx}^{-1}$  to the matrix in (2.24). This first require us to evaluate  $K_\Omega$  at the interior cell edges, i.e.,  $(E_{i,\alpha})_i \setminus \Gamma$ .

Recall the notation from Sec. 2.5 for uniform rectangular grid covering  $\Omega$ . The harmonic averaged values of  $K_\Omega$  at cell edges  $E_{i,\alpha}$  of the cell  $V_i$  are denoted by  $K|_{E_{i,\alpha}}$ . We write the collection of  $K|_{i,\alpha}$  for all  $i = 1, 2, \dots, M$  as  $K_u$  for  $\alpha = w, e$  and  $K_v$  for  $\alpha = s, n$ . Then the Darcy resistance term  $\mu k_{bx}^{-1}u$  and  $\mu k_{bx}^{-1}v$  are approximated by  $\mu K_u^{-1}$  and  $\mu K_v^{-1}$ . The MAC method for (7.1) is

$$\begin{bmatrix} \mu(A_u + K_u^{-1}I_u) & & B_u^T \\ & \mu(A_v + K_v^{-1}I_v) & B_v^T \\ B_u & & B_v \end{bmatrix} \begin{bmatrix} U \\ V \\ P \end{bmatrix} = F, \quad (7.2)$$

with identity matrices  $I_u, I_v = I_{M(M+1)}$ .

### 7.1.2 Computational complexity for the flow solver and upscaling

Now we discuss the computational complexity to solve (7.1) for  $(U, V, P)$  using the MAC scheme that we described above. Here we also give the computational cost to calculate the upscaled permeability.

Recall that we discretize  $\Omega$  into  $M = M_x \times M_y$  grid cells. Again, the actual degrees of freedom would be less than  $M$  since we only solve for  $M|\Omega_n|/|\Omega|$ . Since  $P$  is defined at the cell centers, there are  $M$  degrees of freedom. The velocity components  $U$  and  $V$  are defined at the cell edges, so they have  $(M_x + 1)M_y$  and  $M_x(M_y + 1)$  degrees of freedom. If  $M_x = M_y$ , then the total degrees of freedom for  $(U, V, P)$  is  $3M + 2\sqrt{M}$ .

For the flow we first write the block  $2 \times 2$  linear system. This involves calculating permeability at the cell edges and other operations which cost about  $10(M + \sqrt{M})$ . Next we solve this saddle point problem using the banded QR in MATLAB. The band size  $p = 4(M + \sqrt{M}) + 1$ , and the cost of banded QR in MATLAB is  $O(12M^2 + 20M^{3/2} + 11M + 2\sqrt{M})$ .

We calculate the scalar permeability by the volume averaging method which we described in Sec. 2.4. The cost of this upscaling step is about  $5M$ .

The total cost of flow solver and upscaling is about  $O(12M^2)$ .

## 7.2 Illustration of heterogeneous Brinkman flow and upscaling

The following examples are designed to study the robustness of heterogeneous Brinkman flow (7.1).

As we know (7.1) depends on the Darcy resistance term which includes permeability of biofilm  $k_{bx}$ .  $k_{bx}$  can be obtained experimentally. However, the reported values in literature vary. In [70, 71],  $k_b = 10^{-9}$  or  $k_b = 10^{-10}$  [m<sup>2</sup>] were used and [28] consider  $k_b \in [10^{-15}, 5 \times 10^{-9}]$  [m<sup>2</sup>]. Thus, we observe the impact of  $k_{bx}$  on the flow patterns. Since our model is equipped with the spatially varying  $k_{bx}(x)$ , we also consider the flow at different length scales. We demonstrate the relationship between  $k_{bx}$  and the upscaled permeability  $K_\Omega$  as well.

In this section we consider three examples of flow through 1) a channel with bio-gel Fig. 7.1(a), 2) a channel with biofilm at the walls Fig. 7.1(b), and 3) converging channels Fig. 7.1(c).

**Example 7.2.1.** *Consider  $\Omega = (0, L)^2$  [mm<sup>2</sup>] with bio-gel in the center as in Fig. 7.1(a) with varying  $k_b$ . The fluid flows from left to right, with the average of the parabolic inflow values  $\bar{u}_D = 36$  [mm/hr]. After  $(u, p)$  is found, we compute  $K_\Omega$  of  $\Omega$  by the volume averaging method [109] which is also described in Sec. 2.4. We vary  $L$  and  $k_b$  while fixing other parameters; see Tab. 7.2 for values of  $L$  and  $k_b$  used.*

The flow results of Ex. 7.2.1 are shown in Fig. 7.2 and Tab. 7.2. The transition of the flow from inside to the outside of  $\Omega_b^*$  over a large range of choices of  $L, k_b$  is smooth which suggests that the model (7.1) and our implementation are robust, but more analysis is needed (underway).

Furthermore, the flow depends significantly on  $L$  and  $k_b$ , as expected; see, e.g., the plots of  $|u(L/2, y)|$  in Fig. 7.2. In a small pore with  $L = 0.01$  [mm], the flow streamlines and velocity magnitude appear as if there was no biofilm, but for larger pores the flow is directed partially outside the biofilm, and with  $L = 1$  [mm] the flow behaves as if the biofilm was impermeable. In Tab. 7.2 for intermediate  $L = 0.1$  [mm] we see that as  $k_b$  increases, the resulting  $K_\Omega \rightarrow k_b$ , but the effect for the large pore is less significant for the  $k_b$  we used.

	Data		Results	
	$L$ [mm]	$k_b$ [mm <sup>2</sup> ]	$K_\Omega$ [mm <sup>2</sup> ]	$\   u  \ _\infty$ [mm/hr]
(a)	0.01	0	$1.75 \times 10^{-7}$	$1.58 \times 10^2$
(b)	0.01	$10^{-5}$	$7.8 \times 10^{-6}$	$3.42 \times 10^{-1}$
(c)	0.01	$10^{-4}$	$5 \times 10^{-6}$	$3.37 \times 10^{-1}$
(e)	0.1	0	$1.75 \times 10^{-5}$	$1.58 \times 10^2$
(f)	0.1	$10^{-5}$	$3.17 \times 10^{-5}$	$5.87 \times 10^{-1}$
(g)	0.1	$10^{-4}$	$1.28 \times 10^{-4}$	$3.08 \times 10^{-1}$
(i)	1	0	$1.75 \times 10^{-3}$	$1.58 \times 10^2$
(j)	1	$10^{-5}$	$1.69 \times 10^{-3}$	$9.84 \times 10^{-1}$
(k)	1	$10^{-4}$	$1.45 \times 10^{-3}$	$8.94 \times 10^{-1}$

Table 7.2: Data and results for Ex. 7.2.1. (a – c) micro-pore, (e–g) meso-pore, (i–k) macro-pore.

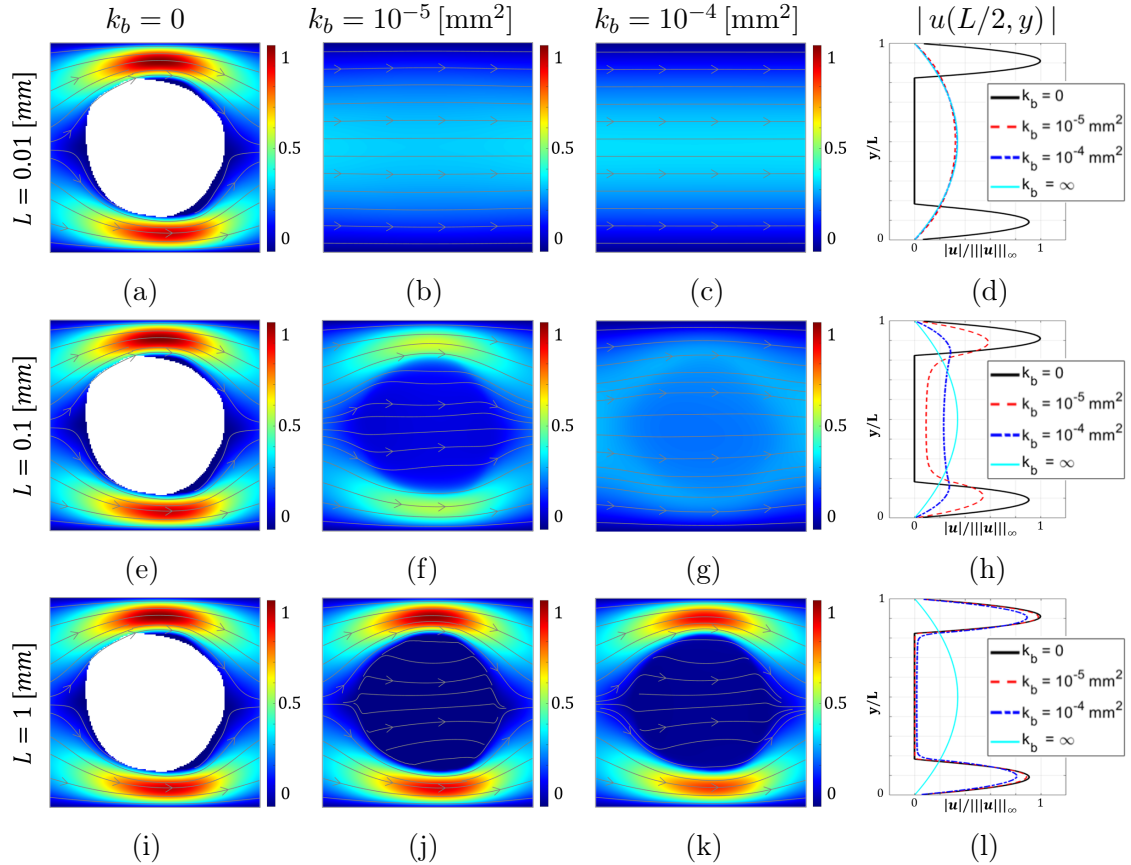


Figure 7.2: Illustration of velocity profiles for Ex. 7.2.1 for  $L \in \{0.01, 0.1, 1\}$  and  $k_b \in \{0, 10^{-5}, 10^{-4}, \infty\}$ : (Top)  $L = 0.01$ . (Middle)  $L = 0.1$ . (Bottom)  $L = 1$ . See Tab. 7.2 for data. Figures (d), (h), and (l) show the velocity profiles at the center of biofilm obstacle  $|u(L/2, y)|$ .

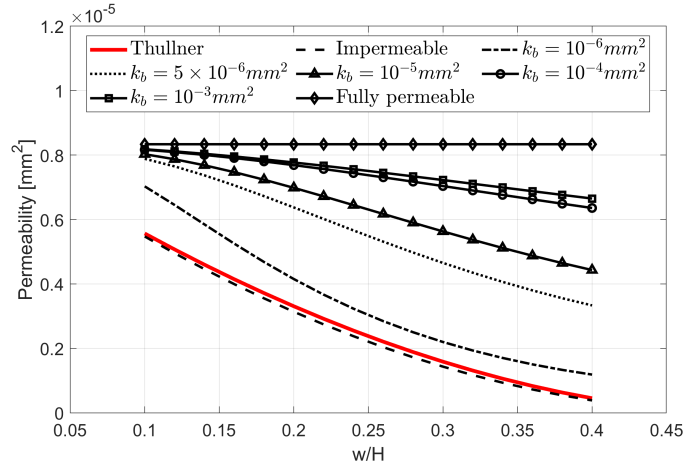


Figure 7.3: Permeability  $K_{\Omega} = K_{\Omega}(k_b; w/H)$  from Ex. 7.2.2 depending on the width  $w$  of biofilm layer relative to the channel width  $H$  and on the biofilm phase permeability. For reference we present the match with Thullner’s model from [145], with Thullner parameter  $b = 1.81$ .

Another class of approaches directs their focus on the thickness of biofilm as an independent variable rather than on  $B$  itself; this is essentially a “model reduction” which we illustrate now.

**Example 7.2.2.** Consider flow in a channel  $\Omega = (0, 1.5) \times (0, 0.1)$  [mm<sup>2</sup>] with biofilm growing next to the walls; see Fig. 7.1(b). This study for  $k_b = 0$  and  $k_b \uparrow \infty$  can be reduced to the Poiseuille flow example [109]. When  $k_b > 0$  there is additional flow through the biofilm layer, and we compare the variation of Darcy permeability  $K_{\Omega}$  with different  $k_b \in \{0, 10^{-6}, 5 \times 10^{-6}, 10^{-5}, 10^{-4}, 10^{-3}, \infty\}$  [mm<sup>2</sup>], where  $w$  represents the assumed width of one side of biofilm in this channel of height  $H = 0.1$  [mm].

Fig. 7.3 shows that, as expected,  $K_{\Omega}$  decreases with  $w/H \uparrow$  for all  $k_b < \infty$ . As  $k_b \uparrow$ , the biofilm presence affects the flow less, as expected. Our result for the impermeable case aligns well with Thullner’s permeability–porosity correlation model [145].

Furthermore, motivated by recent work in [22] we illustrate flow pattern through converging channels filled with biofilms of different widths.

**Example 7.2.3.** We consider flow from left to right through three channels that converge together as illustrated in Fig. 7.1(e), with  $\Omega$  embedded in  $(-L, 2L) \times (0, L)$  [mm<sup>2</sup>]. The width of two diagonal channels are  $0.18L$ , the middle channel is  $0.09L$ , and the merged channel is  $0.404L$  thick. Two diagonal channels are filled with biofilm next to the walls of different widths,  $0.045L$  and  $0.043L$  for top and bottom channels, respectively; see Fig. 7.1(e). We use  $L = 1$ ,  $\bar{u}_D = 3.6$  [mm/hr], and solve for flow without obstacles, i.e.,  $k_b = \infty$ . Then we

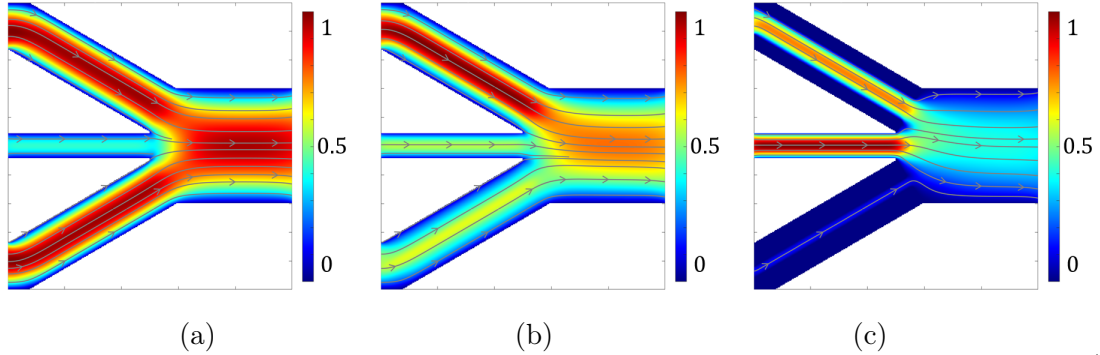


Figure 7.4: Flow through channels filled with biofilm of different width for Ex. 7.2.3 for (a)  $k_b = \infty$ , (b)  $k_b = 10^{-3} [\text{mm}^2]$ , and (c)  $k_b = 0$ . The width of the middle channel is about half of that for other channels.

$k_b [\text{mm}^2]$	$\infty$	$10^{-3}$	0
$K_\Omega [\text{mm}^2]$	$2.6386 \times 10^{-3}$	$1.4765 \times 10^{-3}$	$8.6665 \times 10^{-4}$
$\ u\ _\infty [\text{mm/hr}]$	13.82	17.26	32.98

Table 7.3: Results for converging channels in Ex. 7.2.3: permeability  $K_\Omega$  and maximum flow rate  $\|u\|_\infty$  depending on  $k_b$ .

compare calculated  $K_\Omega$  to the cases with biofilm of  $k_b = 0$  or  $k_b = 10^{-3} [\text{mm}^2]$ .

Results for Ex. 7.2.3 are shown in Fig. 7.4 and Tab. 7.3. Fig. 7.4(a) with  $k_b = \infty$  illustrates symmetric flow behavior with highest flow rate through the wider channels. When a partially permeable biofilm of different widths is present, we lose the symmetric behavior. Since 83% of the lower diagonal channel is filled with biofilm while only 50% of the upper diagonal channel is filled, we see more flow goes through the upper channel than the lower one. Also, the upper diagonal channel permits more flow than the middle channel due to the difference in channel widths. With  $k_b = 0$ , the width of upper diagonal and middle channels are the same  $0.045L$ , but we see higher flow traffic in the middle than upper diagonal channel because we set the parabolic inflow condition  $\bar{u}_D(-L, y)$ . We also confirm that  $K_\Omega \downarrow$  as  $k_b \downarrow$ .

Our flow solver is also implemented so it can solve 3d problems. In following example we extend 2d example from Ex. 7.2.1 to 3d.

**Example 7.2.4.** Let  $\Omega = (-0.5, 0.5)^3 [\text{mm}^3]$  with a rock of radius  $0.125 [\text{mm}]$  in the middle. We also have some biofilms evenly covering the rock. The radius of both biofilm and rock is  $0.25 [\text{mm}]$ ; see Fig. 7.5(a) for a sketch of this  $\Omega$ . Let the average inflow velocity  $\bar{u}_D = 36 [\text{mm/h}]$ . We simulate the flow from bottom to top around impermeable region while

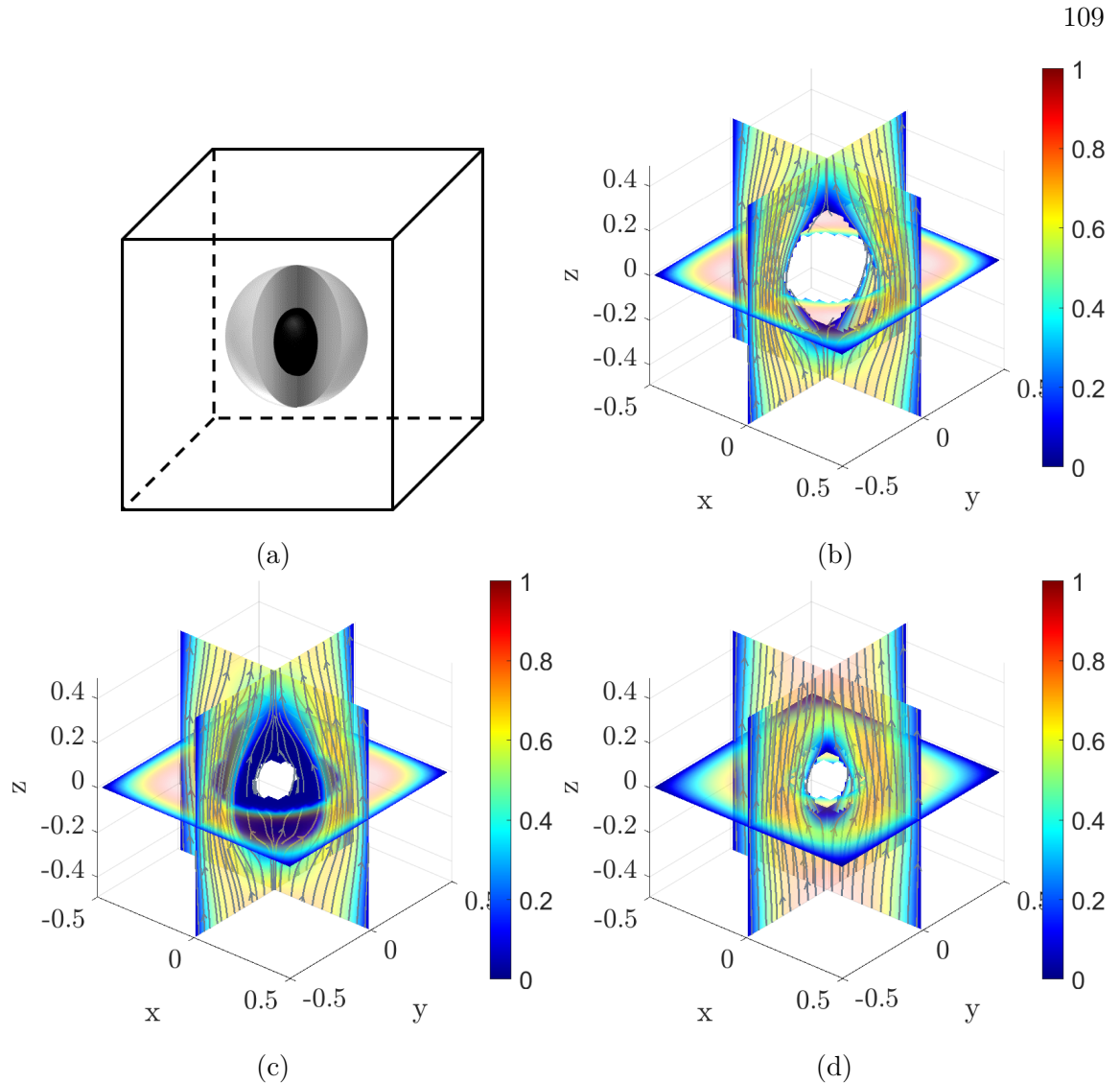


Figure 7.5: For Ex. 7.2.4, (a) a sketch of  $\Omega$  with rock in the middle (black) and surrounding biofilm (gray), and slices of velocity profiles with the permeability of biofilm: (b)  $k_b = 0$ , (c)  $k_b = 10^{-4} [\text{mm}^2]$ , and (d)  $k_b = \infty$ .

the permeability of biofilm varies  $k_b \in \{0, 10^{-4}, \infty\} [\text{mm}^2]$ . We also calculate the upscaled permeabilities  $K_\Omega$ .

For Ex. 7.2.4, we want to work with fully developed inflow conditions to avoid boundary effects. One can use the analytical solution to Hagen-Poiseuille flow in a rectangular duct [159](Sec. 3.3.3). Alternatively, one can superimpose  $\Omega$  in a larger domain which supplies the flow entrance region. Here we embed  $\Omega$  in a region with a long enough entrance length along with the parabolic inflow condition satisfying the no-slip boundary condition:

$$u_0(x, y) = -36\bar{u}_D(x + 0.5)(x - 0.5)(y + 0.5)(y - 0.5).$$

The results of Ex. 7.2.4 are shown in Fig. 7.5 and they are 3d cases of Ex. 7.2.1 in

Fig. 7.2.4	$k_b$ [mm <sup>2</sup> ]	$K_\Omega$ [mm <sup>2</sup> ]	$\ u\ _\infty$ [mm/hr]
(b)	0	0.0394	75.6901
(c)	$10^{-4}$	0.0180	73.9133
(d)	$\infty$	0.0181	67.3310

Table 7.4: Results of Ex. 7.2.4.

a macro channel  $L = 1$  [mm]. Unlike the Ex. 7.2.1, the biofilms are in sphere shape and attached to the rock surface. As we have seen in previous examples, we can see (some) flow through  $\Omega_b^*$  for  $k_b > 0$ . When  $k_b = 0$   $\Omega_b^*$  is treated as  $\Omega_r$ . We also report the upscaled permeability  $K_\Omega$  and the maximum velocity in Tab. 7.4.

After substantial further testing (not shown) we believe our flow model is robust and ready to be coupled with the full biomass–nutrient dynamics. This will be done in Sec. 7.3.

### 7.3 Coupled biomass-nutrient-flow dynamics

We first discuss the coupling of the flow model (7.1) and biomass-nutrient model (6.6), both written in the domain  $\Omega_n$  as is done usually in porous media. In every time step we resolve

$$\text{flow} \rightarrow \text{advection} \rightarrow \text{reaction-diffusion}.$$

See, e.g., [112, 113] for the workflow as well as Sec. 2.5.

We choose  $h = O(h_c)$  to adhere to the voxel resolution of the image, and to ensure reasonable accuracy of the biofilm layer. In particular, we also choose  $\tau$  to satisfy at least the CFL condition, as well as to obtain reasonable accuracy and resolution of the nonlinear reaction-diffusion dynamics. A fully coupled model requires that we solve for the flow at many time steps. Since calculating  $u$  at every time step is computationally expensive, we update the flow  $u$  only every so many time steps. For example in a complex porous domain  $\Omega = (0, 1)^2$  [mm<sup>2</sup>] illustrated in Fig. 7.1(d) with  $h = 0.005$  [mm] and  $\tau = 10^{-3}$  [h] with flow  $\text{Pe} \approx 30$ , we observe that there is little change in the flow pattern for 0.2 [h]. Thus, for our examples we choose  $\tau = 10^{-2}$  [h] and compute  $u$  at every  $10\tau = 0.1$  [h], so that  $u(x, t) = u(x, t^n)$  for  $t \in [t^n, t^{n+10})$ .

We solve this coupled process by using the numerical method described in Sec. 6.4 and 7.1.1. Next, we discuss the computational complexity for coupled flow and BN dynamics

follow by two examples of coupled flow and biofilm-nutrient dynamics.

### 7.3.1 Computational complexity of coupled biomass-nutrient-flow solver

In this section we discuss the total cost of the BN\_Flow solver [132]. As we discussed above, the flow is resolved at some macro time-steps  $K\tau$ . Here we consider the case when  $K = 10$ .

We recall the total computational cost for the BN solver from Sec. 6.4.4, which is  $O(10^4 M^2)$  after about 1000 time-steps. We also recall that the cost of flow solver is about  $O(12M^2)$  from Sec. 7.1.2 per time-step. Since we resolve the flow at every  $10\tau$ , the total computational cost of the BN\_Flow solver is about  $O(2 \times 10^4 M^2)$  per simulation.

### 7.3.2 Simulation results for coupled flow and biomass-nutrient dynamics

Now we are ready to test the importance of including the flow in  $\Omega_b$  coupled to the biofilm-nutrient model.

We start with an example in a micro-channel (micro-pore) in Ex. 7.3.1 and study the coupled effects of flow and biomass-nutrient. Next we consider a many-pore example.

In a micro-pore with  $L = O(60 [\mu\text{m}])$ , in order to see the evolution of nutrient penetration in  $\Omega_b^*$ , we must consider very small time scale and small  $\tau$ . At high flow rates, some microbes within  $x : B(x, t) < B_*$  can be carried away by advection before nutrient arrives which may result in limited biomass growth in that particular pore.

**Example 7.3.1** (Coupled flow and biomass-nutrient dynamics, micro-pore geometry). *We consider the biofilm growth and nutrient consumption coupled to the flow in a micro-channel  $\Omega = 65 \times 130 [\mu\text{m}^2]$ . We use the following parameters:*

$\rho_B B^* [\text{kg}/\text{m}^3]$	$B_*$	$B_{init}$	$B_{inlet}$	$N_{init}$	$\rho_N N_{inlet} [\text{kg}/\text{m}^3]$
$10^{-4}$	$0.9B^*$	$0.6B^* \mathbb{1}_{\Omega_b(0)}$	0	0	$10^{-2}$
$d_{B,0} [\text{mm}^2/\text{h}]$	$d_{N,w}$	$R_{N,bw}$	$k_N, \kappa, \alpha$	$\bar{u}_D [\text{mm}/\text{h}]$	$k_b [\text{mm}^2]$
0.1	$d_m$	0.1	2	0.5148	$10^{-5}$

The velocity, biofilm, and nutrient profiles at selected time  $t \in \{1.44, 2.88, 4.32\} [\text{s}]$  are shown in Fig. 7.6. We see that since the nutrient enters from the left, there is less microbial growth near the right boundary, and biomass and biofilm grow initially faster on the left side than on the right side. This lack of symmetry disappears later.

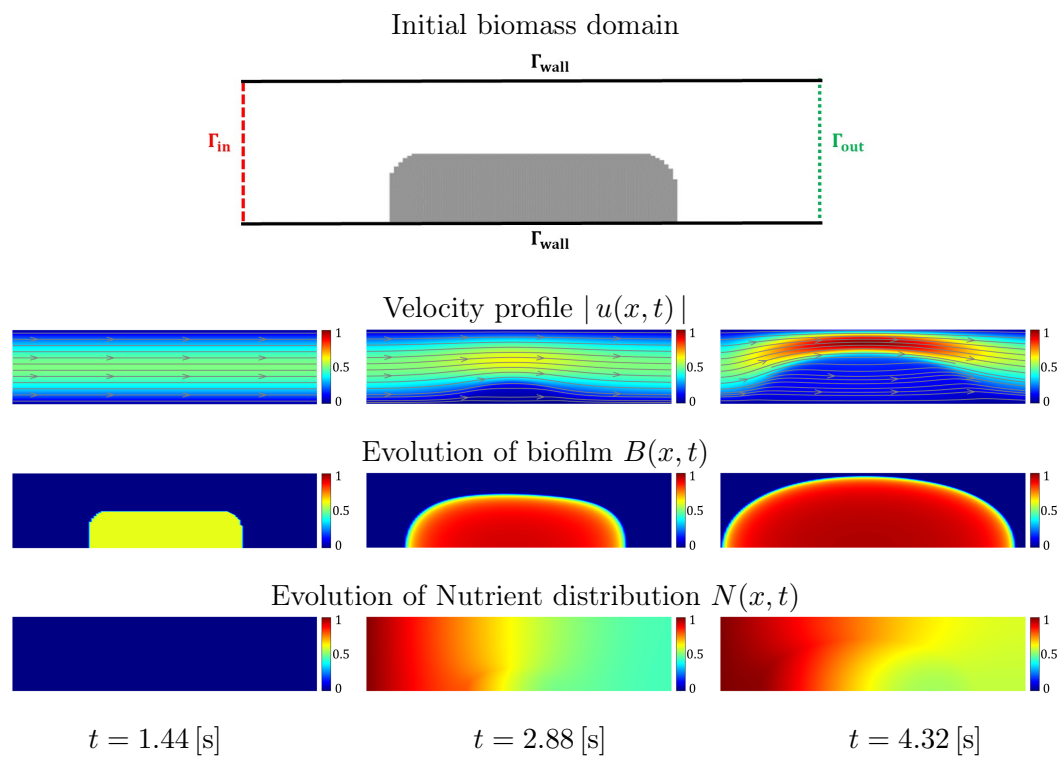


Figure 7.6: Illustration for Ex. 7.3.1 in a study of a micro-channel. Top: geometry of the domain including the initial biomass domain and the information about the boundaries. Bottom: evolution of velocity, biofilm and nutrient profiles at selected time  $t \in \{1.44, 2.88, 4.32\}$  [s].

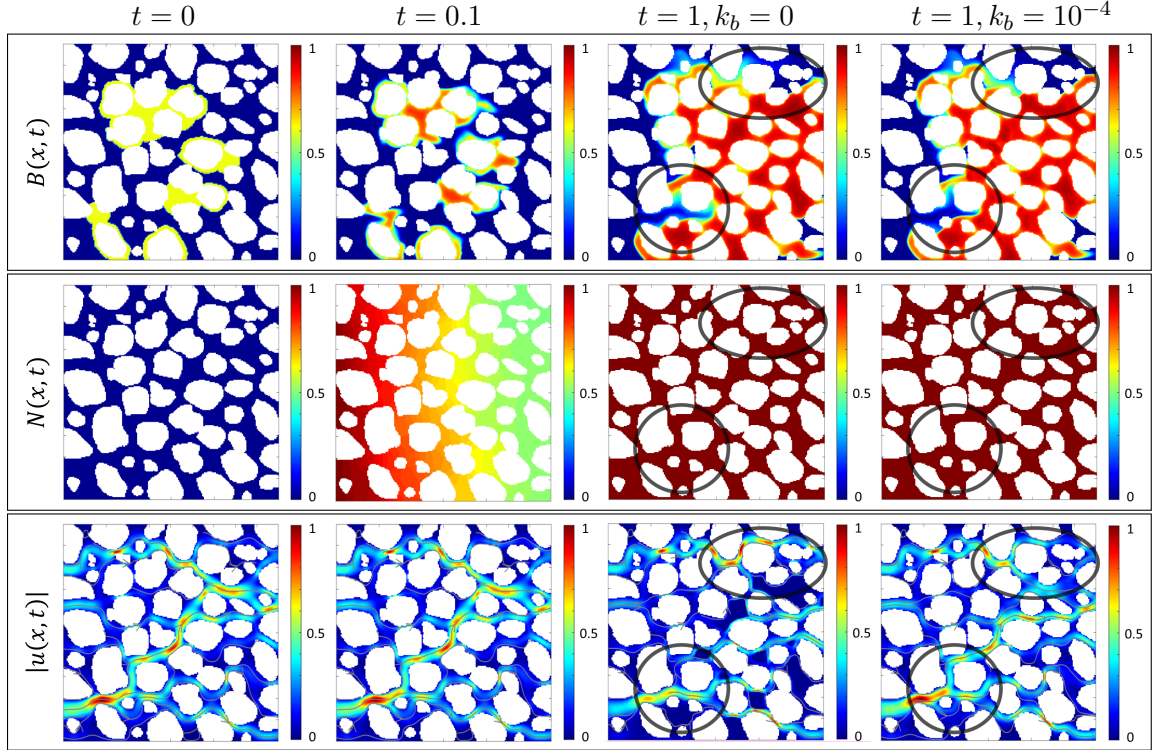


Figure 7.7: Ex. 7.3.2 biofilm–nutrient dynamic in complex geometry. Top:  $B(x, t)$ , middle:  $N(x, t)$ , and bottom:  $|u(x, t)|$ , as indicated in the leftmost panel. Two simulation cases are shown when  $k_b = 0$  (biofilm is impermeable), and  $k_b = 10^{-4}$  (biofilm is partially permeable). From left to right the columns show the initial condition at  $t = 0$ , and the results at  $t = 0.1$  (essentially identical for impermeable and permeable biofilm), and the results at  $t = 1$  separately for impermeable and permeable biofilm. The regions indicated with ellipses at  $t = 1$  show the differences in biofilm growth depending on  $k_b$ . The units are as usual  $L$  [mm],  $t$  [h].

In our next example we compare biofilm–nutrient dynamics under the conditions when  $\Omega_b$  is permeable and impermeable. We consider a complex “many–pore” geometry shown in Fig. 7.1 (d).

**Example 7.3.2** (Coupled flow and biomass–nutrient dynamics, many–pore geometry). *Assume parameters as follows*

$B^*$	$B_*$	$B_{init}, B_{inlet}$	$N_{init}, N_{inlet}$	$d_{B,0}$	$d_{N,w}, R_{N,bw}$	$k_N, \kappa$	$\alpha$	$\bar{u}_D$
1	$0.9B^*$	$0.6B^* \mathbb{1}_{\Omega_b(0)}, 0$	0, 1	$3.6 \times 10^{-4}$	$d_m, 0.1$	2	2	0.1

with  $\Omega$  as in Fig. 7.1(d). Consider dynamics of biofilm growth and nutrient consumption when the nutrient is injected from the left boundary of  $\Omega$ . Assume the natural outflow boundary conditions for  $B$  and  $N$  on the right boundary, and no–flow conditions on top and bottom. Consider two cases when  $k_b = 0$  or when  $k_b = 10^{-4}$  [mm<sup>2</sup>].

From the initial state shown in Fig. 7.7 (left) at  $t = 0$ , some of the microbes at low concentrations are first transported by advection before nutrient arrives and are transported

$k_b$ [mm <sup>2</sup> ]	$K_\Omega$ [mm <sup>2</sup> ]	$\ u\ _\infty$ [mm/hr]
0	$3.0059 \times 10^{-5}$	1.6391
$10^{-4}$	$5.6532 \times 10^{-5}$	1.2816

Table 7.5: Results for Ex. 7.3.2 at  $t = 1$  [h].

away before reaching more mature phase with  $B \approx B_*$  as you can see in Fig. 7.7 (second column) at  $t = 0.1$  with the results almost identical to the case  $k_b = 0$  and  $k_b = 10^{-4}$ . However, once they reach some of the pore throats with low flow rates  $|u|$ , and the nutrient becomes available; they grow and reach mature state.

The results at  $t = 1$  look similar at glance, but they show different biofilm formation patterns. For example, we focus on two regions as indicated by ellipses and located in the bottom left and top right in Fig. 7.7 for  $k_b = 0$  to  $k_b = 10^{-4}$ . At  $t = 1$  [h], the nutrient has reached steady state and fully penetrates the entire domain  $\Omega$ .

We also show the permeability of this entire volume in Tab. 7.5. The flow rates are lower when  $k_b > 0$ , but overall, the permeability  $K_\Omega$  is higher for the case of partially permeable biofilm.

## 7.4 Conclusions

In this chapter we formulated a model for biomass-nutrient dynamics which can be coupled to the flow at pore scale. The model is continuum and monolithic, i.e., it is written as a system of partial differential equations for the microbial species and nutrient ( $B, N$ ) and for fluid flow variables ( $u, p$ ) over the entire domain  $\Omega$  where fluid and microbes and nutrient exist. Our model does not explicitly track any interfaces or free boundaries; tracking free boundaries puts an additional burden on the solver and may require regriding. Instead, the interfaces can be found implicitly in our model by postprocessing the values of  $B(x, t)$ . For the flow we use a new approach by blending the Brinkman flow in (partially) permeable biofilm domain with that in the bulk fluid: this is done with a Brinkman flow model in which we adapt the biofilm permeability coefficient  $k_{bx}(x)$  depending on the microbial concentration  $B(x, t)$ . Our model can demonstrate the evolution of biofilm growth but is computationally expensive since it depends on the multitude of parameters. The computational complexity of our model is considerable for 3d. If one is interested in generating

pore scale geometry with biofilm or other obstructions such as hydrate, we refer to [115] for non-DNS reduced models.

Although our biomass-nutrient model does not include the biofilm surface attraction parameter, we did not see unphysical biofilm growth behavior in our examples. As shown in [114], our simulation results significantly depend on the original geometry and the initial data. Since we started with enough quantity of biomass close to the grains, we were able to avoid any issue that could arise from missing biofilm adhesion modeling parameters. In the next section, we include this modeling component to reflect the adhesive property even with a small quantity of initial biomass.

The study of the fine properties of the CCFD method in the context of degenerate and singular diffusivities is subject to the current work. We also need further study of our model in relation to other coupled models for bulk fluid-Darcy flows including the consideration of Beavers-Joseph-Saffman conditions. The challenges remain as length scales are concerned since we wish to apply the model from the single micro-pore size of  $10 [\mu\text{m}]$  to columns of  $[\text{mm}]$  size.

## 8 Biomass-nutrient dynamics with surface attraction component

In this chapter we discuss the dependence of the BN model on the initial data, in particular, to the initial biomass amount. This corresponds to the work presented in [115](Sec. 3 and part of Sec. 6).

**Challenges addressed: uncertainty.** When working with the biofilm-nutrient model or its version coupled to the flow, it is immediately clear that the pattern of the biofilm growth depends significantly on the initial distribution of biomass. This problem is also very hard to address using experimental data. Consider growing biofilm in a core sample. We first need to inoculate some amount of microbes into the core sample. Unfortunately, it is hard to guess where microbes would settle down and grow. This means that when the same amount of microbes are injected into the identical core samples, their distributions are hardly ever the same. We also expect the uncertainty of initial biomass distribution to increase when the volume fraction of inoculated initial biomass  $V_b(0) = |\Omega_b(0)| / |\Omega_n|$  decreases.

These observations stimulate our interest in biofilm growth patterns depending on the initial data and in the uncertainty of the final biofilm pattern depending on the initial biomass distribution.

**Challenges addressed: adhesion to the grains.** Moreover, our model does not feature the biofilm surface attraction mechanism (“pore-coating” behavior). If  $V_b(0)$  is large enough and the majority of  $\Gamma_{rn}$  is covered by initial biomass like in Ex. 6.5.1 in which  $V_b(0) > 0.6$  and over 80% of  $\Gamma_{rn}$  were covered by the initial biomass, we may expect physical biofilm growth as in Fig. 6.5. However, if  $V_b(0)$  is small, microbes are likely to be sparsely distributed which can result in violating the pore-coating behavior since  $d_B$  is not suppressed in a certain direction. This motivated us to introduce a modeling component that “promotes” biofilm growth on the surface.

**Our contributions to solving these challenges.** Our idea is to introduce a biofilm surface “attraction” parameter to (6.6) in Sec. 8.1 and compare the simulation results between the case with and without the surface attraction enforcement in Sec. 8.2. We also consider the probability of upscaled permeabilities of Monte Carlo simulation results to show the impact of attraction parameter on biofilm growth effectively.

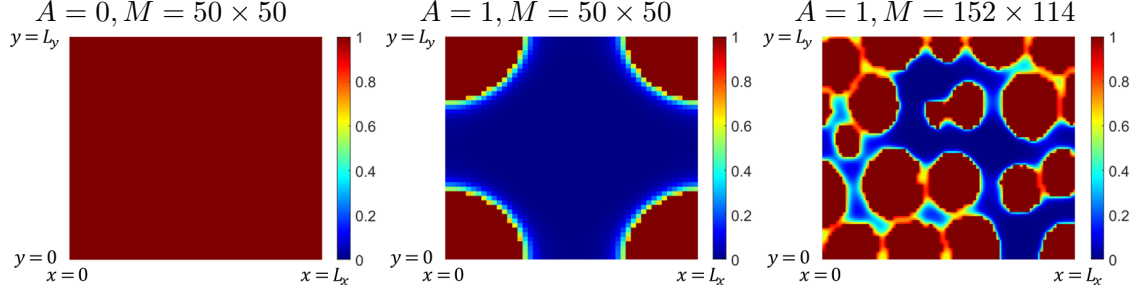


Figure 8.1: Contours of the attraction coefficient  $a(x)$  defined by (8.2) (left)  $A = 0$ , (middle)  $A = 1$  in single-pore geometry, and (right)  $A = 1$  in vertical lice from  $\mu$ -CT column of glass beads. pore scale geometries are illustrated in Fig. 8.2.

### 8.1 “Promoting” biofilm adhesion to surfaces

Recall the BN model (6.6) for  $u \equiv 0$ . The reaction term for  $B$  is

$$r_B^{growth}(B, N) = \kappa_B B m(N).$$

Based on the definition of  $r_B^{growth}$  (6.5), it does not involve the pore-coating mechanism. In fact, the surface attraction behavior is difficult to calibrate quantitatively. Thus, we choose to do this heuristically by decreasing the reaction rates away from  $\Gamma_{rn}$ .

The modified reaction term for  $B$  read as

$$r_B^{growth}(B, N, x) = \kappa_B B(x, t) m(N) a(x), \quad (8.1)$$

where the attraction parameter  $a(x)$  is defined as

$$a(x) = \begin{cases} 1, & \text{if } A = 0, \\ \frac{2}{1 + e^{10a_o(x)/\|a_o\|_\infty}}, & \text{if } A = 1. \end{cases} \quad (8.2)$$

Here  $a_o$  is the solution to the Poisson equation

$$-\Delta a_o = A,$$

with homogeneous Dirichlet boundary conditions on  $\Gamma_{rn}$  and homogeneous Neumann boundary conditions on  $\partial\Omega \cap \partial\Omega_n = \Gamma_{in} \cup \Gamma_{out} \cup \Gamma_{wall}$ . We provide the plots of  $a(x)$  in Fig. 8.1. With  $A = 0$ , we have  $a \equiv 1$ , and the rate  $r_B^{growth}(B, N, x) = \kappa_B B(x, t) m(N)$ . However, with  $A = 1$ , we see that  $a \downarrow 0$  as the distance from the wall  $\Gamma_{rn}$  increases.

Next, we compare the biofilm growth pattern with attraction “off”, i.e.,  $A = 0$ , to the case with attraction “on”, i.e.,  $A = 1$ .

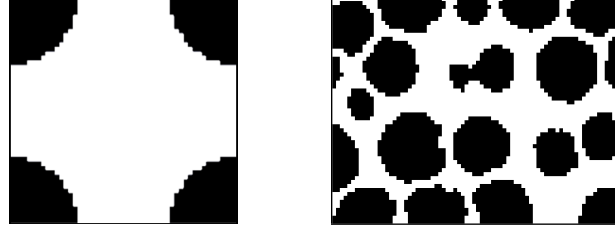


Figure 8.2: Illustration of (left) idealized single-pore geometry with  $M = 50 \times 50$  voxels, and (right) vertical slice from  $\mu$ -CT column of glass beads with  $M = 152 \times 114$  voxels.  $\Omega_r$  is in black, and  $\Omega_n$  in white.

## 8.2 Uncertainty in biofilm growth depending on initial data and upscaled permeability

In this section we provide simulation results of biofilm growth in the idealized single-pore geometry illustrated in Fig. 8.2 on the left. We show how the initial biomass  $V_b$  and the attraction parameter  $a(x)$  influence the biofilm growth pattern as well as the upscaled flow properties.

**Example 8.2.1** (Biofilm growth with variant  $V_b$  and  $A$ ). *Consider the nutrient-rich idealized single-pore geometry  $\Omega = (0, L_x) \times (0, L_y)$  [mm<sup>2</sup>] illustrated in Fig. 8.2(left). We use the parameters listed in Tab. 8.1 and simulate the biofilm growth using the numerical model for (6.6) with  $u \equiv 0$  which was described in Sec. 6.4. The randomly generated  $\Omega_b(0)$  for cases (a–b) are shown in Fig. 8.3 at the top.*

The biomass in each case evolves first, and the biofilm phase becomes mature when  $B_* \leq B(x, t) \leq B^*$ . Then this biofilm phase continues growing by interface creating new biofilm phase  $\Omega_b^*(t)$ .  $|\Omega_b^*(t)|$  increases with time. The growth pattern depends on the initial state. Fig. 8.3(middle) and (bottom) rows show biofilm distribution evolved from the initial states Fig. 8.3(top) row with  $A = 0$  and  $A = 1$ , respectively.

Consider  $V_b = 0.0045$  for  $A = 0$ . We start with the sparsely distributed initial biomass. We see that the biofilm tends to grow spherically without strictly adhering to the walls as expected. However, when we increase  $V_b$ , i.e., case (c–d), to cover  $\Gamma_{rn}$  evenly, the biofilm sticks together but grows gradually away from walls.

On the other hand, with  $A = 1$  the growth away from the walls is suppressed to promote growth near the walls. We see a dramatic difference as compared to the cases when  $A = 0$ .

Now we consider two cases (a–b) with  $V_b = 0.0045$  and  $A = 1$ , the left bottom two figures in Fig. 8.3. These two have very different  $\Omega_b^*(t)$ , and they have different permeabilities.

Parameter	Description	Value/Units	Ref.
Model parameters (fixed)			
$L_x \times L_y$	Dimensions of domain $\Omega$	$1 \times 1$ [mm]	[114]
$\alpha$	Exponent in diffusivity, in eqn. (6.6c)	2	[39, 131]
$d_{B,0}$	Motility coefficient of microbe	$10^{-4}$ [mm <sup>2</sup> /h]	[39, 131]
$\kappa$	Utilization rate	$O(1/h)$	[39]
$\kappa_N$	Specific substrate update rate	0.5	[39]
$N_0$	Monod half-life	$1.18 \times 10^{-3}$ [-]	[39]
$B^*$	Maximum density of biofilm (relative)	1 [-]	[114]
$B_*$	Threshold for $B > B_*$ which determines $\Omega_b^*$	$0.9B^*$	[114]
Model parameters (varying)			
$\Omega_b(0)$	Localization of initial biomass	-	random
$V_b(0)$	Ratio of $ \Omega_b(0) $ to $ \Omega_n $ in initial conditions	0.0045 (a,b), 0.03 (c,d)	ad-hoc
$B_0$	Initial biomass density	0.6 (a,b), 0.8 (c,d)	ad-hoc
$A$	Attraction parameter in (8.2)	$\{0, 1\}$	ad-hoc
Discretization parameters			
$M_x \times M_y$	Spatial grid	$50 \times 50$	N/A
$h$	Spatial discretization parameter	0.02 [mm]	N/A
$\tau$	Time step	$10^{-2}$ [h]	N/A

Table 8.1: Parameters for the DNS model and simulations of  $(B, N)$  described in Sec. 6.3. Simulations cases (a,b,c,d) for Ex. 8.2.1 are presented.

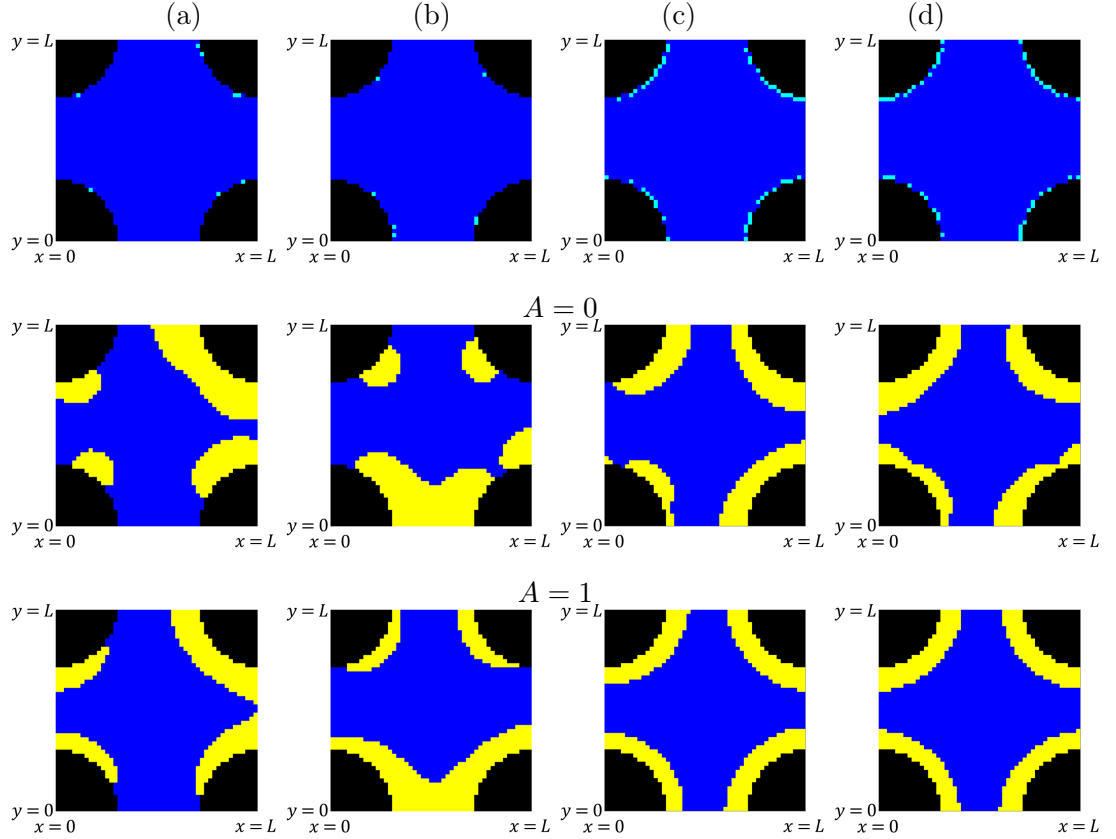


Figure 8.3: Generation of  $\Omega_b(0)$  with the biomass-nutrient for single-pore geometry on  $50 \times 50$  grid, with simulation parameters for cases (a–d) are given in Tab. 8.1. Top row: randomly chosen regions  $\Omega_b^{(i)}$  used for initialization in  $B(x, 0) = B_0 \mathbb{1}_{\Omega_b}(x)$  for each case (a–d), with small relative volume  $V_b = 0.0045$  in (a–b) and larger volume  $V_b = 0.03$  in (c–d). Middle and bottom rows: regions  $\Omega_b^{(i)}$  obtained with the BN model at the time  $t^{(i)}$  when the corresponding obstruction volume  $V_o(t^{(i)}) = 0.3$ ; each region was obtained by simulation with initial conditions shown in the top row, respectively. Smaller  $V_b$  and  $A = 0$  corresponds to less pronounced coating behavior.

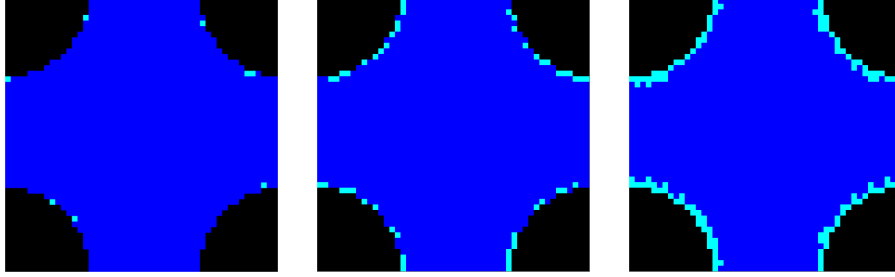


Figure 8.4: Realization of  $\Omega_b^{(i)}$ : (left)  $V_b = 0.0045, B_0 = 0.6B^*$ , (middle)  $V_b = 0.03, B_0 = 0.8B^*$ , (right)  $V_b = 0.07, B_0 = 0.6B^*$

Let  $K_0$  be the permeability of the original geometry and  $K_{(i)}$  be the upscaled permeability for case  $(i)$ . The flow profiles in  $\Omega_n$  for (a–b) with the boundary conditions used in Ex. 7.2.1 or Ex. 7.3.2 are very different since flow interferes with biofilm phase. This scenario results  $K_{(a)} < K_0 < K_{(b)}$ . Since every case depends on the randomly generated  $\Omega_b(0)$ , we consider the probability of upscaled permeability.

### 8.2.1 Monte Carlo simulations

We now proceed to address the uncertainty of the simulation results with respect to the initial biomass distribution. We do so by constructing Monte-Carlo simulations. We generate a random set of initial conditions, proceed with simulations of the BN model in each, and upscale to get the permeability.

**Example 8.2.2.** *We follow Ex. 8.2.1, but now we perform Monte Carlo Simulations with collection of  $I$  realizations of  $\Omega_b^{(i)}(0)$ , which lead to the biofilm evolution and formation of  $\Omega_b^{*,(i)}(t)$ . In this example we keep all input parameters fixed except  $V_b(0)$  and  $A$ . We consider  $V_b(0) \in \{0.0045, 0.03, 0.07\}$  and  $A \in \{0, 1\}$ . For  $V_b(0) = 0.07$ , we use  $B_0 = 0.6B^*$ . We also use  $k_b = 0$ , i.e., impermeable biofilm, and calculate the upscaled permeability at every  $t$  for each evolution. Simulation ceases when pores get clogged.*

Fig. 8.4 shows examples of  $\Omega_b^{(i)}(0)$  for each  $V_b(0)$ . Fig. 8.5 shows that the relationship between  $K_\Omega$  and  $V_o = |\Omega_b^*| / |\Omega_n|$  depends on how these geometries were created, and in particular on the choice for  $A$ . We see that  $K_\Omega(t)$  decays close to linearly with  $V_o = \frac{|\Omega_b^*|}{|\Omega_n|}$  with more uniform pore-coating behavior for  $A = 1$  and large  $V_b(0)$ , but we see faster decay of  $K_\Omega$  with  $A = 0$  or large  $V_b(0)$ .

In the following remark we compare our permeability trends with the well-known Carman-Kozeny correlation model.

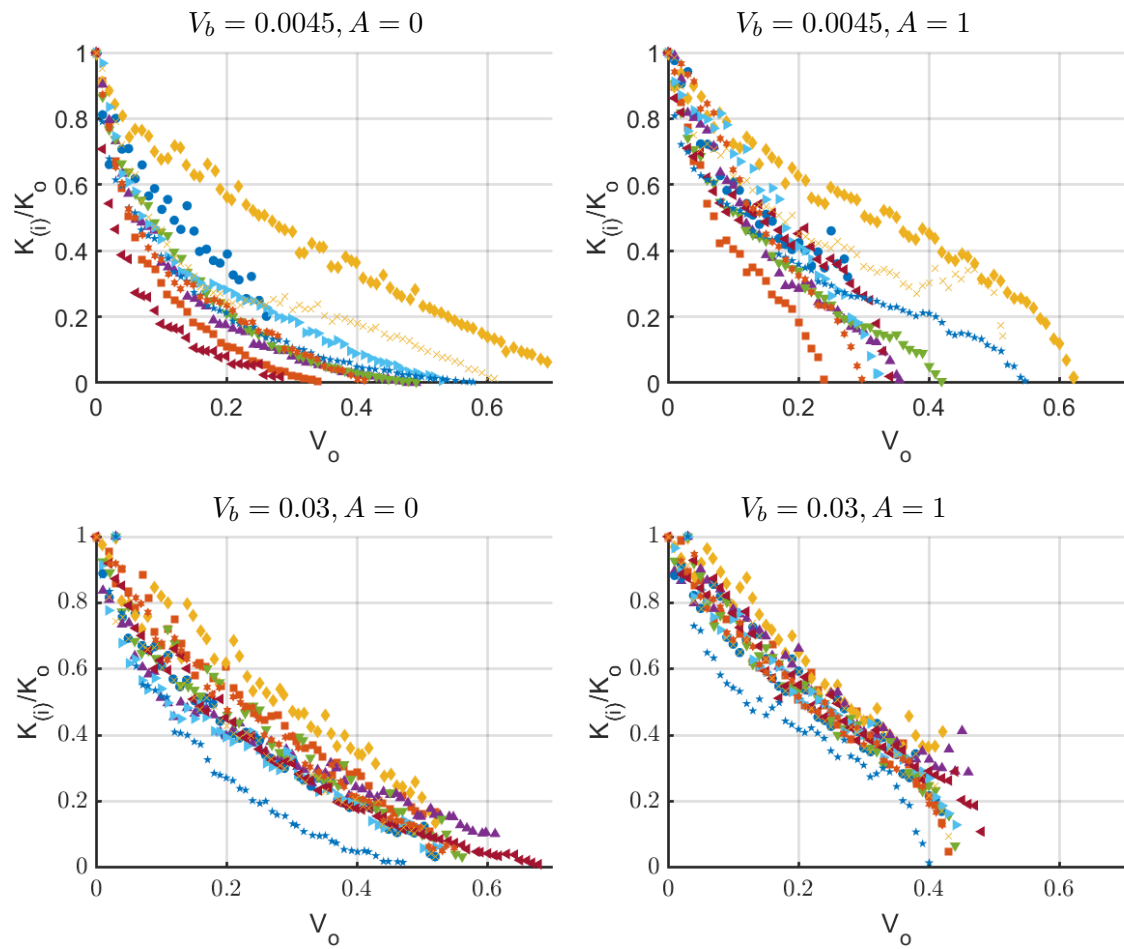


Figure 8.5: Dependence of  $K_{\Omega}(t)$  on  $V_o(t)$  with the BN model (6.6) discussed in Sec. 6.3. Results for Ex. 8.2.1 are shown for 10 selected out of  $I = 100$  realizations of geometries generated with  $V_b$  and  $A$  as shown.

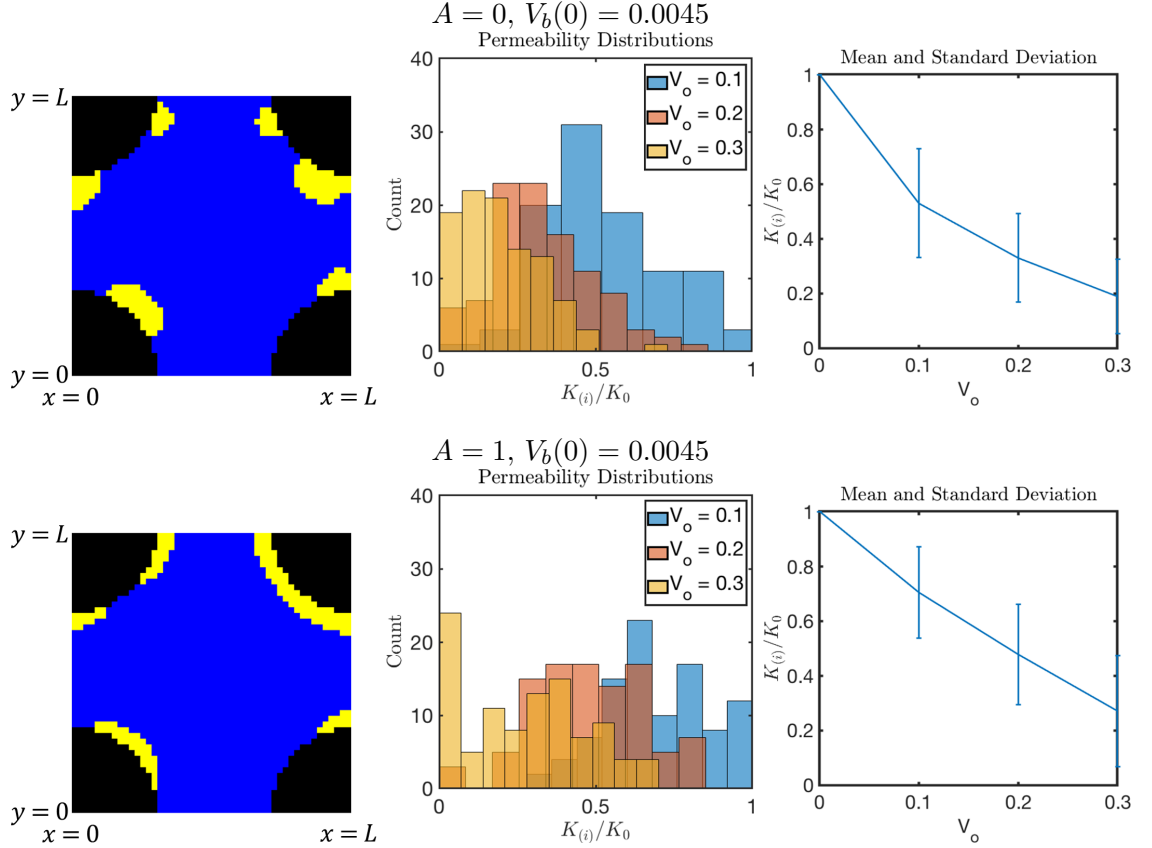


Figure 8.6: Results of the BN model with  $V_b(0) = 0.0045$  and  $A$  as shown. Left: one of the realizations  $\Omega_b^{*,(i)}$  for  $V_o = 0.1$ . Middle: histogram of  $(K_{(i)})_i$  for  $V_o \in \{0.1, 0.2, 0.3\}$ . Right: mean and standard deviation of  $(K_{(i)}/K_0)_i$  for  $V_o \in \{0.1, 0.2, 0.3\}$

**Remark 8.2.1.** Furthermore, we want to know whether the trends in the decrease in permeabilities predicted by our model and plotted in Fig. 8.5 are realistic, and how they compare with the realistic data. For this we recall the model for the dependence of  $K_\Omega$  on  $V_o$  based on Carman-Kozeny models for pore-coating scenarios [145] given from algebraic expressions

$$K_\Omega(V_o) = K_0 \left( 1 - V_o + \frac{2(1 - V_o)^2}{\log(V_o)} \right).$$

In the range  $V_o \in [0, 0.5]$  considered here, these formulas predict a dramatic decrease (convex) in  $K_\Omega$ .

In Fig. 8.6–8.8, we present the histograms and other statistical information about the permeability distribution along with the cartoon of a sample geometry  $\Omega_b^{*,(i)}$  for  $V_b(0) \in \{0.0045, 0.03, 0.07\}$  and  $A \in \{0, 1\}$ . The mean and standard deviation values of the normalized permeability  $K_{(i)}/K_0$  for  $V_o \in \{0.1, 0.2, 0.3\}$  are shown in Tab. 8.2.

With these results, we are ready to comment on the sensitivity of our model (6.6) to the input parameters based on the qualitative observation from Ex. 8.2.2 since the compa-

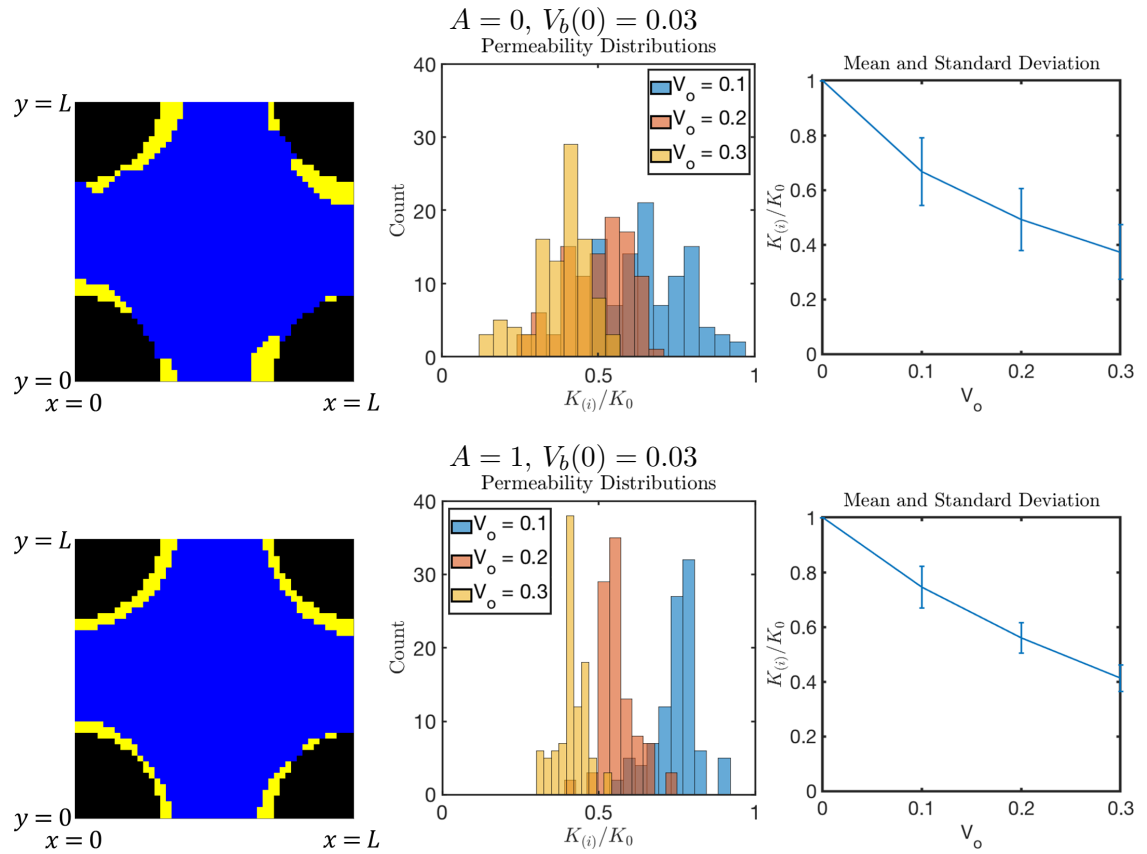


Figure 8.7: Results of the BN model with  $V_b(0) = 0.03$  and  $A$  as shown. Left: one of the realizations  $\Omega_b^{*,(i)}$  for  $V_o = 0.1$ . Middle: histogram of  $(K_{(i)})_i$  for  $V_o \in \{0.1, 0.2, 0.3\}$ . Right: mean and standard deviation of  $(K_{(i)}/K_0)_i$  for  $V_o \in \{0.1, 0.2, 0.3\}$

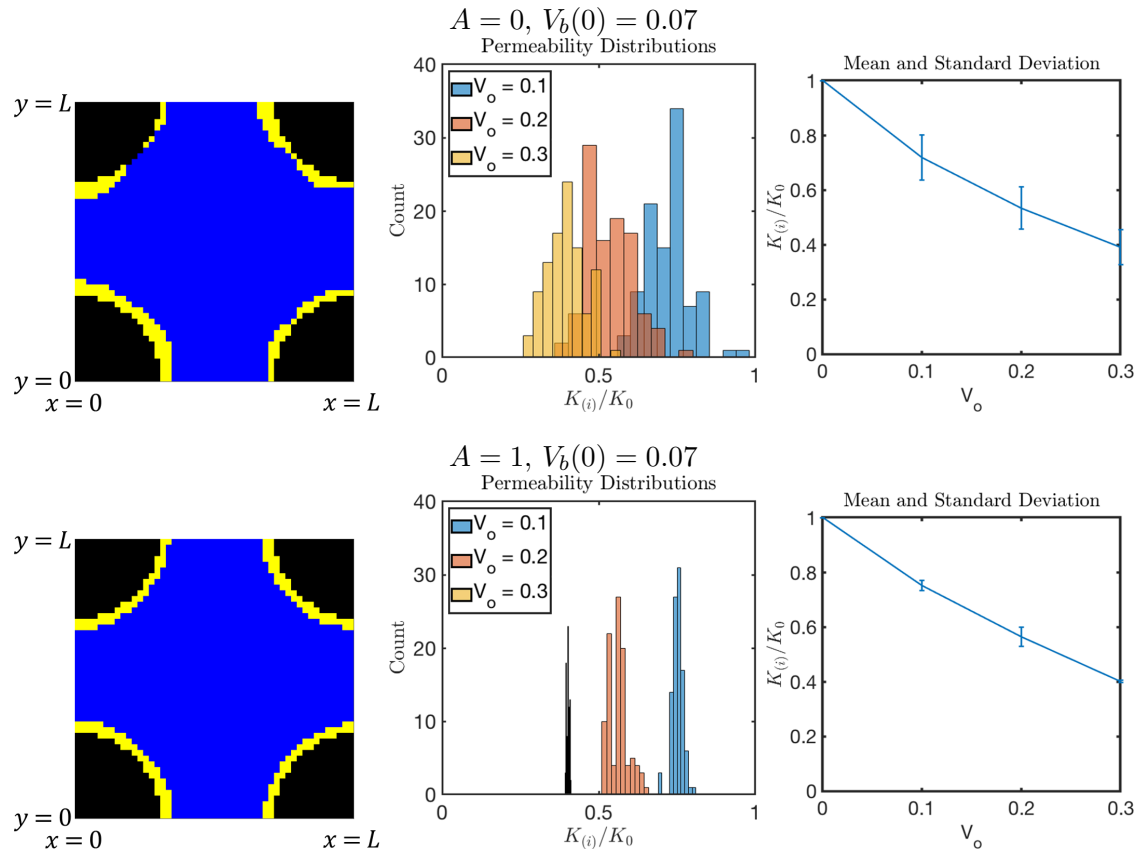


Figure 8.8: Results of the BN model with  $V_b(0) = 0.07$  and  $A$  as shown. Left: one of the realizations  $\Omega_b^{*,(i)}$  for  $V_o = 0.1$ . Middle: histogram of  $(K_{(i)})_i$  for  $V_o \in \{0.1, 0.2, 0.3\}$ . Right: mean and standard deviation of  $(K_{(i)}/K_0)_i$  for  $V_o \in \{0.1, 0.2, 0.3\}$

Pore coating, single-pore geometry							
$V_b$	$V_o$	$A$	mean	std. dev.	$A$	mean	std. dev.
0.0045	0.1	0	0.5563	0.1998	1	0.7002	0.1855
0.0045	0.2	0	0.3564	0.1714	1	0.4842	0.1861
0.0045	0.3	0	0.1911	0.1660	1	0.2750	0.2087
0.03	0.1	0	0.6680	0.1233	1	0.7460	0.0754
0.03	0.2	0	0.4929	0.1130	1	0.5613	0.0554
0.03	0.3	0	0.3742	0.1001	1	0.4141	0.0480
0.07	0.1	0	0.7197	0.0825	1	0.7526	0.0184
0.07	0.2	0	0.5349	0.0780	1	0.5648	0.0341
0.07	0.3	0	0.3921	0.0641	1	0.4015	0.0043

Table 8.2: Sensitivity of the probability distribution of  $K_{(i)}/K_0$  to the simulation parameters  $V_b$  and  $A$  for the geometries  $\Omega_b^*$  obtained with DNS for pore coating scenarios. The values  $K$  presented here correspond to three selected values of the relative volume  $V_o = \frac{|\Omega_b^*|}{|\Omega_n|}$  from the set  $\{0.1, 0.2, 0.3\}$ .

rable quantitative data are unavailable. The input parameters we used in Ex. 8.2.2 are from literature; see [114, 131].

When  $V_b(0)$  is small, the variability of permeability is very high; see Fig. 8.6. This means that it is hard to predict the permeability since the calculated  $K_{(i)}/K_0$  are less consistent. As biofilms fill up the pore, we see that the widespread unimodal permeability distribution skew to the left except for the case with  $V_b(0) = 0.0045$  and  $A = 1$ . For  $V_b(0) = 0.0045$  and  $A = 1$ , the mean permeability decrease linearly with respect to  $V_o$ , but permeabilities are randomly distributed. For large(r)  $V_b(0)$  the variability of permeability decrease significantly when we turn on the attraction parameter. This is expected since the evolution is initiated from the evenly distributed biomass as we see in Fig. 8.4.

We conclude that our model (6.6) is sensitive to  $V_b(0)$  and  $A$ . Both  $V_b(0)$  and  $A$  play a significant role in biofilm growth pattern. In particular we show that the realizations produced from large enough  $V_b(0)$  with  $A = 1$  can give a approximate permeability close to the mean value.

Next we summarize the remaining contents of [115].

## 8.2.2 Comparison of DNS to non-DNS approaches for biofilm domain generation

As we showed above, DNS can demonstrate the evolution of realistic biofilm domains. However, DNS are very complex and depend on a multitude of parameters which may or may not be possible to calibrate. Thus, DNS would be computationally too expensive to use if we aim to generate some realistic biofilm domains for a given  $V_b^*$ .

Alternatively, one can use non-DNS approaches as was first explored in [150] for the generation of obstructions in pore scale domains inspired by both biofilm and hydrate crystal applications. These approaches were compared to DNS for the biofilm application in [115].

In [115, 150] two non-DNS approaches are used. These are (1) CLPS model, a constrained version of Allen-Cahn model [152] for phase separation with a localization term, and (2) LP method, the Markov Chain Monte Carlo method using a lattice Ising-type model [89]. Both methods can produce realizations of obstructed domains by finding the local minima of some nonconvex energy functional. We first briefly describe the CLPS model followed by the LP method. Then we report the comparison results with our BN model.

**CLPS model.** The CLPS model is a reduced model that uses the ability of the Allen-Cahn equation for phase separation with volume constraint to produce the obstructed domain. The rock surface  $\Gamma_{rn}$  is detected heuristically through a localization function rather than introducing additional complexity from electrochemical interactions. We also use the Lagrange multiplier to keep the volume constraint. Here we only need to solve for an order parameter.

**LP method.** The LP model is motivated by the statistical mechanics of discrete lattice models which improves the dynamics for phase transition. Given an initial domain  $\Omega$  with some  $V_b^*$  where biofilms are randomly simulated in some voxels in  $\Omega_n$ . Each voxel is equivalent to a node of a lattice for the LP method with values  $\{0, 1, 2\}$  which indicate rock, void, and biofilm phases, respectively. Using the Metropolis algorithm [85, 89, 133], we swap a pair of nodes at each time-step and seek its stationary state by minimizing the Hamiltonian energy functional.

**Summary of BN vs CLPS vs LP for biofilm domain.** The CLPS model produces qualitatively similar biofilm domains from the BN model with  $A = 0$ . Biofilms aggregate in distinct "colonies" while not covering the entire  $\Gamma_{rn}$ . When we use the LP method, we can generate the domain with biofilm covering  $\Gamma_{rn}$  evenly which is similar to our case with

$A = 1$ . These similarities are also confirmed by comparing the histograms of upscaled permeability and the standard deviation plots.

**Computational complexity of DNS versus non-DNS approaches.** Next, we compare the computational complexity of BN with CLPS and LP.

We recall first the computational cost for one realization of BN solver from Sec. 6.4.4. After  $N$  time-steps, the computational cost of BN solver for one realization is  $O(12NM^2)$ . For every realization, we also solve for flow and calculate the upscaled permeability. The computational cost of this post-process is about  $O(12M^2)$  per realization.

In addition, we implemented the new biofilm surface adhesion term involving the attraction parameter  $A = 1$  described in Sec. 8.1. Hence, we also need to pre-compute the value  $a(x)$  prior to simulations. This step costs about  $O(M^{3/2})$  from CCFD and other operations. We know that this step is only calculated once for  $I$  Monte Carlo simulations.

To give a concrete example, consider a simulation with the BN model until clogging. The average wall clock time for Ex. 8.2.2 with  $V_b = 0.07$  are 30 [s] for  $A = 0$  and 2.2 [m] for  $A = 1$  for one realization. We see a big difference due to a more controlled growth pattern corresponding to  $A = 1$ ; simulations take longer because the clogging occurs at a later time.

Overall, the total cost of  $I$  Monte-Carlo realizations of BN simulations will be  $I \times O(12M^2(N + 1))$  after  $N$  time-step.

**Cost of CLPS.** The number of unknowns for CLPS is  $M$ , and we solve for a linear symmetric non-degenerate system by time-lagging. Also, the localization functions are pre-computed. The cost per time-step is about  $5M$  operations which includes dealing with the volume constraint plus the cost of the linear solver  $solver(M + 1)$ . Each realization takes 100 to 1000 time-steps to reach the stationary solution where the average simulation time is about 10 [s].

**Cost of LP.** The LP method takes up to  $O(10^5)$  times-steps to reach its steady state. However, the cost per time-step is only about 10 operations regardless of how large  $M$  is since we only require a pair of nodes swapping and recalculation of Hamiltonian update. We find that the average wall clock time for the LP method is less than 1 [s].

In the end we see that the non-DNS approaches are computationally effective and provide an alternative to DNS of BN. Clearly, they do not represent physical reality but produce meaningful distributions of upscaled permeability for the biofilm domains at low cost. For more information we refer readers to [115, 150].

## 9 Summary, conclusions, and outlook

In this dissertation we presented the two important models of multiphase flow and transport in porous media at multiple scales. Both models have different challenges, and we were able to address some of them, but more work is needed, with some work underway.

We discussed the methane gas transport phenomena in the subsurface at Darcy scale in Ch. 3–5 and presented rigorous stability analysis as well as some simulations illustrating why the models are interesting and important. Our current work involves gas transport in the gas zone below the hydrate zone as well as extensions to three-phase conditions, both in equilibrium and non-equilibrium conditions. Furthermore, we wish to extend the study on the hydrate model to pore scale which we need to obtain the upscaled permeability for Darcy scale simulations using the coupled thermo-transport models that we described in Sec. 3.11 and Sec. 5.3. The results from pore scale hydrate model can also be compared to the non-DNS results for “pore-filling” cases from [115].

In Ch. 6–8 we discussed the biofilm growth model at pore scale coupled to flow. Our main contribution is the fact that the coupled biomass-nutrient-flow model is monolithic which we are able to use effectively to obtain permeability of complex geometry. We also were able to compare our work with certain non-DNS approaches. Current and future work includes error analyses for the monolithic model which would help to identify proper time stepping.

## References

1. Azhar Alhammali. *Numerical analysis of a system of parabolic variational inequalities with application to biofilm growth*. PhD thesis, Oregon State University, 2019.
2. Azhar Alhammali and Malgorzata Peszynska. Numerical analysis of a parabolic variational inequality system modeling biofilm growth at the porescale. *Numerical Methods for Partial Differential Equations*, 36(5):941–971, 2020.
3. T Almani, Kundan Kumar, A Dogru, G Singh, and MF Wheeler. Convergence analysis of multirate fixed-stress split iterative schemes for coupling flow with geomechanics. *Computer Methods in Applied Mechanics and Engineering*, 311:180–207, 2016.
4. Erik Alpkvist, Cristian Picioreanu, Mark C. M. van Loosdrecht, and Anders Heyden. Three-dimensional biofilm model with individual cells and continuum eps matrix. *Biotechnology and Bioengineering*, 94(5):961–979, 2006.
5. Todd Arbogast, Clint N. Dawson, Philip T. Keenan, Mary F. Wheeler, and Ivan Yotov. Enhanced cell-centered finite differences for elliptic equations on general geometry. *SIAM Journal on Scientific Computing*, 19(2):404–425, mar 1998.
6. Todd Arbogast, Mary F. Wheeler, and Ivan Yotov. Mixed finite elements for elliptic problems with tensor coefficients as cell-centered finite differences. *SIAM Journal on Numerical Analysis*, 34(2):828–852, 1997.
7. Viorel Barbu. *Nonlinear differential equations of monotone types in Banach spaces*. Springer Monographs in Mathematics. Springer, New York, 2010.
8. Ilenia Battiato, Peter T. Ferrero V, Daniel O’ Malley, Cass T. Miller, Pawan S. Takhar, Francisco J. Valdés-Parada, and Brian D. Wood. Theory and applications of macroscale models in porous media. *Transport in Porous Media*, 130(1):5–76, apr 2019.
9. Jacob Bear and Alexander H. D. Cheng. *Modeling groundwater flow and contaminant transport*. Theory and Applications of Transport in Porous Media. Springer Netherlands, 2010.
10. Christian Berndt, Tomas Feseker, Tina Treude, Sebastian Krastel, Volker Liebertrau, H Niemann, Victoria J Bertics, Ines Dumke, Karolin Dunnbier, B Ferre, et al. Temporal constraints on hydrate-controlled methane seepage off Svalbard. *Science*, 343(6168):284–287, 2014.
11. Christopher E. Brennen. *Fundamentals of Multiphase Flow*. Cambridge University Press, 2012.
12. H. Brézis. *Opérateurs maximaux monotones et semi-groupes de contractions dans les espaces de Hilbert*. North-Holland Publishing Co., Amsterdam, 1973. North-Holland Mathematics Studies, No. 5. Notas de Matemática (50).

13. H. C. Brinkman. A calculation of the viscous force exerted by a flowing fluid on a dense swarm of particles. *Applied Scientific Research Section A—Mechanics Heat Chemical Engineering Mathematical Methods*, 1(1):27–34, 1947.
14. Steven Bryant and Larry Britton. Mechanistic understanding of microbial plugging for improved sweep efficiency. Technical report, The University Of Texas At Austin, 2008.
15. Yuncheng Cao, Duofu Chen, and Lawrence M. Cathles. A kinetic model for the methane hydrate precipitated from venting gas at cold seep sites at hydrate ridge, Cascadia margin, Oregon. *Journal of Geophysical Research: Solid Earth*, 118(9):4669–4681, sep 2013.
16. Matthew A. Clarke and P. R. Bishnoi. Measuring and modelling the rate of decomposition of gas hydrates formed from mixtures of methane and ethane. *Chemical Engineering Science*, 56(16):4715–4724, 2001.
17. M. B. Clennell, M. Hovland, J.S. Booth, P. Henry, and W. Winters. Formation of natural gas hydrates in marine sediments: 1. conceptual model of gas hydrate growth conditioned by host sediment properties. *Journal of Geophysical Research*, 104:22,985–23,003, 1999.
18. Bernardo Cockburn and Pierre Alain Gremaud. A priori error estimates for numerical methods for scalar conservation laws. part ii : flux-splitting monotone schemes on irregular cartesian grids. *Mathematics of Computation of the American Mathematical Society*, 66(218):547–572, 1997.
19. N. G. Cogan and James P. Keener. The role of the biofilm matrix in structural development. *Mathematical Medicine and Biology: a Journal of the IMA*, 21(2):147–166, 2004.
20. Frederick S. Colwell, Robert W. Smith, F. Grant Ferris, Anna-Louise Reysenbach, Yoshiko Fujita, Tina L. Tyler, Joanna L. Taylor, A. Banta, Mark E. Delwiche, Travis L. McLing, and Mary E. Watwood. Microbially mediated subsurface calcite precipitation for removal of hazardous divalent cations: microbial activity, molecular biology, and modeling. In *ACS Symposium Series*, pages 117–137. American Chemical Society, apr 2005.
21. Timothy B Costa, Kenneth Kennedy, and Malgorzata Peszynska. Hybrid three-scale model for evolving pore-scale geometries. *Computational Geosciences*, 22:925–950, 2018.
22. Katharine Z. Coyte, Hervé Tabuteau, Eamonn A. Gaffney, Kevin R. Foster, and William M. Durham. Microbial competition in porous environments can select against rapid biofilm growth. *Proceedings of the National Academy of Sciences - PNAS*, 114(2):E161–E170, 2017.
23. Alfred B. Cunningham, William G. Characklis, Feisal Abedeen, and David Crawford. Influence of biofilm accumulation on porous media hydrodynamics. *Environmental Science & Technology*, 25(7):1305–1311, 1991.

24. H. Daigle and B. Dugan. Capillary controls on methane hydrate distribution and fracturing in advective systems. *Geochemistry, Geophysics, Geosystems*, 12(1), 2011.
25. M. K. Davie and B. A. Buffett. A numerical model for the formation of gas hydrate below the seafloor. *Journal of Geophysical Research: Solid Earth*, 106(B1):497–514, jan 2001.
26. M. K. Davie and B. A. Buffett. A steady state model for marine hydrate formation: Constraints on methane supply from pore water sulfate profiles. *Journal of Geophysical Research: Solid Earth*, 108(B10):n/a–n/a, oct 2003.
27. M. K. Davie, O. Y. Zatsepina, and B. A. Buffett. Methane solubility in marine hydrate environments. *Marine Geology*, 203(1-2):177–184, jan 2004.
28. Wen Deng, M. Bayani Cardenas, Matthew F. Kirk, Susan J. Altman, and Philip C. Bennett. Effect of permeable biofilm on micro- and macro-scale flow and transport in bioclogged pores. *Environmental Science & Technology*, 47(19):11092–11098, sep 2013.
29. G. R. Dickens. Rethinking the global carbon cycle with a large, dynamic and microbially mediated gas hydrate capacitor. *Earth Planet. Sci. Lett.*, 213:169–183, 2003.
30. Marco Discacciati, Edie Miglio, and Alfio Quarteroni. Mathematical and numerical models for coupling surface and groundwater flows. *Appl. Numer. Math.*, 43(1-2):57–74, 2002. 19th Dundee Biennial Conference on Numerical Analysis (2001).
31. Knut Drescher, Yi Shen, Bonnie L. Bassler, and Howard A. Stone. Biofilm streamers cause catastrophic disruption of flow with consequences for environmental and medical systems. *Proceedings of the National Academy of Sciences*, 110(11):4345–4350, 2013.
32. Louis J. Durlofsky. Coarse scale models of two phase flow in heterogeneous reservoirs: volume averaged equations and their relationship to existing upscaling techniques. *Computational Geosciences*, 2(2):73–92, 1998.
33. H. J. Eberl, C. Picioreanu, J. J. Heijnen, and M. C. M. van Loosdrecht. A three-dimensional numerical study on the correlation of spatial structure, hydrodynamic conditions, and mass transfer and conversion in biofilms. *Chemical Engineering Science*, 55(24):6209–6222, 2000.
34. Hermann J. Eberl and Laurent Demaret. A finite difference scheme for a degenerated diffusion equation arising in microbial ecology. *Electronic Journal of Differential Equations*, 15:77–95, 2007.
35. Anozie Ebigbo, Rainer Helmig, Alfred B. Cunningham, Holger Class, and Robin Gerlach. Modelling biofilm growth in the presence of carbon dioxide and water flow in the subsurface. *Advances in Water Resources*, 33(7):762–781, 2010.
36. Messoud Efendiev. *Evolution equations arising in the modelling of life sciences*, volume 163. Springer Basel AG, Basel, 2013 edition, 2013;2012;.

37. Howard Elman, David Silvester, and Andrew Wathen. *Finite Elements and Fast Iterative Solvers: With Applications in Incompressible Fluid Dynamics*, volume 557. Cambridge University Press (CUP), 01 2006.
38. P. Englezos, N. Kalogerakis, P. D. Dholabhai, and P. R. Bishnoi. Kinetics of formation of methane and ethane gas hydrates. *Chemical Engineering Science*, 42(11):2647–2658, 1987.
39. Mallory R. Frederick, Christina Kuttler, Burkhard A. Hense, and Hermann J. Eberl. A mathematical model of quorum sensing regulated eps production in biofilm communities. *Theoretical Biology and Medical Modelling*, 8(1):8–8, 2011.
40. S. K. Garg, J. W. Pritchett, A. Katch, K. Baba, and T. Fijii. A mathematical model for the formation and dissociation of methane hydrates in the marine environment. *Journal of Geophysical Research*, 113:B08201, 2008.
41. Nathan L. Gibson, F. Patricia Medina, Malgorzata Peszynska, and Ralph E. Showalter. Evolution of phase transitions in methane hydrate. *Journal of Mathematical Analysis and Applications*, 409(2):816 – 833, 2014.
42. V. GIRAULT and H. LOPEZ. Finite-element error estimates for the MAC scheme. *IMA Journal of Numerical Analysis*, 16(3):347–379, 07 1996.
43. Roland Glowinski. *Numerical methods for nonlinear variational problems*. Springer Series in Computational Physics. Springer-Verlag, New York, 1984.
44. Edwige Godlewski and Pierre-Arnaud Raviart. *Numerical approximation of hyperbolic systems of conservation laws*. Springer, New York, 1996.
45. Romain Guibert, Pierre Horgue, Debenest Gerald, and Michel Quintard. A comparison of various methods for the numerical evaluation of porous media permeability tensors from pore-scale geometry. *Mathematical geosciences*, 48(3):329–347, 04 2016.
46. Romain Guibert, Pierre Horgue, Debenest Gerald, and Michel Quintard. A comparison of various methods for the numerical evaluation of porous media permeability tensors from pore-scale geometry. *Mathematical geosciences*, 48(3):329–347, 04 2016.
47. Bo Guo, Yashar Mehmani, and Hamdi Tchelepi. Multiscale formulation of pore-scale compressible darcy-stokes flow. *Journal of Computational Physics*, 397:108849, 07 2019.
48. Shubhangi Gupta, Rainer Helmig, and Barbara Wohlmuth. Non-isothermal, multi-phase, multi-component flows through deformable methane hydrate reservoirs. *Computational Geosciences*, 19(5):1063–1088, sep 2015.
49. Shubhangi Gupta, Barbara Wohlmuth, and Rainer Helmig. Multi-rate time stepping schemes for hydro-geomechanical model for subsurface methane hydrate reservoirs. *Advances in Water Resources*, 91(C):78–87, may 2016.
50. Houde Han and Xiaonan Wu. A new mixed finite element formulation and the MAC method for the stokes equations. *SIAM Journal on Numerical Analysis*, 35(2):560–571, apr 1998.

51. Francis H. Harlow and J. Eddie Welch. Numerical calculation of time-dependent viscous incompressible flow of fluid with free surface. *Physics of Fluids*, 8(12):2182, 1965.
52. P. Henry, M. Thomas, and M. B. Clennell. Formation of natural gas hydrates in marine sediments: 2. thermodynamic calculations of stability conditions in porous sediments. *Journal of Geophysical Research*, 104:23,005–23,022, 1999.
53. Wei-Li Hong and Malgorzata Peszynska. Geochemical aspects. In Daviel Broseta, Livio Ruffine, and Arnaud Desmedt, editors, *Gas Hydrates 2: Geoscience Issues and Potential Industrial Applications*, pages 219–241. Wiley, 2018. Numerical modeling of gas hydrate dynamics in nature marine sediments: Case studies from Hydrate Ridge, Cascadia Margin and Ulleung Basin.
54. Ulrich Hornung and R. E. Showalter. Elliptic-parabolic equations with hysteresis boundary conditions. *SIAM Journal on Mathematical Analysis*, 26(4):775, 1995.
55. S. J. Hunter, D. S. Goldobin, A. M. Haywood, A. Ridgwell, and J. G. Rees. Sensitivity of the global submarine hydrate inventory to scenarios of future climate change. *Earth and Planetary Science Letters*, 367:105–115, 2013.
56. M.R Islam. A new recovery technique for gas production from Alaskan gas hydrates. *Journal of Petroleum Science and Engineering*, 11(4):267–281, 1994.
57. Pahala G. Jayathilake, Saikat Jana, Steve Rushton, David Swailes, Ben Bridgens, Tom Curtis, and Jinju Chen. Extracellular polymeric substance production and aggregated bacteria colonization influence the competition of microbes in biofilms. *Frontiers in Microbiology*, 8:1865–1865, 2017.
58. Claes Johnson. A convergence estimate for an approximation of a parabolic variational inequality. *SIAM J. Numer. Anal.*, 13(4):599–606, 1976.
59. K. H. Karlsen and J.D. Towers. Convergence of the Lax-Friedrichs scheme and stability for conservation laws with a discontinuous space-time dependent flux. *Chinese Annals of Mathematics*, 25(3):287–318, 2004.
60. Kenneth Karlsen.  $L^1$  stability for entropy solutions of nonlinear degenerate parabolic convection-diffusion equations with discontinuous coefficients. *Skrifter. Det Kongelige Norske Videnskabers Selskab. Transactions of the Royal Norwegian Society of Sciences and Letters*, pages 1–49, 2003.
61. C. T. Kelley. *Iterative Methods for Linear and Nonlinear Equations*. Society for Industrial and Applied Mathematics, jan 1995.
62. H. C. Kim, P. R. Bishnoi, R. A. Heidemann, and S. S. H. Rizvi. Kinetics of methane hydrate decomposition. *Chemical Engineering Science*, 42(7):1645–1653, 1987.
63. I. Klapper and J. Dockery. Finger formation in biofilm layers. *SIAM Journal on Applied Mathematics*, 62(3):853–869, 2002.
64. Isaac Klapper and Jack Dockery. Mathematical description of microbial biofilms. *SIAM Review*, 52(2):221–265, 2010.

65. Jisheng Kou and Shuyu Sun. A new treatment of capillarity to improve the stability of impes two-phase flow formulation. *Computers & fluids*, 39(10):1923–1931, 2010.
66. Jan-Ulrich Kreft, Cristian Picioreanu, Mark C. M van Loosdrecht, and Julian W. T. Wimpenny. Individual-based modelling of biofilms. *Microbiology (Society for General Microbiology)*, 147(11):2897–2912, 2001.
67. Marcin Krotkiewski, Ingeborg S. Ligaarden, Knut-Andreas Lie, and Daniel W. Schmid. On the importance of the stokes-brinkman equations for computing effective permeability in karst reservoirs. *Communications in Computational Physics*, 10(5):1315–1332, nov 2011.
68. S. N. Kruzhkov. The Cauchy problem in the large for certain nonlinear first-order differential equations. *Dokl. Akad. Nauk SSSR*, 132:36–39, 1960.
69. N.N Kuznetsov. Accuracy of some approximate methods for computing the weak solutions of a first-order quasi-linear equation. *USSR Computational Mathematics and Mathematical Physics*, 16(6):105–119, 1976.
70. David Landa-Marbán, Gunhild Bødtker, Kundan Kumar, Iuliu S. Pop, and Florin A. Radu. An upscaled model for permeable biofilm in a thin channel and tube. *Transport in Porous Media*, 132(1):83–112, 2020.
71. David Landa-Marbán, Na Liu, Iuliu S. Pop, Kundan Kumar, Per Pettersson, Gunhild Bødtker, Tormod Skauge, and Florin A. Radu. A pore-scale model for permeable biofilm: numerical simulations and laboratory experiments. *Transport in Porous Media*, 127(3):643–660, 2018;2019;.
72. Antonio C. Lasaga. *Kinetic Theory in the Earth Sciences*, volume 402. Princeton university press, 2014.
73. Randall J. LeVeque. *Numerical Methods for Conservation Laws*. Lectures in Mathematics. ETH Zürich. Birkhäuser Basel : Imprint: Birkhäuser, Basel, second edition. edition, 1992.
74. Randall J. LeVeque. *Finite Volume Methods for Hyperbolic Problems*. Cambridge texts in applied mathematics. Cambridge University Press, Cambridge ; New York, 2002.
75. Randall J. LeVeque. *Finite difference methods for ordinary and partial differential equations*. Society for Industrial and Applied Mathematics (SIAM), Philadelphia, PA, 2007. Steady-state and time-dependent problems.
76. Jichun Li and Shuyu Sun. The superconvergence phenomenon and proof of the MAC scheme for the stokes equations on non-uniform rectangular meshes. *Journal of Scientific Computing*, 65(1):341–362, dec 2014.
77. Yanghui Li, Mingjun Yang, Jiafei Zhao, Haifeng Liang, Yongchen Song, and Xuke Ruan. Numerical simulation of methane production from hydrates induced by different depressurizing approaches. *Energies*, 5(2):438–458, feb 2012.

78. Dominique H. Limoli, Christopher J. Jones, and Daniel J. Wozniak. Bacterial extracellular polysaccharides in biofilm formation and function. *Microbial Biofilms*, pages 223–247, 2015.
79. X. Liu and P. B. Flemings. Passing gas through the hydrate stability zone at southern hydrate ridge, offshore Oregon. *EPSL*, 241:211–226, 2006.
80. X. Liu and P. B. Flemings. Dynamic multiphase flow model of hydrate formation in marine sediments. *Journal of Geophysical Research*, 112:B03101, 2008.
81. Xiaoli Liu and Peter B. Flemings. Capillary effects on hydrate stability in marine sediments. *Journal of Geophysical Research: Solid Earth (1978–2012)*, 116(B7), 2011.
82. Lin Longwei, Blake Temple, and Wang Jinghua. Suppression of oscillations in Godunovs method for a resonant non-strictly hyperbolic system. *SIAM Journal on Numerical Analysis*, 32(3):841–864, 1995.
83. Bradley J. Lucier. Error bounds for the methods of Glimm, Godunov and LeVeque. *SIAM Journal on Numerical Analysis*, 22(6):1074–1081, 1985.
84. F. A. MacLeod, H. M. Lappin-Scott, and J. W. Costerton. Plugging of a model rock system by using starved bacteria. *Applied and Environmental Microbiology*, 54(6):1365–1372, 1988.
85. Neal Noah Madras. *Lectures on Monte Carlo Methods*. American Mathematical Soc., 2002.
86. Tatsuo Maekawa, Shiro Itoh, Susumu Sakata, Shun-Ichiro Igari, and Noboru Imai. Pressure and temperature conditions for methane hydrate dissociation in sodium chloride solutions. *Geochemical Journal*, 29(5):325–329, 1995.
87. A. Malinverno, M. Kastner, M.E. Torres, and U.G. Wortmann. Gas hydrate occurrence from pore water chlorinity and downhole logs in a transect across the northern Cascadia margin (integrated ocean drilling program expedition 311). *Journal of Geophysical Research*, 113:B08103, 2008.
88. Héctor Marín-Moreno, Michela Giustiniani, Umberta Tinivella, and Elena Piñero. The challenges of quantifying the carbon stored in arctic marine gas hydrate. *Marine and Petroleum Geology*, 71:76–82, Mar 2016.
89. Nicholas Metropolis, Arianna W. Rosenbluth, Marshall N. Rosenbluth, Augusta H. Teller, and Edward Teller. Equation of state calculations by fast computing machines. *The Journal of Chemical Physics*, 21(6):1087–1092, June 1953.
90. A Moncorgé, H.A Tchelepi, and P Jenny. Modified sequential fully implicit scheme for compositional flow simulation. *Journal of Computational Physics*, 337:98–115, 2017.
91. Fernando A Morales and Ralph E Showalter. A Darcy–Brinkman model of fractures in porous media. *Journal of Mathematical Analysis and Applications*, 452(2):1332–1358, 2017.

92. George J. Moridis, Timothy S. Collett, Scott R. Dallimore, Tohru Satoh, Steven Hancock, and Brian Weatherill. Numerical studies of gas production from several  $CH_4$  hydrate zones at the Mallik site, Mackenzie Delta, Canada. *Journal of Petroleum Science and Engineering*, 43(3-4):219–238, 2004.
93. George J Moridis and E. Dendy Sloan. Gas production potential of disperse low-saturation hydrate accumulations in oceanic sediments. *Energy Conversion and Management*, 48(6):1834–1849, 2007.
94. J. Nimblett and C. Ruppel. Permeability evolution during the formation of gas hydrates in marine sediments. *Journal of Geophysical Research*, 108:B9, 2420, 2003.
95. Naoki Nishiyama and Tadashi Yokoyama. Permeability of porous media: role of the critical pore size: critical pore size-permeability relation. *Journal of Geophysical Research. Solid Earth*, 122(9):6955–6971, 2017.
96. T.L Noorden, van, I. S. Pop, A. Ebigbo, and R. Helmig. An upscaled model for biofilm growth in a thin strip. *Water Resources Research*, 46(6):W06505–1/14, 2010.
97. J Alberto Ochoa-Tapia and Stephen Whitaker. Momentum transfer at the boundary between a porous medium and a homogeneous fluid—i. theoretical development. *International Journal of Heat and Mass Transfer*, 38(14):2635–2646, 1995.
98. J Alberto Ochoa-Tapia and Stephen Whitaker. Momentum transfer at the boundary between a porous medium and a homogeneous fluid—ii. comparison with experiment. *International Journal of Heat and Mass Transfer*, 38(14):2647–2655, 1995.
99. M. Ossiander, M. Peszynska, and V. Vasylykivska. Conditional stochastic simulations of flow and transport with karhunen-loeve expansions, stochastic collocation, and sequential gaussian simulation. *Journal of Applied Mathematics*, Volume 2014:21 pages, 2014.
100. Mina Ossiander, Malgorzata Peszynska, Lisa Madsen, Alan Mur, and William Harbert. Estimation and simulation for geospatial porosity and permeability data. *Environmental and Ecological Statistics*, 24(1):109–130, 2017.
101. Jong-Shi Pang. Newton's method for b-differentiable equations. *Mathematics of Operations Research*, 15(2):311–341, may 1990.
102. S.V. Patankar. *Numerical heat transfer and fluid flow*. Series in Computational Methods in Mechanics and Thermal Sciences. Routledge, 1980.
103. M. Peszynska. Never Heard of Methane Hydrate? That Might be Good News. *SIAM News*, January 2018.
104. M. Peszynska, E. Jenkins, and M. F. Wheeler. Boundary conditions for fully implicit two-phase flow model. In Xiaobing Feng and Tim P. Schulze, editors, *Recent Advances in Numerical Methods for Partial Differential Equations and Applications*, volume 306 of *Contemporary Mathematics Series*, pages 85–106. American Mathematical Society, 2002.

105. M. Peszynska, Q. Lu, and M. F. Wheeler. Coupling different numerical algorithms for two phase fluid flow. In J. R. Whiteman, editor, *MAFELAP Proceedings of Mathematics of Finite Elements and Applications*, pages 205–214, Uxbridge, U.K., 1999. Brunel University.
106. M. Peszynska and C. Shin. Stability of a numerical scheme for methane transport in hydrate zone under equilibrium and non-equilibrium conditions. 2021 (in press).
107. M. Peszynska, R. Showalter, and J. Webster. Advection of methane in the hydrate zone: Model, analysis and examples. *Mathematical Methods in Applied Sciences*, 38:4613–4629, November 2015.
108. M. Peszynska and A. Trykozko. Pore-to-core simulations of flow with large velocities using continuum models and imaging data. *Computational Geosciences*, 17:623–645, 2013. DOI: 10.1007/s10596-013-9344-4.
109. Malgorzata Peszynska and Trykozko Anna. Convergence and stability in upscaling of flow with inertia from porescale to mesoscale. *International Journal for Multiscale Computational Engineering*, 9(2):215–229, 2011.
110. Malgorzata Peszynska, Wei-Li Hong, Marta E. Torres, and Ji-Hoon Kim. Methane Hydrate Formation in Ullung Basin Under Conditions of Variable Salinity: Reduced Model and Experiments. *Transport in Porous Media*, 114:1–27, 2016.
111. Malgorzata Peszynska, Francis Patricia Medina, Wei-Li Hong, and Marta E Torres. Reduced numerical model for methane hydrate formation under conditions of variable salinity. time-stepping variants and sensitivity. *Computation*, 4(1):1, 2015.
112. Malgorzata Peszynska and Shuyu Sun. Reactive transport module TRCHEM in IPARS. Technical report, TICAM Report 01-32, 2001.
113. Malgorzata Peszynska and Shuyu Sun. Reactive transport model coupled to multiphase flow models. In S. M. Hassanizadeh, R.J. Schotting, W.G. Gray, and G.F. Pinder, editors, *Computational Methods in Water Resources*, pages 923–930. Elsevier, 2002.
114. Malgorzata Peszynska, Anna Trykozko, Gabriel Iltis, Steffen Schlueter, and Dorthe Wildenschild. Biofilm growth in porous media: Experiments, computational modeling at the porescale, and upscaling. *Advances in water resources*, 95:288–301, 2016.
115. Malgorzata Peszynska, Joseph Umhoefer, and Choah Shin. Reduced model for properties of multiscale porous media with changing geometry. *Computation*, 9(3):28, mar 2021.
116. Cristian Picioreanu, Mark C. M van Loosdrecht, and Joseph J. Heijnen. Mathematical modeling of biofilm structure with a hybrid differential-discrete cellular automaton approach. *Biotechnology and Bioengineering*, 58(1):101–116, 1998.
117. Cristian Picioreanu, Mark C. M van Loosdrecht, and Joseph J. Heijnen. A new combined differential-discrete cellular automaton approach for biofilm modeling: Application for growth in gel beads. *Biotechnology and Bioengineering*, 57(6):718–731, 1998.

118. SJ Pirt. A kinetic study of the mode of growth of surface colonies of bacteria and fungi. *Microbiology*, 47(2):181–197, 1967.
119. L. Qi and Jie Sun. A nonsmooth version of newton’s method. *Math. Program.*, 58:353–367, 01 1993.
120. Florin Adrian Radu, Jan Martin Nordbotten, Iuliu Sorin Pop, and Kundan Kumar. A robust linearization scheme for finite volume based discretizations for simulation of two-phase flow in porous media. *Journal of Computational and Applied Mathematics*, 289:134–141, 2015.
121. A. W. Rempel. A model for the diffusive growth of hydrate saturation anomalies in layered sediments. *Journal of Geophysical Research*, 116(B10), Oct 2011.
122. A. W. Rempel and B. A. Buffett. Formation and accumulation of gas hydrate in porous media. *Journal of Geophysical Research: Solid Earth*, 102(B5):10151–10164, may 1997.
123. Benjamin Rostron. Multiphase flow in permeable media. a pore-scale perspective: Book review. *Groundwater*, 56, 08 2018.
124. Carolyn Ruppel. Tapping methane hydrates for unconventional natural gas. *Elements*, 3(3):193–199, 2007.
125. T. F. Russell and M. F. Wheeler. Finite element and finite difference methods for continuous flows in porous media. In R. E. Ewing, editor, *The Mathematics of Reservoir Simulation*, pages 35–106. SIAM, Philadelphia, 1983.
126. Iryna Rybak, Christoph Schwarzmeier, Elissa Eggenweiler, and Ulrich Rüde. Validation and calibration of coupled porous-medium and free-flow problems using pore-scale resolved models. *Computational Geosciences*, page arXiv:1906.06884, sep 2020.
127. Ulrich Rüde, Karen Willcox, Lois Curfman McInnes, and Hans De Sterck. Research and education in computational science and engineering. *SIAM Review*, 60(3):707–754, jan 2018.
128. Florin Sabac. The optimal convergence rate of monotone finite difference methods for hyperbolic conservation laws. *SIAM Journal on Numerical Analysis*, 34(6):2306–2318, 1997.
129. Riccardo Sacco, Paola Causin, Chiara Lelli, and Manuela T. Raimondi. A poroelastic mixture model of mechanobiological processes in biomass growth: theory and application to tissue engineering. *Meccanica (Milan)*, 52(14):3273–3297, 2017.
130. Steffen Schlüter, Adrian Sheppard, Kendra Brown, and Dorthe Wildenschild. Image processing of multiphase images obtained via x-ray microtomography: a review. *Water Resources Research*, 50(4):3615–3639, 2014.
131. Choah Shin, , Azhar Alhammali, Lisa Bigler, Naren Vohra, and Malgorzata Peszynska. Coupled flow and biomass-nutrient growth at pore-scale with permeable biofilm, adaptive singularity and multiple species. *Mathematical Biosciences and Engineering*, 18(3):2097–2149, 2021.

132. Choah Shin. Coupled biomass-nutrient-flow simulation code for bio2020 project, 2020.
133. Ronald W. Shonkwiler and Franklin Mendivil. *Explorations in Monte Carlo Methods*. Springer Science & Business Media, 2009.
134. R. E. Showalter. *Monotone operators in Banach space and nonlinear partial differential equations*, volume 49 of *Mathematical Surveys and Monographs*. American Mathematical Society, Providence, RI, 1997.
135. R.E. Showalter. *Hilbert Space Methods for Partial Differential Equations*. Electronic library of mathematics. Pitman, 1977.
136. E. D. Sloan and C. A. Koh. *Clathrate Hydrates of Natural Gases*, volume 130. CRC Press, third edition, 2009.
137. Andrew J. Smith, Peter B. Flemings, Xiaoli Liu, and Kristopher Darnell. The evolution of methane vents that pierce the hydrate stability zone in the world's oceans. *Journal of Geophysical Research: Solid Earth*, 119(8):6337–6356, 2014.
138. Tao Tang and Zhen Huan Teng. The sharpness of Kuznetsov's  $O(\sqrt{\Delta x})$   $l^1$ -error estimate for monotone difference schemes. *Mathematics of Computation*, 64(210):581–589, 1995.
139. Youneng Tang, Albert J. Valocchi, Charles J. Werth, and Haihu Liu. An improved pore-scale biofilm model and comparison with a microfluidic flow cell experiment. *Water Resources Research*, 49(12):8370–8382, 2013.
140. Luc Tartar. Incompressible fluid flow in a porous medium—convergence of the homogenization process. In *Nonhomogeneous media and vibration theory*, volume 127 of *Lecture Notes in Physics*, pages 368–377. Springer-Verlag, Berlin, 1980.
141. C. E. Taylor, D. D. Link, and N. English. Methane hydrate research at NETL Research to make methane production from hydrates a reality. *JPSE*, 56:186–191, 2007.
142. The National Methane Hydrates R&D Program. <http://www.netl.doe.gov/technologies/oil-gas/FutureSupply/MethaneHydrates/maincontent.htm>.
143. The National Methane Hydrates R&D Program Methane Hydrate Reservoir Simulator Code Comparison Study. [http://www.netl.doe.gov/technologies/oil-gas/FutureSupply/MethaneHydrates/MH\\_CodeCompare/MH\\_CodeCompare.html](http://www.netl.doe.gov/technologies/oil-gas/FutureSupply/MethaneHydrates/MH_CodeCompare/MH_CodeCompare.html).
144. Martin Thullner. Comparison of bioclogging effects in saturated porous media within one-and two-dimensional flow systems. *Ecological Engineering*, 36(2):176–196, 2010.
145. Martin Thullner, Josef Zeyer, and Wolfgang Kinzelbach. Influence of microbial growth on hydraulic properties of pore networks. *Transport in Porous Media*, 49(1):99–122, 2002.
146. Pavel Tishchenko, Christian Hensen, Klaus Wallmann, and Chi Shing Wong. Calculation of the stability and solubility of methane hydrate in seawater. *Chemical Geology*, 219(1-4):37–52, jun 2005.

147. M. E. Torres, K. Wallmann, A. M. Tréhu, G. Bohrmann, W. S. Borowski, and H. Tomaru. Gas hydrate growth, methane transport, and chloride enrichment at the southern summit of Hydrate Ridge, Cascadia margin off Oregon. *Earth and Planetary Science Letters*, 226(1-2):225 – 241, 2004.
148. John D. Towers. Convergence of a difference scheme for conservation laws with a discontinuous flux. *SIAM Journal on Numerical Analysis*, 38(2):681–698, 2000.
149. Michael Ulbrich. Semismooth newton methods for operator equations in function spaces. *SIAM Journal on Optimization*, 13(3):805–841, jan 2002.
150. Joseph Umhoefer. *Modeling Flow and Transport at Pore Scale with Obstructions*. PhD thesis, Oregon State University, 2019.
151. Brandon P. VanderBeek and Alan W. Rempel. On the importance of advective versus diffusive transport in controlling the distribution of methane hydrate in heterogeneous marine sediments. *Journal of Geophysical Research: Solid Earth*, 123(7):5394–5411, Jul 2018.
152. Augusto Visintin. *Models of phase transitions*. Progress in Nonlinear Differential Equations and their Applications, 28. Birkhäuser Boston Inc., Boston, MA, 1996.
153. Klaus Wallmann, M. Riedel, W. Hong, H. Patton, A. Hubbard, T. Pape, C. Hsu, C. Schmidt, J. Johnson, M. Torres, K. Andreassen, C. Berndt, and G. Bohrmann. Gas hydrate dissociation off Svalbard induced by isostatic rebound rather than global warming. *Nat Commun*, 9(1):83–83, 2018.
154. Matthew R Walsh, Carolyn A Koh, E Dendy Sloan, Amadeu K Sum, and David T Wu. Microsecond simulations of spontaneous methane hydrate nucleation and growth. *Science (New York, N.Y.)*, 326(5956):1095–1098, 2009.
155. Alan Weiser and Mary Fanett Wheeler. On convergence of block-centered finite differences for elliptic problems. *SIAM Journal on Numerical Analysis*, 25(2):351–375, 1988.
156. M. F. Wheeler and M. Peszynska. Computational engineering and science methodologies for modeling and simulation of subsurface applications. *Advances in Water Resources*, 25(8-12):1147–1173, 2002.
157. Mary F. Wheeler and Ivan Yotov. A cell-centered finite difference method on quadrilaterals. In Douglas N. Arnold, Pavel B. Bochev, Richard B. Lehoucq, Roy A. Nicolaides, and Mikhail Shashkov, editors, *Compatible Spatial Discretizations*, pages 189–207, New York, NY, 2006. Springer New York.
158. Stephen Whitaker. Flow in porous media i: A theoretical derivation of darcy's law. *Transport in Porous Media*, 1(1):3–25, 1986.
159. Frank White. *Viscous Fluid Flow*. MCGRAW HILL BOOK CO, January 2005.
160. M. D. White, T.J. Kneafsey, Y. Seol, W. F. Waite, S. Uchida, J.S. Lin, E. M. Myshakin, X. Gai, S. Gupta, M. T. Reagan, A. F. Queiruga, S. Kimoto, Baker. R. C.,

- R. Boswell, J. Ciferno, T. Collett, J. Choi, S. Dai, M. de La Fuente, P. Fu, T. Fujii, C. G. Intihar, J. Jang, X. Ju, J. Kang, J. H. Kim, J. T. Kim, S. J. Kim, C. Koh, Y. Konno, K. Kumagai, J. Y. Lee, W. S. Lee, L. Lei, F. Liu, H. Luo, G. J. Moridis, J. Morris, M. Nole, S. Otsuki, M. Sanchez, S. Shang, C. Shin, H. S. Shin, K. Soga, X. Sun, S. Suzuki, N. Tenma, T. Xu, K. Yamamoto, Yoneda. J., C. M. Yonkofski, H. C. Yoon, K. You, Y. Yuan, L. Zerpa, and M. Zyrianova. An international code comparison study on coupled thermal, hydrologic and geomechanical processes of natural gas hydrate-bearing sediments. *Marine and Petroleum Geology*, 120:104566, oct 2020.
161. Dorthe Wildenschild and Adrian P. Sheppard. X-ray imaging and analysis techniques for quantifying pore-scale structure and processes in subsurface porous medium systems. *Advances in Water Resources*, 51:217–246, jan 2013.
162. Joseph W. Wilder, George J. Moridis, Scott J. Wilson, Masanori Kurihara, Yoshihiro Masuda, Brian J. Anderson, Timothy S. Collett, Robert B. Hunter, Hideo Narita, Mehran Pooladi-Darvish, and Ray Boswell. An international effort to compare gas hydrate reservoir simulators. In *Proceedings of the 6th International Conference on Gas Hydrates (ICGH 2008)*, volume 28, pages 493–501, 2008.
163. K. Williamson and P. Mccarty. A model of substrate utilization by bacterial films. *Water Pollution Control Federation*, 48 1:9–24, 1976.
164. Joao B. Xavier and Kevin R. Foster. Cooperation and conflict in microbial biofilms. *Proceedings of the National Academy of Sciences - PNAS*, 104(3):876–881, 2007.
165. W. Xu. Modeling dynamic marine gas hydrate systems. *American Mineralogist*, 89:1271–1279, 2004.
166. W. Xu and C. Ruppel. Predicting the occurrence, distribution, and evolution of methane hydrate in porous marine sediments. *Journal of Geophysical Research*, 104:5081–5095, 1999.
167. Catherine M.R Yonkofski, Jake A Horner, and Mark D White. Experimental and numerical investigation of hydrate-guest molecule exchange kinetics. *Journal of Natural Gas Science and Engineering*, 35:1480–1489, 2016.
168. Kehua You, Timothy J Kneafsey, Peter B Flemings, Peter Polito, and Steven L Bryant. Salinity-buffered methane hydrate formation and dissociation in gas-rich systems. *Journal of Geophysical Research: Solid Earth*, 120(2):643–661, 2015.
169. M.H Yousif, H.H Abass, M.S Selim, and E.D Sloan. Experimental and theoretical investigation of methane-gas-hydrate dissociation in porous media. *SPE (Society of Petroleum Engineers) Reservoir Engineering; (United States)*, 6(1):69–76, 1991.
170. T. Zhang and I. Klapper. Mathematical model of biofilm induced calcite precipitation. *Water Science and Technology*, 61(11):2957–2964, 2010.
171. Tianyu Zhang, N. G. Cogan, and Qi Wang. Phase-field models for biofilms. i. theory and one-dimensional simulations. *SIAM Journal on Applied Mathematics*, 69(3):641–669, 2008.

172. Youxue Zhang. *Geochemical Kinetics*. Princeton University Press, Princeton, N.J., 2008.